

UNIVERSITY OF CALIFORNIA

Los Angeles

Studies of Weak Boson - Photon Production in
 $\sqrt{s} = 1.8 \text{ TeV}$ $p\bar{p}$ Collisions at the Tevatron
Collider.

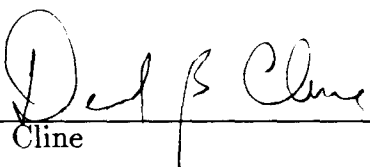
A dissertation submitted in partial satisfaction of the
requirements for the degree Doctor of Philosophy
in Physics

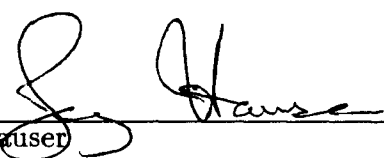
by

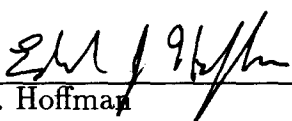
Dirk Neuberger

1995

The dissertation of Dirk Neuberger is approved.


D. Cline


J. Hauser


E. Hoffman


T. Müller, Committee Chair

University of California, Los Angeles

1995

Contents

List of Figures	vi
List of Tables	xi
Acknowledgements	xv
Vita	xvii
Abstract of the Dissertation	xix
1 Introduction	1
1.1 General Overview	1
1.2 Organization of the Thesis	4
2 Theoretical Background	6
2.1 $W\gamma$ Couplings	7
2.2 $Z\gamma$ Couplings	17
2.3 Unitarity Constraints	20
3 Present Experimental Knowledge	23
3.1 The Coupling Parameters κ , λ , $\tilde{\kappa}$ and $\tilde{\lambda}$	23
3.2 The Coupling Parameters h_{i0}	26
3.3 WW , WZ and ZZ Couplings	27
4 The Experimental Apparatus	29
4.1 The Tevatron	29
4.2 The CDF Detector	32
4.2.1 Calorimeters	34
4.2.2 Tracking	38
4.2.3 Event Reconstruction	40
4.2.4 Triggering	46
4.2.5 Data Acquisition	48

5	Particle Identification	50
5.1	W and Z Boson Selection	50
5.2	Photon Selection	53
5.3	Monte Carlo Programs	55
5.3.1	The Baur $W\gamma/Z\gamma$ Monte Carlo	56
5.3.2	Detector Simulations	58
5.3.3	Other Monte Carlo Programs	58
5.4	Efficiencies	59
5.4.1	Photon Efficiencies	59
5.4.2	Electron Efficiencies	64
5.5	Acceptances	65
5.6	Systematic Uncertainties	68
5.6.1	Background	68
5.6.2	Monte Carlo Simulations	68
6	Background	72
6.1	QCD Jet Fragmentation Background	72
6.1.1	Discussion	78
6.2	Others Background Sources	83
6.3	Error Determination	84
6.4	Signal to Background Summary	87
7	Analysis Results	88
7.1	Measurement of $\sigma \cdot B(Z\gamma \rightarrow e^+e^-\gamma)$ and $\sigma \cdot B(W\gamma \rightarrow e\nu_e\gamma)$	88
7.2	Kinematic Distributions	90
7.3	Anomalous W-Photon and Z-Photon Couplings	95
7.4	Electromagnetic Moments of the W and Z Bosons	104
8	Results from the Ongoing Tevatron Run	108
8.1	Preliminary Measurement of $\sigma \cdot B(W\gamma \rightarrow e\nu_e\gamma)$ and $\sigma \cdot B(Z\gamma \rightarrow e^+e^-\gamma)$	109
8.2	Kinematic Distributions	110
8.3	Preliminary Limits on Anomalous Couplings	116
9	$W\gamma$ Production at High Photon Rapidities	120
9.1	Event selection	121
9.2	Efficiencies	125
9.3	Background	130
9.3.1	Comparison of the Shower Profile Method with the <i>EMF7</i> Method	145
9.4	Kinematic Distributions	147
9.5	Asymmetries in Photon Rapidity Distributions	150

10 Conclusions	154
10.1 Summary of Results	154
10.2 Other Measurements of Vector Boson Self-Interactions at CDF and DØ	157
10.3 The Future	160
10.3.1 Anomalous Couplings at the Hadron Colliders TEV * and LHC	161
10.3.2 Anomalous Couplings at the e^+e^- Colliders LEP II and NLC	165
A Summary of Limits	168
B Jet Identification	173
C Electron Efficiencies	175

List of Figures

2.1	Lowest order $W\gamma$ Feynman diagrams in hadron collisions. Lines with arrows pointing to the right (left) symbolize incoming (outgoing) fermions, bosons are represented by curly lines.	8
2.2	Monte Carlo simulation of the a) $\cos \Theta^*$, and b) W charge-signed pseudorapidity difference in $W\gamma$ processes ($E_T^\gamma > 7$ GeV), using Standard Model and anomalous coupling parameters. Θ^* is the angle between the photon and incoming quark in the $W\gamma$ center-of-mass frame.	13
2.3	Simulated photon E_T distribution in $W\gamma$ processes for Standard Model and anomalous coupling parameters.	15
2.4	Monte Carlo simulation of the a) transverse cluster mass and b) photon - lepton separation spectrum in $W\gamma$ processes ($E_T^\gamma > 7$ GeV), using Standard Model and anomalous coupling parameters.	16
2.5	Lowest order $Z\gamma$ Feynman diagrams. Lines with arrows pointing to the right (left) symbolize incoming (outgoing) fermions, bosons are represented by curly lines.	18
3.1	Loop-order flavor changing Feynman diagram $b \rightarrow s + \gamma$ involving a $WW\gamma$ vertex.	24
3.2	Loop diagram contributions to the anomalous electromagnetic moment of the muon, a) involving a $WW\gamma$ vertex, b) involving a $Z\gamma\gamma$ vertex.	25
4.1	Schematic view of the Tevatron Collider.	30
4.2	Schematic view of one half of the CDF detector. The other half is the mirror image of this picture. For an explanation of the acronyms, see the text.	31
4.3	Segmentation and coverage of the CDF calorimeters.	34
4.4	Light gathering system of a CEM wedge consisting of ten towers.	35
4.5	Schematic view of the anode wires and cathode strips in the Central Strip Chamber.	36
4.6	End view of the Central Tracking Chamber showing the location of the slots in the aluminum endplates.	38
4.7	Central Tracking Chamber efficiency as a function of pseudorapidity.	46

5.1	Isolation efficiency as a function of the transverse energy cut value, determined from random cone studies in the electron $W\gamma$ sample.	61
5.2	a) Observed number of fiducial electromagnetic CEM clusters in the P16 sample as a function of transverse energy. The data points above 6 GeV fit well to an exponential (see inset). The event decrease at low energies is due to a clustering algorithm inefficiency. b) Corresponding efficiency distribution. QFL Monte Carlo results are compared to data.	63
5.3	$W\gamma$ Baur plus Fast Monte Carlo prediction for various structure functions.	69
6.1	Jet fragmentation probability in neutral mesons that fake a photon as a function of E_T determined from the P16 QCD data sample. The bin sizes are chosen according to the $W\gamma$ ($Z\gamma$) analysis.	76
6.2	Comparison of the jet fragmentation probability for two different sets of photon selection requirements.	80
6.3	Comparison of jet fragmentation probabilities in the combined electron + muon $W\gamma$ sample and in the P16 sample with a) no direct photon subtraction, b) subtraction of direct photons using the shower profile method.	82
7.1	Comparison of observed to predicted a) transverse photon energy b) $ee\gamma$ three-body mass spectrum for Z + central photon events in $\approx 20 \text{ pb}^{-1}$ electron + muon data.	91
7.2	Comparison of observed to predicted photon transverse energy spectrum for W + central photon events in $\approx 20 \text{ pb}^{-1}$ electron + muon data. For illustration, the Standard Model prediction plus background estimate and the background distribution are plotted in the bin sizes of a) 4 GeV (default) and b) 1 GeV.	92
7.3	Comparison of the observed to predicted spectrum of the photon-lepton separation, $\Delta R_{e\gamma}$, for W + central photon events in $\approx 20 \text{ pb}^{-1}$ electron + muon data.	93
7.4	Comparison of observed to predicted transverse cluster mass spectrum for W + central photon events in $\approx 20 \text{ pb}^{-1}$ electron + muon data.	94
7.5	Negative log-likelihood distributions for the \mathcal{CP} -conserving couplings $\Delta\kappa$ and λ in the individual electron channel (a and b) and combined electron + muon channel (c and d).	96
7.6	Negative log-likelihood distributions for the \mathcal{CP} -violating couplings $\tilde{\kappa}$ and $\tilde{\lambda}$ in the individual electron channel (a and b) and combined electron + muon channel (c and d).	97

7.7	Negative log-likelihood distributions for the \mathcal{CP} -violating (\mathcal{CP} -conserving) couplings h_{10}^Z (h_{30}^Z) and h_{20}^Z (h_{40}^Z) in the individual electron channel (a and b) and combined electron + muon channel (c and d).	98
7.8	Negative log-likelihood distributions for the \mathcal{CP} -violating (\mathcal{CP} -conserving) couplings h_{10}^γ (h_{30}^γ) and h_{20}^γ (h_{40}^γ) in the individual electron channel (a and b) and combined electron + muon channel (c and d).	99
7.9	Limit contours at 68%, 90% and 95% CL (inner, middle and outer ellipse) for the W-photon coupling pairs $(\Delta\kappa, \lambda)$ and $(\tilde{\kappa}, \tilde{\lambda})$ in the individual electron channel and combined electron + muon channel. Displayed are also the theoretical WW and $W\gamma$ unitarity bounds, and the axes on which either the dipole or the quadrupole moment of the W boson vanishes.	100
7.10	Limit contours at 68%, 90% and 95% CL (inner, middle and outer ellipse) for the Z-photon coupling pairs (h_{10}^Z, h_{30}^Z) and (h_{20}^Z, h_{40}^Z) in the individual electron channel and combined electron + muon channel. Displayed are also the theoretical ZZ γ unitarity bounds.	101
7.11	Limits on electromagnetic W moments at 68%, 90% and 95% CL (inner, middle and outer ellipse) in the electron and combined electron + muon channel. Displayed are also the theoretical WW and $W\gamma$ unitarity bounds, and the axes on which either the coupling λ or κ would vanish.	105
7.12	Limits on electromagnetic transition moments for Z γ processes at 68%, 90% and 95% CL (inner, middle and outer ellipse) in the individual electron and combined electron + muon channel. Displayed are also the theoretical ZZ γ unitarity bounds.	107
8.1	Lego plot of a Z γ event with a $E_T \sim 200$ GeV photon. Shown is a (η, ϕ) projection of the CDF calorimeters. The two electron clusters are located to the right of the photon cluster.	112
8.2	Display of the photon energy deposition in ‘tower 6’ of the Central Electromagnetic Calorimeter. The corresponding projections of the shower profile is shown in the CES strip chamber histograms. (The box to the very right represents the CPR response, which can be ignored here.)	113
8.3	Cross section of the Central Tracking Chamber (not to scale). Two opposite-signed, three-dimensional high P_T tracks are pointing electron clusters (shaded boxes). No high P_T track is associated with the photon cluster. Several low P_T track below ≈ 2 GeV are also shown.	114
8.4	Comparison of observed to predicted a) transverse photon energy b) $ee\gamma$ three-body mass spectrum for Z + central photon events in preliminary 67 pb^{-1} electron + muon data.	115

8.5	Comparison of observed to predicted transverse photon energy spectrum for $W +$ central photon events in preliminary 67 pb^{-1} electron + muon data. Four events with the following photon transverse energies are outside the plotted range: 37 GeV, 46 GeV, 48 GeV and 49 GeV.	116
8.6	Comparison of observed to predicted a) photon-lepton separation, b) transverse cluster mass spectrum for $W +$ central photon events in preliminary 67 pb^{-1} electron + muon data.	117
8.7	Comparison of limit contours at 95% CL for the \mathcal{CP} -conserving coupling pair $(\Delta\kappa, \lambda)$, measured at hadron colliders between the years 1988 and 1995.	118
9.1	Two-dimensional projection of the CDF calorimeters into the (η, ϕ) space. The height of the towers represents the electromagnetic energy deposition of a 30 GeV central W decay electron (right tower) and a 41 GeV plug photon. The ellipses around the tower mark the boundaries of a cone with radius $\Delta R_{e\gamma} = 0.7$	123
9.2	Projection of the photon shower profile in the η - and ϕ -views, as measured by the plug calorimeter (CAL) and strip chamber (STRIP).	124
9.3	Track display of the W decay electron of a $W +$ plug photon event in the Central Tracking Chamber (straight line). The shaded box represents the corresponding energy deposition. The arrow point in the direction of the neutrino momentum vector ('missing energy').	124
9.4	HAD/EM cut values at an energy dependent efficiency of 95% for three sets of bin sizes, determined using P15 plug triggers.	128
9.5	$EMF7$ spectra for photons from 'hybrid' Monte Carlo studies in the photon trigger sample P23 for each analysis bin.	133
9.6	Comparison of the 'W+jet' jet $EMF7$ spectrum (solid line) with the P23 ' $\chi^2_{3 \times 3} > 6$ ' jet $EMF7$ spectrum (dashed line), as defined in the text, for the first two analysis bins.	134
9.7	The P23 ' $\chi^2_{3 \times 3} > 6$ ' jet $EMF7$ spectrum in the rapidity region not covered by the PES, after applying all plug photon analysis requirements (except $\chi^2_{3 \times 3} < 5$) for each analysis bin.	136
9.8	P23 $EMF7$ distributions in the plug region covered by the PES for each analysis bin. The dashed line shows the spectrum of the direct photon contamination.	138
9.9	P23 $EMF7$ distributions in the plug region not covered by the PES for each analysis bin. The dashed line shows the spectrum of the direct photon contamination.	139
9.10	Transverse photon energy spectrum for central $W +$ plug photon events.	148
9.11	Transverse cluster mass distribution for central $W +$ plug photon events.	149

9.12	Charge-signed photon pseudorapidity distribution for central W + plug photon events.	150
9.13	Charge-signed pseudorapidity difference between the photon and the W decay lepton in central W + plug photon events.	151
9.14	Photon-lepton pseudorapidity difference, $d\hat{\sigma}/d\Delta\eta(\gamma, \ell^+)$ for $W^+\gamma$ processes, calculated with the Baur Monte Carlo in the Born approximation. The following interactions were simulated: sea - sea quark (dotted line), sea - valence quark (dash-dotted line) and valence - valence quark (dashed line). The solid line shows the sum of these contributions. The plot is taken from Ref. [19], where also the corresponding selection cuts are discussed.	152
10.1	Comparison of two-dimensional limit contours at 95% CL for the \mathcal{CP} -conserving couplings λ and $\Delta\kappa$ measured by CDF and DØ from analyzing $W\gamma$ and WW, WZ processes. The scale sensitivity is 1.5 TeV. $\Delta\kappa_\gamma = \Delta\kappa_Z$ and $\lambda_\gamma = \lambda_Z$ is assumed in the WW/WZ analyses. In other scenarios weaker limits result. The $W\gamma$ analysis does not depend on such assumptions.	158
10.2	Comparison of two-dimensional limit contours at 95% CL for the \mathcal{CP} -conserving couplings h_3^Z and h_4^Z measured from analyzing $Z\gamma$ production in the electron + muon (CDF and DØ) and neutrino (L3) decay channel. The scale sensitivity is 500 GeV. The displayed bounds are the most stringent to date.	160
10.3	Expected sensitivities on the \mathcal{CP} -conserving couplings κ_γ and λ_γ at LHC, TEV* and LEP II. The 95% CL contours are calculated in the HISZ scenario [27].	162
10.4	Expected sensitivities at 95% CL on the \mathcal{CP} conserving couplings h_3^Z and h_4^Z at LHC and TEV*.	163
10.5	Expected photon E_T spectrum at ATLAS for Standard Model (SM) and anomalous ($\kappa_\gamma = 1.2$) W-photon couplings.	164

List of Tables

5.1	Summary of central electron requirements.	51
5.2	Summary of the requirements for the second Z electron. † Plug region only.	53
5.3	Number of events in the inclusive W, Z and the 16 GeV photon background sample (P16) passing the photon requirements in successive order. In the case of the P16 sample, the first row indicates the number of central and fiducial objects that have no three-dimensional track associated with. Trigger objects are excluded.	56
5.4	Central photon efficiencies for electromagnetic shower variables determined from electron testbeam data samples at various energies. The statistical uncertainties are given.	60
5.5	E_T dependent central photon isolation efficiencies for the cut $ISO4 < 0.15$. The difference in the results from random cone studies in the electron and muon W and Z samples suggests a conservative estimate for the uncertainties of 1.0%.	62
5.6	Summary of individual CEM photon selection efficiencies (\pm stat. \pm syst.). The overall efficiency includes a—over the Standard Model E_T distribution—weighted average of the $ISO4$ isolation cut (Table 5.5). † Not actually used.	64
5.7	Acceptances (A) and geometrical fractions (f) in the $W\gamma$ and $Z\gamma$ analyses.	65
5.8	Systematic uncertainties in the absolute number of $W\gamma$ and $Z\gamma$ events obtained from Baur plus Fast Monte Carlo simulations in the electron and combined electron + muon channels.	70
6.1	Number of jets and electromagnetic clusters that pass the photon requirement per analysis E_T bin in the P16 data sample.	74
6.2	Fraction of direct and fake photons among the fake photon candidates found in the P16 data sample per analysis E_T bin (\pm stat. \pm syst.). The number of direct photons is determined using the shower profile method.	75
6.3	Jet fragmentation probability into neutral mesons, all faking photons, as a function of E_T determined from the P16 data sample (\pm stat. \pm syst.).	75

6.4	Number of jets in the inclusive W and Z sample in the electron and combined electron + muon channels.	77
6.5	Jet fragmentation background in the $W\gamma$ and $Z\gamma$ samples as a function of photon E_T (\pm stat. \pm syst.).	77
6.6	Comparison of the background-subtracted $W\gamma$ signal in the electron channel per analysis bin (in GeV) using three different photon selection sets: Default analysis cuts (Set A), ‘loose isolation cuts’ (Set B) and ‘only isolation cuts’ (Set C), as defined in the text. The errors are purely statistical with the common error ignored. χ^2_{stat} determines the goodness of the agreement between the results for Set A and those for Set B or C, respectively.	81
6.7	Comparison of the measured jet fragmentation backgrounds with the VECBOS Monte Carlo prediction.	83
6.8	Non-QCD backgrounds in the $W\gamma$ and $Z\gamma$ data samples in the individual electron and combined electron + muon channels obtained from Baur plus Fast Monte Carlo studies.	84
6.9	Systematic uncertainties in the background estimate in the $W\gamma$ ($Z\gamma$) electron and combined electron + muon channels.	85
6.10	Total background in the $W\gamma$ and $Z\gamma$ data samples in the individual electron and combined electron + muon channels (\pm stat. \pm syst.).	86
6.11	Comparison of $W\gamma$ and $Z\gamma$ signal in the individual electron and combined electron plus muon channels to the Standard Model (SM) prediction obtained from Baur plus Fast Monte Carlo calculations (\pm stat. \pm syst.). N_{obs} is the number of observed events.	87
8.1	Summary of the backgrounds in the preliminary Run 1a+b $W\gamma$ and $Z\gamma$ data samples for the electron and combined electron + muon channels (\pm stat.). N_{tot} is the total number of background.	110
8.2	Comparison of the preliminary Run 1a+b $W\gamma$ and $Z\gamma$ signal in the electron and combined electron + muon channels to the Standard Model prediction obtained from Baur plus Fast Monte Carlo calculations (\pm stat.). N_{obs} is the number of observed events.	111
9.1	Summary of plug photon requirements.	122
9.2	E_T -dependent plug photon isolation efficiencies, $\epsilon_{iso4}^{perm\gamma}$, in %, determined at random points in the W sample (electron channel).	126
9.3	VTX occupancy efficiency for plug photons with an VTX occupancy less than 0.4, determined by studying random rays in the W sample (electron channel). The errors are statistical.	126
9.4	Coefficients a and b for the sliding cut $HAD/EM(E) < a + b \cdot E$ at 95% efficiency. The errors represent the uncertainties of the fit.	127
9.5	Efficiencies (\pm stat.) for the cut $HAD/EM(E) < 0.028 + 0.00019 \cdot E$ in various energy regions, determined from plug electron samples.	129

9.6	Efficiencies (\pm stat.) of shower variables determined from ‘loose’ plug Z electron samples. N_{tot} is the sample size.	130
9.7	Number of electromagnetic objects (EM) passing the plug photon analysis cuts and number of jets in the QCD trigger samples P23 and P16 per E_T bin (in GeV) for the two rapidity regions $1.28 < \eta < 1.78$ (PES) and $1.10 < \eta < 1.28$ or $1.78 < \eta < 2.40$ (no PES). [†] Minimum trigger transverse energy raised to 55 GeV.	132
9.8	Number of the direct photons $N_{dir\gamma}$ and number of background events (fake photons from jet fragmentation), N_{bkg} , in the rapidity regions $1.28 < \eta < 1.78$ (PES) and $1.10 < \eta < 1.28$ or $1.78 < \eta < 2.40$ (no PES) of the P16 and P23 photon trigger samples (\pm stat. \pm syst.). All events pass the plug photon analysis requirements. The results are obtained via a study of the electromagnetic fraction in a cone of $\Delta R_{\ell\gamma} = 0.7$ of a cluster (<i>EMF7</i>).	140
9.9	Fragmentation probability $\mathcal{P}_i^{pem}(jet \rightarrow \gamma')$ in the plug rapidity regions $1.28 < \eta < 1.78$ (PES) and $1.10 < \eta < 1.28$ or $1.78 < \eta < 2.40$ (no PES) determined with the P16 and P23 trigger samples. The numbers are in units of 10^{-5} (\pm stat. \pm syst.)	141
9.10	Number of jets per analysis bin with $\Delta R_{jet\ell} > 0.7$ in the electron $W\gamma$ sample for the photon rapidity regions $1.28 < \eta < 1.78$ (PES) and $1.10 < \eta < 1.28$ or $1.78 < \eta < 2.40$ (no PES)	142
9.11	Summary of non-QCD backgrounds in the Run 1a+b central W + plug photon data sample in the individual electron and combined electron + muon channels, obtained from Baur plus Fast Monte Carlo studies.	143
9.12	Total number of QCD background events per analysis bin (\pm stat. \pm syst.) for the Run 1a+b central W + plug photon sample in the electron channel, determined from the P23 photon trigger sample.	144
9.13	Absolute and fractional number of jets in the highest P23 <i>EMF7</i> bin, estimated by the two methods discussed in the text, per analysis bin.	146
9.14	Comparison of the number of the direct photons $N_{dir\gamma}$ (\pm stat. \pm syst.) obtained via the shower profile or <i>EMF7</i> method in the central region of the QCD samples P16 and P23, per analysis bin (in GeV). $N_{tot\gamma}$ is the total number of electromagnetic clusters that pass all central photon analysis cuts.	147
9.15	Ratio of the number of positive-signed values to the total number of events for a) the W charge-signed pseudorapidity difference between the photon and the W decay lepton and b) the W charge-signed pseudorapidity of the photon. The numbers are corrected for background. The uncertainties are statistical.	153

A.1	Summary of the one-dimensional limits on the coupling parameters $\Delta\kappa$ and λ for a form factor scale of 1.5 TeV.	169
A.2	Summary of the one-dimensional limits on the coupling parameters $\tilde{\kappa}$ and $\tilde{\lambda}$ for a form factor scale of 1.5 TeV.	169
A.3	Summary of the one-dimensional limits on the $ZZ\gamma$ coupling parameters h_{30}^Z and h_{40}^Z for a form factor scale of 500 GeV.	170
A.4	Summary of the one-dimensional limits on the $ZZ\gamma$ coupling parameters h_{10}^Z and h_{20}^Z for a form factor scale of 500 GeV.	170
A.5	Summary of the one-dimensional limits on the $Z\gamma\gamma$ coupling parameters h_{10}^γ and h_{20}^γ for a form factor scale of 500 GeV.	171
A.6	Summary of the one-dimensional limits on the \mathcal{CP} -conserving electromagnetic moments g_W and q_W^e for a form factor scale of 1.5 TeV.	171
A.7	Summary of the one-dimensional limits on the \mathcal{CP} -violating electromagnetic moments d_W and q_W^m for a form factor scale of 1.5 TeV.	172
A.8	Summary of the one-dimensional limits on the electromagnetic transition moments for Z-photon processes for a form factor scale of 500 GeV.	172
C.1	Central W and Z electron selection efficiencies.	176
C.2	Second central Z electron selection efficiencies.	176
C.3	Plug Z electron selection efficiencies.	177
C.4	Forward Z electron selection efficiencies.	177
C.5	Electron Trigger Efficiencies.	177

ACKNOWLEDGEMENTS

The most difficult part of this thesis is finding the right words of thanks to all the folks I had the pleasure to work with. This work could not have been successfully completed without the combined effort of literally hundreds of people.

I would like to say ‘thank you’ to all of them: to my colleagues at CDF who build and maintained this magnificent detector, and recorded the signature of millions of proton-antiproton collisions, to the Fermilab staff whose skill and hard work ultimately make these collisions happen, and to the ingenious theorists without whom we experimentalists wouldn’t know what to look for in our analyses. Thanks also to the folks in the UCLA physics department who did all the bureaucracy for me.

I would like to thank very much Jay Hauser and Stephan Lammel for their help and their patience in answering all kinds of physics or computer related questions. Many thanks to the ‘Dibozos’, Bob, Debbie, Doug, Mark, Mike, Sato, Steve and Thomas. I was a pleasure to be on your team, the CDF ‘diboson’ group.

I would like to express special thanks to those who were essential to the success of this thesis:

First of all, I am in great debt to Thomas Müller who gave me the opportunity to study at UCLA and work in CDF on this fascinating topic. He has been a great advisor, and I have learned a lot from him (I hope). Herzlichen Dank, Thomas for all the help, advice, support and freedom you gave me.

When I came from Germany more than four and a half years ago, the first person I met at CDF was the ‘big guy’, Mike Lindgren. He not only showed me how to polish scintillating fibers but helped me survive in CDF and in the harsh environment around Fermilab. Since these days, I’ve had a great time working closely with him on the analysis. Thanks Mike, for everything.

I am very grateful to Steve Errede. His physics knowledge and his nice character seem to be somehow proportional to the length of his e-mail messages. Thanks Steve for your help, for writing and maintaining the Fast Monte Carlo, and for all the other contributions to the $W\gamma$ and $Z\gamma$ analyses; I enjoyed a lot working with you.

I would like to express my deep gratitude to Ulrich Baur, the great meister of vector boson interactions. His Monte Carlo and his work are the foundation of this thesis. Thanks Uli for your kind explanations of all these theoretical intricacies.



I want to thank all of you for being such nice guys. I am glad to have found friends in you.

Thanks to Jay, Mike, Steve, Thomas and Uli for proof-reading my thesis.

Last, but not least, a special thanks to my parents for their support throughout my career as a physics student.

This work was supported by the U.S. Department of Energy (DOE) and the German Academic Exchange Service (DAAD).

VITA

	
1985	Abitur C.-F.-Gauss Gymnasium Hockenheim, Germany
1987	Vordiplom, Physics University of Karlsruhe Karlsruhe, Germany
1991	Diplom, Physics University of Karlsruhe Karlsruhe, Germany
1991-1995	Graduate Research Assistant University of California, Los Angeles California, Los Angeles
1995	Teaching Assistant University of California, Los Angeles California, Los Angeles

PUBLICATIONS AND PRESENTATIONS

- J. Hauser, M. Lindgren, T. Müller, D. Neuberger et al.. A Scintillating Fiber Detector for Electron and Photon Identification at High Luminosity Colliders. Nucl. Instr. Meth. A321, 497 (1992).
- C.M. Raiteri, R. Gallino, M. Busso, D. Neuberger et al.. The Weak s -Component and Nucleosynthesis in Massive Stars. Astrophys. J. 419, 207 (1993).
- F. Abe et al.. Measurement of W - Photon Couplings with CDF in $p\bar{p}$ Collisions at $s^{1/2} = 1.8$ TeV. Phys. Rev. Lett. 74, 1936 (1995).
- F. Abe et al.. Limits on Z - Photon Couplings from $p\bar{p}$ Interactions at $s^{1/2} = 1.8$ TeV. Phys. Rev. Lett. 74, 1941 (1995).

- D. Neuberger, M. Tepe, F. Käppeler. The Stellar Cross Sections for ^{87}Rb and ^{192}Pt . Proceedings of the International Conference on Nuclear Data for Science and Technology, Jülich, Germany (1991).
- D. Neuberger. Ein neuartiger Positionsdetektor für CDF. Talk given at the "Spring Meeting of the German Physical Society", Berlin, Germany (1992).
- D. Neuberger. Search for anomalous $Z\gamma$ Couplings with CDF at the Tevatron Collider. Talk given at the "Spring Meeting of the American Physical Society", Washington D.C., USA (1994).
- D. Neuberger. Suche nach anomalen $W\gamma/Z\gamma$ Kopplungen. Talk given at the "Spring Meeting of the German Physical Society", Dortmund, Germany (1994).
- D. Neuberger. Results on $W\gamma$ Production at CDF. Proceedings of the "W γ Z International Symposium on Vector Boson Self-Interactions", Los Angeles, USA (1995).
- D. Neuberger. Anomale $W\gamma/Z\gamma$ Kopplungen. Talk given at the "Spring Meeting of the German Physical Society", Karlsruhe, Germany (1995).
- D. Neuberger. Electroweak Measurements from CDF and DØ. To be published in the Proceedings to the "International Europhysics Conference on High Energy Physics", Brussels, Belgium (1995).

ABSTRACT OF THE DISSERTATION

Studies of Weak Boson - Photon Production in $\sqrt{s} = 1.8$ TeV $p\bar{p}$ Collisions at the
Tevatron Collider.

by

Dirk Neuberger

Doctor of Philosophy in Physics

University of California, Los Angeles, 1995

Professor T. Müller, Chair

Presently, there is little experimental knowledge about weak boson - photon couplings, which are a direct consequence of the non-abelian gauge structure of the Standard Model. In a data set of 19.6 pb^{-1} taken by the CDF collaboration during the Tevatron collider run 1992-93, the inclusive $W + \text{photon}$ and $Z + \text{photon}$ cross sections were measured to $\sigma \cdot B(W\gamma \rightarrow \ell\nu\ell\gamma) = 13.2 \pm 4.5 \text{ pb}$ and $\sigma \cdot B(Z\gamma \rightarrow \ell^+\ell^-\gamma) = 5.1 \pm 1.9 \text{ pb}$, ($\ell = e + \mu$). The ratio of these $W\gamma$ to $Z\gamma$ cross sections is about 3 times smaller than the inclusive W to Z cross section ratio, thus confirming the presence of gauge cancellations, which are predicted to occur in $W\gamma$ production only. Anomalous weak boson - photon couplings would disturb these $W\gamma$ gauge cancellations and allow direct interactions between a Z boson and a photon. A log-likelihood fit of the photon transverse energy spectrum yields limits on the \mathcal{CP} -conserving anomalous coupling parameters at 95% CL for a form factor scale $\Lambda_{VV\gamma}$: $-2.3 < \Delta\kappa < 2.2$ ($\lambda = 0$), $-0.7 < \lambda < 0.7$ ($\Delta\kappa = 0$) for $\Lambda_{WW\gamma} = 1.5$ TeV; $-3.0 < h_{30}^Z < 2.9$ ($h_{20}^Z = 0$), $-0.7 < h_{40}^Z < 0.7$ ($h_{10}^Z = 0$) for $\Lambda_{ZZ\gamma} = 0.5$

TeV. The limits on the \mathcal{CP} -violating couplings differ by less than 3%. Bounds on $Z\gamma\gamma$ couplings, h_{i0}^γ , are very similar to those on $ZZ\gamma$ couplings, h_{i0}^Z . The results provide corresponding limits on higher-order electromagnetic (transition) moments of the W (Z) boson. The data prove at 95% CL that the W boson has at least one non-vanishing electromagnetic moment. The measurements are sensitive to a distance scale of $L_W = 1.3 \cdot 10^{-4}$ fm and $L_Z = 4.0 \cdot 10^{-4}$ fm and show no deviation from the Standard Model. An update of these analyses using additional, preliminary data from the ongoing Tevatron run gives consistent results. Furthermore, a pronounced asymmetry in photon rapidity distributions was observed: in $W\gamma$ production, $77 \pm 7\%$ of the photons were measured to have a positive value in the charge-signed pseudorapidity distribution, while $70 \pm 8\%$ of the photons have a positive charge-signed pseudorapidity difference between the photon and the W decay lepton.

Chapter 1

Introduction

1.1 General Overview

All known particles in nature can be divided into two groups: fermions and bosons. *Fermions* have an half-valued intrinsic angular momentum, called spin. To the group of fermions belong six quarks (up, down, strange, charm, bottom, top) and six leptons (electron, muon, tau, and their associated neutrinos). Leptons can exist as isolated particles, quarks have to form bound systems (hadrons) of two (mesons) or three (baryons) members. *Bosons* have integer spin. Members of the group of bosons are the photon, the W^\pm and Z bosons, the gluon, and the graviton. At a fundamental level, bosons act as force mediators in particle interactions.

Four theories describe all presently known fundamental phenomena in nature through the exchange of mediating bosons. In *electromagnetism*, electrically charged particles interact through *photons*. In the theories of *gravitation* and *strong interactions*, the force carrying bosons are *gravitons* and *gluons*, respectively. And in the theory of *weak interactions* three different particles serve as mediators: The W^+ , the W^- , and the Z *vector bosons*.

Physicists believe that these four fundamental theories are special manifestations of *one* unified theory. In the 60's, it was Sheldon Glashow, Abdul Salam and Steven Weinberg [1] who succeeded for the first time to combine the electromagnetic with the weak interaction to a unified gauge theory, using the photon, the W and Z bosons as carrier of *electroweak* interactions. The so-called *Standard Model* of particle physics is commonly referred to this theory, in which elements of the two major gauge field theories, quantum electrodynamics (QED) and quantum chromodynamics (QCD) are incorporated. Those theories describe the quantum nature of strong (QCD) and electromagnetic (QED) interactions, based on the epochal work of Richard P. Feynman, Julian Schwinger, Sin-itiro Tomonaga [2] and others.

In the Standard Model, mass is given to the weak bosons W and Z by a process called *spontaneous symmetry breaking*, for which a new particle, the Higgs boson, has to be introduced. The Higgs boson is the only particle within the Standard Model that has not yet been found in an experiment. Fundamental particles that have been found most recently are the weak bosons and the top quark. In the early 80's, the UA1 and UA2 ¹ collaborations proved the existence of the W and Z bosons [3], which in 1986 led to the award of the Nobel Prize to Carlo Rubbia and Simon van de Meer. In March 1995, the CDF ² and DØ ³ collaborations announced the discovery of the top quark [4] [5], the last of the six quarks in the Standard Model that had not been detected so far.

The Standard Model has shown an impressive predictive power in a variety of experiments in the last couple of decades. Earlier attempts to unify the weak and

¹Named after the Underground Area 1 and 2 at the CERN p̄p collider Sp̄pS.

²Collider Detector at Fermilab.

³Named after the interaction region 'DØ' of the Fermilab Tevatron collider.

electromagnetic sector had encountered problems with correctly predicting quantities like the magnitude of the mass of the W boson. By incorporating the correct V–A ⁴ structure of the weak interaction, the Standard Model, for the first time, was able to predict the mass and width of the W and Z bosons, their production cross sections, decay properties and couplings ⁵ to quarks, gluons, leptons and photons. Electroweak theory and experiment agree fantastically. For example, the theoretical and experimental determination of vector boson couplings to fermions differ by less than 1% [7].

However, all measurements so far have probed the Standard Model at energy scales below 1 TeV. In addition, the theory has no predictive power for 18 parameters that have to be put in based on experimental data. Therefore, we expect the Standard Model not to be elementary but rather an effective low energy limit of a so-far unknown, more fundamental theory.

Measurements which test the Standard Model in the TeV range allow an exciting look beyond our present understanding of the electroweak unification. High energy proton-(anti)proton colliders, are excellent tools for such studies. The particle accelerator with the presently highest energies is the Tevatron collider at Fermilab with a radius of about 1 km. A quarter million proton-antiproton ($p\bar{p}$) collisions per second at a center-of-mass energy of 1.8 TeV result in a small number of rare events that allow precise and direct measurements of deviations from the Standard Model.

A sensitive way to study these deviations is to measure rare couplings between vector bosons. Despite the success of the Standard Model, there is presently little

⁴Vector–axial vector symmetry [6].

⁵Interactions between particles are commonly referred to as ‘couplings’ of one particle to another; both terms are often used synonymously.

experimental evidence for vector boson self-interactions, which are the most direct consequences of the non-abelian gauge symmetry of this theory [6]. The Standard Model makes precise predictions about the rate at which such processes occur, based on the assumption of pointlike vector bosons. However, some theories view the weak bosons as composite entities [8] acting as mediating particles in the electroweak sector in a similar way as the ρ meson in nuclear physics. Several decades ago mesons were found to be carrier of the nuclear force at low energies. Today we know that all mesons are composite of quarks, and that the nuclear force is a manifestation of the more fundamental strong interaction. The quark substructure is the reason why mesons have non-integer magnetic moments. In direct analogy, the measurement of electromagnetic moments of the weak bosons yields information about new interactions or possible substructures of the W or Z boson.

A small number of $p\bar{p}$ collisions produce events with two bosons in the final state, so-called diboson events. Novel phenomena would reveal themselves in a higher rate of diboson events than predicted by the Standard Model. During the collider run 1992–93, the CDF experiment had collected a sufficient amount of data to be able to study Standard Model predictions of processes involving vector boson self-couplings and to measure the electromagnetic moments of the W and Z bosons.

Measuring vector boson self-interactions is a crucial test of the Standard Model. In this dissertation, we will concentrate on W-photon and Z-photon production.

1.2 Organization of the Thesis

We discuss various measurements in connection with W-photon and Z-photon processes. We begin with a theoretical overview of vector boson self-couplings in Chapter 2, followed by a brief summary of the present knowledge of the strength

of weak boson - photon couplings. The Tevatron collider and the CDF experiment are described in Chapter 4. We then discuss the extraction of W-photon and Z-photon events from CDF data (Run 92/93) and the measurement of background in Chapter 5 and 6, respectively. In Chapter 7, we present the analysis of these data. The results include the measurement of inclusive $W\gamma$ and $Z\gamma$ cross sections, tests of the Standard Model through various kinematic studies, the measurement of limits on the anomalous coupling parameters and on the electromagnetic (transition) moments of the W (Z) boson. In Chapter 8, these results are compared to an updated analysis of approximately 3 times larger samples that combine the data from Run 92/93 with preliminary data from the present, ongoing Tevatron run. In a further analysis of this combined data set, we report in Chapter 9 on an asymmetry in certain angular distributions in $W\gamma$ production, which has not been observed in earlier experiments. This analysis differs in various aspects from the analyses described in Chapter 5–8. A summary of the main results and an outlook into the future completes our discussion in Chapter 10.

Chapter 2

Theoretical Background

The Standard Model of particle physics is an example of a Yang-Mills gauge field theory [9]. It unifies the electromagnetic and weak interaction to a single interaction with a $SU(2)_L \otimes U(1)_Y$ symmetry, which is a cross product of the two-dimensional weak isospin space and the one-dimensional hypercharge space Y [10].

An important concept of the Standard Model is spontaneous symmetry breaking based on the fundamental work of Nambu, Goldstone, and Higgs [11]. Spontaneous symmetry breaking separates the gauge fields into a massless photon (γ) and the massive vector bosons, W^\pm , Z . The photon acts as the propagator of the electromagnetic current, the W and Z bosons are the massive propagators of the charged and neutral weak currents, respectively. Since the Standard Model is a non-abelian theory, multi-boson couplings among the four electroweak gauge bosons W^\pm , Z and γ are predicted. The structure of the general Lagrangian for vector boson self-couplings is fixed by gauge invariance [12]:

$$L_{vector} = -\frac{1}{4}W_{i\mu\nu}W^{i\mu\nu} - \frac{1}{4}B_{\mu\nu}B^{\mu\nu} \quad (2.1)$$

with

$$W_{i\mu\nu} \equiv \partial_\mu W_{i\nu} - \partial_\nu W_{i\mu} - g\epsilon_{ijk}W_\mu^jW_\nu^k, \quad (2.2)$$

$$B_{\mu\nu} \equiv \partial_\mu B_\nu - \partial_\nu B_\mu, \quad (2.3)$$

where ϵ_{ijk} is the totally antisymmetric unit tensor, g is the weak coupling constant, and $i=1,2,3$. The tensor products in the Lagrangian contain only combinations of the non-abelian field $W_{i\mu}$ or the abelian field B_μ which represent trilinear WWV , ZZV and quartic $WWVV'$, $ZZVV'$, but no higher order couplings. V or V' stand for W , Z or γ . Note that some couplings such as $Z\gamma\gamma$ or $ZZZZ$ do not exist in the tree level Standard Model.

In turn, a measurement of trilinear (or quartic) couplings, which agrees with the Standard Model predictions, would corroborate spontaneously broken, non-abelian gauge theories as the basic theoretical structure describing fundamental interactions in nature. Direct tests of trilinear vertices are possible in collider experiments via pair production processes like $q\bar{q} \rightarrow W\gamma$, $Z\gamma$, W^+W^- , WZ or $e^+e^- \rightarrow W^+W^-$, $Z\gamma$. Information can also be obtained from indirect, high precision measurements; these results are model-dependent (see Chapter 3).

2.1 $W\gamma$ Couplings

There are several processes $W \rightarrow \ell\nu$ which lead to a final state of a W boson and a photon, shown in Figure 2.1 in form of Feynman diagrams. Feynman diagrams, in general, are not only of pictorial use to illustrate couplings between particles, but also represent individual contributions (amplitudes) to the matrix elements in the cross section calculation of the corresponding process. Specific and well defined rules apply [12].

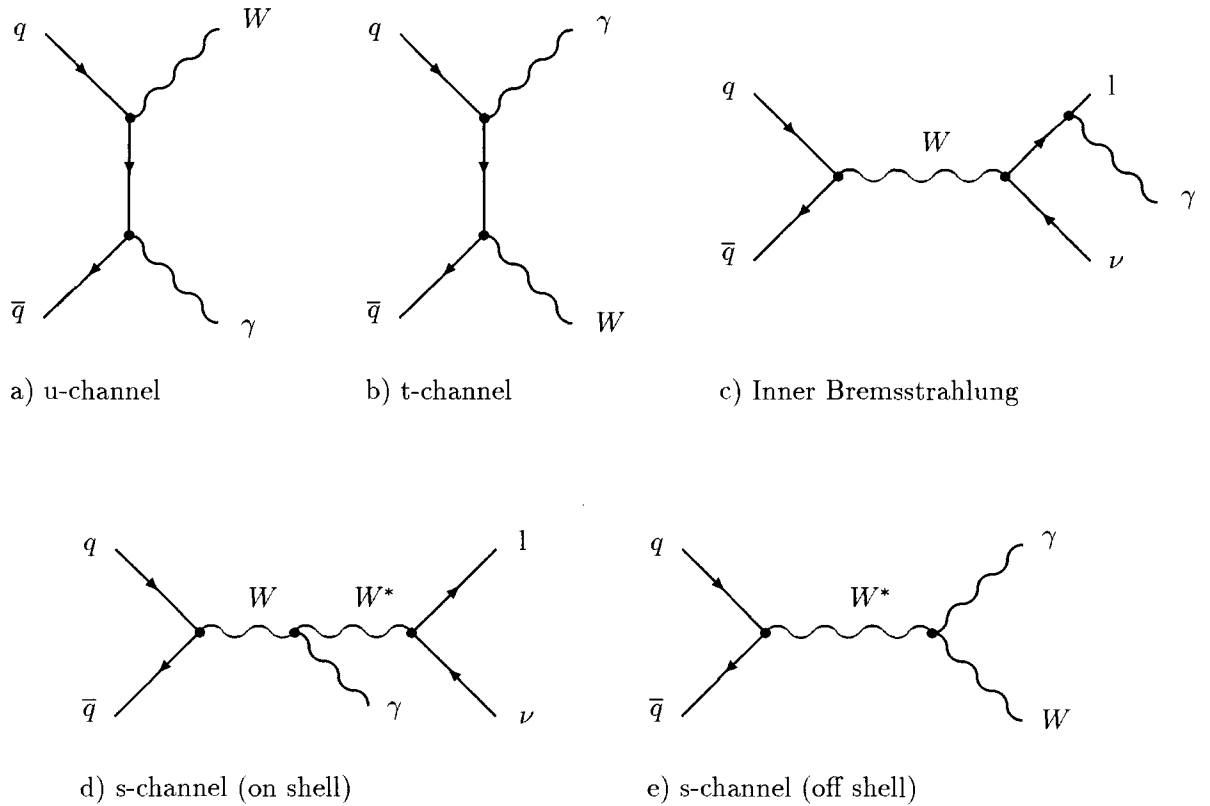


Figure 2.1: Lowest order $W\gamma$ Feynman diagrams in hadron collisions. Lines with arrows pointing to the right (left) symbolize incoming (outgoing) fermions, bosons are represented by curly lines.

The diagrams in Figure 2.1 depict all Feynman graphs contributing to $W\gamma$ production in hadron collisions at tree-level, that is, without taking loop diagrams (particle interactions with itself) into account.

The first two diagrams, the u- and t-channel graphs, are associated with initial state radiation off of the incoming quark lines. Figure 2.1c and d illustrate radiative W decays. Events corresponding to Figure 2.1c shall be referred to as radiative events.

There are two different s-channel diagrams which involve a three-boson vertex (Figure 2.1d and e). They are the actual $W\gamma$ production diagrams, of interest for

the study of anomalous couplings between a W boson and a photon. In Figure 1d, the intermediate W does not violate energy conservation, whereas in Figure 1e it does, as allowed by the Heisenberg uncertainty relation. The W bosons is called ‘on or off (the mass) shell’, respectively.

The different processes could be distinguished if the W had zero decay width. However, due to the finite width of $\Gamma_W = 2.1$ GeV the five final states are indistinguishable. In the calculation of the $W\gamma$ cross section, *all* amplitudes represented by the five diagrams must be added together coherently in order to preserve electromagnetic gauge invariance [13].

Imposing electromagnetic gauge invariance and Lorentz invariance, and assuming the photon to be on-shell, the most general $WW\gamma$ vertex can be parameterized by a phenomenological effective Lagrangian of the form ¹ [13][14]

$$\begin{aligned}
L_{WW\gamma} = & -ie[W_{\mu\nu}^\dagger W^\mu A^\nu - W_\mu^\dagger A_\nu W^{\mu\nu} + \kappa_f W_\mu^\dagger W_\nu F^{\mu\nu} + \frac{\lambda_f}{M_W^2} W_{\lambda\mu}^\dagger W_\nu^\mu F^{\nu\lambda} \\
& + \tilde{\kappa}_f W_\mu^\dagger W_\nu F'^{\mu\nu} + \frac{\tilde{\lambda}_f}{M_W^2} W_{\lambda\mu}^\dagger W_\nu^\mu F'^{\nu\lambda}].
\end{aligned} \tag{2.4}$$

Here, A^μ and W^μ are the photon and W fields, respectively, e is the charge of the proton, and M_W is the mass of the W. The rank 2 tensors are defined as $W_{\mu\nu} = \partial_\mu W_\nu - \partial_\nu W_\mu$, $F_{\mu\nu} = \partial_\mu A_\nu - \partial_\nu A_\mu$, $F'_{\mu\nu} = \frac{1}{2}\epsilon_{\mu\nu\rho\sigma} F^{\rho\sigma}$, where $F^{\rho\sigma}$ is the electromagnetic field tensor. κ_f , λ_f , $\tilde{\kappa}_f$ and $\tilde{\lambda}_f$ are form factors a_f , which can be written in generalized dipole form, in analogy to the nucleon form factors, as

$$a_f(P^2 = \hat{s}, q_1^2 = M_W^2, q_2^2 = 0) = \frac{a_0}{(1 + \hat{s}/\Lambda_W^2)^n}, \tag{2.5}$$

¹In equations, we will use the convention $\hbar = c = 1$ throughout this thesis.

where P is the four-momentum of the incoming W boson and q_1 and q_2 are the four momenta of the final state W and photon, respectively. The constants a_0 in the case where the form factor $a_f = \kappa_f, \lambda_f, \tilde{\kappa}_f$ or $\tilde{\lambda}_f$, are the dimensionless anomalous couplings $a_0 = \Delta\kappa, \lambda, \tilde{\kappa}$ or $\tilde{\lambda}$, where $\Delta\kappa \equiv \kappa - 1$. Λ_W represents a form factor energy scale. Such a ‘cut-off’ parameter plus setting the exponent $n > 1$ ($n > 0.5$) for $\kappa_f, \lambda_f, \tilde{\lambda}_f$ ($\tilde{\kappa}_f$) is required in case of anomalous gauge boson couplings in order to preserve unitarity of the S-matrix in the cross-section calculation at high energies. The choice $n = 2$ is motivated by the functional form of the nucleon form factor. At energies higher than Λ_W , we expect new physics to become important, for example due to a composite structure of the W boson (see Section 2.3).

In absence of a specific model for novel phenomena, an effective Lagrangian parameterizes low energy effects caused by new physics at higher energies. Such techniques are model-independent. This approach is similar to the introduction of vector and axial vector couplings g_V and g_A for $V\bar{f}f$ interactions, where $V = W$ or Z and $f = \text{lepton or quark}$. Different but equivalent parameterizations are possible [15].

Deviations from the Standard Model are expressed by the anomalous couplings $\Delta\kappa, \lambda, \tilde{\kappa}$ and $\tilde{\lambda}$. Since these parameters vanish in the Standard Model at tree-level ($a_0 = 0$), any measurement of non-zero values ² would mean the presence of new physics beyond the Standard Model, e.g. the existence of a W boson substructure. The form factor Λ_W is the scale for such new physics. Four parameters suffice to describe $W\gamma$ couplings because, due to conservation of angular momentum, there are only four combinations between the W and photon helicity states allowed. Only

²Within the present experimental precision one-loop corrections in the order of α , which contribute only to the \mathcal{CP} -conserving parameters λ and $\Delta\kappa$, can be neglected.

the helicity combination $(\beta_W, \beta_\gamma) = (1, -1) (1, 0) (0, 1) (1, -1)$ but not $(-1, -1)$ and $(1, 1)$ add up to the possible helicity eigenvalues $0, \pm 1$ of the initial W boson in $WW\gamma$ processes. The corresponding quantum mechanical amplitudes are called helicity amplitudes.

In the static limit (photon energy $\rightarrow 0$) the anomalous couplings are proportional to the more familiar classical electromagnetic multipole moments of the W boson in the following way:

$$\text{Magnetic Dipole Moment} \quad \mu_W = \frac{e}{2M_W}(2 + \Delta\kappa + \lambda) \quad (2.6)$$

$$\text{Electric Quadrupole Moment} \quad Q_W^e = -\frac{e}{M_W^2}(1 + \Delta\kappa - \lambda) \quad (2.7)$$

$$\text{Electric Dipole Moment} \quad d_W^e = \frac{e}{2M_W}(\tilde{\kappa} + \tilde{\lambda}) \quad (2.8)$$

$$\text{Magnetic Quadrupole Moment} \quad Q_W^m = -\frac{e}{M_W^2}(\tilde{\kappa} - \tilde{\lambda}) \quad (2.9)$$

The anomalous couplings can also be related to mean-squared charge radius of the W boson

$$\langle R_W^2 \rangle = \frac{1}{M_W^2}(1 + \Delta\kappa + \lambda) \quad (2.10)$$

In the Standard Model the W boson (spin $S = 1$) has $2 \cdot S + 1 = 3$ \mathcal{CP} -conserving electromagnetic moments [16]: In addition to its charge, it has both a non-vanishing magnetic dipole and electric quadrupole moment. The electric dipole moment and the magnetic quadrupole moment, and hence $\tilde{\kappa}$ and $\tilde{\lambda}$, are odd under the parity operation, \mathcal{P} , and violate the product of charge conjugation and parity operation, \mathcal{CP} . Similarly, the electric quadrupole moment and the magnetic dipole moment, and hence κ and λ , are \mathcal{CP} -conserving and \mathcal{P} even.

Although all five diagrams in Figure 2.1 must be coherently taken into account, there are kinematical differences between radiative decays and $W\gamma$ production pro-

cesses. The angular distribution of the photons depends on the particle to which the photon couples. Photons from the initial state radiation processes (Figure 2.1a and b) are predominantly collinear with the incident quark direction, that is at CDF along the proton-antiproton beam in forward/backward direction. In contrast, the majority of photons from final state radiative W decay tend to be collinear with the decay lepton. Contributions from anomalous $W\gamma$ production are isotropic in the center-of-mass system, whereas the t- and u-channel diagrams lead to an excess of events with small angular separation from the incoming/outgoing quark or antiquark. The cross section for initial and final state radiation, as well as for $W\gamma$ production, decreases rapidly with photon energy, but for the latter there are no kinematic correlations with the decay lepton and the final photon state is not constrained by the mass of the W boson.

How can anomalous couplings between a W boson and a photon be measured in the most sensitive way? There are several options ³ :

At a certain scattering angle Θ_0^* between the photon and incoming quark in the $W\gamma$ center-of-mass frame, the u- and t-channel diagrams cancel the s-channel diagram, so that the Standard Model helicity amplitudes vanish. This angle is given by [17]

$$\cos \Theta_0^* = \frac{q_1 + q_2}{q_1 - q_2} = -\frac{1}{3}, \quad (2.11)$$

where q_1 and q_2 are the charges of the two interacting quarks. As a consequence of such ‘gauge cancellations’, the differential cross section $d\hat{\sigma}/d \cos \Theta^*$ for $W\gamma$ production drops to zero [17]. This so-called radiation amplitude zero is partially filled due to structure function effects, finite W-width effects and higher order QCD cor-

³Quantities mentioned in this section, such as pseudorapidity, transverse energy, photon lepton separation and transverse cluster mass are defined in Equation 4.1, 4.2, 4.3 and 7.2 respectively.

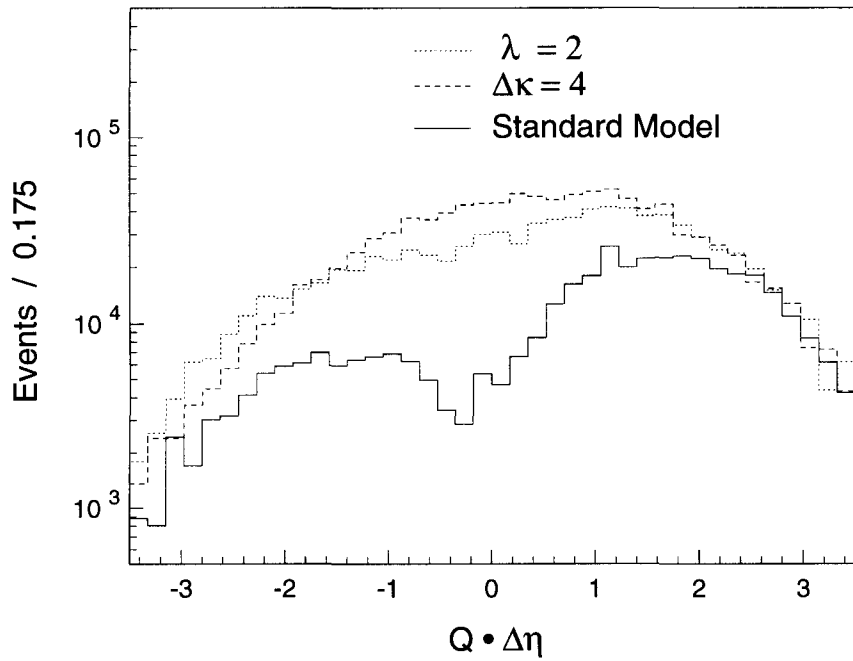
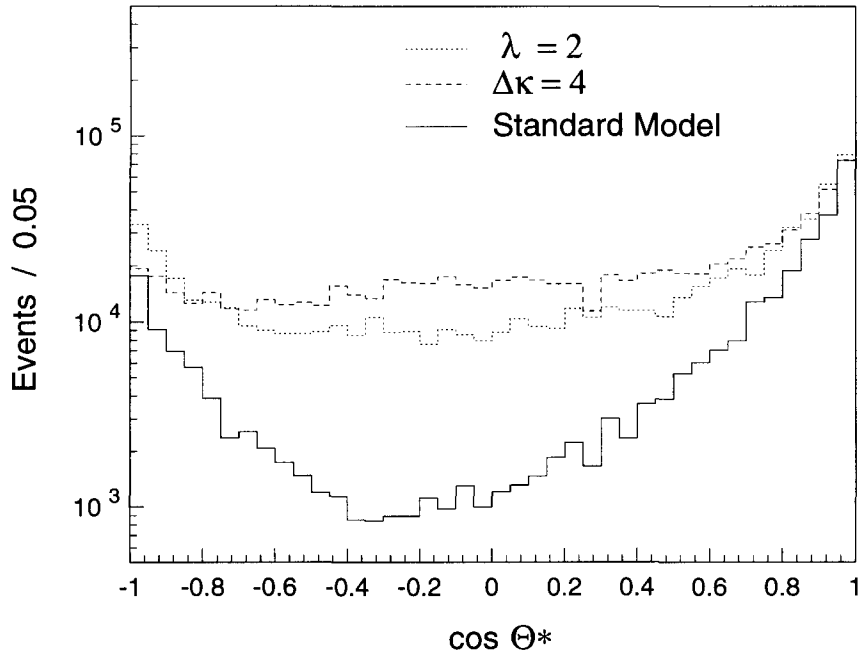


Figure 2.2: Monte Carlo simulation of the a) $\cos \Theta^*$, and b) W charge-signed pseudorapidity difference in $W\gamma$ processes ($E_T^\gamma > 7$ GeV), using Standard Model and anomalous coupling parameters. Θ^* is the angle between the photon and incoming quark in the $W\gamma$ center-of-mass frame.

rections [18]. In real data, also background processes and event misreconstruction due to a two-fold ambiguity of the longitudinal component of the neutrino momentum additionally contribute to the partial filling of the radiation zero ‘dip’. For anomalous couplings, i.e. non-zero values of $\Delta\kappa$, λ , $\tilde{\kappa}$ and $\tilde{\lambda}$, the gauge cancellation is incomplete and the dip is filled depending on the magnitude of the anomalous couplings (Figure 2.2a). Because of that, the determination of the depth of the radiation zero and the shape of the $\cos\Theta^*$ distribution provide a reasonably sensitive measurement of the anomalous coupling parameters. Unfortunately, this method depends on large statistic samples.

It is also possible to observe the radiation zero by looking at the lepton-photon pseudorapidity correlation $\Delta\eta_{\gamma l\pm} \equiv \eta_{\gamma} - \eta_{l\pm}$. The Standard Model predicts a pronounced dip at $\Delta\eta_{\gamma l\pm} \approx \mp 0.3$ for $W\gamma$ production [19]. Similarly to the $\cos\Theta^*$ distribution, this dip is caused by gauge cancellations. Again, large statistic samples are necessary in order to measure anomalous coupling by studying the shape and the depth of the dip. However, this method has the advantage that reconstruction of the $W\gamma$ center-of-mass system is not required and hence no smearing effects due to event misreconstruction can occur.

The distribution of the transverse photon energy, E_T , is sharply peaked at low energies and decreases dramatically at higher energies due to phase space and parton distribution effects of the (anti)proton. The presence of gauge cancellations cause a stronger decrease in the photon E_T spectrum for $W\gamma$ processes than for $Z\gamma$ processes, where no such cancellations occur. In the case of anomalous couplings, incomplete cancellations (and non-Standard Model $ZZ\gamma$ couplings for $Z\gamma$ processes) lead to an excess of high E_T photons. Figure 2.3 shows this effect for two cases where one of four $W\gamma$ coupling parameters is set to a non-Standard Model

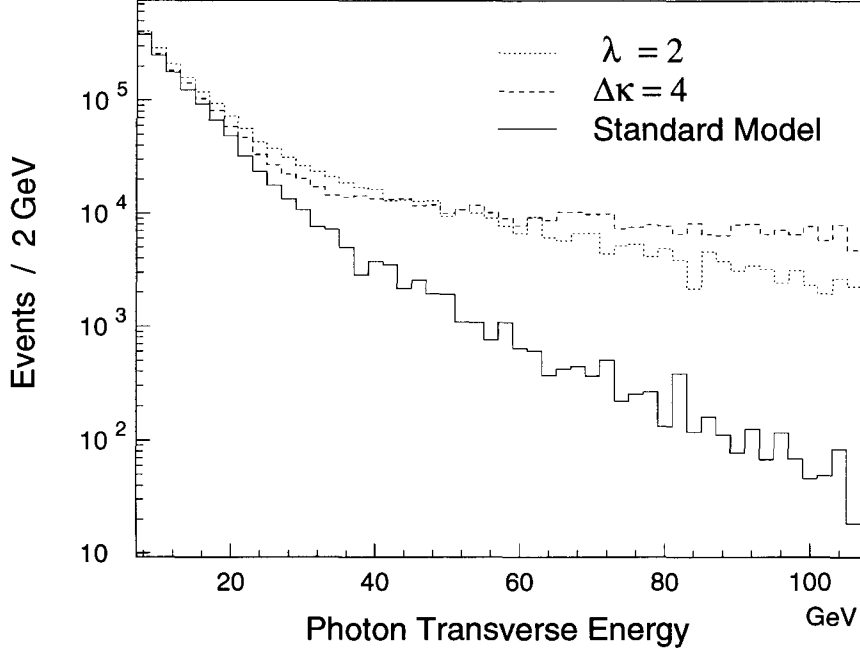


Figure 2.3: Simulated photon E_T distribution in $W\gamma$ processes for Standard Model and anomalous coupling parameters.

value. A fit of the photon E_T spectrum provides a very sensitive way to set limits on anomalous $W\gamma$ couplings.

The gauge cancellations also affect the shape of the transverse cluster mass spectrum, which peaks at the W mass, and the angular separation between the photon and the W decay lepton (Figure 2.4). Events with large separations, $\Delta R_{\ell\gamma}$, and high transverse cluster masses, M_{TC} , originate predominantly from s-channel $W\gamma$ production. Radiative events are generally found at small $\Delta R_{\ell\gamma}$ and low M_{TC} .

Radiative decays exhibit only little sensitivity to anomalous $WW\gamma$ couplings, as the center-of-mass energy of the colliding quarks is restricted to $\sqrt{\hat{s}} = M_W$, while for $W\gamma$ production the total center-of-mass energy range up to $\sqrt{\hat{s}} = 1.8$ TeV is accessible. Anomalous contributions to the $W\gamma$ helicity amplitudes grow like some power of the ratio of $\sqrt{\hat{s}}$, to the mass of the W boson ($\sqrt{\hat{s}}/M_W$ for κ and

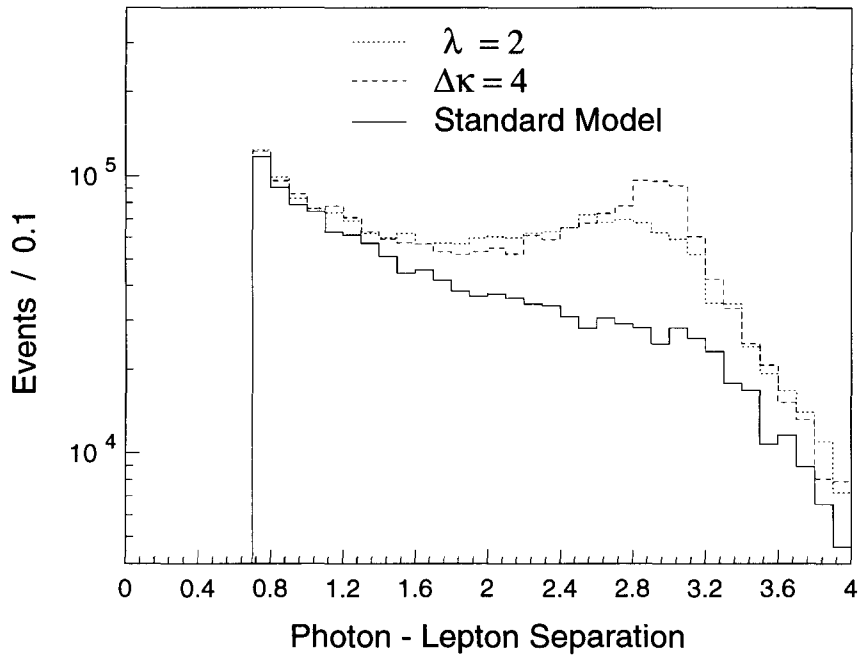
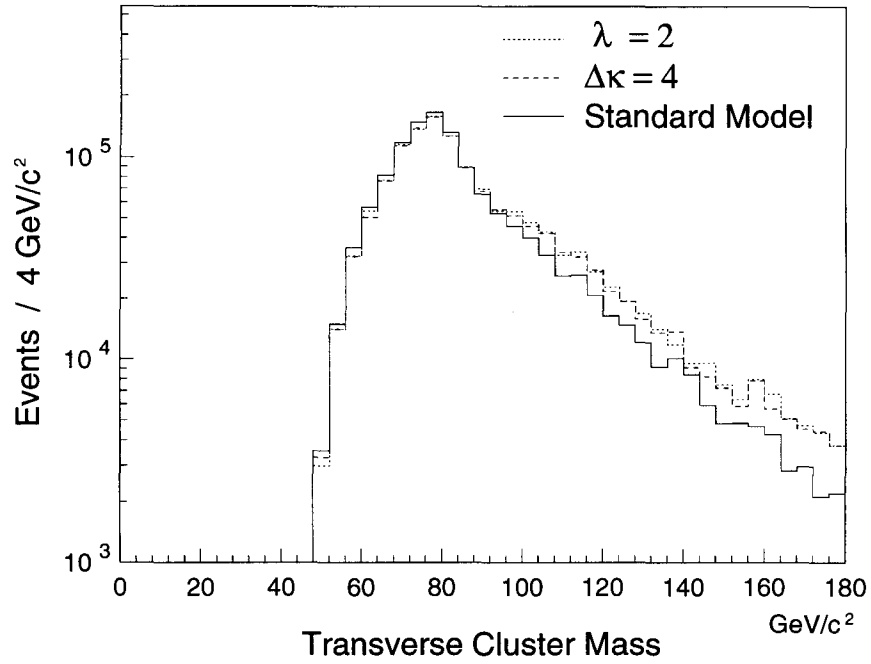


Figure 2.4: Monte Carlo simulation of the a) transverse cluster mass and b) photon - lepton separation spectrum in $W\gamma$ processes ($E_T^\gamma > 7$ GeV), using Standard Model and anomalous coupling parameters.

$\tilde{\kappa}$, and $(\sqrt{\hat{s}}/M_W)^2$ for λ and $\tilde{\lambda}$). Hence, the sensitivity to anomalous couplings for radiative events, and therefore at small $\Delta R_{\ell\gamma}$ and low M_{TC} , is much smaller than for production events.

Finally, the $W\gamma$ cross section for anomalous couplings is larger than predicted by the Standard Model due to the incomplete gauge cancellations. A comparison of the measured $W\gamma$ cross section with the Standard Model prediction provides another way to set limits on anomalous couplings [20].

2.2 $Z\gamma$ Couplings

The Standard Model Feynman diagrams at tree level contributing to the production of a Z boson and a photon in hadron collisions are shown in Figure 2.5 a–c. Since the Z boson is a Majorana particle, i.e. its own anti-particle, it cannot have any static electromagnetic multipole moments according to the \mathcal{CPT} theorem. Hence, direct $ZZ\gamma$ couplings shown in Figure 2.5d and 2.5e (and also $Z\gamma\gamma$ couplings) do not exist in the tree-level Standard Model. An observation of these processes would imply physics beyond the Standard Model.

The most general $ZZ\gamma$ vertex function allowed by electromagnetic gauge invariance can be written as [21]

$$\begin{aligned} \Gamma_{Z\gamma Z}^{\alpha\beta\mu}(q_1, q_2, P) &= \left(\frac{P^2 - q_1^2}{M_Z^2}\right) \times [h_1^Z(q_2^\mu g^{\alpha\beta} - q_2^\alpha g^{\mu\beta}) + \frac{h_2^Z}{M_Z^2} P^\alpha (P \cdot q_2 g^{\mu\beta} - q_2^\mu P^\beta) \\ &\quad + h_3^Z \epsilon^{\mu\alpha\beta\rho} q_{2\rho} + \frac{h_4^Z}{M_Z^2} P^\alpha \epsilon^{\mu\beta\rho\sigma} P_\rho q_{2\sigma}] \end{aligned} \quad (2.12)$$

where M_Z is the Z mass, P and q_1 are the incoming and outgoing Z four-momenta (Lorentz indices μ and α , respectively), and q_2 is the four-momenta of the outgoing on-shell photon (Lorentz index β). The form factors h_i^Z ($i = 1-4$) are dimensionless

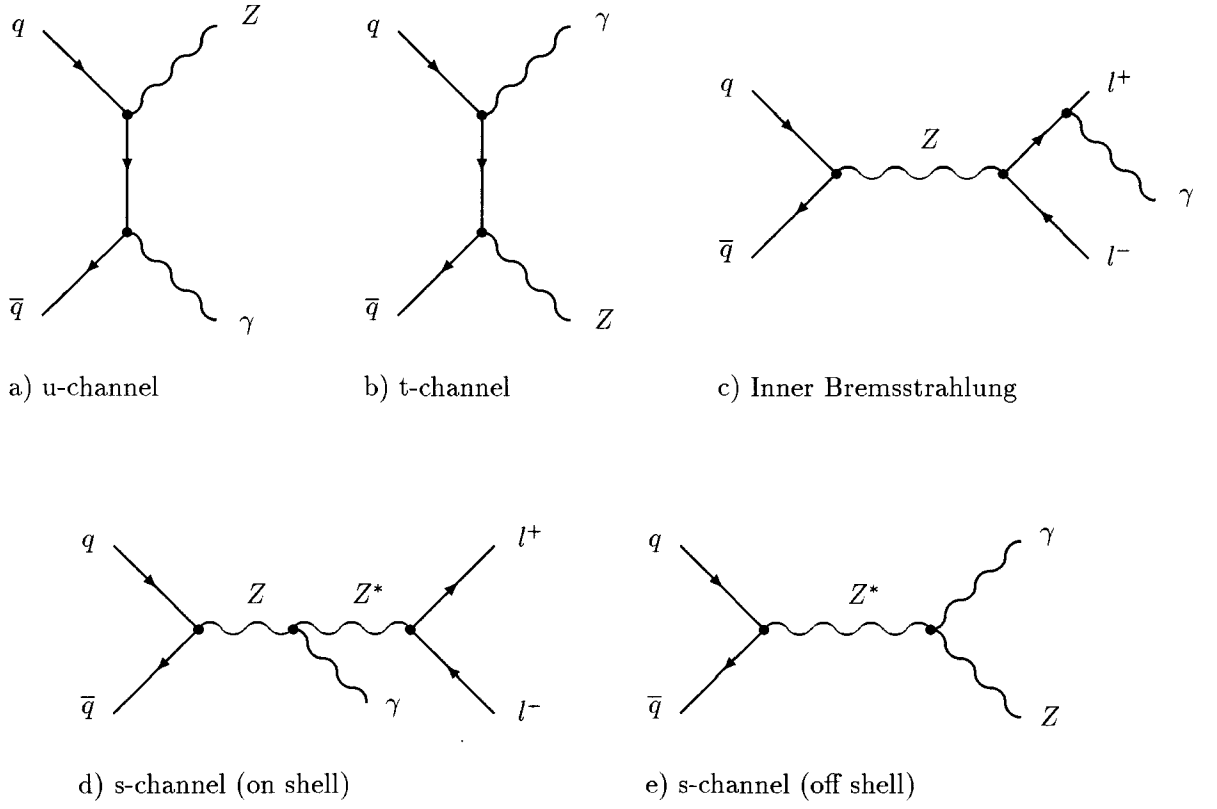


Figure 2.5: Lowest order $Z\gamma$ Feynman diagrams. Lines with arrows pointing to the right (left) symbolize incoming (outgoing) fermions, bosons are represented by curly lines.

functions of q_1^2 , q_2^2 and P^2 . They are assumed to be of generalized dipole form

$$h_i^V(P^2 = \hat{s}, q_1^2 = M_Z^2, q_2^2 = 0) = \frac{h_{i0}^V}{(1 + \hat{s}/\Lambda_Z^2)^n} \quad (2.13)$$

with form factor scale Λ_Z analogous to the scale Λ_W in the $W\gamma$ form factor. The choice $n = 3$ for $h_{1,3}^V$ and $n = 4$ for $h_{2,4}^V$ preserves unitarity at high energies. With such a choice the matrix terms proportional to $h_{2,4}^V$ have the same high energy behavior as those proportional to $h_{1,3}^V$.

As for the $W\gamma$ case, helicity arguments limit the number of anomalous couplings

to four. In the static limit (photon energy $\rightarrow 0$) they are related to the more familiar electromagnetic transition moments (TM) [22]:

$$\text{Electric Dipole TM} \quad d_{Z_T} = -\frac{e}{M_Z} \frac{1}{\sqrt{2}} \frac{k^2}{M_Z^2} (h_{30}^Z - h_{40}^Z) \quad (2.14)$$

$$\text{Electric Quadrupole TM} \quad Q_{Z_T}^m = \frac{e}{M_Z^2} \sqrt{10} (2h_{30}^Z) \quad (2.15)$$

$$\text{Magnetic Dipole TM} \quad \mu_{Z_T} = -\frac{e}{M_Z} \frac{1}{\sqrt{2}} \frac{k^2}{M_Z^2} (h_{10}^Z - h_{20}^Z) \quad (2.16)$$

$$\text{Magnetic Quadrupole TM} \quad Q_{Z_T}^e = \frac{e}{M_Z^2} \sqrt{10} (2h_{10}^Z) \quad (2.17)$$

These transition moments correspond to $E1$, $E2$, $M1$ and $M2$ transitions of the photon, respectively. $E2$ and $M1$, and hence h_{10}^Z and h_{20}^Z , violate \mathcal{CP} and are \mathcal{P} even; $E1$ and $M2$, and hence h_{30}^Z and h_{40}^Z , are \mathcal{CP} -conserving and \mathcal{P} odd. All couplings vanish in the Standard Model at tree level.⁴ As for $W\gamma$ couplings, the measurement of non-zero values for the coupling parameters would be evidence for physics beyond the Standard Model, e.g. compositeness of the Z boson.

For $Z\gamma$ couplings, there is no destructive interference of diagrams which would result in a radiation amplitude zero as in the $W\gamma$ case. However, due to the behavior of the anomalous contributions (Figure 2.5d and 2.5e) to the helicity amplitudes at high energies, the photon E_T distribution is sensitive to the non-Standard Model couplings.

Because there are—in contrast to the $W\gamma$ case—no interference effects for Standard Model $Z\gamma$ processes, the ratio of the $W\gamma/Z\gamma$ cross section \times branching ratios is expected to be noticeably smaller than the inclusive W/Z cross section \times branching ratios. For selected topological cuts (Chapter 5), we expect from Monte Carlo

⁴One loop corrections in the order of $< 10^{-4}$ contribute to only the \mathcal{CP} -conserving parameters h_{30}^Z and h_{40}^Z , and can be assumed to be negligible.

studies $\sigma B(W\gamma)/\sigma B(Z\gamma) \approx 4$, whereas $\sigma B(W \rightarrow \ell\nu)/\sigma B(Z \rightarrow \ell^+\ell^-) \approx 11$.

It is straight forward to apply the discussion of $ZZ\gamma$ to $Z\gamma\gamma$ couplings by replacing the virtual Z boson in the s-channel graph by a photon. One only has to make the following substitutions in the vertex function, Equation 2.12 :

$$\frac{P^2 - q_1^2}{M_Z^2} \rightarrow \frac{q_2^2}{M_Z^2} \quad (2.18)$$

and

$$h_i^Z \rightarrow h_i^\gamma, \quad i = 1, \dots, 4. \quad (2.19)$$

Note that for anomalous $Z\gamma\gamma$ couplings, the electromagnetic transition moments are not well defined in the static limit, photon energy $\rightarrow 0$, since the excited photon state γ^* is far off shell.

In analogy to $W\gamma$ production, the presence of non-Standard Model couplings leads to an excess of $Z\gamma$ events with high photon transverse energy. A fit of the E_T distribution is the most sensitive way to obtain limits on anomalous $Z\gamma$ couplings. The separation between the photon and one of the decay leptons or the three-body mass spectrum are less sensitive to anomalous couplings. As for $W\gamma$ production, the $Z\gamma$ production cross section is enhanced due to a growth of the helicity amplitudes for anomalous couplings $\sim (\sqrt{\hat{s}}/M_Z)^m$ ($m = 3$ for $h_{1,3}^V$ and $m = 5$ for $h_{2,4}^V$).

2.3 Unitarity Constraints

Unitarity of the S-matrix implies that any partial wave amplitude is bounded by a constant. This leads to the conclusion that any deviation from the Standard Model three boson couplings must be described in form of a form factor which vanishes asymptotically at large energies [23]. The actual functional form of the

anomalous coupling form factor is arbitrary. A simple step function as well as a general dipole form could be used. The latter choice, introduced in the previous section (Equations 2.5 and 2.13), is motivated by the known behavior of the nucleon form factor. Its exponent, n , and ‘cut-off’ parameter Λ_V must be chosen so that S-matrix unitarity of the inelastic vector boson pair production amplitude for $p\bar{p}$ annihilation at center-of-mass energies $\sqrt{\hat{s}}$ is not violated.

Λ_V defines an energy scale (e.g. compositeness scale) beyond which novel phenomena are expected to dominate. Assuming the existence of these unknown phenomena, their low energy consequences are measured in form of the anomalous coupling parameters. The actual value of the scale is not (yet) predicted by a theory. However, Λ_V must be larger than ≈ 100 GeV ($\mathcal{O}(M_V)$) since no deviations from the Standard Model have been detected in experiments.

On the other hand, Λ_V cannot be chosen too large because the measurement would yield bounds on the anomalous couplings which are less stringent than the unitarity constraints, as we will see in the following:

If, for the sake of simplicity, only one coupling is assumed to deviate from its Standard Model value, a partial wave calculation yields unitarity bounds on the following three-boson couplings [13] [23] [24] :

$$\begin{array}{lcl}
\text{WWV couplings :} & |\Delta\kappa| < \frac{n^n}{(n-1)^{n-1}} \cdot \frac{1.81 \text{ TeV}^2}{\Lambda_W^2} & \stackrel{n=2}{=} \frac{7.24 \text{ TeV}^2}{\Lambda_W^2} \\
& |\Delta\tilde{\kappa}| < \frac{(2n)n^n}{(2n-1)^{n-\frac{1}{2}}} \cdot \frac{11.5 \text{ TeV}}{\Lambda_W} & = \frac{35.4 \text{ TeV}}{\Lambda_W} \\
& |\lambda|, |\tilde{\lambda}| < \frac{n^n}{(n-1)^{n-1}} \cdot \frac{0.96 \text{ TeV}^2}{\Lambda_W^2} & = \frac{3.84 \text{ TeV}^2}{\Lambda_W^2}
\end{array}$$

$$\begin{array}{lcl}
\text{ZZ}\gamma \text{ couplings :} & |h_{10}^Z|, |h_{30}^Z| < \frac{(\frac{3}{2}n)^n}{(\frac{3}{2}n-1)^{n-\frac{3}{2}}} \cdot \frac{0.126 \text{ TeV}^3}{\Lambda_Z^3} & \stackrel{n=3}{=} \frac{7.44 \text{ TeV}^3}{\Lambda_Z^3} \\
& & \downarrow \\
& |h_{20}^Z|, |h_{40}^Z| < \frac{(\frac{5}{2}n)^n}{(\frac{5}{2}n-1)^{n-\frac{5}{2}}} \cdot \frac{2.1 \cdot 10^{-3} \text{ TeV}^5}{\Lambda_Z^5} & \stackrel{n=4}{=} \frac{0.78 \text{ TeV}^5}{\Lambda_Z^5}
\end{array}$$

$Z\gamma\gamma$ couplings : The bounds on h_{i0}^γ can be obtained by multiplying the above relations for h_{i0}^Z with a factor of 1.19.

These bounds are computed with $M_W = 80 \text{ GeV}$ and $M_Z = 91.1 \text{ GeV}$. In the case of the WWV couplings, the smallest unitarity limits derived from either $W\gamma$ or WW, WZ processes are presented.

Obviously, experimental limits on the anomalous couplings must be tighter than the unitarity constraints to yield non-trivial information. The scale quoted in the following chapters is the maximum energy scale beyond which the unitarity constraint become more stringent than the experimental result. Larger energies, or equivalently, smaller distances cannot be probed in the individual measurements.

Note that $W\gamma$ couplings depend on the form factor for low values of Λ_W , but are essentially form factor independent for Λ_W above a few hundred GeV. In contrast, $Z\gamma$ couplings show a significant dependence on the form factor Λ_Z [20].

Chapter 3

Present Experimental Knowledge

Vector boson self-couplings are well described within the Standard Model. To date, however, there is only limited experimental knowledge about vector boson self-interactions.

3.1 The Coupling Parameters κ , λ , $\tilde{\kappa}$ and $\tilde{\lambda}$

The UA2 collaboration was the first to set limits on anomalous $W\gamma$ couplings from a direct measurement of $W\gamma$ events in high energy $p\bar{p}$ collisions at $\sqrt{s} = 630$ GeV [25]. At 95% CL they measured the following limits:

$$\begin{aligned} -4.5 < \Delta\kappa < 4.9 & \quad \text{for } \lambda = 0 \\ -3.6 < \lambda < 3.5 & \quad \text{for } \Delta\kappa = 0 \end{aligned}$$

Similar limits at 95% CL were obtained by CDF from measurement of the production cross section times branching ratio, $\sigma B(W\gamma)$ and $\sigma B(Z\gamma)$, using ≈ 4 pb⁻¹ electron and muon data from the Tevatron Run 88/89:

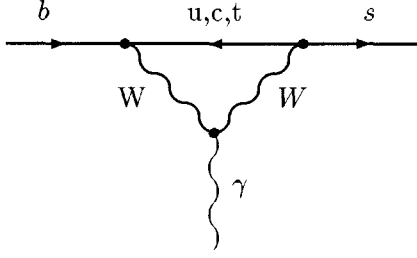


Figure 3.1: Loop-order flavor changing Feynman diagram $b \rightarrow s + \gamma$ involving a $WW\gamma$ vertex.

$$\begin{aligned}
 -6.5 < \Delta\kappa < 7.0 & \quad \text{for} \quad \lambda = 0 \\
 -3.1 < \lambda < 3.1 & \quad \text{for} \quad \Delta\kappa = 0
 \end{aligned}$$

These results are sensitive to a compositeness scale of $\Lambda_W = 1$ TeV.

Parallel to the work described in this thesis, the DØ collaboration has analyzed $W\gamma$ and WW events found with the DØ detector during the Tevatron Run 92/93. The results from their $W\gamma$ analysis are very similar to those from CDF. A comparison will be given in the last chapter.

Because of ambiguities and model-dependencies in the results, no rigorous limits on anomalous $W\gamma$ couplings are available from LEP I e^+e^- data if correlations between different contributions to the anomalous couplings are fully taken into account [26] [27].

Bounds on $\Delta\kappa$ and λ can also be extracted from the CLEO measurement of the branching ratio $B(b \rightarrow s\gamma)$ (Figure 3.1) [28]:

$$\begin{aligned}
 -2.6 < \Delta\kappa < 1.2 \quad \text{and} \quad -0.5 < \Delta\kappa < 0.4 & \quad \text{for} \quad \lambda = 0 \\
 -1.7 < \lambda < 1.0 & \quad \text{for} \quad \Delta\kappa = 0
 \end{aligned}$$

It is desirable to combine collider limits from vector boson self-couplings with limits obtained through $B(b \rightarrow s\gamma)$, as they are complementary. In the $(\Delta\kappa, \lambda)$ plane,

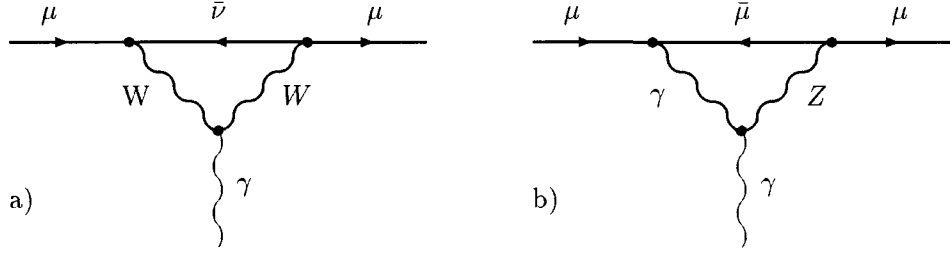


Figure 3.2: Loop diagram contributions to the anomalous electromagnetic moment of the muon, a) involving a $WW\gamma$ vertex, b) involving a $Z\gamma\gamma$ vertex.

bounds from measurements of vector boson self-couplings exclude $(\Delta\kappa, \lambda)$ pairs in an area outside an *ellipse*, whereas those from a measurement of $B(b \rightarrow s\gamma)$ exclude pairs outside *bands*.

Indirect, low energy limits had been derived earlier from measurements of the anomalous magnetic moment of the muon [29] [30]. These limits are, however, model dependent. They are sensitive to the regularization scheme used in the loop calculations (Figure 3.2a) and to the cutoff parameter used to regulate divergences:

$$\begin{aligned} \Delta\kappa \cdot \ln \frac{\Lambda^2}{M_W^2} &< 5 && \text{for } \lambda = 0 \\ \lambda &< 5 \cdot \mathcal{O}(1) && \text{for } \Delta\kappa = 0 \end{aligned}$$

More stringent indirect limits on $\Delta\kappa$ and λ have been derived from the W/Z mass ratio [30] [31] and from a measurement of the photon propagator at PETRA [32]. These bounds are controversial because radiative and loop corrections are ill defined.

Indirect limits on the \mathcal{CP} -violating coupling $\tilde{\kappa}$ are derived from the measured electric dipole moment of the neutron, $|d_n| < 6 \cdot 10^{-25} \text{ e}\cdot\text{cm}$ [33]:

$$|\tilde{\kappa}| < 10^{-3}.$$

The authors make the assumption that the electric dipole moment depends only on $\tilde{\kappa}$, not on the coupling $\tilde{\lambda}$. A discussion of a calculation which includes a $\tilde{\lambda}$ dependence is given in Ref. [29]. However, the results are model-dependent and also sensitive to the regularization scheme and to the loop cutoff parameter to regulate divergences. The interplay between $\tilde{\kappa}$ and $\tilde{\lambda}$ may lead to looser limits than quoted above on either couplings.

3.2 The Coupling Parameters h_{i0}

Results from the $Z\gamma$ analysis of the $D\bar{O}$ collaboration, which was performed parallel to this work based on the Tevatron Run 92/93, will be discussed in the last chapter.

Indirect low energy limits from contributions to the electric dipole moment of the neutron could also be derived for the $h_{1,2}^V$ couplings, similar to the bounds obtained for the \mathcal{CP} -violating $W\gamma$ couplings. A calculation, however, is presently not available. Again, model-dependent results and a sensitivity to both the regularization scheme used in the loop calculations and the cutoff parameter used to regulate divergences are expected.

These problems are also present when low energy bounds on the \mathcal{CP} -conserving couplings from the measured gyromagnetic ratio of the muon ($g_\mu - 2$) [34] are extracted. From the two possible diagrams $Z\gamma\gamma$ and $ZZ\gamma$, only the latter gives a non-zero contribution to the anomalous magnetic moment of the muon (Figure 3.2b). For $h_4^\gamma = 0$ one finds [24]

$$|h_3^\gamma \log(\frac{\Lambda^2}{M_Z^2})| < 9,$$

where M_Z is the Z mass and Λ the loop cutoff scale.

There is only little sensitivity to anomalous $Z\gamma$ couplings from cross section

measurements at the Z resonance at LEP I. Despite the large number of $Z \rightarrow \ell^+ \ell^- \gamma$ events, only relatively weak limits can be extracted [24]. However, recently the L3 collaboration was able to obtain $ZZ\gamma$ limits by comparing the observed to the expected number of $Z \rightarrow \nu\bar{\nu}\gamma$ events in a 50.8 pb^{-1} large data sample [35]. This decay channel with its large branching ratio is most sensitive to anomalous couplings. Moreover, there is no QCD background due to misidentified photons from jet fragmentation, the main background source in $Z\gamma$ analyses at hadron colliders. L3 measures for a form factor scale of $\Lambda_Z = 0.5 \text{ TeV}$:

$$\begin{aligned}
|h_{30}^Z(h_{10}^Z)| &< 2.30 && \text{for } h_{40}^Z(h_{20}^Z) = 0 \\
|h_{40}^Z(h_{20}^Z)| &< 0.85 && \text{for } h_{30}^Z(h_{10}^Z) = 0
\end{aligned}$$

Due to the high statistics, the limits on h_{30}^Z (h_{10}^Z) are rather competitive with Tevatron experiments, whereas the limits on h_{40}^Z (h_{20}^Z) tend to be weaker for LEP I experiments (see also Chapter 10).

The anomalous $Z\gamma\gamma$ couplings could also be probed at LEP I through e^+e^- annihilation into a virtual photon which couples to a $Z\gamma$ pair. However, photon exchange at the Z resonance is highly suppressed, and there is essentially no sensitivity to $Z\gamma\gamma$ couplings at LEP I.

3.3 WW, WZ and ZZ Couplings

To complete the discussion, we mention that at Tevatron center-of-mass energies of 1.8 TeV, the Standard Model cross section for WW and WZ production is comparable to that for $W\gamma$ production [36], while the ZZ signal is very weak in the present data set.

In a preliminary analysis of 65 pb^{-1} , CDF has identified five WW events in the

$WW \rightarrow \ell\ell + \cancel{E}_T$ decay channel ($\ell = e$ or μ). The corresponding cross section was measured to $\sigma(p\bar{p} \rightarrow WW + X) = 13.8_{-7.9}^{+9.6}$ pb [37].

A more detailed discussion of weak boson self-interactions can be found elsewhere [37] – [40]. Here, we present only a brief summary of the CDF/DØ search for anomalous couplings in WW and WZ production. Since $p\bar{p} \rightarrow (\gamma^*, Z^*) \rightarrow W^+W^-$ is mediated both by the photon and the Z boson, both $WW\gamma$ and WWZ anomalous couplings, a_γ and a_Z , have to be considered. For W + photon processes only $WW\gamma$ couplings are relevant, so the index γ can be dropped.

The Standard Model predicts gauge cancellations between WWZ, WW γ Feynman diagrams, which are particularly pronounced at high invariant diboson masses and at high boson transverse momenta P_T^V . These cancellations are incomplete for non-Standard Model couplings, and a large excess of events in the high P_T^V region is expected. Moreover, the W/Z + QCD jet background, which is overwhelmingly present in all semihadronic channels, is suppressed in this region.

To measure the couplings, CDF (DØ) has searched for WW and WZ candidates consistent with a leptonic decay of one boson (a W boson) and a hadronic decay of the other. This decay channel exhibits a higher sensitivity than the purely leptonic decay channels, mainly because of the small leptonic branching ratios of the weak bosons.

DØ has also obtained limits by analyzing the double leptonic decay channel. This analysis is less sensitive than the single leptonic decay channel [38].

Recently, DØ has obtained limits on anomalous couplings by fitting the background corrected P_T^W spectrum in $WW, WZ \rightarrow \ell\nu jj$ processes [39].

The limits on anomalous couplings obtained from these analyses will be presented in Section 10.2. Further details can be found in [38] [40].

Chapter 4

The Experimental Apparatus

4.1 The Tevatron

The Fermilab Tevatron collider is presently the world's most powerful particle accelerator, colliding protons and antiprotons at a center-of-mass energy of 1.8 TeV. This is achieved by using 4.4 T superconducting magnets in a ring of 1 km radius (Figure 4.1).

To collect antiprotons in quantity, a complex set of operations is necessary. Protons, on the other hand, are more easily produced by stripping off electrons from negative hydrogen ions while travelling through a carbon foil at energies between 200 and 400 MeV. Before reaching this energy in the 150 m long linear accelerator (LINAC), the ions were preaccelerated to 750 keV in the Cockroft-Walton accelerator. The protons are subsequently accelerated in 'bunches' up to 8 GeV in a small synchrotron ring, the Booster Ring. The bunches are then injected into the Main Ring where their kinetic energy increases to 120 GeV. At this point, the protons are released into the Tevatron where they reach the final energy of 0.9 TeV.

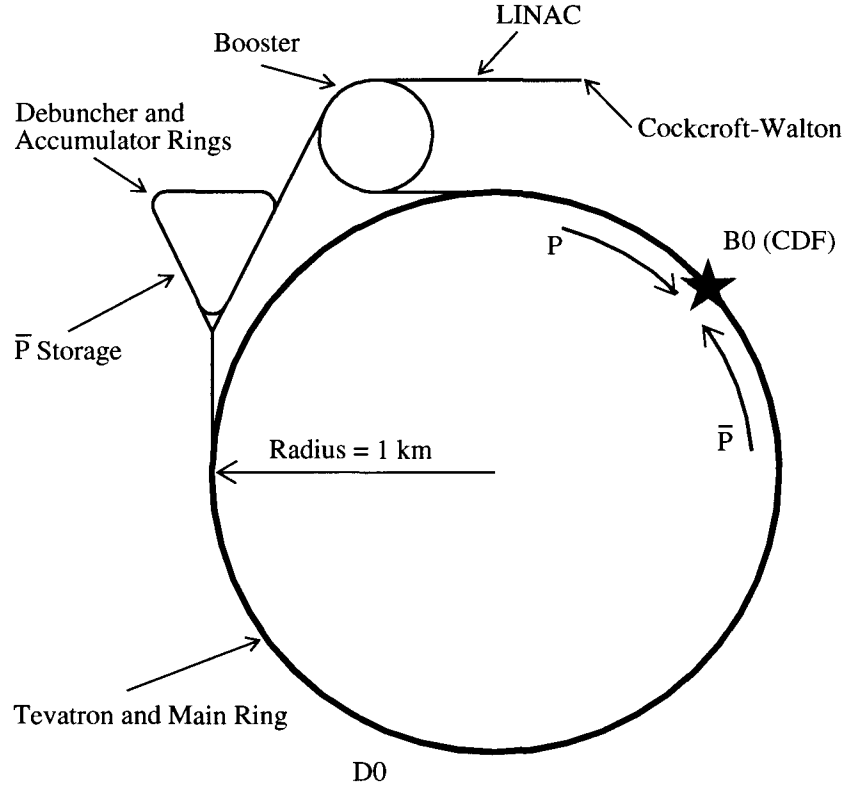


Figure 4.1: Schematic view of the Tevatron Collider.

A fraction of the protons circulating in the Main Ring are extracted and shot on a tungsten target. Antiprotons arising from $p\bar{p}$ pair production are focused with a lithium magnetic lens. In the ‘Debuncher Ring’, a mono-chromatic antiproton beam is formed by reducing the energy spread through debunching and stochastic cooling. The antiprotons are then stored in the accumulator and released in bunches into the Main Ring when an amount sufficient for the desired luminosity is accumulated.

Preaccelerated to 150 GeV by the Main Ring, six bunches of antiprotons are added to the six bunches of protons circulating in opposite direction inside the Tevatron Ring. Before collisions take place at 2×0.9 TeV, the beam is tuned with

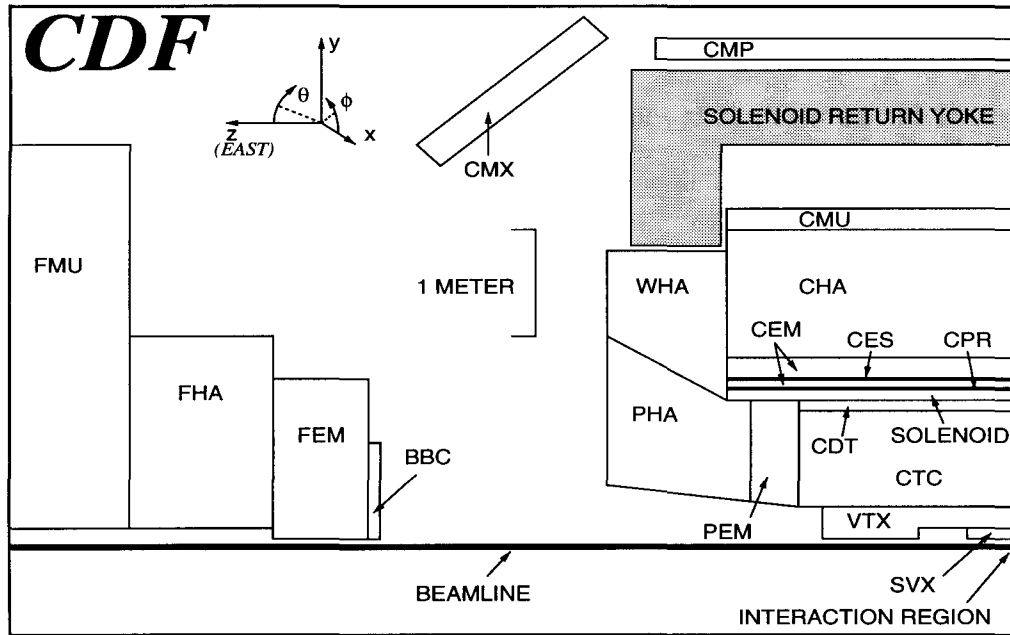


Figure 4.2: Schematic view of one half of the CDF detector. The other half is the mirror image of this picture. For an explanation of the acronyms, see the text.

the help of magnets and collimators.

During the Run 92/93, a bunch consisted of typically 10^{11} protons and $5 \cdot 10^{10}$ antiprotons. A measure for the interaction rate is the luminosity, which is proportional to the number of colliding particles and their interaction cross section [6]. The total, time integrated luminosity, which has the unit of an inverse cross section, was about 20 pb^{-1} during the ten months runtime.

The ongoing run operates at a higher luminosity, so that during the runtime from late Winter '93 to Spring '95, a total amount of approximately 70 pb^{-1} of data has been collected.

4.2 The CDF Detector

There are two detectors to study 1.8 TeV $p\bar{p}$ collisions at the Tevatron Collider: the DØ detector [41] and the CDF detector [42], with which the data for this analysis were taken.

The 5000 tons heavy CDF detector was designed with azimuthal and forward/backward symmetry allowing an almost 4π coverage. The analysis of events produced through $p\bar{p}$ collisions is based on identifying leptons and jets. For this purpose the CDF detector was built of fine-grained calorimeters, charged particle tracking chambers and a superconducting 1.4 T solenoid (5 m long and 3 m in diameter) to measure charged particle momenta. In the polar direction, it is divided into three segments: the central, the plug and the forward region.

Figure 4.2 shows a projective view of the CDF detector. By definition the coordinate system is right-handed, with the z-axis pointing east in direction of the incoming protons. Due to the detector symmetry a cylindrical coordinate system is commonly used. The polar angle, θ , is generally replaced by the variable pseudorapidity

$$\eta = -\ln \left[\tan\left(\frac{\theta}{2}\right) \right]. \quad (4.1)$$

The use of the pseudorapidity is motivated by the fact that it is invariant and additive under Lorentz boosts along the z-axis and that the particle density per unit of rapidity in $p\bar{p}$ collisions is approximately constant for $|\eta| \lesssim 3$ ¹.

Relativistic particles, emerging from the collisions point close to the center of

¹At high particle energies ($E \gg m$), the pseudorapidity is a good approximation of the rapidity

$$y = 0.5 \ln \frac{E + P_z}{E - P_z},$$

where E is the energy and P_z is the momentum in z-direction. Both names are used synonymously.

the detector, travel through various tracking chambers in which they lose only a negligible fraction of their energy, due to the light weight, low density construction of these modules. Located closest to the beam line is a Silicon Vertex Chamber (SVX) with excellent tracking resolution of $11 \mu\text{m}$ for a single hit [44]. Just outside the beam line is the Vertex Time Projection Chamber (VTX), followed by the large Central Tracking Chamber (CTC). Each chamber allows three-dimensional track reconstruction and event vertex identification. The tracking chambers and an additional tracking device, the Central Drift Tube array (CDT), are placed inside a 1.4 T superconducting solenoid.

The tracking system is hermetically enclosed by a set of electromagnetic and hadronic calorimeters in which photons, electrons and hadrons are absorbed. During this process, extended multiple particle showers are formed. The acronym for electromagnetic (hadronic) calorimeters at CDF is XEM (XHA), where X = C, P, F represents the central, plug or forward region.

Muons have to be detected separately. Although interacting with matter in the same way as electrons, they are 200 times heavier and therefore do not lose much energy through emission of bremsstrahlung when traveling through the detector. Muons are to first approximation minimum ionizing particles.

Drift tube arrays which measure muon track information are located behind the hadronic calorimeters. CDF has four muon chambers, the Central Muon Chamber (CMU), the Central Muon Upgrade (CMP), the Central Muon Extension (CMX) and the Forward Muon Detector (FMU). The CMP serves as veto detector for the CMU to reduce background from high energy hadrons which have traversed the hadronic calorimeter ('punch through').

Other detectors within CDF are the Wall Hadron Calorimeters (WHA), which

fills up the gap between the CHA and PHA, the Central Preradiator (CPR), placed in front of the CEM for early shower detection, and the Beam Beam Counters (BBC) for the measurement of the $p\bar{p}$ interaction rate (luminosity).

In the following sections, we describe detector parts relevant for this analysis. A complete description of the detector and further references can be found in [43].

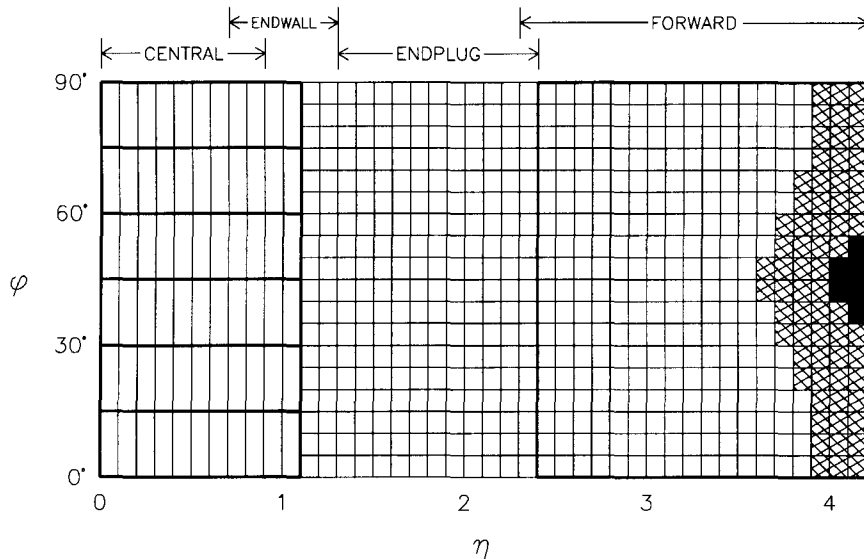


Figure 4.3: Segmentation and coverage of the CDF calorimeters.

4.2.1 Calorimeters

The CDF calorimeters are segmented into projective towers with a complete azimuthal coverage and ranging from 2° to 178° in the polar angle θ , which corresponds to the η region -4.2 to 4.2 covered by three calorimeters (Figure 4.3) : the Central Calorimeter ($|\eta| < 1.1$), the Plug Calorimeter ($1.1 < |\eta| < 2.4$) and the Forward Calorimeter ($2.4 < |\eta| < 4.2$).

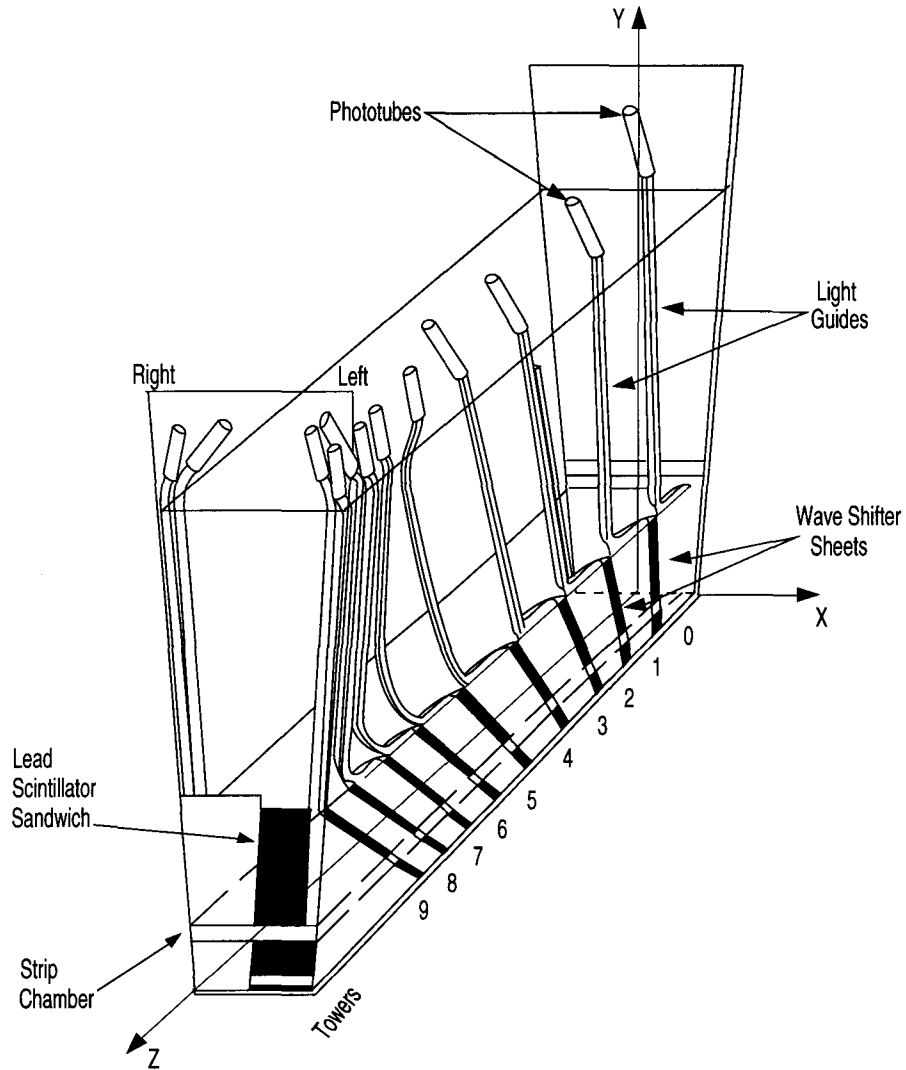


Figure 4.4: Light gathering system of a CEM wedge consisting of ten towers.

The Central Calorimeter

The electromagnetic calorimeter (CEM) in the central region is built of 48 modules each divided into 10 towers of the size 0.1 in η and 15° in ϕ (Figure 4.4). It uses SCSN-38 polystyrene scintillator and Y7 UVA acrylic wavelength shifter combined with Hamamatsu R580 phototube readout. Interleaved with the scintillator are layers of lead. The CEM is 18 radiation lengths and 1 absorption length thick. Its energy resolution is $13.7\%/\sqrt{E_T}$.

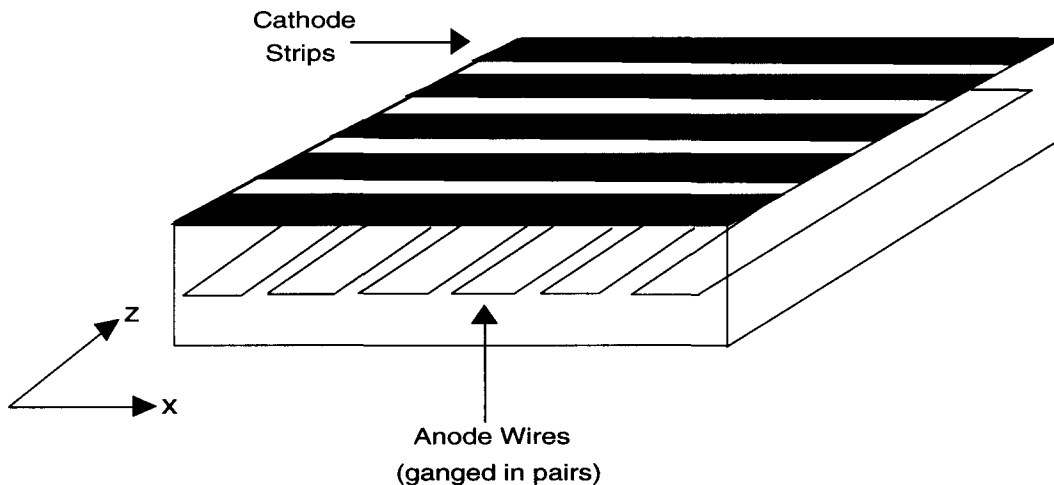


Figure 4.5: Schematic view of the anode wires and cathode strips in the Central Strip Chamber.

At about 6 radiation lengths within each central calorimeter module a proportional multiwire chamber (CES) filled with a mix of 95% argon and 5% CO_2 is located. The CES measures the transverse profile of electromagnetic showers through anode wire read-out in x-direction and orthogonal cathode strip read-out in z-direction. Figure 4.5 depicts a schematic view of the CES and defines the local coordinate system (x,z) . The strip (wire) spacing is 18 mm (6.3 mm). There are 64 channels in both x- and z-views. The CES has a spatial resolution of ± 2 mm for precise shower position and width measurement.

The central hadronic calorimeter (CHA) consists of 48 modules which are each divided into 8 towers of the size 0.1 in η and 15° in ϕ . Layers of scintillating plastic (acrylic PMMA) are interleaved with steel plates. UVA PMMA doped wavelength shifter are read out by Thorn-EMI 9954 phototubes. The CHA is 4.5 absorption lengths thick. It has an energy resolution of $50\%/\sqrt{E}$.

The Plug Calorimeter

In the forward region, the calorimeter consists of gas proportional chambers with cathode pad readout, filled with a 50 : 50% mix of argon and ethane. The electromagnetic plug calorimeter (PEM) is built of 34 layers of plastic proportional tubes interspersed with lead absorber panels. There are four quadrants, each of which has a segmentation of 0.09 in η and 5° in ϕ . The PEM is 18–21 radiation lengths and 0.9–1.0 absorption lengths deep. Its energy resolution is $22\%/\sqrt{E}$.

For precise shower position and width information, strips and wires are built into the PEM at a depth of 4.4 radiation lengths (PES). The strips are oriented in azimuthal direction, and the wires point in η -direction away from the beamline. The PES has a spacial resolution of 2 mm. Its coverage is limited to the region $\eta = 1.20 - 1.84$.

The hadronic compartment (PHA) is built similarly to the PEM with lead absorber panels replaced by steel panels. It is 5.7 absorption lengths thick and has an energy resolution of $106\%/\sqrt{E}$.

The Forward Calorimeter

In the extreme forward region, the Forward Calorimeter is built similarly to the Plug Calorimeter with a somewhat larger segmentation of 0.1 in η and 5° in ϕ . The electromagnetic part (FEM) is 25.5 radiation lengths and 0.8 absorption lengths thick. The thickness of the hadronic part (FHA) is 7.7 absorption lengths. The FEM and FHA have energy resolutions of $26\%/\sqrt{E}$ and $137\%/\sqrt{E}$, respectively.

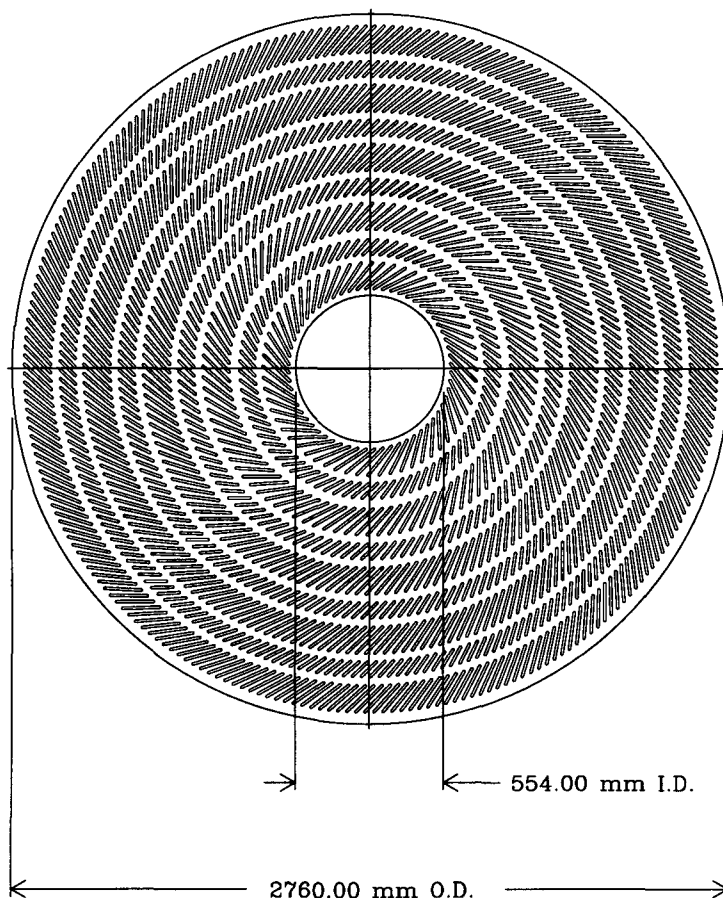


Figure 4.6: End view of the Central Tracking Chamber showing the location of the slots in the aluminum endplates.

4.2.2 Tracking

Two of the three CDF tracking systems are used for this analysis: The Central Tracking Chamber (CTC) within pseudorapidities of $|\eta| < 1.5$ and the Vertex Time Projection Chamber (VTX) in the region $|\eta| < 3.2$. Both systems are contained within a 1.4 T axial magnetic field.

The Central Tracking Chamber

The Central Tracking Chamber (Figure 4.6) is a cylindrical drift chamber of 1.3 m radius and 3.2 m length. It is ≈ 0.015 radiation lengths thick. Precise momentum and position determination is achieved by using 84 layers of sense wires which are arranged in 5 axial superlayers with the wires parallel to the beam line and 4 stereo superlayers with the wires tilted by $\pm 3^\circ$ relative to the beam line. The wire spacing is 10 mm. Altogether, there are 60 axial and 24 stereo layers.

An equal mixture of argon and ethane, with a little ethanol added, is used as the drift gas. The direction of the drift field, which has a field gradient of 1340 V/cm and a uniformity of $dE_0/E_0 \sim 1.5\%$ (rms), is approximately 45° with respect to the radial direction. The drift time to the nearest wire is 40 ns. The drift direction is parallel to the circumferential direction at a magnetic field of 1.4 T. Since the CTC single wire resolution is less than $200\ \mu\text{m}$, the spatial resolution in the z -direction is $200\ \mu\text{m}/\sin(3^\circ) = 4\ \text{mm}$. For isolated tracks not coming from the vertex the momentum resolution over a track fitting range of 1 m is $\delta P_T/P_T < 0.002 \cdot P_T$, where P_T is the transverse component of the momentum vector (see Section 4.2.3). For tracks originating at the event vertex the momentum resolution improves to $\delta P_T/P_T < 0.0011 \cdot P_T$ over a track fitting range of 1.3 m.

The Vertex Time Projection Chamber

The VTX consists of eight individual time projection chambers filled with a 50 : 50% mix of argon and ethane. It is 2.8 m long and extends from 8° to 172° ($|\eta| < 3.25$) outside the beam line. Track coordinates in the z -direction are measured through 24 layers of sense wires (in ϕ -direction cathode pads are used). The wire spacing is 6.3 mm. For an accurate measurement of the primary event

z-vertex, the VTX has a spatial resolution of 1 mm in z-direction. The chamber is about 0.045 radiation lengths thick.

Luminosity Monitors

An array of 16 scintillator plates plus photomultiplier tubes, so called Beam-Beam Counters (BBCs), are used to determine the actual luminosity during collisions. They are located at a distance of 5.8 m from the nominal interaction point and extend from 0.32° to 4.47° ($3.24 < |\eta| < 5.9$). Due to their excellent timing properties, the BBCs can accurately measure the time of the interaction. Because of that, the BBCs are also used as minimum bias trigger for the trigger system (Section 4.2.4).

The BBC cross section of $\sigma_{bbc} = 51.2 \pm 1.7$ mb was obtained in a direct measurement [4] [45]. This value was used in the determination of the luminosity.

4.2.3 Event Reconstruction

Calorimetry

Because the CDF detector has a cylindrically symmetric geometry, it is natural and often times necessary to express physics quantities in terms of a ‘transverse component’. In case of scalars, like the energy deposited in an electromagnetic calorimeter, a three dimensional ‘vector’ is artificially created by multiplying the scalar with a unit vector $\hat{n} = (\sin\theta \cdot \cos\phi, \sin\theta \cdot \sin\phi, \cos\theta)$, which originates at the event vertex and points to the center of the particle cluster. The transverse component of the ‘energy vector’, $E \cdot \hat{n}$, is hence given by

$$E_T = \sqrt{E_x^2 + E_y^2} = E \cdot \sin\theta, \quad (4.2)$$

with the polar angle θ .

A cluster is formed by the CDF offline code according to the following cluster algorithm: the detector is searched for a tower with a transverse energy deposition, E_T , above 3 GeV. If such a tower is found and any of its adjacent towers has a higher energy deposition, that tower's neighborhood is searched. This process continues until the tower with the highest E_T , called the seed tower, is determined. A particle cluster is then defined as a matrix of towers with the seed tower as centroid. The maximum size of a cluster matrix depends on the detector.

In the CEM, there is no energy sharing between adjacent ϕ towers since electromagnetic showers in the ϕ -direction are smaller than the space between two towers, as testbeam results have shown. Therefore, only the two neighboring η towers are added to form a 3×1 cluster matrix, spanning $\Delta\eta \sim 0.3$ and $\Delta\phi \sim 15^\circ$. The finer segmentation of the forward calorimeters requires inclusion of more towers in the cluster matrix than in case of the central calorimeter. In the PEM, the maximum cluster size is a 5×5 matrix, $(\Delta\eta, \Delta\phi) \sim (0.5, 25^\circ)$. In the FEM the cluster limit is 7×7 towers, $(\Delta\eta, \Delta\phi) \sim (0.6, 35^\circ)$. Only towers with an energy deposition above 100 MeV are included. A cluster is retained if the cluster E_T is above 5 GeV and the ratio of the hadronic to electromagnetic energy, HAD/EM , is below 0.125. Once a cluster is accepted, it is excluded from the search for additional clusters.

The cluster centroid is measured in the CEM by the CES position information, and in the PEM and FEM by the cluster center-of-gravity or by the PES position information, where applicable. To locate the cluster in the strip chamber, the CES (PES) clustering algorithm searches for the strip with the highest energy above

500 MeV (400 MeV). Any of 11 (10) channels centered on the seed is included in the cluster energy sum if its individual energy is above 57.2 MeV (100 MeV).

A cluster is called isolated if the sum of the electromagnetic and hadronic transverse energy in a cone of

$$\Delta R = \sqrt{\Delta\eta^2 + \Delta\phi^2} \quad (4.3)$$

around the cluster, $E_{T,\Delta R} - E_{T,cluster}$, falls below a threshold, usually less than a few GeV. $\Delta\eta$ ($\Delta\phi$) is the rapidity (azimuth) difference between the centroids of a given tower and the particle cluster. Commonly, the *relative* isolation, ISO , is used:

$$ISO \equiv \frac{E_{T,\Delta R} - E_{T,cluster}}{E_{T,cluster}} \quad (4.4)$$

Several corrections have to be applied to obtain a good estimate of the electromagnetic particle's energy.

Energy corrections in the CEM calorimeter:

- From testbeam electron data, a tower response map as a function of η and ϕ is created. Using the location of the CES cluster, a correction factor corresponding to the particle's (η, ϕ) -position is applied.
- Intrinsic differences in the tower-to-tower responses are mapped by matching the calorimeter energy to the track momentum of sample electrons with $E_T > 12$ GeV.
- The global energy scale is determined by a comparison of the E/P distribution of W electrons simulated by a radiative Monte Carlo and a full detector simulation to the one of inclusive W electron data where the above corrections

have already been applied. To do so, the momentum scale has to be corrected by studying the invariant mass spectrum from $J/\psi \rightarrow \mu\mu$ decays.

Energy corrections in the forward calorimeters:

- With time, several anode layers lost their high voltage. In such a case, a ‘dead layer’ energy correction is applied based on an interpolation of the average longitudinal shower profile as measured at the testbeam.
- A tower-to-tower response map is obtained for the PEM using 100 GeV testbeam electron data. For the FEM, the tower-to-tower response has not been measured, and is assumed to be 1.
- The forward calorimeters are non-linear at high energies. Non-linearity corrections and the overall energy scale are measured in testbeam energy scans up to 175 GeV. These corrections are modified, so that the invariant mass spectrum of Z bosons, where one decay electron is found in the CEM and the other in the PEM (FEM), is correctly reproduced.

For some particles like neutrinos, the interaction cross section with matter is so small that they completely escape detection. Momentum conservation requires the neutrino transverse momentum to be balanced by the transverse momentum of all other particles. Undetected particles therefore lead to a ‘momentum imbalance’ in the detector. Because the neutrino is massless and the massive particles are relativistic, energy and momentum can be treated equivalently and an ‘energy imbalance’ can be expressed in form of the missing E_T vector

$$E_T = -\left| \sum_i^{towers} E^i \cdot \hat{n}_i \right|, \quad (4.5)$$

where E^i is the uncorrected energy deposition in tower i , and \hat{n}_i is the corresponding unit vector perpendicular to the beam axis which points to the i^{th} tower center. The sum includes all calorimeter towers within the region $|\eta| < 3.6$ whose energy deposition falls below a detector dependent threshold ². The missing E_T vector vanishes if the energy is balanced, i.e. *all* the energy in an event was deposited and measured in the calorimeters.

The quality of a cluster transverse profile is determined by comparison with the ‘template’ of the transverse shower profile of testbeam electrons. A χ^2 variable is used as an estimator of the goodness of the profile fit to the electron hypothesis. The smaller the χ^2 , the more likely it is that the cluster was produced by an electron (or photon, as electrons and photons have almost identical calorimeter responses).

The χ^2 variable is usually used for electron quality cuts or to separate photons from isolated neutral meson background. The offline code calculates a χ^2 for the CES strip and wire profile, for PES profiles in η and ϕ -direction and for a PEM 3×3 tower matrix centered on the cluster seed tower. Unfortunately, all these variables are differently normalized; their values cannot be directly compared with each other.

Another variable defined only for the CEM is the transverse profile, L_{shr} , which estimates the goodness of the fit of the lateral shower shape to the lateral electron testbeam profile. It is defined as

²The energy threshold are for the following calorimeters: CEM, CHA > 0.1 GeV; PEM > 0.3 GeV; PHA, FEM > 0.5 GeV; FHA > 0.8 GeV.

$$L_{shr} = 0.14 \cdot \sum_i \frac{E_i^{obs} - E_i^{exp}}{\sqrt{0.14^2 \cdot E + (\Delta E_i^{exp})^2}}, \quad (4.6)$$

where E_i^{obs} is the measured energy in a tower i adjacent to the seed tower, and E_i^{exp} is the expected energy in the same tower, inferred from the seed tower energy information. The square root in the denominator contains the corresponding uncertainties, added in quadrature. Good electrons have $|L_{shr}| \lesssim 0.2$.

Tracking

The high resolution tracking chamber, CTC, allows complete three-dimensional track reconstruction and a precise measurement of the momentum vector of a charged particle. CTC tracking is fully efficient only in the region $|\eta| < 1.1$ (Figure 4.7). The extrapolated position of a reconstructed CES track can be compared to the CES shower position, and the difference in Δz (z -view) and Δx ($(r-\phi)$ -view) be used to remove background events from overlapping charged and neutral hadrons in the electron identification.

At higher rapidities tracks are identified by the Vertex Chamber, VTX, by comparing the number of layers (wires) in the VTX with hits along the particle trajectory from the collision point to the cluster centroid. The width of this road is 0.035–0.41 radians in ϕ and 0.022–0.125 units in $\cot\theta$, depending on the angle between the electromagnetic cluster and the z -direction. The VTX occupancy is defined by the ratio of the number of observed to the number of expected hits along this road. A good track is characterized by a high VTX occupancy, close to 1. Values below 0.5 are more likely due to the passage of a neutral particle. The VTX also provides the z -position of the primary vertex for every event.

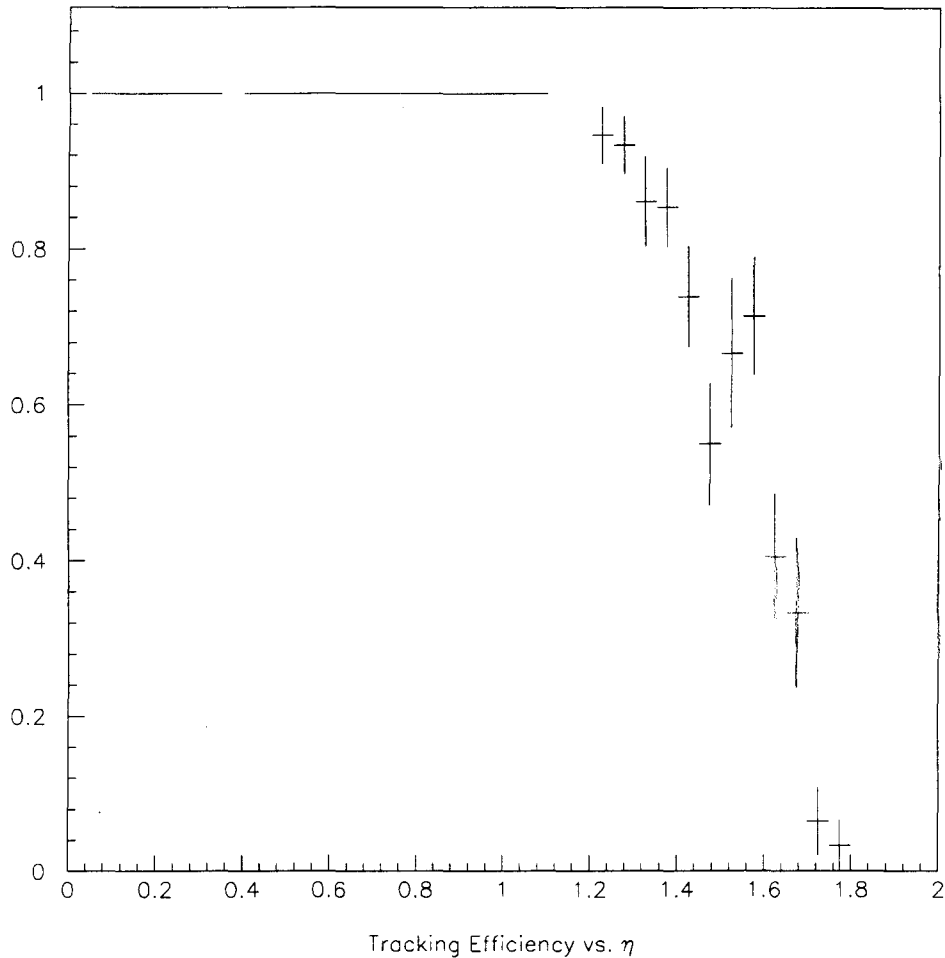


Figure 4.7: Central Tracking Chamber efficiency as a function of pseudorapidity.

4.2.4 Triggering

With an inelastic $p\bar{p}$ cross section of about 50 mb at typical luminosities of $5 \cdot 10^{30} \text{ cm}^{-2}\text{s}^{-1}$, the rate at which particles pass through the detector is about 250 kHz. To extract rare events, a careful preselection has to be performed. Only events that pass certain trigger requirements get written out to 8 mm tape at a rate of about 5 Hz. To optimize the data acquisition CDF uses *three* staged trigger levels. The events for this analysis were collected using inclusive electron triggers that make use of tracking and calorimetry information.

Level 1

The Level 1 trigger decision is based on the transverse energy (E_T) in the electromagnetic calorimeter. Level 1 requires for electrons that one trigger tower (two physical towers) be above a 6 GeV (8 GeV) in the CEM (PEM, FEM). The decision is made within 3.5 μ s for each accepted event. The acceptance rate at Level 1 is in the range of a few kHz.

Level 2

The trigger at Level 2 makes use of calorimetry as well as tracking information. For this analysis, the Level 2 accepts an event if it passes either one of the following electron/photon triggers, denoted by L2A and L2B :

L2A The ratio of the total to the electromagnetic cluster energy must be less than 1.125 and a stiff track of transverse momentum $P_T > 9.2$ GeV/c can be matched to the cluster. A cluster is formed by a hardware cluster finder, which scans the calorimeter for towers above a threshold E_T of 9 GeV. Adjacent neighbors and neighbors to the neighbors etc. are included in the cluster array if their E_T is above 7 GeV. The total cluster energy is the summed energy of the electromagnetic as well as the hadronic cluster towers. The track information comes from the central fast tracker (CFT), a hardware track processor, that compares hits in the axial sense wires of the CTC with already known hit patterns within a P_T range from 2.5 to 15 GeV/c. This way fast two dimensional tracking information is available with a momentum resolution of $\delta P_T/P_T = 0.035 \cdot P_T$.

L2B The clustering algorithm, as described for trigger L2A, uses a seed threshold of 16 GeV. The ratio of the total to the electromagnetic cluster energy must

be less than 1.125. The cluster must be isolated [46]. There is no track requirement.

The Level 2 trigger rate for electrons of $E_T > 10$ GeV is in the order of 20 Hz with an efficiency of $\approx 94\%$.

Level 3

Level 3 is the highest trigger level. The trigger processing is performed by a farm of 48 Silicon Graphics multi-CPU computers with RS3000 processors, which has a processing power of about 10^9 instructions per second. The complete detector information is available. The CFT information, described above, and a special (streamlined) version of the CDF offline code is used to filter events that were accepted by Level 2. Typically several events per second are accepted and written out to tape.

For this analysis, the central electron Level 3 trigger is used. A three-dimensional track with $P_T > 13$ GeV/c is required to point at the electron cluster with $E_T > 18$ GeV, $\chi_{strip}^2 < 10$ and $L_{shr} < 0.2$. A match between the track and the CES shower centroid in x- and z-direction is additionally imposed: $\Delta x < 3$ cm and $\Delta z < 5$ cm. The Level 3 electron trigger efficiency in the fiducial region is about 98%.

4.2.5 Data Acquisition

The calorimeter voltages before and after the crossing of a (anti)proton bunch are read in by 129 modules, so-called RABBIT crates [47], which are mounted on the detector. If an event passes Level 2 the difference between the two voltages before and after bunch crossing is digitized by an ADC card. Signals from the tracking

system are read in by FASTBUS TDC modules [46] [48] and digitized, if Level 2 accepts. The digital information is subsequently read out by special scanners³ and transferred to the software ‘Event Builder’. The event builder converts the event to the same bank structures that are used in the offline analyses. At this point the Level 3 trigger makes the final decision whether or not the event gets written to tape.

³MX scanners for the calorimetry signal and SSP scanners for the tracking signal.

Chapter 5

Particle Identification

5.1 W and Z Boson Selection

During the Run 1a in 1992–1993, CDF wrote 19.6 pb⁻¹ of electron data to tape. Central electrons above 18 GeV were preselected to define an inclusive electron data set. From this electron data sample, we extracted a subsample containing clean W and Z events by the applying the following requirements (see also Tables 5.1 and 5.2) :

- The event vertex must be constrained within 60 cm of the nominal interaction point.
- The cluster must be found in a central and fiducial region, $|\eta_{det}| < 1.1$.
- The transverse energy E_T must be greater than 20 GeV.
- The electron must be isolated in a cone of $\Delta R_{\ell\gamma} < 0.4$,

$$ISO4 \equiv \frac{E_{T,\Delta R < 0.4} - E_{T,cluster}}{E_{T,cluster}} < 0.1.$$

	Cut
Pseudorapidity Range	$ \eta_{det} < 1.1$
z-Vertex Match	$ z_{vertex} < 60 \text{ cm}$
Transverse Energy	$E_T > 20.0 \text{ GeV}$
Isolation	$ISO4 < 0.1$
Energy Ratio HAD/EM	$HAD/EM < 0.055 + 0.00045 \cdot E \text{ (GeV)}$
Strip Profile	$\chi_{strip}^2 < 10$
Lateral Shower Shape	$L_{shr} < 0.2$
3D Track	$N3D = 1$
Ratio Energy/Momentum	$0.5 < E/P < 2.0.$
Track Match in z	$ \Delta z < 3.0 \text{ cm}$
Track Match in x	$ \Delta x < 1.5 \text{ cm}$

Table 5.1: Summary of central electron requirements.

- The ratio of hadronic energy to electromagnetic energy must be less than $HAD/EM < 0.055 + 0.00045 \cdot E$, where E is the total energy of the CEM cluster (in GeV).
- The CES strip shower profile χ_{strip}^2 must be less than 10.
- The lateral shower shape must be less than 0.2.
- A single three-dimensional track must point from the event vertex to the cluster.
- The ratio of electromagnetic cluster energy, E , to track momentum, P , must lie between 0.5 and 2.0.
- The track - CES shower profile match must be better than 3 cm (1.5 cm) in the z-view (x-view).

The fiducial region is determined by the CES shower position which is required to lie within $9 \text{ cm} < z_{ces} < 217 \text{ cm}$ and $x_{ces} < 21 \text{ cm}$ from the center of the CEM. In addition, two uninstrumented regions are excluded: $|\eta_{det}| < 0.05$ (border region of the two halves of the detector), $0.77 < \eta_{det} < 1.0$ and $75^\circ < \phi < 90^\circ$ (penetration of cryogenic connections to the solenoidal magnet).

The isolation, HAD/EM energy ratio and the profile quality cuts are used to reduce hadronic background. The energy dependent term in the HAD/EM requirement is a correction for energy leakage from the electromagnetic into the hadronic calorimeter, to obtain an energy independent efficiency. The $N3D$, E/P and track-profile match cuts ensure the presence of a three-dimensional track associated with the electron cluster. A relatively wide E/P range was chosen to account for emission of bremsstrahlung.

W events were extracted from this common sample by additionally requiring

- the missing transverse energy be greater than 20 GeV.

13920 W events passed these requirements.

Z events were extracted from the common sample by additionally requiring a second electron in either the central, plug or forward section of the CDF detector. The associated electromagnetic cluster had to pass the following requirements (see also Table 5.2) :

- The transverse energy E_T in the CEM / PEM / FEM must be greater than 10 / 15 / 20 GeV.
- The electron must be isolated in a cone of $\Delta R_{e\gamma} < 0.4$,

$$ISO4 \equiv \frac{E_{T,\Delta R < 0.4} - E_{T,cluster}}{E_{T,cluster}} < 0.1.$$

Transverse Energy	$E_{T, cem/pem/fem} > 10 / 15 / 20 \text{ GeV}$
Isolation	$ISO4 < 0.1$
Energy Ratio HAD/EM	$HAD/EM < 0.1$
Ratio Energy/Momentum	$E/P_{ctc} < 2.0$
3×3 Tower Profile [†]	$\chi^2_{3 \times 3} < 3.0$
VTX Occupancy [†]	$f_{vtx} > 0.5$
Z Boson Mass	$70 < M_{ee} < 110 \text{ GeV}/c^2$.

Table 5.2: Summary of the requirements for the second Z electron. [†] Plug region only.

- The ratio of hadronic energy to electromagnetic energy must be less than 10%.
- In the *central* region, a second electromagnetic cluster must have a three-dimensional track with an energy to momentum ratio less than 2.0.
- In the *plug* region, a second electromagnetic cluster must have a 3×3 tower χ^2 less than 3, and a VTX occupancy greater than 0.5.
- The invariant mass of the two electrons must lie between $70 \text{ GeV}/c^2$ and $110 \text{ GeV}/c^2$.

1237 Z events passed these requirements.

5.2 Photon Selection

A photon event in the central calorimeter ($|\eta_{det}| < 1.1$) is defined as an electromagnetic object that passes the following requirements (Fig. 5.3) :

- The photon cluster must be found in a central and fiducial region, $|\eta_{det}| < 1.1$.

- The transverse electromagnetic energy must be at least 7 GeV.
- The photon must be separated from the W or Z electron by $\Delta R_{\ell\gamma} > 0.7$ (equivalent to an angular separation of $\Delta\phi \sim 40^\circ$).
- The cluster must be isolated in a cone of $\Delta R_{\ell\gamma} < 0.4$,

$$ISO4 \equiv \frac{E_{T,\Delta R \leq 0.4} - E_{T,cluster}}{E_{T,cluster}} < 0.15.$$

- Only a very limited number of low energy tracks may exist in the vicinity of the cluster. Quantitatively, the sum of the transverse momentum of all three-dimensional CTC tracks in a cone of $\Delta R_{\ell\gamma} = 0.4$ around the photon direction, $\Sigma PT4$, must be less than 2 GeV/c. These tracks have to originate within 10 cm of the event vertex.
- No charged three-dimensional track must point from *any* vertex to the cluster.
- The lateral shower shape must be less than 0.5.
- The ratio of hadronic energy to electromagnetic energy must be less than $HAD/EM < 0.055 + 0.00045 \cdot E$, where E is the total energy of the photon cluster.
- The CES strip and wire χ^2 must be less than 20.
- No second CES cluster with energy above 1 GeV is allowed within the tower region associated CEM cluster.

The photon-lepton separation requirement ensures that the two corresponding clusters are sufficiently separated in the (η, ϕ) -space. It also favors $V\gamma$ ($V = W$ or Z) production events over radiative W/Z decays. The isolation cuts $ISO4$ and $\Sigma PT4$,

the HAD/EM and the shower shape quality cuts are used to reduce QCD jet backgrounds. The no-2nd-CES-cluster requirement further suppresses multiphoton background from neutral meson decays.

One background to $W\gamma$ production are $(Z \rightarrow \ell^+\ell^-) + \gamma$ events where one lepton escapes detection (Chapter 6). This ‘one-legged Z’ background is suppressed by rejecting events with a second isolated high momentum track ($P_T > 10$ GeV/c) and opposite charge sign to the first electron, and a pair mass constructed from the kinematical properties of the electron and the track, $M_{e\text{track}} < 70$ GeV/c². Since we do not veto $W\gamma + \text{jet}$ events, these high P_T tracks must not be found inside a jet ($\Delta R_{jet\text{track}} < 0.7$) which has an electromagnetic fraction greater than 0.85.

Table 5.3 summarizes the photon cuts and lists the number of events surviving each selection criteria in successive order. Finally, there are 18 $W\gamma$ events in the sample of 13920 W events, and 4 $Z\gamma$ events in the sample of 1237 Z events, which pass *all* selection requirements.

Examples of event displays of W and Z bosons with central or plug photons are shown in Section 8.2 and Section 9.1.

5.3 Monte Carlo Programs

In the $W\gamma$ and $Z\gamma$ analyses, Monte Carlo programs are used to obtain Standard Model and background predictions, to perform detector simulations and to determine acceptances. We will refer frequently to the various programs which we are going to discuss briefly in the following section.

	$W\gamma$	$Z\gamma$	P16
Inclusive W/Z or P16 Samples	13920	1237	6062
Fiducial, $ \eta_{det} < 1.1$, $E_T^\gamma > 7.0$ GeV, $\Delta R_{\ell\gamma} > 0.7$	487	48	3067
$ISO4 < 0.15$	73	14	704
$\Sigma PT4 < 2.0$ GeV	34	10	513
$N3D = 0$	31	9	—
$HAD/EM < 0.055 + 0.00045 \cdot E$ (GeV)	31	9	507
$L_{shr} < 0.5$	27	7	407
$\chi_{strip}^2 < 20$, $\chi_{wire}^2 < 20$	21	6	287
no 2 nd CES > 1 GeV	19	4	216
no 2 nd Track ($W\gamma$ only)	18	—	—

Table 5.3: Number of events in the inclusive W, Z and the 16 GeV photon background sample (P16) passing the photon requirements in successive order. In the case of the P16 sample, the first row indicates the number of central and fiducial objects that have no three-dimensional track associated with. Trigger objects are excluded.

5.3.1 The Baur $W\gamma/Z\gamma$ Monte Carlo

The Baur Monte Carlo [49] creates $W\gamma$ and $Z\gamma$ events in each of the decay channels through a complete helicity calculation of all Feynman diagram contributions in Figure 2.1 and Figure 2.5. Kinematic phase space integration is performed by Monte Carlo techniques using the adaptive multi-dimensional integration code VEGAS [50]. The CERN PDFLIB library of structure functions [51] was included with MRSD-' [52] as default. CDF has found that simulations using the structure function MRSD-' provide the closest match to results in electroweak analyses, for example the measurement of the W asymmetry [53]. Implemented in the Baur Monte Carlo is a complete set of the Cabibbo-Kobayashi-Maskawa quark-mixing matrix elements [54].

The Monte Carlo scales the $W\gamma$ and $Z\gamma$ production cross sections by a K-factor,

constant over a large rapidity range, in order to approximate higher order QCD processes like $q + \bar{q} \rightarrow g + V + \gamma$ and $q + g \rightarrow q + V + \gamma$ [55]:

$$\left[1 + \frac{8\pi}{9}\alpha_s(M_V^2)\right] \approx 1.35,$$

V represents a W or Z vector boson and $\alpha_s(M_V^2)$ is the strong coupling constant at $Q^2 = M_V^2$, where Q is the $q\bar{q}$ momentum transfer and M_V is the vector boson mass. It has been shown [56] that at Tevatron energies such a constant scale factor is a reasonable choice. Recent calculations of QCD corrections to $WW\gamma$ production additionally lend support [57].

The Baur Monte Carlo produces weighted events. The weight associated with each event is the probability that such an event would occur in an experiment.

For this analysis, Monte Carlo samples of the order of half a million events were generated using different sets of anomalous $W\gamma$ ($Z\gamma$) coupling constants as input parameters. To avoid potential kinematic or geometrical biases, only loose W (Z) and photon selection cuts were applied:

- The photon E_T must be greater than 1 GeV,
- The lepton P_T must be greater than 1 GeV/ c ,
- The electron-photon separation $\Delta R_{\ell\gamma}$ must be greater than 0.3 to avoid divergences in the Monte Carlo,
- A lower limit for the transverse cluster mass was set to 40 GeV/ c^2 ,
- The maximal photon, lepton or neutrino rapidity was set to ± 6.0 .

5.3.2 Detector Simulations

Two different CDF detector simulations are used in this analysis, QFL [58] and the Fast Monte Carlo [59].

QFL is the standard Monte Carlo used at CDF which simulates the response of CDF detector components by a detailed parameterization. The four vectors of the final state particles is used as input information. The physics output banks have the same structure as those produced by the CDF offline code, so that the same analysis code can be applied to QFL Monte Carlo data and real data.

The Fast Monte Carlo uses the final state four vectors input as well, but its simulation of the CDF detector response is accelerated by using an optimized parameterization of the detector resolution and geometry. Efficiencies for various cut variables are put in by hand and therefore must be known from other studies. Since neither experimental data nor a complete calculation of diboson P_T distributions exist, the Fast Monte Carlo boosts the $W\gamma$ ($Z\gamma$) system according to the W or Z P_T distributions measured by CDF [60] (see Chapter 5.6 for further discussion).

5.3.3 Other Monte Carlo Programs

Underlying events in $W\gamma$ data created by the Baur Monte Carlo were produced by ISAJET [61]. For background studies, $W + \text{jet}$ and $Z + \text{jet}$ events were created by the VECBOS Monte Carlo [62]. The jet fragmentation was accomplished by HERWIG [63].

5.4 Efficiencies

In general, event selection cuts do not perfectly separate signal from background; a fraction of signal events will always be lost when cuts are applied to a data sample. It is convenient to divide the total detector efficiency into two separate pieces; the first is the efficiency associated with angular and momentum coverage and the second is the efficiency (acceptance) associated with the spatial coverage of the detector. The following section discusses the determination of efficiencies for the W (Z) electron and photon selection cuts, and summarizes the electron selection efficiencies. The acceptance will be discussed in the next section.

5.4.1 Photon Efficiencies

Since electrons have a very similar response in calorimeters as photons, the efficiencies, ϵ^γ , of the some cut variables can be determined from electron testbeam data:

- $\epsilon_{had/em}^\gamma$ for the ratio of hadronic to electromagnetic energy cut.
- ϵ_{lshr}^γ for the lateral energy sharing cut.
- $\epsilon_{\chi^2}^\gamma$ for the CES strip and wire shower profile cuts.
- $\epsilon_{no\ 2^{nd}\ ces}^\gamma$ for the no-second-CES-cluster cut.

These efficiencies were calculated from the number of well defined testbeam electrons above the corresponding cut, divided by the total number of electrons in the sample. The results are listed in Table 5.4. Within the statistical errors, the efficiencies appear to be energy independent.

Electron Sample	$\epsilon_{had/em}^\gamma$	ϵ_{lshr}^γ	$\epsilon_{\chi^2}^\gamma$	$\epsilon_{no2^{nd}ces}^\gamma$
5 GeV	$98.9 \pm 0.2\%$	$99.9 \pm 0.1\%$	$97.3 \pm 0.3\%$	$98.0 \pm 0.1\%$
10 GeV	$99.6 \pm 0.1\%$	$98.8 \pm 0.4\%$	$96.2 \pm 0.4\%$	$97.9 \pm 0.1\%$
18 GeV	$99.1 \pm 0.9\%$	$100.0^{+0.0}_{-1.7}\%$	$98.2 \pm 1.8\%$	$98.2 \pm 1.6\%$
30 GeV	$98.9 \pm 0.9\%$	$100.0^{+0.0}_{-1.1}\%$	$99.2 \pm 0.7\%$	$98.2 \pm 1.0\%$
50 GeV	$98.0 \pm 0.3\%$	$99.9 \pm 0.1\%$	$99.2 \pm 0.2\%$	$97.6 \pm 0.2\%$

Table 5.4: Central photon efficiencies for electromagnetic shower variables determined from electron testbeam data samples at various energies. The statistical uncertainties are given.

Due to the presence of underlying events, the isolation cuts $ISO4$ and $\Sigma PT4$, $\epsilon_{\Sigma pt4}^\gamma$ and ϵ_{iso4}^γ , and the 3D-track cut, ϵ_{n3d}^γ , are not fully efficient. We measured their efficiencies from random cone studies in the inclusive electron W and Z samples. In each W (Z) event, cones of the size $\Delta R_{\ell\gamma} = 0.4$, which are $\Delta R_{\ell\gamma} > 0.7$ away from the decay lepton(s), were formed at random points within the central region of the detector ($|\eta_{det}| < 1.1$). Values for $\Sigma PT4$, $ISO4$ and $N3D$ at the random cone position were determined using the same algorithm that calculates these quantities in the CDF offline data reconstruction code.

The efficiency of the $\Sigma PT4$ cut is defined as the number of random cones with a track P_T sum less than 2 GeV, divided by the total number of random cones. Similarly, the efficiency of the $N3D$ track cut is given by the ratio of the number of random cones with no three-dimensional track pointing at the random cone cluster to the total number of random cones.

To determine the efficiency for the sliding cut $ISO4 = ET4/E_T$, the sum of the electromagnetic energy in a ring of $\Delta R_{\ell\gamma} = 0.4$ around the random cluster, $ET4$, was measured. The ratio of number of events with $ET4 < n \cdot 0.25$ GeV ($n = 1, 2, \dots, 40$) to the total number of random cones, was recorded (Figure 5.1 and

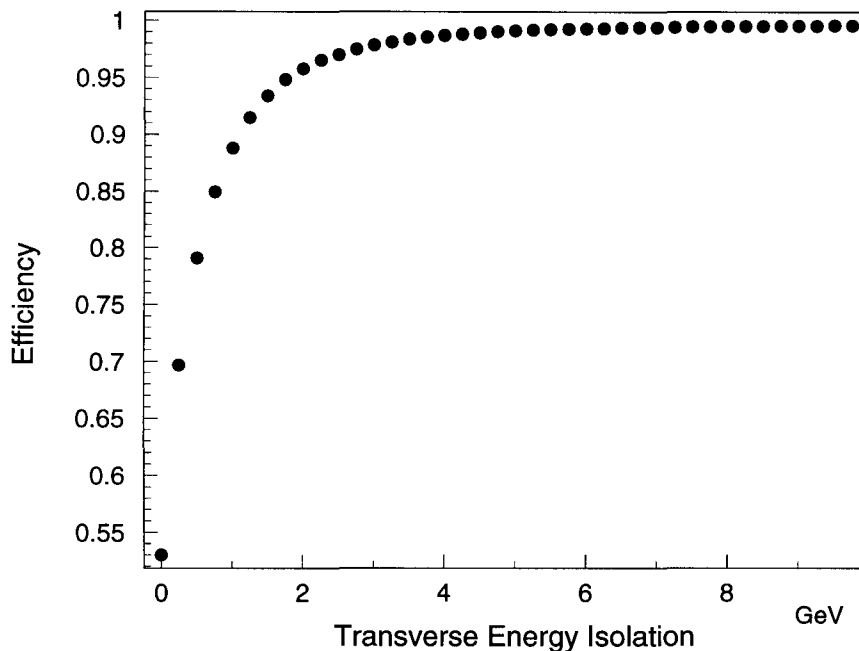


Figure 5.1: Isolation efficiency as a function of the transverse energy cut value, determined from random cone studies in the electron $W\gamma$ sample.

Table 5.5). Since $ISO4 < 0.15$ can be written as $ET4 < 0.15 \cdot E_T$, the efficiency for a particular photon transverse energy can be taken directly from the random cone distribution. Notice the saturation at high energies above ≈ 30 GeV, where the efficiency reaches almost 100%.

Three other correction factors that are not photon selection cut efficiencies have to be determined:

A photon moving through matter may undergo a conversion into a e^+e^- pair. The probability that a photon will not convert in an absorber of thickness x and radiation length X_0 is given by $\mathcal{P}_{conv}^\gamma = \exp(-7 \cdot x/9 \cdot X_0)$. In the CEM region of the CDF detector the average amount of material the photon has to pass through is $8.9 \pm 0.9\%$ of a radiation lengths [64]. Hence, the photon survival probability becomes $\mathcal{P}_{conv}^\gamma = 93.4 \pm 0.6\%$. Several cross-checks on this variable are discussed

E_T Bin (GeV)	7-11	11-15	15-19	19-23	23-27	27+
ϵ_{iso4}	89.2%	94.2%	96.5%	97.6%	98.3%	99.1%

Table 5.5: E_T dependent central photon isolation efficiencies for the cut $ISO4 < 0.15$. The difference in the results from random cone studies in the electron and muon W and Z samples suggests a conservative estimate for the uncertainties of 1.0% .

in Ref. [20].

Some of the photon efficiencies were determined from testbeam electron data. Due to a slight difference in the development between a photon and an electron shower a correction factor $\mathcal{S}_{e \rightarrow \gamma}^{cem}$ has to be applied. It is defined as the product of the ratios of photon to electron selection efficiencies, which were determined by QFL photon and electron Monte Carlo simulations.

Since the minimum transverse energy for clusters found by the Level 3 algorithm is set to 5 GeV, a clustering inefficiency in the low photon E_T region might exist. To investigate this question, we plot the E_T of fiducial CEM clusters from the unbiased, large statistics sample P16 in Figure 5.2a . The distribution in the region between 6 and 10 GeV was fitted to an exponential function of the form $N(E_T) = N_0 \cdot \exp(a \cdot E_T)$. In the region where the clustering algorithm becomes inefficient, the data points fall below the fitted line. However, for the photons above the analysis cut $E_T > 7$ GeV, the algorithm appears to be fully efficient. The ‘turn-on’ efficiency $\epsilon_{turn-on}^\gamma$ shown in Figure 5.2b as a function of CEM cluster E_T is defined as the number of observed events to the number of predicted events from the fit in Figure 5.2a . For comparison, the QFL Monte Carlo E_T prediction of the turn-on efficiency agrees well with the P16 data.

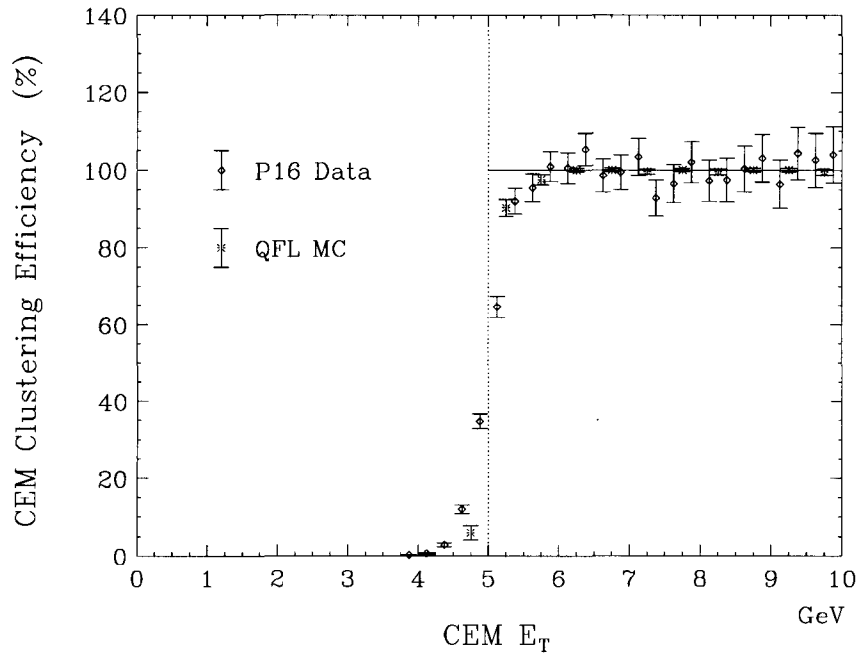
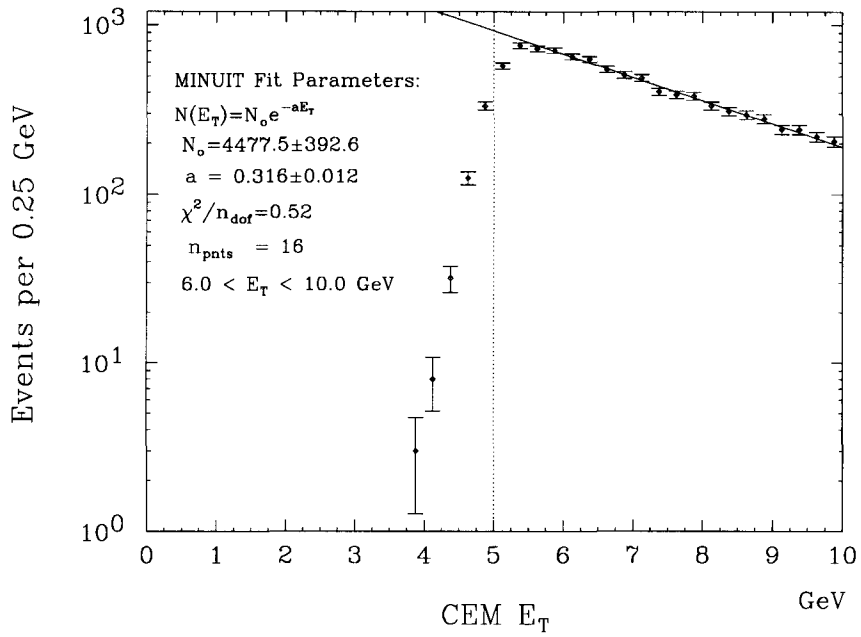


Figure 5.2: a) Observed number of fiducial electromagnetic CEM clusters in the P16 sample as a function of transverse energy. The data points above 6 GeV fit well to an exponential (see inset). The event decrease at low energies is due to a clustering algorithm inefficiency. b) Corresponding efficiency distribution. QFL Monte Carlo results are compared to data.

$\epsilon_{\Sigma pt4}^{\gamma}$	$95.2 \pm 0.1 \pm 0.8\%$	Tracking Isolation
ϵ_{n3d}^{γ}	$95.6 \pm 0.1 \pm 0.7\%$	No 3D Track
$\epsilon_{had/em}^{\gamma}$	$99.2 \pm 0.9 \pm 0.8\%$	<i>HAD/EM</i>
ϵ_{lshr}^{γ}	$99.9 \pm 0.1 \pm 0.3\%$	Lateral Shower Profile
$\epsilon_{\chi_{strip}^2 + \chi_{wire}^2}^{\gamma}$	$98.4 \pm 0.1 \pm 0.9\%$	CES Strip / Wire χ^2
$\epsilon_{no\ 2^{nd}\ ces}^{\gamma}$	$97.9 \pm 0.7 \pm 1.0\%$	No 2 nd CES Clusters
$\epsilon_{turn-on}^{\gamma}$	100% †	‘Turn-On’
$\mathcal{P}_{conv}^{\gamma}$	$93.4 \pm 0.6\%$	Photon Survival
$\mathcal{S}_{e \rightarrow \gamma}^{cem}$	$100.3 \pm 0.6 \pm 1.0\%$	γ vs. e Shower Development
ϵ_{cem}^{γ}	$81.2 \pm 1.3 \pm 1.9\%$	Overall Photon Efficiency

Table 5.6: Summary of individual CEM photon selection efficiencies (\pm stat. \pm syst.). The overall efficiency includes a—over the Standard Model E_T distribution—weighted average of the *ISO4* isolation cut (Table 5.5). † Not actually used.

Taking all these individual efficiencies into account, the overall photon detection efficiency is 81.2%. Note, that the *ISO4* contribution to this number is a weighted average over the Standard Model E_T distribution.

5.4.2 Electron Efficiencies

Since in this analysis the same W and Z selection cuts are used as those in the measurement of the ratio of the inclusive W/Z cross sections in the electron channel, all electron efficiencies can be taken from there [65], with one exception. In order to increase statistics we included additional events from a trigger stream that imposes somewhat looser selection criteria at Level 2 (Section 4.2.4, trigger L2B) while maintaining the standard tight Level 3 selection cuts. We thereby improve the total CEM trigger efficiency from 89.2% to 95.2%.

For completeness, the individual electron efficiencies from Ref. [65] are summa-

Term	Value (%)
A_e^W	20.10 \pm 0.02
$A_{M_T^e}^e$	98.29 \pm 0.03
$A_{W, cem}^\gamma$	76.45 \pm 0.55
$f_{W, cem}^\gamma$	47.69 \pm 0.20
$A_e^{W\gamma} \cdot \epsilon_e^{W\gamma}$	4.2 \pm 0.1
A_Z^e	28.57 \pm 0.09
$A_{M_Z^e}$	85.27 \pm 0.08
$1/f_{DY}$	98.5 \pm 0.5
f_{Zcc}^γ	9.00 \pm 0.16
f_{Zcp}^γ	12.30 \pm 0.18
f_{Zcf}^γ	3.18 \pm 0.01
A_{Zcc}^γ	76.40 \pm 0.09
A_{Zcp}^γ	75.66 \pm 0.09
A_{Zcf}^γ	78.29 \pm 0.37
$A^{Z\gamma} \cdot \epsilon^{Z\gamma}$	4.7 \pm 0.2

Table 5.7: Acceptances (A) and geometrical fractions (f) in the $W\gamma$ and $Z\gamma$ analyses.

ized in Appendix C. Taking all these efficiencies into account, the overall electron identification efficiency becomes 84.5%.

5.5 Acceptances

Geometric and kinematic acceptances were determined using the Baur Monte Carlo as $W\gamma$ ($Z\gamma$) event generator and the Fast Monte Carlo as CDF detector simulation. We obtained consistent results when the QFL detector simulation was used as a cross check.

The overall acceptance for $W\gamma$ in the electron channel can be expressed as:

$$A_e^{W\gamma} = A_e^W \cdot f_{W,cem}^\gamma \cdot A_{W,cem}^\gamma \cdot A_{M_T^W}^e. \quad (5.1)$$

$A_e^W = A_{E_T}^W \cdot A_{fid}^W \cdot A_{\cancel{E}_T}^W$ is the W acceptance with $A_{E_T}^W$ (A_{fid}^W) being the kinematic (geometrical) acceptance for central fiducial electrons with $E_T > 20$ GeV, and $A_{\cancel{E}_T}^W$ being the kinematic acceptance for the $\cancel{E}_T > 20$ GeV cut. The factor $f_{W,cem}^\gamma$ represents the fraction of central photons in $W\gamma$ events, where the photon above $E_T = 7$ GeV is $\Delta R_{\ell\gamma} = 0.7$ from the W decay lepton apart. $A_{cem}^\gamma = A_{E_T}^\gamma \cdot A_{fid}^\gamma \cdot A_{\Delta R_{e\gamma}}^\gamma = A_{fid}^\gamma$ is the photon acceptance with A_{fid}^γ being the geometrical acceptance for central photons in $W\gamma$ events ($|\eta_{det}| < 1.1$) above $E_T = 7$ GeV and $\Delta R_{\ell\gamma} = 0.7$ away from the W decay lepton. By definition, $A_{E_T}^\gamma = A_{\Delta R_{e\gamma}}^\gamma = 1$ since we measure only that part of the total $W\gamma$ production cross section that refers to photons which are above $E_T = 7$ GeV and separated from the W decay lepton by $\Delta R_{\ell\gamma} = 0.7$. $A_{M_T^W}^e$ is acceptance of the transverse mass cut $M_T^W > 40$ GeV/ c^2 for $W\gamma$ events passing *all* other cuts.

The calculation of the overall acceptance for $Z\gamma$ is more complicated. Since the second decay electron is allowed to go into three different detector regions (central, plug and forward), the acceptance and efficiency factors cannot be factorized, but must be written in a combined form¹ :

¹Double indices like cc, cp or cf represent the part of the detector in which the first and second of the Z decay electrons is found. c, p and f stand for central, plug and forward, respectively.

$$\begin{aligned}
A^{Z\gamma} \cdot \epsilon^{Z\gamma} &= \frac{1}{f_{DY}} \cdot \epsilon_{zvx} \cdot A_{M_Z}^e \cdot A_Z^e \cdot (T^e \cdot \epsilon_{cent,T}^e) \\
\times [& f_{Zcc}^e \cdot (2\epsilon_{cent,L}^e - (T^e \cdot \epsilon_{cent,T}^e)) \cdot (f_{Zcc}^\gamma \cdot A_{Zcc}^\gamma \cdot \epsilon_{cem}^\gamma) \\
& + (f_{Zcp}^e \cdot \epsilon_{plug}^e) \cdot (f_{Zcp}^\gamma \cdot A_{Zcp}^\gamma \cdot \epsilon_{cem}^\gamma) \\
& + (f_{Zcf}^e \cdot \epsilon_{fwd}^e) \cdot (f_{Zcf}^\gamma \cdot A_{Zcf}^\gamma \cdot \epsilon_{cem}^\gamma)] \quad (5.2)
\end{aligned}$$

The efficiencies ϵ^e , T^e and ϵ_{cem}^γ are mentioned in the previous section and in Appendix C. ϵ_{zvx} is the efficiency for the cut that requires the event z-vertex to be within 60 cm of the interaction point. $\frac{1}{f_{DY}}$ is a small correction factor (< 1) which explicitly takes into account the removal of the Drell-Yan $+\gamma$ contributions within the $Z \rightarrow e^+e^-$ mass window and corrects for event loss outside the mass window. $A_{M_Z}^e$ is the acceptance of the Z-mass window cut for $Z\gamma$ events passing *all* other cuts. The overall acceptance factors in Equation 5.2 are given by

$$A_{Zcx}^e = (A_{Zc,E_T}^{e1} \cdot A_{Zc,fid}^{e1}) \cdot (A_{Zx,E_T}^{e2} \cdot A_{Zx,fid}^{e2}), \quad (5.3)$$

where $x = c, p$ or f ; A_{Zc,E_T}^{e1} is the kinematic acceptance for electrons passing the ‘tight’ requirements for the central Z leg, A_{Zx,E_T}^{e2} is the kinematic acceptance for electrons passing the ‘loose’ requirements for the second Z leg (see Appendix C), and $A_{Zx,fid}$ is the geometrical fiducial acceptance associated with the central, plug or forward electromagnetic calorimeter. The factors f_{Zcx}^γ represent the fraction of central photons in $Z\gamma$ events where the second leg of the Z decay is found in either the central ($x=c$), plug ($x=p$) or forward ($x=f$) detector. The other decay electron must be central by default. Similarly, the geometrical acceptances A_{Zcx}^γ are defined with respect to three Z decay lepton combinations cc , cp and cf .

5.6 Systematic Uncertainties

There are several sources that carry systematic uncertainties in the $W\gamma$ and $Z\gamma$ analyses. Main contributions come from

- the number of background events,
- the Monte Carlo simulations through
 - the choice of the structure functions,
 - the P_T boost algorithm of the diboson system,
 - the choice of the four-momentum of the intermediate W or Z boson, Q^2 ,
 - differences between the QFL and Fast Monte Carlo predictions.

5.6.1 Background

We will discuss the determination of the systematic error on the background estimate in Section 6.3 in detail. In summary, the overall systematic uncertainty on the $W\gamma$ ($Z\gamma$) background is found to be 1.5 (0.2) events in the electron channel and 1.6 (0.2) events in the combined electron + muon channel.

5.6.2 Monte Carlo Simulations

To obtain the Standard Model prediction for $W\gamma$ and $Z\gamma$ processes, the Baur Monte Carlo in combination with the Fast Monte Carlo detector simulation was used. We tested various parameters that could systematically affect the results.

All Monte Carlo related uncertainties are summarized in Table 5.8. The largest variation in the event prediction comes from the choice of the structure function MRS D-'. Taking the sum in quadrature of all the contributions to the $W\gamma$ ($Z\gamma$)

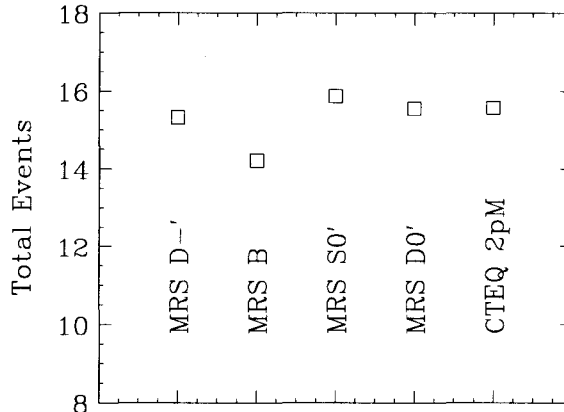


Figure 5.3: $W\gamma$ Baur plus Fast Monte Carlo prediction for various structure functions.

analyses yields a total uncertainty due to Monte Carlo effects of 2.3 (0.5) events in the electron channel and 3.0 (0.6) in the combined electron + muon channel.

Structure Functions

We chose four alternative sets of structure functions, HMRS-B [66], MRSS0' [67], MRSD0' [52], CTEQ 2pM [68], and compared the resulting $W\gamma$ ($Z\gamma$) cross sections to those obtained using the default MRSD--' structure function. The largest difference is interpreted as a systematic uncertainty due to the choice of MRSD--' (Figure 5.3).

The Transverse Momentum of the Diboson System

Traditionally, the P_T boost of the $W\gamma$ ($Z\gamma$) system is performed in the Fast Monte Carlo routine after the event was created by the Baur event generator ². Because there is no experimental data for the P_T spectrum of the $W\gamma$ ($Z\gamma$) system, each event is instead assigned a transverse momentum according to the W (Z) P_T dis-

²Most recently this procedure has been changed. The P_T boost of the $W\gamma$ ($Z\gamma$) system is now accomplished at the generator level [59]. The change in the kinematic distributions and the event yield prediction (a $\approx 2\%$ increase) is negligible for the central photon analyses.

	W γ sample		Z γ sample	
	e	e + μ	e	e + μ
Structure Function	1.8	2.2	0.5	0.6
P_T Boost	0.9	1.1	0.1	0.1
Four-Momentum	0.7	0.7	0.1	0.1
Monte Carlo Difference (Fast MC, QFL)	0.8	1.4	0.1	0.1
Total Uncertainty	2.3	3.0	0.5	0.6

Table 5.8: Systematic uncertainties in the absolute number of W γ and Z γ events obtained from Baur plus Fast Monte Carlo simulations in the electron and combined electron + muon channels.

tribution, which is well measured by CDF [60]. Differences in the shape of the W (Z) and W γ (Z γ) P_T spectra are assumed to be negligible since the majority of photons in this analysis are found at relatively low energies, and the higher order QCD corrections to the photon P_T distributions are very small [56]. To investigate the sensitivity of the Monte Carlo W γ (Z γ) production cross sections on changes in the P_T spectrum we increased/decreased the W γ (Z γ) transverse momentum by one standard deviation in the fit of the W (Z) P_T distribution. The systematic uncertainty is given by the difference in the event prediction.

The Four-Momentum of the Intermediate Weak Boson

Small contributions to the systematic error come from studying the choice of the four-momentum transfer, Q^2 . The default value is set to $Q^2 = M_V^2$, where $V = W$ or Z . Two alternative values, $Q^2 = 4 \cdot M_V^2$ and $Q^2 = M_V^2/4$ were investigated. The difference in the event yield gives an estimate for the corresponding systematic uncertainty.

QFL Monte Carlo Prediction

The Standard Model $W\gamma$ ($Z\gamma$) production cross section should not depend on the detector simulation used. The difference in the results obtained with the default Fast Monte Carlo and the QFL detector simulations provides a another contribution to the systematic error.

Chapter 6

Background

Processes that lead to a misidentification of a W or Z boson or photon enter the $W\gamma$ ($Z\gamma$) data sample as background events. These are

- QCD background events from jet fragmentation into neutral mesons, which subsequently decay into two photons,
- W or Z decays into τ 's, the τ subsequently decaying into an electron,
- ‘one-legged Z’ events, misidentified as W events when one decay lepton escapes detection.

QCD jet fragmentation is the dominant background source.

6.1 QCD Jet Fragmentation Background

Jets in the W sample predominantly originate from gluon bremsstrahlung. Some of these jets fragment into a leading neutral meson, such as π^0 , η . Their decay products, two photons, can be misidentified as a single particle when one of the

photons remains undetected or when their shower profiles overlap so that the clustering algorithm is not able to resolve them. An estimate for this kind of QCD background in the $W\gamma$ ($Z\gamma$) sample can be obtained by determining the probability that a jet in a W (Z) event is mistakenly identified as a single photon.

Because such a misidentification happens only for about one jet in a thousand, a large statistics QCD sample is necessary. The 16 GeV photon trigger sample ('P16 sample') was found to be a suitable candidate. At Level 2, the trigger requires an isolated central cluster of at least 16 GeV with a ratio of hadronic energy to electromagnetic energy of less than 12.5%. At Level 3, the event had to be within the fiducial CES region $|x_{wire}| < 17.5$ cm and 14 cm $< |z_{strip}| < 217$ cm, and isolated so that the transverse energy in a cone of $\Delta R_{\ell\gamma} = 0.7$ around the cluster is less than 4 GeV.

To measure the QCD jet fragmentation background in the $W\gamma$ ($Z\gamma$) sample, we counted all jets above $E_T = 7$ GeV in both the W (Z) and P16 sample, and the number of electromagnetic objects in the P16 sample that pass *all* photon analysis cuts. To avoid energy sharing, these fake photons and the jets are required to be separated in ΔR by 1.4 units from the 16 GeV trigger cluster. The trigger cluster itself is not counted as a jet or electromagnetic object to avoid a bias in the background estimate by selecting, i.e. triggering on specific events. Taking the ratio between the number of fake photon clusters $n_{\gamma'}$ and the number of jets in the P16 sample, n_{jet} , and multiplying it by the number of jets found in the inclusive W (Z) sample, N_{jet} , which are 0.7 in $\Delta R_{\ell\gamma}$ away from the decay electron(s), *directly* yields the number of QCD background events N_{qcd} in the $W\gamma$ ($Z\gamma$) sample:

$$N_{qcd,i} = \mathcal{P}_i(jet \rightarrow '\gamma') \cdot N_{jet,i} = \frac{n_{\gamma',i}}{n_{jet,i}} \cdot N_{jet,i} , \quad (6.1)$$

E_T Bin (GeV)	Fake Photon Candidates	Jets
7–11	90	70795
11–15	45	37416
15–19	27	27104
19+	54	66744
7+	216	202059

Table 6.1: Number of jets and electromagnetic clusters that pass the photon requirement per analysis E_T bin in the P16 data sample.

where $V = W$ or Z , $\mathcal{P}_i(jet \rightarrow '\gamma')$ is the jet fragmentation probability and the index i stands for the i^{th} E_T bin. Systematic uncertainties due to differences in the shape of the jet or photon E_T distributions between the P16 and inclusive W (Z) sample, are somewhat reduced because all factors in Eq. 6.1 are determined for each analysis bin of 4 GeV transverse energy separately.

In some cases a fake photon might have a slightly lower energy than the corresponding jet so that both objects wind up in adjacent E_T bins. However, these smearing effects were found to be negligible compared to the overall systematic error.

The described algorithm is based on the assumption that *all* electromagnetic objects that pass the analysis requirements are indeed coming from neutral meson decays. This is not correct for the P16 trigger sample, which contains an admixture of *direct photon* + jet events, originating from Compton processes $qg \rightarrow \gamma q$, and from QCD dijet events, where one of the jets fragments into a neutral meson. To a minor degree, the P16 data set contains also diphoton events from quark and gluon annihilation and bremsstrahlungs processes like $qg \rightarrow \gamma\gamma q$.

Most of the direct photons pass the analysis cuts and have to be subtracted off of the number of fake photons in the denominator of Eq. 6.1. To estimate the fraction

E_T Bin (GeV)	Direct Photons	Fake Photons
7-11	$33.8 \pm 14.9 \pm 13.5$	$56.2 \pm 15.6 \pm 13.5$
11-15	$30.2 \pm 9.1 \pm 5.7$	$14.8 \pm 8.8 \pm 5.8$
15-19	$18.2 \pm 6.8 \pm 3.4$	$8.8 \pm 6.1 \pm 3.4$
19+	$44.8 \pm 12.8 \pm 15.9$	$9.2 \pm 11.3 \pm 15.9$
7+	$127.0 \pm 22.7 \pm 38.7$	$89.0 \pm 21.8 \pm 38.7$

Table 6.2: Fraction of direct and fake photons among the fake photon candidates found in the P16 data sample per analysis E_T bin (\pm stat. \pm syst.). The number of direct photons is determined using the shower profile method.

of these isolated direct photons, we use a ‘shower profile method’ that compares the CES transverse shower profiles of real photons with that of fake photons from jet fragmentation into a neutral meson.

Quantitatively, a fit of the shower profile was performed with reference to a ‘standard’ electron testbeam profile, corrected for differences between electrons and photons. The goodness of the fit is given by the average χ_{ces}^2 in both CES strip and wire views, $\chi_{ces}^2 = 0.5 \cdot (\chi_{strip}^2 + \chi_{wire}^2)$. QFL Monte Carlo studies using ‘templates’ of typical electron testbeam shower profiles have shown that χ_{ces}^2 for isolated direct

E_T Bin (GeV)	$\mathcal{P}_i(jet \rightarrow '\gamma')$
7-11	$0.00079 \pm 0.00021 \pm 0.00019$
11-15	$0.00040 \pm 0.00024 \pm 0.00015$
15-19	$0.00032 \pm 0.00022 \pm 0.00013$
19+	$0.00014 \pm 0.00017 \pm 0.00024$
7+	$0.00062 \pm 0.00011 \pm 0.00020$

Table 6.3: Jet fragmentation probability into neutral mesons, all faking photons, as a function of E_T determined from the P16 data sample (\pm stat. \pm syst.).

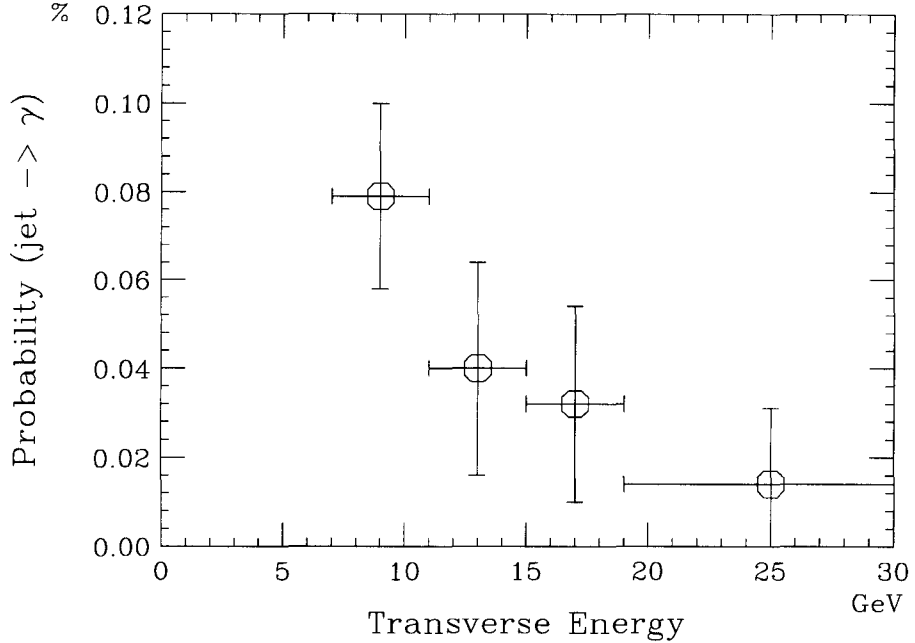


Figure 6.1: Jet fragmentation probability in neutral mesons that fake a photon as a function of E_T determined from the P16 QCD data sample. The bin sizes are chosen according to the $W\gamma$ ($Z\gamma$) analysis.

photons is usually smaller than for jets ¹, as jets generally produce wider showers than electromagnetic particles. Based on that difference, a χ^2_{ces} dependent weight factor for being a direct photon or jet can be assigned to every event. These weight factors were determined by extensive QFL detector studies employing real showers of testbeam electrons, corrected for photon - electron differences. The sum over all weights gives an estimate of the number of direct photon and the number jet events in a given data sample. Because the weight factors can be relatively large, the accuracy of this profile method depends on *high statistic* samples.

The results in Table 6.1 – 6.5 are quoted per analysis E_T bin. Table 6.1 lists the number of fake photon candidates and the number of jets found in the complete

¹The notation ‘jet’ in this discussion of the shower profile method is referred to a jet that fragments into neutral mesons decaying into multiple photons. These objects have to pass the same selection requirements as the direct photons.

Number of Jets				
E_T Bin (GeV)	W + jet		Z + jet	
	e	e + μ	e	e + μ
7–11	4592	6449	372	458
11–15	1753	2438	134	165
15–19	682	970	58	86
19+	1728	2140	127	162
7+	8755	11997	646	871

Table 6.4: Number of jets in the inclusive W and Z sample in the electron and combined electron + muon channels.

P16 data set. The fraction of direct photons determined with the shower profile method and the resulting number of fake photons is summarized in Table 6.2. The probability for jet fragmentation into a photon faking neutral mesons is shown in Table 6.3 and Figure 6.1. We find an energy dependent probability $\mathcal{P}_i(jet \rightarrow '\gamma')$ in the order of $\lesssim 10^{-3}$.

Finally, using the $\mathcal{P}_i(jet \rightarrow '\gamma')$ distribution and the number of jets in the W + jet (Z + jet) sample (Table 6.4) we obtain from Eq. 6.1 a total QCD jet fragmentation background estimate of 4.6 ± 1.9 (0.4 ± 0.2) events in the electron

E_T Bin (GeV)	Jet Fragmentation Background	
	$W\gamma$	$Z\gamma$
7–11	$3.6 \pm 1.0 \pm 0.9$	$0.3 \pm 0.1 \pm 0.1$
11–15	$0.7 \pm 0.4 \pm 0.3$	$0.05 \pm 0.03 \pm 0.02$
15–19	$0.2 \pm 0.2 \pm 0.1$	$0.02 \pm 0.01 \pm 0.01$
19+	$0.2 \pm 0.3 \pm 0.4$	$0.02 \pm 0.01 \pm 0.02$

Table 6.5: Jet fragmentation background in the $W\gamma$ and $Z\gamma$ samples as a function of photon E_T (\pm stat. \pm syst.).

$W\gamma$ ($Z\gamma$) sample. The various contributions per E_T bin are listed in Table 6.5. In the combined electron and muon $W\gamma$ ($Z\gamma$) sample we obtain similarly 6.5 ± 2.0 (0.5 ± 0.2) QCD background events.

6.1.1 Discussion

The correctness of the jet fragmentation (QCD) background determination depends on two assumptions:

- a reasonable similarity of the jet fragmentation properties in the both samples P16 and V+jet ($V = W$ or Z),
- a correct estimate of the direct photon contribution.

The Jet Fragmentation Difference

The P16 sample contains predominantly low E_T jets (< 30 GeV) originating from gluon fragmentation. A PYTHIA/HERWIG Monte Carlo [69] / [63] study predicts a ratio of gluon to quark jets of $\approx 3:1$ [70]. On the other hand, jets in the V + jet sample ($V = W$ or Z) are also mostly gluon jets. VECBOS predicts a gluon to quark jet ratio of approximately 3:2 [71]. Unfortunately, there are no experimental results that could confirm these Monte Carlo predictions. However, it was found by the OPAL Collaboration [72] [73] that quark and gluon jet fragmentation properties are not dramatically different at transverse energies of less than 30 GeV. The mean particle multiplicities in gluon relative to quark jets of about 25 GeV was measured to differ by only $5 \pm 1\%$ to $27 \pm 7\%$ using two different methods [72]. In the same analysis, the difference in the total particle momentum in or out the jet plane between these two types of jets was found to be $10 \pm 2\%$.

The Direct Photon Contribution

The determination of the weight factors used in the shower profile method is based on slightly different photon selection requirements than those applied in this analysis [74].

- The fiducial region within which photons in the $W\gamma$ ($Z\gamma$) analysis are accepted is somewhat larger than the one in the shower profile analysis.
- Unlike in the $W\gamma$ ($Z\gamma$) analysis, no L_{shr} or HAD/EM requirement, nor an explicit χ_{wire}^2 cut is present in the shower profile analysis ². Instead, the *average* $\chi_{ces}^2 = 0.5 \cdot (\chi_{strip}^2 + \chi_{wire}^2)$ is required to be less than 20.

To investigate what effect these differences have on the estimate of the fraction of direct photons we remeasured the fragmentation function, replacing the $W\gamma$ ($Z\gamma$) by the shower profile analysis cuts. We found very similar results for both photon definitions (Figure 6.2). The numbers obtained using shower profile cuts are efficiency \times acceptance corrected by $\approx 10\%$. This correction is mainly due to the larger fiducial region in which a photon may be found in the $W\gamma$ ($Z\gamma$) analysis. Within the uncertainties we find no discrepancies.

Consider the ratio of the number of electromagnetic clusters that pass the photon analysis cuts (fake photons) to the number of jets in the P16 sample. Take the same ratio in the $V\gamma$ data sample ($V = W$ or Z) with the Standard Model prediction subtracted. Both ratios will agree if and only if the direct photon correction was correctly applied to the ratio for the P16 data. This is verified in Figure 6.3; only when the fraction of direct photons is subtracted from the number of fake

²The data sample used in the shower profile study has, at trigger Level 2, an extremely loose cut of $HAD/EM < 0.125$ applied, which for our discussion is equivalent to no HAD/EM requirement.

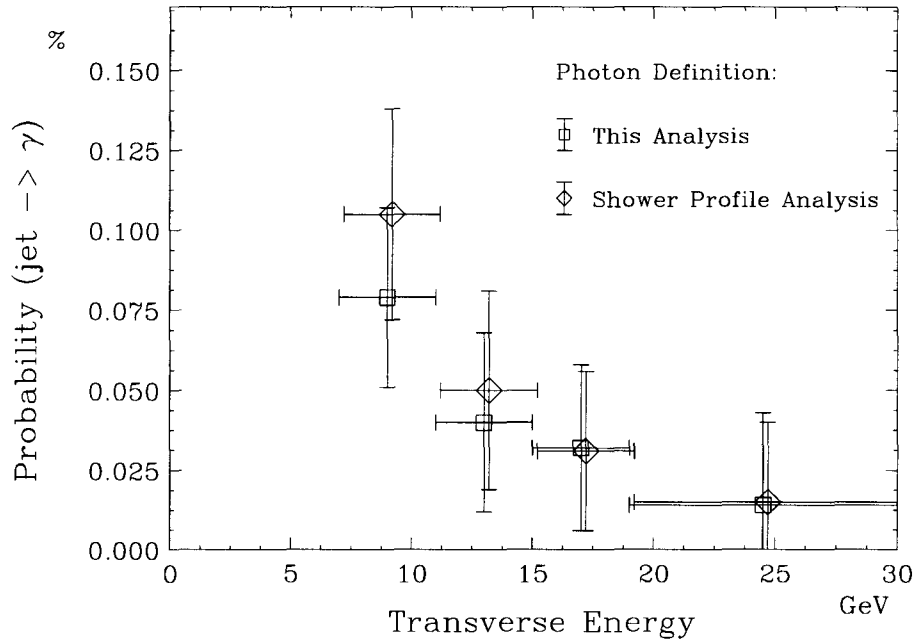


Figure 6.2: Comparison of the jet fragmentation probability for two different sets of photon selection requirements.

photons found in the P16 sample, the ratios are consistent within the error bars (Figure 6.3b). This result also supports the assumption that the fragmentation probability is similar in both data samples, as discussed above.

The photon cuts in the $W\gamma$ and $Z\gamma$ analyses are chosen in order to optimize the signal to background ratio while retaining a high efficiency. Looser photon cuts will add a large amount of QCD background events to the $W\gamma$ ($Z\gamma$) sample but will increase the number of signal events only slightly. The additional background can be predicted correctly with the help of the P16 data set.

In the following, we compare the background subtracted $W\gamma$ signal in the electron channel for three different sets of photon selection criteria ³ :

³Due to the small number of $Z\gamma$ events, statistically significant conclusions can only be drawn in the $W\gamma$ case.

E_T Bin	Set A	Set B	Set C	χ_{stat}^2 Set B	χ_{stat}^2 Set C
7–11	4.4 ± 1.0	0.7 ± 2.9	3.0 ± 2.6	1.45	0.25
11–15	7.3 ± 0.4	6.6 ± 1.6	6.4 ± 1.1	0.18	0.59
15–19	2.8 ± 0.2	2.7 ± 1.0	3.5 ± 1.0	0.01	0.47
19+	-0.2 ± 0.3	1.1 ± 1.1	0.3 ± 1.1	0.93	0.07

Table 6.6: Comparison of the background-subtracted $W\gamma$ signal in the electron channel per analysis bin (in GeV) using three different photon selection sets: Default analysis cuts (Set A), ‘loose isolation cuts’ (Set B) and ‘only isolation cuts’ (Set C), as defined in the text. The errors are purely statistical with the common error ignored. χ_{stat}^2 determines the goodness of the agreement between the results for Set A and those for Set B or C, respectively.

Set A Default photon analysis cuts.

Set B Same as Set A , but *looser isolation cuts*: $ISO4 < 0.5$, $L_{shr} < 1.5$ and no $\Sigma PT4$ requirement.

Set C *Only isolation cuts*, i.e. the HAD/EM , $N3D$ and no 2^{nd} CES cluster requirements removed from Set A .

Table 6.6 summarizes the resulting, background subtracted $W\gamma$ signal for the three cases. Since we are dealing with small statistics samples, we express the degree of agreement by the statistical χ_{stat}^2 , defined as

$$\chi_{stat}^2 = \frac{(N_A - N_X)^2}{\sigma_A^2 - \sigma_X^2} \quad (6.2)$$

with $X = B$ or C , and N_A and N_X are the number of photons that pass the Set A and Set X requirements, respectively. The sigmas are the statistical uncertainties on those numbers, common errors excluded. Due to larger relative uncertainties in the background estimate in case of Set B and C, the results fluctuate more than

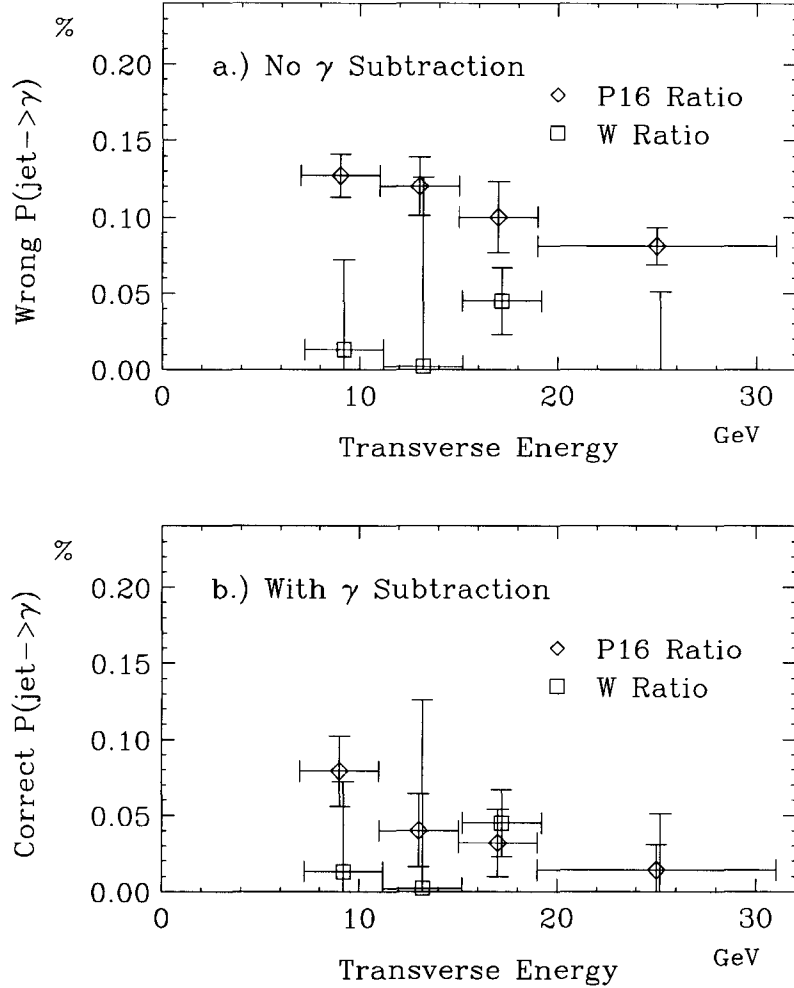


Figure 6.3: Comparison of jet fragmentation probabilities in the combined electron + muon $W\gamma$ sample and in the P16 sample with a) no direct photon subtraction, b) subtraction of direct photons using the shower profile method.

those for the default Set A. We find that the $W\gamma$ signal is independent of the photon cuts within the errors quoted ($\chi_{stat}^2 \lesssim 1$).

To obtain a theoretical estimate of the jet fragmentation background, samples of zero, one and two jets were created by the VECBOS event generator. Jet fragmentation was accomplished by the HERWIG Monte Carlo. QFL was used as the detector simulation. Table 6.7 shows the good agreement between the P16 background measurement and the VECBOS Monte Carlo prediction in the $W\gamma$

Sample	VECBOS	P16 (\pm stat. \pm syst.)
W (electron)	3.5 ± 1.3	$4.6 \pm 1.1 \pm 1.5$
W (electron + muon)	5.2 ± 1.6	$6.5 \pm 1.2 \pm 1.6$
Z (electron)	0.3 ± 0.1	$0.4 \pm 0.1 \pm 0.2$
Z (electron + muon)	0.4 ± 0.1	$0.5 \pm 0.1 \pm 0.2$

Table 6.7: Comparison of the measured jet fragmentation backgrounds with the VECBOS Monte Carlo prediction.

and $Z\gamma$ data samples.

In Chapter 9 we will discuss another method to measure the number of direct photons in the P16 sample. A study of the difference in the electromagnetic fraction of a photon or jet cluster will provide very similar results to those obtained with the shower profile method.

6.2 Others Background Sources

Two additional processes can contribute to $W\gamma$ background:

- $Z\gamma$ and $Z + \text{jet}$ events, where the Z boson is misidentified as a W boson. This can happen, when one of the Z-decay electrons is missed (one-legged Z), e.g. in a non-instrumented region of the detector or because of undetected electrons, mostly due to tracking inefficiencies at higher rapidities ($|\eta_{det}| > 1.1$).
- $W \rightarrow \tau \bar{\nu}_\tau + \gamma(+jet)$ events, where the τ decays into an electron neutrino pair.

The suppression of such background events is discussed in Section 5.2. Remaining contributions were determined in a full Fast Monte Carlo detector simulation using the Baur Monte Carlo as event generator. The results are listed in Table 6.8.

Sample	Tauonic Decays	One-Legged $Z\gamma$
W (electron)	0.3 ± 0.01	0.4 ± 0.1
W (electron + muon)	0.5 ± 0.02	1.5 ± 0.2
Z (electron)	0.0003 ± 0.0001	—
Z (electron + muon)	0.0014 ± 0.0002	—

Table 6.8: Non-QCD backgrounds in the $W\gamma$ and $Z\gamma$ data samples in the individual electron and combined electron + muon channels obtained from Baur plus Fast Monte Carlo studies.

Due to the small branching ratio, $B(\tau \rightarrow e\bar{\nu}_e\nu_\tau) \sim 17.8\%$ [75], and the three-body decay of the τ , leading to soft final state products, $W\gamma$ events in the τ channel are relatively rare. For the same reason, $(Z \rightarrow \tau^+\tau^-) + \gamma$ is highly suppressed and can be neglected as a background source.

Note, that $Z + \text{jet}$ and $W \rightarrow \tau\bar{\nu}_\tau + \text{jet}$ events are implicitly included in the QCD background estimate described above.

6.3 Error Determination

The statistical uncertainty on the QCD jet fragmentation background estimate in Table 6.7 is the square root of the sum of the weight factors of the profile method, added in quadrature. Since the number of extra jets in the P16 sample is large, the uncertainty of the jet fragmentation probability into neutral mesons is given solely by the statistical error on the number of fake photon events.

Systematic error on the total number of QCD background events is due to uncertainties in

- the estimate of the direct photon contamination in the P16 sample using the shower profile method,

	W γ sample		Z γ sample	
	e	e + μ	e	e + μ
QCD Background Contributions				
Direct Photon Estimate	1.0	1.1	0.1	0.1
Difference Monte Carlo – Data	1.1	1.1	0.1	0.1
Binning	0.4	0.6	0.1	0.1
Other Background Contributions				
One-legged Z + γ	0.02	0.05	—	—
W $\gamma \rightarrow \tau\nu_\tau + \gamma, \tau \rightarrow e\bar{\nu}_e\nu_\tau$	0.01	0.01	< 0.01	< 0.01
Total Systematic Background Uncertainty	1.5	1.6	0.2	0.2

Table 6.9: Systematic uncertainties in the background estimate in the W γ (Z γ) electron and combined electron + muon channels.

- the choice of a particular binning in E_T
- differences between the measurement and the VECBOS/HERWIG/QFL Monte Carlo prediction.

In the previous section, we mentioned that each electromagnetic cluster in the P16 sample that passes the photon selection cuts, is assigned a probability for being a direct photon or background event. Each factor can vary within a certain systematic uncertainty which was determined in earlier, detailed Monte Carlo and testbeam studies [76].

In the measurement of the jet fragmentation background, we had chosen the same E_T bin width of 4 GeV as in the W γ and Z γ analyses. To test the effect of different binning schemes, we repeated the background analysis using bin sizes between 1 and 5 GeV, and additionally one single bin with $E_T > 7$ GeV. The difference between the default background estimate and the lowest value is interpreted as a systematic uncertainty.

Sample	Total Background
W (electron)	$5.3 \pm 1.0 \pm 1.5$
W (electron + muon)	$8.5 \pm 1.5 \pm 1.6$
Z (electron)	$0.4 \pm 0.1 \pm 0.2$
Z (electron + muon)	$0.5 \pm 0.1 \pm 0.2$

Table 6.10: Total background in the $W\gamma$ and $Z\gamma$ data samples in the individual electron and combined electron + muon channels (\pm stat. \pm syst.).

Samples of $W+0$ jets, $W+1$ jet and $W+2$ jets were created with the VECBOS Monte Carlo [62]. The jet fragmentation was done by HERWIG [63], and QFL was used for the detector simulation. The resulting data sample was searched for central jet clusters that pass the photon analysis requirements. A Monte Carlo jets fragmentation probability was obtained by taking the ratio of the number of such clusters to the total number of jets generated, per analysis bin. To be conservative, we interpret the difference between the Monte Carlo result and the measurement as another systematic error.

The systematic uncertainties of the non-QCD background contributions, one-legged $Z\gamma$ and $W\gamma \rightarrow \tau\nu_\tau + \gamma$, $\tau \rightarrow e\bar{\nu}_e\nu_\tau$, were determined by studying structure function, Q^2 and P_T boosting effects in the Fast Monte Carlo, as described in the following section.

Table 6.9 summarizes all systematic background contributions. By adding them in quadrature, we arrive at an overall systematic uncertainty of the $W\gamma$ ($Z\gamma$) background of 1.5 (0.2) events in the electron channel and 1.6 (0.2) events in the combined electron + muon channel.

Sample	N_{obs}	Experimental Signal	SM Prediction
$W\gamma$ (electron)	18	$12.7 \pm 4.4 \pm 1.5$	$15.4 \pm 0.7 \pm 2.2$
$W\gamma$ (electron + muon)	25	$16.5 \pm 5.1 \pm 1.6$	$23.3 \pm 1.1 \pm 3.8$
$Z\gamma$ (electron)	4	$3.6 \pm 2.0 \pm 0.2$	$4.3 \pm 0.2 \pm 0.5$
$Z\gamma$ (electron + muon)	8	$7.5 \pm 2.8 \pm 0.2$	$7.1 \pm 0.4 \pm 0.7$

Table 6.11: Comparison of $W\gamma$ and $Z\gamma$ signal in the individual electron and combined electron plus muon channels to the Standard Model (SM) prediction obtained from Baur plus Fast Monte Carlo calculations (\pm stat. \pm syst.). N_{obs} is the number of observed events.

6.4 Signal to Background Summary

Table 6.10 summarizes the total number of background events in the $W\gamma$ and $Z\gamma$ analyses for the electron and combined electron and muon channels. The total background is the sum of jet fragmentation background determined from the P16 QCD data sample and additional background from Monte Carlo studies of tauonic $W(Z)$ decays and one-legged Z events (for W sample only).

The resulting experimental signal is compared in Table 6.11 to the Standard Model Monte Carlo prediction calculated using the Baur event generator plus Fast Monte Carlo detector simulation. We find good agreement within the uncertainties.

Chapter 7

Analysis Results

In the following chapter, we will discuss various physics results derived from the electron $W\gamma$ and $Z\gamma$ data samples described in the previous chapters, and also from corresponding data samples of the combined electron + muon channel. The muon $W\gamma$ and $Z\gamma$ analyses were performed parallel to this work by Mark Vondracek. He found 7 $W\gamma$ and 4 $Z\gamma$ events; further details can be found in Ref. [78]. The various muon efficiencies and acceptances, as well as the background events in the muon channel are taken into account. The photon identification is identical for both channels. Mark's results are included here to present the complete Run 1a data set available at CDF.

7.1 Measurement of $\sigma \cdot B (Z\gamma \rightarrow e^+e^-\gamma)$ and

$$\sigma \cdot B (W\gamma \rightarrow e\nu_e\gamma)$$

In Chapter 2 we discussed that the presence of anomalous couplings would result in a higher rate of $W\gamma$ and $Z\gamma$ events than predicted by the Standard Model,

particularly at high photon E_T . Therefore, it is of interest to compare the measured $W\gamma$ ($Z\gamma$) production cross section to the Standard Model calculation.

The total production cross section \times decay branching ratio for $W\gamma$ ($Z\gamma$) processes can be calculated from the observed number of $W\gamma$ ($Z\gamma$) signal events, $N_{sig}^{V\gamma}$, the run time integrated luminosity, $\mathcal{L} = \int L_e dt$, and the overall $W\gamma$ ($Z\gamma$) acceptance, $A_e^{V\gamma}$, and efficiency, $\epsilon_e^{V\gamma}$:

$$(\sigma * B(V\gamma))_{e\text{-channel}} = \frac{N_{e,obs}^{V\gamma} - N_{e,bkg}^{V\gamma}}{A_e^{V\gamma} \cdot \epsilon_e^{V\gamma} \cdot \mathcal{L}}, \quad (7.1)$$

where V stands for either the W or Z boson, and the signal $N_{sig}^{V\gamma}$ is written as the difference between the observed number of events and the number of background events, $N_{sig}^{V\gamma} = N_{e,obs}^{V\gamma} - N_{e,bkg}^{V\gamma}$.

In $\mathcal{L} = 19.6 \text{ pb}^{-1}$ electron data collected by CDF during the 92/93 Tevatron collider run, we found $N_{e,obs}^{W\gamma} = 18$ $W\gamma$ events and $N_{e,obs}^{Z\gamma} = 4$ $Z\gamma$ events (Chapter 5). The total background was measured to $\Sigma N_{e,bkg}^{W\gamma} = 5.3 \pm 1.8$ events for $W\gamma$ and $\Sigma N_{e,bkg}^{Z\gamma} = 0.4 \pm 0.2$ events for $Z\gamma$ (Chapter 6). The factor ‘acceptance \times efficiency’ is $A_e^{W\gamma} \cdot \epsilon_e^{W\gamma} = 4.2 \pm 0.1\%$ for $W\gamma$ and $A_e^{Z\gamma} \cdot \epsilon_e^{Z\gamma} = 4.7 \pm 0.3\%$ for $Z\gamma$ (Section 5.4). The measured cross section \times branching ratio for $W\gamma$ and $Z\gamma$ in the electron, and combined electron + muon channels is:

$$\sigma * B(W\gamma \rightarrow e\nu_e\gamma) = 15.3 \pm 5.3(stat.) \pm 1.8(syst.) \pm 0.8(lum) \text{ pb},$$

$$\sigma * B(Z\gamma \rightarrow e^+e^-\gamma) = 4.0 \pm 2.3(stat.) \pm 0.2(syst.) \pm 0.2(lum) \text{ pb}.$$

$$\sigma * B(W\gamma \rightarrow l\nu_l\gamma) = 13.2 \pm 4.2(stat.) \pm 0.7(syst.) \pm 1.3(lum) \text{ pb},$$

$$\sigma * B(Z\gamma \rightarrow \ell^+\ell^-\gamma) = 5.1 \pm 1.9(stat.) \pm 0.1(syst.) \pm 0.3(lum) \text{ pb},$$

where $\ell = e + \mu$.

The Standard Model (Baur Monte Carlo) predicts

$$\sigma * B(W\gamma \rightarrow \ell\nu\ell\gamma) = 18.6 \pm 0.1 (stat.) \pm 2.9 (syst.) \text{ pb},$$

$$\sigma * B(Z\gamma \rightarrow \ell^+\ell^-\gamma) = 5.20 \pm 0.02 (stat.) \pm 0.60 (syst.) \text{ pb}.$$

All these cross sections are defined for photons above $E_T = 7$ GeV and $\Delta R_{\ell\gamma} > 0.7$ separated from the decay lepton(s).

The ratio between the inclusive W and Z production cross section times branching ratios is 10.7 ± 0.7 , whereas—due to gauge cancellations—the ratio between the $W\gamma$ and $Z\gamma$ production cross section is predicted to be 4.0 ± 0.1 . The measured ratio $3.8^{+3.1}_{-1.9}$ ($2.6^{+1.8}_{-1.1}$) in the electron (electron + muon) channel agrees with the Standard Model prediction for $W\gamma$ versus $Z\gamma$ production, but disagrees dramatically with the ratio of the inclusive W to Z cross sections. We thus can confirm the occurrence of gauge cancellations in $W\gamma$ and $Z\gamma$ production.

At this point, we could derive limits on anomalous couplings from the cross section measurements. However, since a fit of the photon E_T distribution is far more sensitive, we are going to pursue that approach (Section 7.3).

7.2 Kinematic Distributions

In this paragraph, we present the various physics distributions, and compare the results with the Standard Model plus background predictions.

Figure 7.1 a and Figure 7.2 show the distribution of the photon transverse mo-

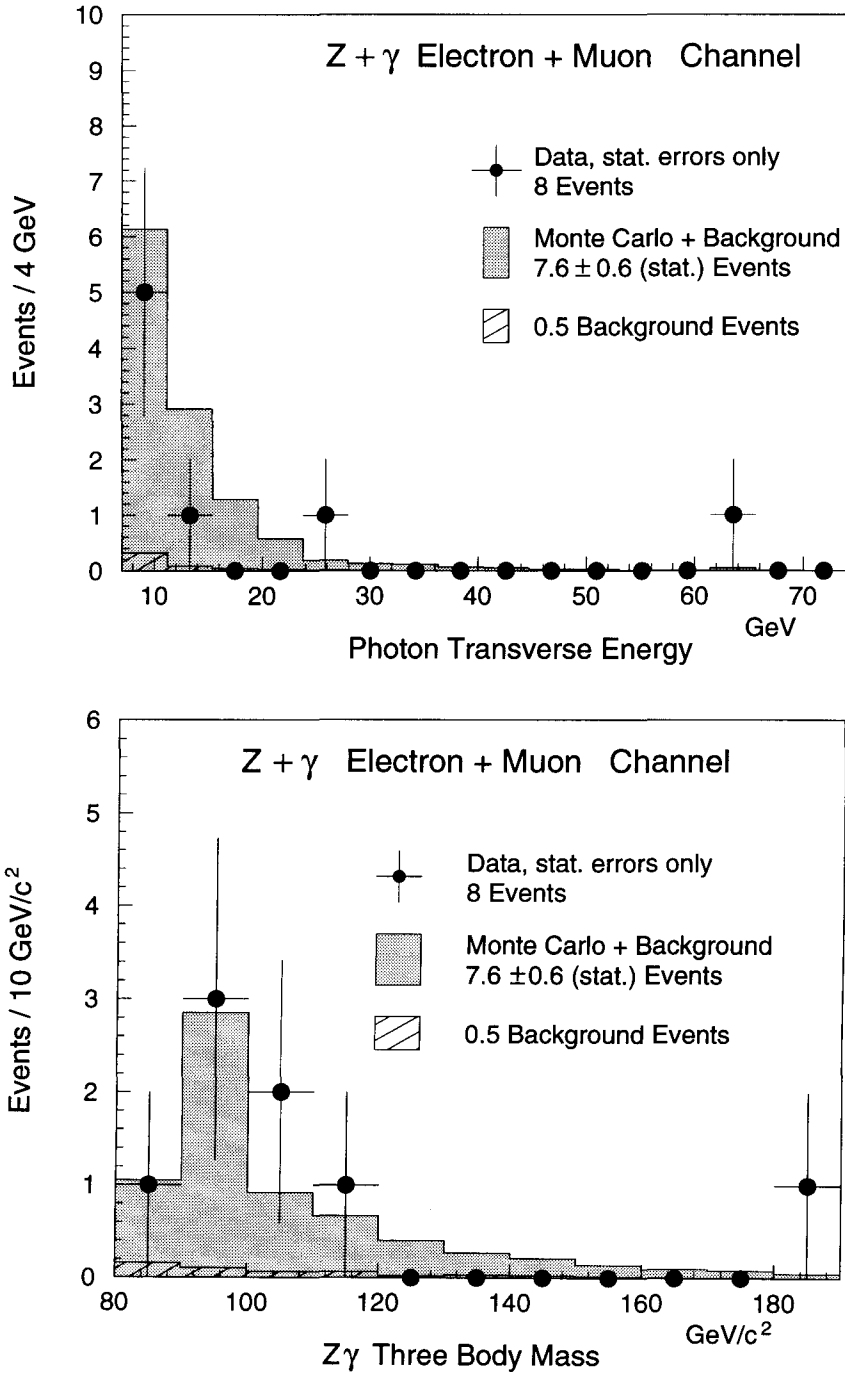


Figure 7.1: Comparison of observed to predicted a) transverse photon energy b) $e\bar{e}\gamma$ three-body mass spectrum for $Z + \text{central photon}$ events in $\approx 20 \text{ pb}^{-1}$ electron + muon data.

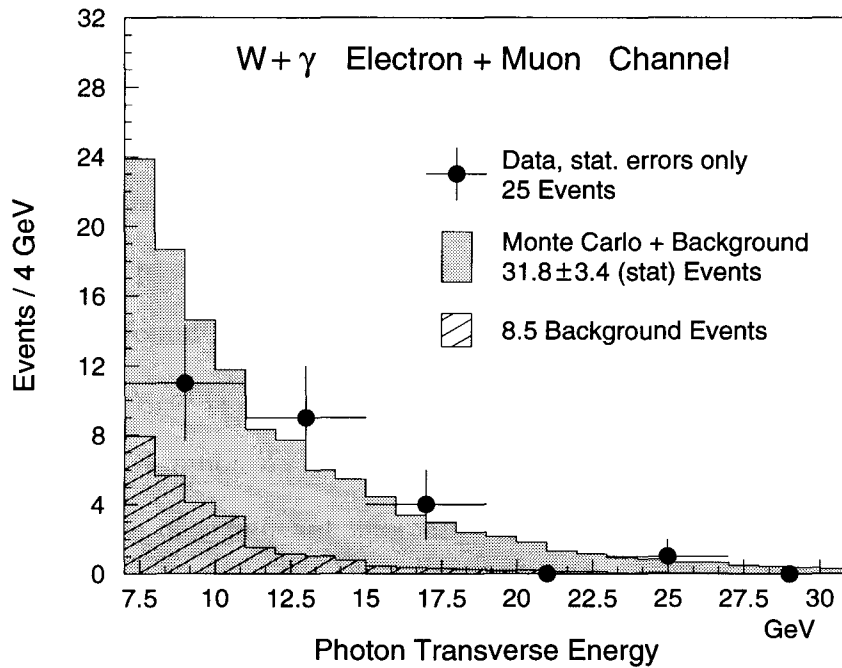
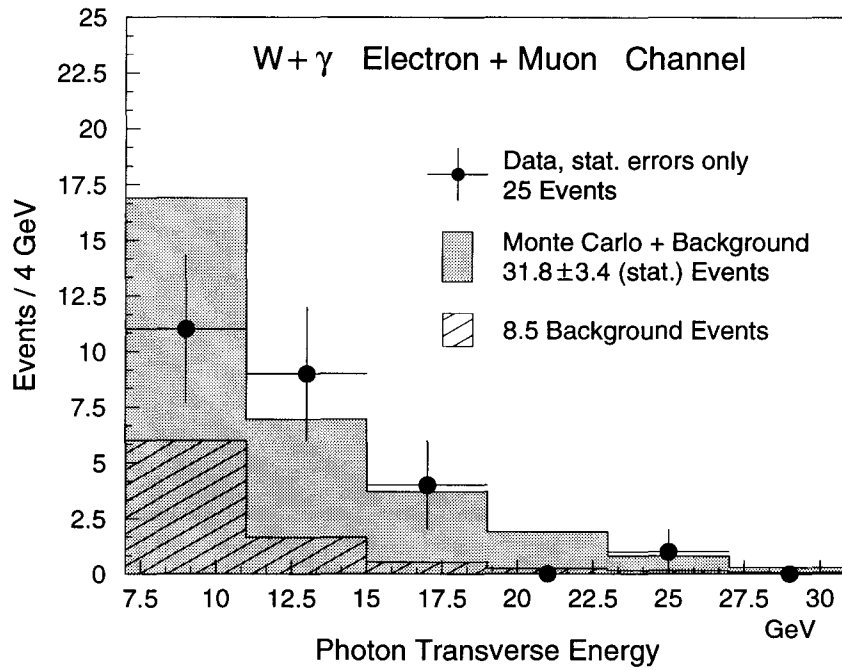


Figure 7.2: Comparison of observed to predicted photon transverse energy spectrum for $W + \gamma$ central photon events in $\approx 20 \text{ pb}^{-1}$ electron + muon data. For illustration, the Standard Model prediction plus background estimate and the background distribution are plotted in the bin sizes of a) 4 GeV (default) and b) 1 GeV.

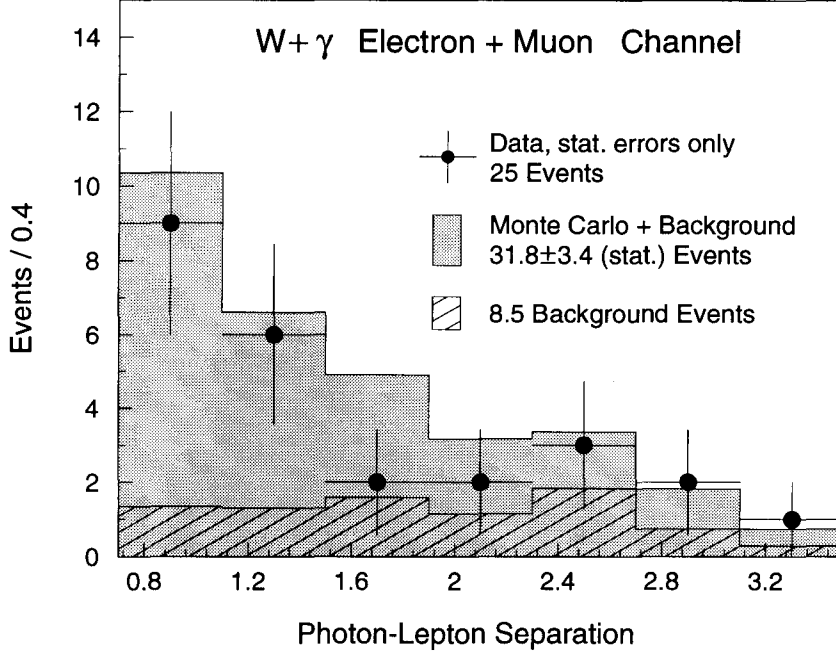


Figure 7.3: Comparison of the observed to predicted spectrum of the photon-lepton separation, $\Delta R_{\ell\gamma}$, for $W + \text{central photon}$ events in $\approx 20 \text{ pb}^{-1}$ electron + muon data.

momentum in $Z\gamma$ and $W\gamma$ events, respectively. As expected, the event rate decreases sharply with energy. We find no evidence for a significant excess of $W\gamma$ or $Z\gamma$ events at high photon E_T . Noteworthy is a $Z\gamma$ event with a $E_T = 64 \text{ GeV}$ photon, that was found in the muon channel analysis [78]. It has a three-body mass $M_{ee\gamma} = 188 \text{ GeV}/c^2$ (Figure 7.1 b). We expect 0.3 events with $M_{ee\gamma} > 150 \text{ GeV}/c^2$ in the electron + muon $Z\gamma$ data set, according to a Standard Model calculation.

The absence of significant anomalies in $W\gamma$ processes is also reflected in the photon-lepton separation distribution (Figure 7.3). We observe no unusual number of events in the region of large separations, where the sensitivity to anomalous couplings is high ($\Delta R_{\ell\gamma} \gtrsim 1.5$).

In $W\gamma$ production, the invariant $W\gamma$ mass proves to be very useful to separate radiative from production events. Since only the imbalance in the *transverse* energy

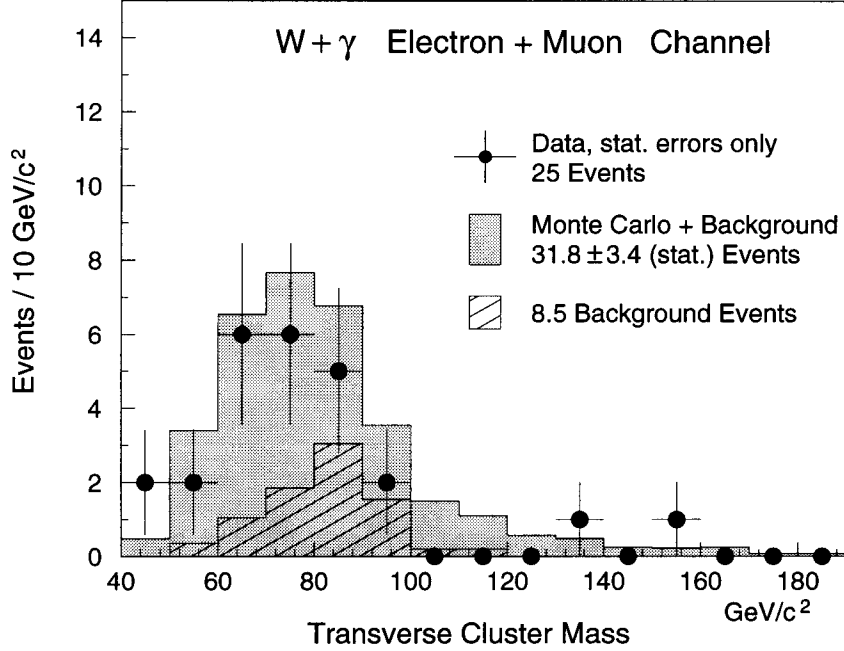


Figure 7.4: Comparison of observed to predicted transverse cluster mass spectrum for $W + \text{central photon}$ events in $\approx 20 \text{ pb}^{-1}$ electron + muon data.

can be detected, the longitudinal momentum of the neutrino is not measurable and a *transverse* cluster mass (minimum invariant mass) of the $W\gamma$ system is used instead of the total invariant $W\gamma$ mass:

$$M_{TC}^{W\gamma} = \sqrt{\left[\left(M_{\ell\gamma}^2 + |\vec{P}_T^\gamma + \vec{P}_T^\ell|^2 \right)^{\frac{1}{2}} + |\vec{P}_T^{\nu\ell}| \right]^2 - |\vec{P}_T^\gamma + \vec{P}_T^\ell + \vec{P}_T^{\nu\ell}|^2}, \quad (7.2)$$

where $M_{\ell\gamma}^2$ is the invariant mass of the electron-photon pair and \vec{P}_T^γ (\vec{P}_T^ℓ , $\vec{P}_T^{\nu\ell}$) is the transverse momentum vector of the photon (lepton, antineutrino).

The region $M_{TC}^{W\gamma} > 90 \text{ GeV}/c^2$ is populated mostly by production events. In the data, 19 out of 25 events fall below this threshold, indicating substantial contributions from radiative events (Figure 7.4). The predicted ratio of the number above 90 GeV/c^2 to the total number, including background is $(0.85 \pm 0.70)/(34.30 \pm 2.70) = 0.25 \pm 0.03$, in good agreement with the measured value 0.24 ± 0.10 .

In summary, all kinematic distributions compare very well with the Standard Model predictions. We observe no significant deviations that would indicate the presence of new physics beyond the Standard Model.

7.3 Anomalous W-Photon and Z-Photon Couplings

As shown in Figure 2.3, the shape of the photon E_T spectrum for $W\gamma$ (and similarly for $Z\gamma$ production) is very sensitive to anomalous couplings. For non-Standard Model coupling parameters, a large excess of photons at high E_T is expected. The following section describes the procedure of how limits on anomalous couplings were calculated [77].

First, the likelihood that the number of simulated events would fluctuate to the number of observed events per E_T bin of the size 4 GeV had to be calculated. To find the maximum likelihood as a function of anomalous couplings, combinations of *all* four couplings ought to be scanned. But, in order to be able to display the results, we set two of the four coupling parameters equal to the Standard Model values; the remaining pair was varied in the simulation, performed with the Baur event generator and the Fast Monte Carlo as the CDF detector simulation.

For such a study, it is necessary to investigate a large number of different sets of couplings (about 500×500 pairs). Fortunately, since the cross section, and hence the number of $W\gamma$ and $Z\gamma$ events, are quadratic in the anomalous couplings ¹, the number of events predicted by the Standard Model can be expressed analytically

¹More precisely, the invariant amplitudes derived from the $W\gamma$ and $Z\gamma$ diagrams are linear in the anomalous couplings. The cross section is proportional to the square of those amplitudes.

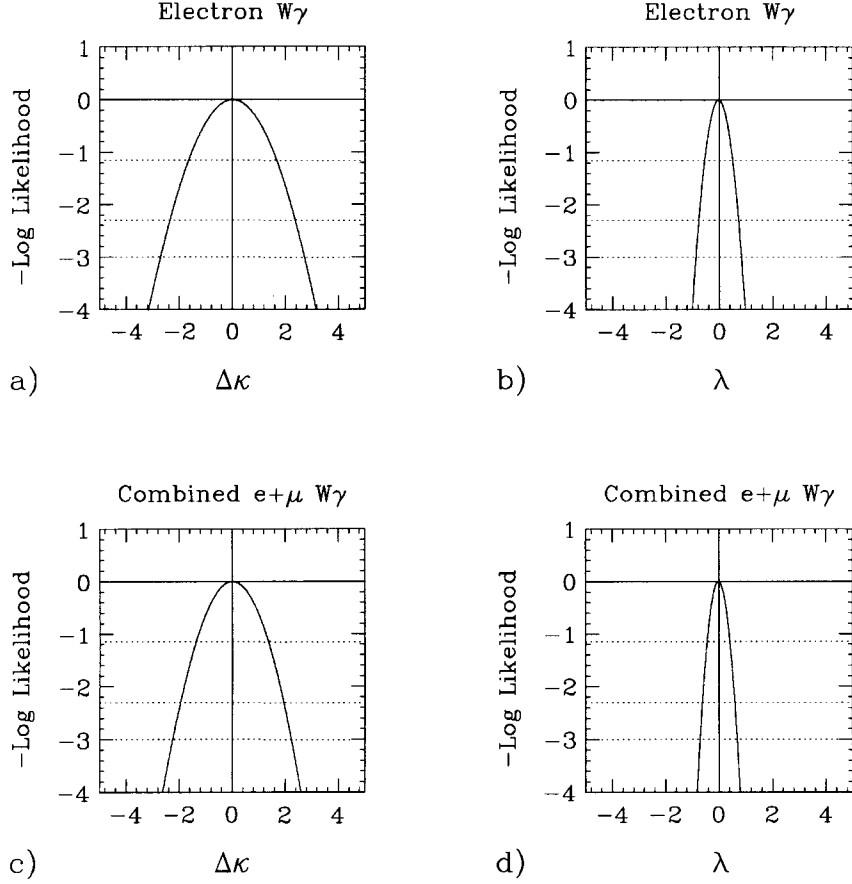


Figure 7.5: Negative log-likelihood distributions for the \mathcal{CP} -conserving couplings $\Delta\kappa$ and λ in the individual electron channel (a and b) and combined electron + muon channel (c and d).

by an elliptical paraboloid with six coefficients

$$N_i^{pred}(\Delta\kappa, \lambda) = N_i^{SM} + A_i \cdot \Delta\kappa + B_i \cdot \lambda + C_i \cdot \Delta\kappa^2 + D_i \cdot \lambda^2 + E_i \cdot \Delta\kappa \cdot \lambda \quad (7.3)$$

where the index i stands for the i^{th} bin. For given couplings the six coefficients were determined for each bin by fitting Baur Monte Carlo $W\gamma$ ($Z\gamma$) samples.

Since there is only a small number of observed events, fluctuations are governed by Poisson statistics. The Poisson probability for bin i , that the predicted number

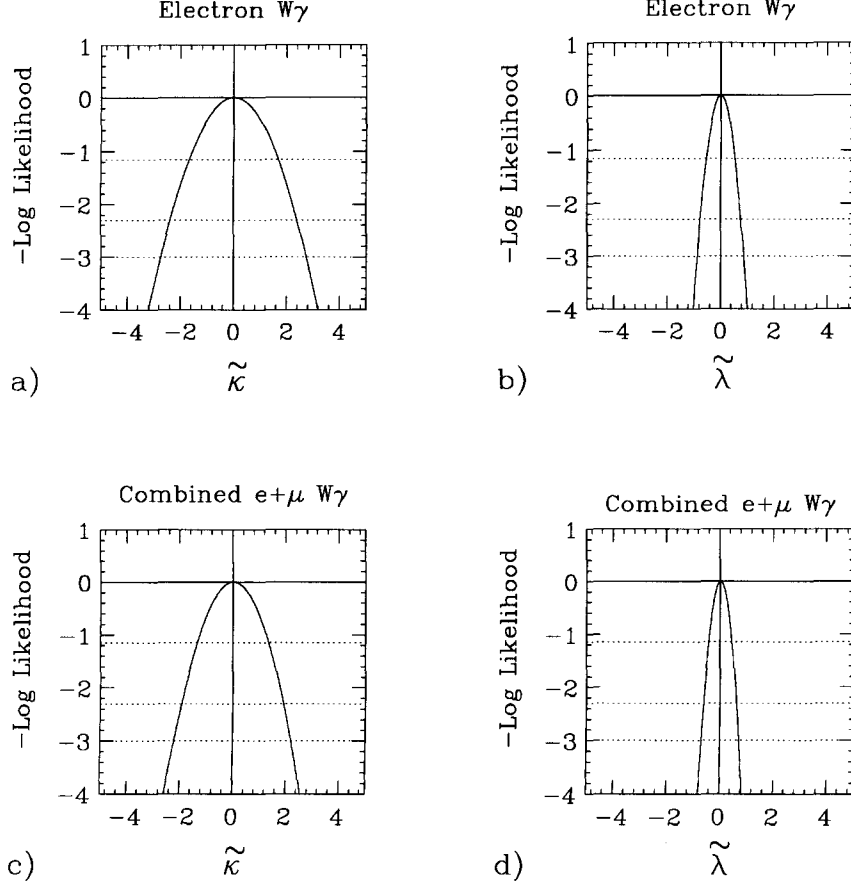


Figure 7.6: Negative log-likelihood distributions for the \mathcal{CP} -violating couplings $\tilde{\kappa}$ and $\tilde{\lambda}$ in the individual electron channel (a and b) and combined electron + muon channel (c and d).

of events for a set of anomalous couplings, N_i^{pred} , including the measured number of background events, N_i^{bkg} , fluctuates to the number of observed events, N_i^{obs} , is

$$\mathcal{P}_i = \frac{e^{-\mu_i} \cdot \mu_i^{N_i^{obs}}}{N_i^{obs}!}, \quad (7.4)$$

where $\mu_i = \mu_i(\Delta\kappa, \lambda) = N_i^{bkg} + N_i^{pred}$.

The total probability is the product over all bins, $\mathcal{P} = \prod_i^{n_{bins}} \mathcal{P}_i$. To account for systematic uncertainties, a gaussian probability density $G(x)$ has to be folded

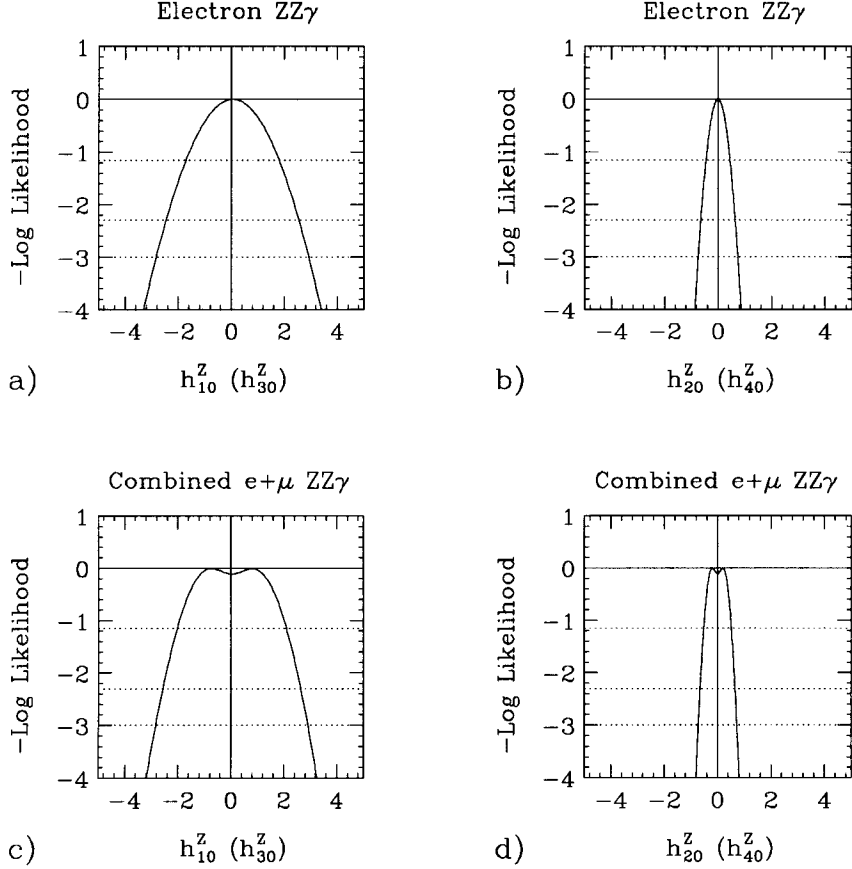


Figure 7.7: Negative log-likelihood distributions for the \mathcal{CP} -violating (\mathcal{CP} -conserving) couplings h_{10}^Z (h_{30}^Z) and h_{20}^Z (h_{40}^Z) in the individual electron channel (a and b) and combined electron + muon channel (c and d).

in. We define the negative log-likelihood variable

$$\mathcal{L}(\Delta\kappa, \lambda) = -\ln \int_{-\infty}^{+\infty} \prod_i^{n\text{bins}} \frac{e^{-\mu_i + \text{sys}_i(x)} \cdot (\mu_i + \text{sys}_i(x))^{N_i^{\text{obs}}}}{N_i^{\text{obs}}!} \cdot G(x) dx, \quad (7.5)$$

The systematic uncertainty $\text{sys}_i(x)$ per bin i is the square-root of the systematic uncertainties on the background estimate, the integrated luminosity, the Q^2 scales and the P_T boosting of the $W\gamma$ ($Z\gamma$) system (see Section 5.6), added in quadrature. The integration was performed by simulating 60 different CDF experiments, in each

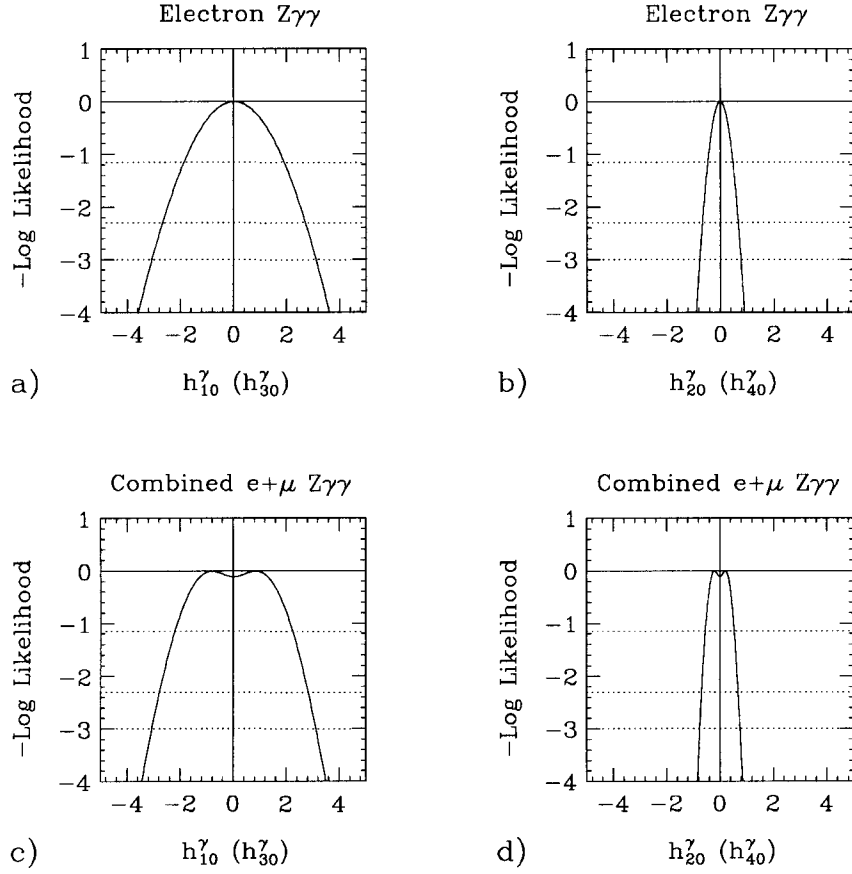


Figure 7.8: Negative log-likelihood distributions for the \mathcal{CP} -violating (\mathcal{CP} -conserving) couplings h_{10}^γ (h_{30}^γ) and h_{20}^γ (h_{40}^γ) in the individual electron channel (a and b) and combined electron + muon channel (c and d).

of which the nominal number of events $\mu_i(\Delta\kappa, \lambda) + sys_i(x)$ is changed by a fraction.

Figure 7.5 – 7.8 show the negative log-likelihood functions \mathcal{L} for the various anomalous coupling parameters in $W\gamma$ and $Z\gamma$ production in the individual electron channel and in the combined electron + muon channel.

Note that the \mathcal{CP} -violating couplings h_{10}^V (h_{20}^V) are indistinguishable from their \mathcal{CP} -conserving counterparts h_{30}^V (h_{40}^V), $V = Z$ or γ .

In all but one of the cases, the maximum, i.e. the most likely value, is identical to the Standard Model prediction. Only the—somewhat improbable—occurrence

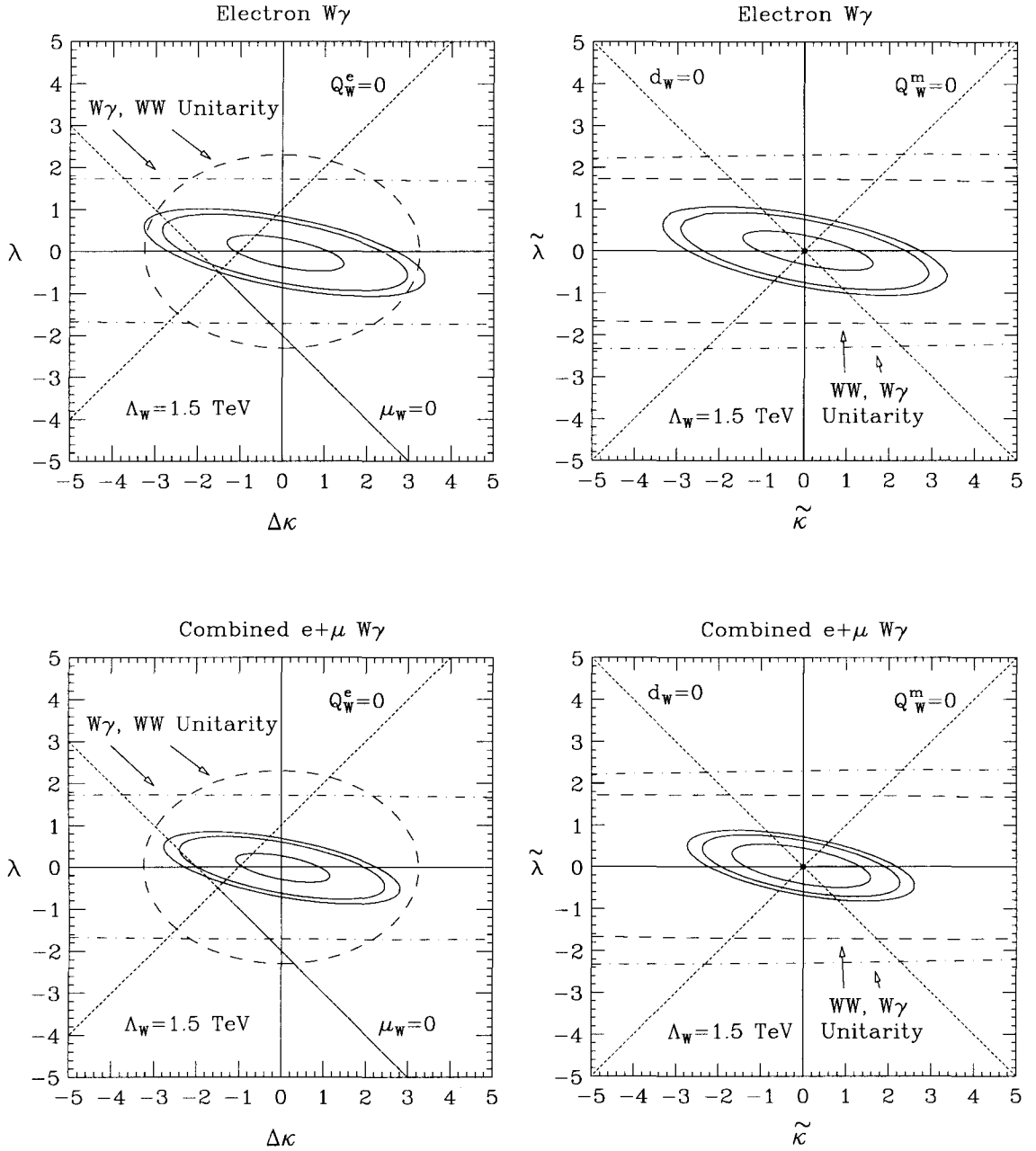


Figure 7.9: Limit contours at 68%, 90% and 95% CL (inner, middle and outer ellipse) for the W-photon coupling pairs $(\Delta\kappa, \lambda)$ and $(\tilde{\kappa}, \tilde{\lambda})$ in the individual electron channel and combined electron + muon channel. Displayed are also the theoretical WW and $W\gamma$ unitarity bounds, and the axes on which either the dipole or the quadrupole moment of the W boson vanishes.

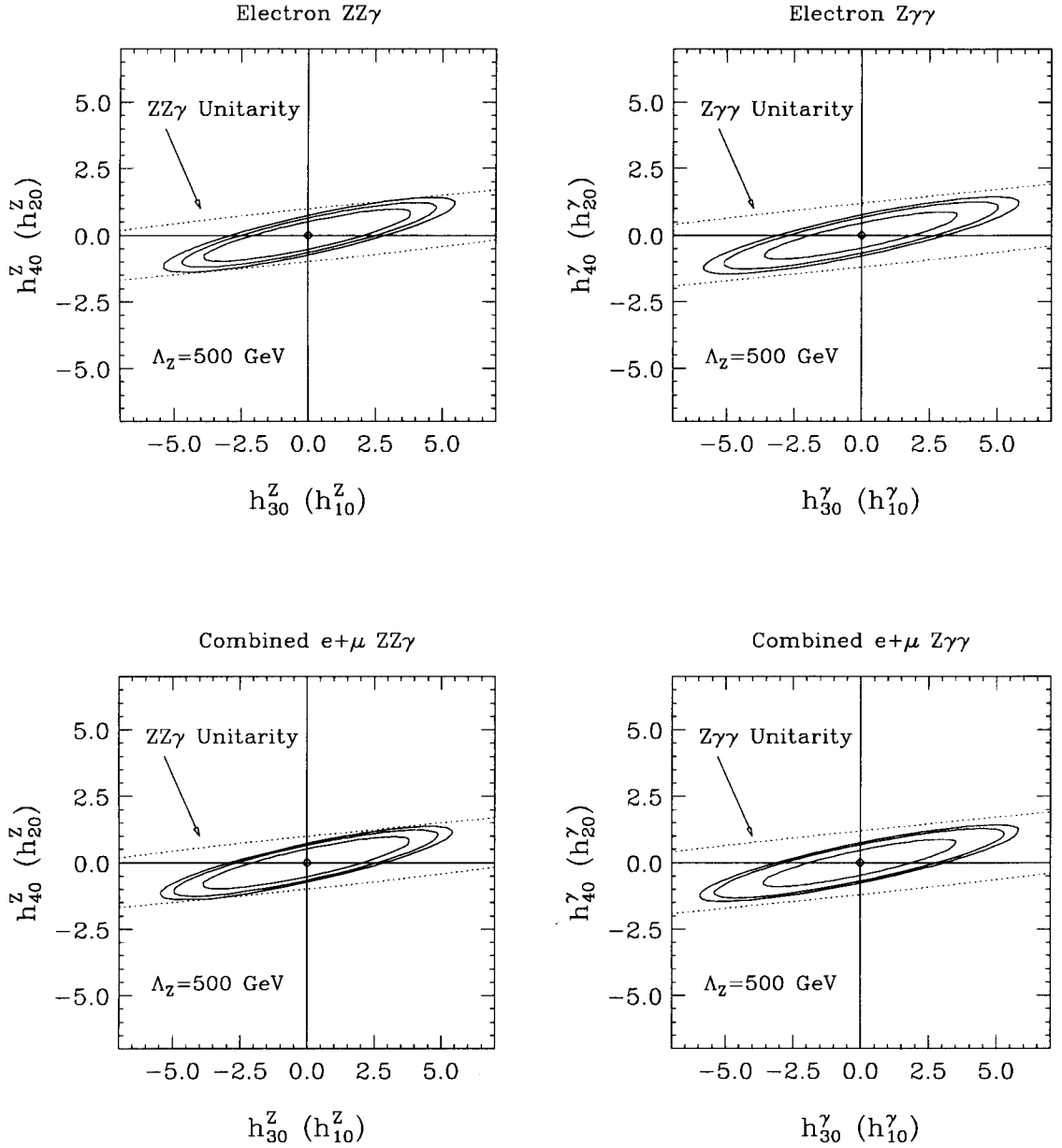


Figure 7.10: Limit contours at 68%, 90% and 95% CL (inner, middle and outer ellipse) for the Z-photon coupling pairs (h_{10}^Z, h_{30}^Z) and (h_{20}^Z, h_{40}^Z) in the individual electron channel and combined electron + muon channel. Displayed are also the theoretical $ZZ\gamma$ unitarity bounds.

of the high E_T photon in the $Z\gamma$ muon channel causes a shift of the maximum away from the Standard Model value (Figure 7.7 c and d, and Figure 7.8 c and d). Limits at 68%, 90% or 95% confidence level (CL) were taken from the negative log-likelihood curves, one, two or three standard deviation away from the maximum. This is at the point where \mathcal{L} equals 0.5, 2.3 and 3, respectively.

When we vary two couplings at the same time, those limits form an ellipse, according to Equation 7.3. The \mathcal{CP} -violating and \mathcal{CP} -conserving couplings are traditionally grouped in pairs. Accordingly, we show for the individual electron and combined electron + muon channel the two-dimensional limit contours on $W\gamma$ and $Z\gamma$ couplings in Figures 7.9 and 7.10, respectively. In either case, the measured bound are smaller than the corresponding unitarity limits at all confidence levels used (with the exception of a small section of the 95% bound in the individual electron channel). Interesting, but not surprising, is the observation that, according to our measurement, the W boson *must* have at least one non-zero electromagnetic moment at a confidence level of at least 95%; the point ($Q_W^e = 0, \mu_W = 0$) lies outside the 95% CL contour in Figure 7.9 (see Chapter 7.4).

It is common to quote one-dimensional limits. They are defined as the intersection points of the ellipses with the coordinate axis where the three other couplings are equal to their Standard Model value of zero. The Tables A.1 – A.5 summarize the measurements of all individual limits on the anomalous $W\gamma$ and $Z\gamma$ couplings at various confidence levels. At 95% CL we find:

W-Photon coupling limits ($\Lambda_W = 1.5$ TeV) :

$$\begin{aligned} -2.3 < \Delta\kappa(\tilde{\kappa}) < 2.2 & \quad \text{for} \quad \lambda(\tilde{\lambda}) = 0 \\ -0.7 < \lambda(\tilde{\lambda}) < 0.7 & \quad \text{for} \quad \Delta\kappa(\tilde{\kappa}) = 0 \end{aligned}$$

Z-Photon coupling limits ($\Lambda_Z = 0.5$ TeV) :

$$-3.0 < h_{30}^Z(h_{10}^Z) < 2.9 \quad \text{for } h_{20}^Z(h_{40}^Z) = 0$$

$$-0.7 < h_{40}^Z(h_{20}^Z) < 0.7 \quad \text{for } h_{10}^Z(h_{30}^Z) = 0$$

$$-3.1 < h_{30}^\gamma(h_{10}^\gamma) < 3.1 \quad \text{for } h_{20}^\gamma(h_{40}^\gamma) = 0$$

$$-0.8 < h_{40}^\gamma(h_{20}^\gamma) < 0.8 \quad \text{for } h_{20}^\gamma(h_{40}^\gamma) = 0$$

It should be noted that there is no a priori reason why all four couplings could not be different from their Standard Model values. However, such a scenario would require the display of four-dimensional ellipsoids.

All bounds on W-photon and Z-photon couplings correspond to a compositeness scale of $\Lambda_W = 1.5$ TeV and $\Lambda_Z = 0.5$ TeV, respectively. Larger scales would provide weaker limits than those given by unitarity constraints.

In other words, our measurement allows us to probe a possible internal structure of the W and Z boson only down to a distance scale of

$$L_W = \frac{1}{\Lambda_W} = 1.3 \cdot 10^{-4} \text{ fm} \quad \text{and} \quad L_Z = \frac{1}{\Lambda_Z} = 4.0 \cdot 10^{-4} \text{ fm}$$

The experimental limits are somewhat model-dependent: As mentioned in Section 2.3, Z-photon bounds depend on the form factor scale, and the bounds on both W-photon and Z-photon couplings depend on the choice of the form factor power n . Recall that mere ‘aesthetic’ reasons led us to the choice of $n = 2$ (though there is a minimum power, allowed for each coupling, in order to avoid undefined terms in the partial wave calculation, see Section 2.1).

7.4 Electromagnetic Moments of the W and Z Bosons

According to Equation 2.6 (2.14), the electromagnetic (transition) multipole moments of the W (Z) boson can be expressed in terms of anomalous couplings. There is an important difference between these two representations. The definition of the coupling parameters is arbitrary depending on the choice of the phenomenological parameterizations of the effective Lagrangian. On the other hand, electromagnetic moments have a true physical meaning. Their values are independent from the way the Lagrangian is parameterized. Therefore, we present limits on the electromagnetic moments of the weak bosons, which were extracted from the bounds on the weak boson-photon couplings. These moments are usually written in form of dimensionless ‘g factors’.

In case of the W-photon couplings we define by convention :

$$\begin{aligned}
 g_W - 2 &= \frac{\mu_W^e}{\mu_W^0} - 2 = \Delta\kappa + \lambda \\
 q_W^e - 1 &= \frac{Q_W^{e0}}{Q_W^{e0}} - 1 = \Delta\kappa - \lambda \\
 \delta_W &= \frac{d_W^e}{d_W^0} = \tilde{\kappa} + \tilde{\lambda} \\
 q_W^m &= \frac{Q_W^{m0}}{Q_W^{m0}} = \tilde{\kappa} - \tilde{\lambda},
 \end{aligned}$$

with the classical W moments $\mu_W^0 = d_W^{e0} = \frac{e}{2M_W}$ and $Q_W^{e0} = Q_W^{m0} = -\frac{e}{M_W^2}$. The corresponding limit contours are shown in Figure 7.11 for the combined electron + muon data sample. From these contour plots we read off one-dimensional limits at 95% CL for a form factor scale $\Lambda_W = 1.5$ TeV

$$\begin{aligned}
 -1.2 < g_W - 2 (\delta_W) < 1.1 & \quad \text{for } q_W^e - 1 (q_W^m) = 0 \\
 -1.6 < q_W^e - 1 (q_W^m) < 1.7 & \quad \text{for } g_W - 2 (\delta_W) = 0
 \end{aligned}$$

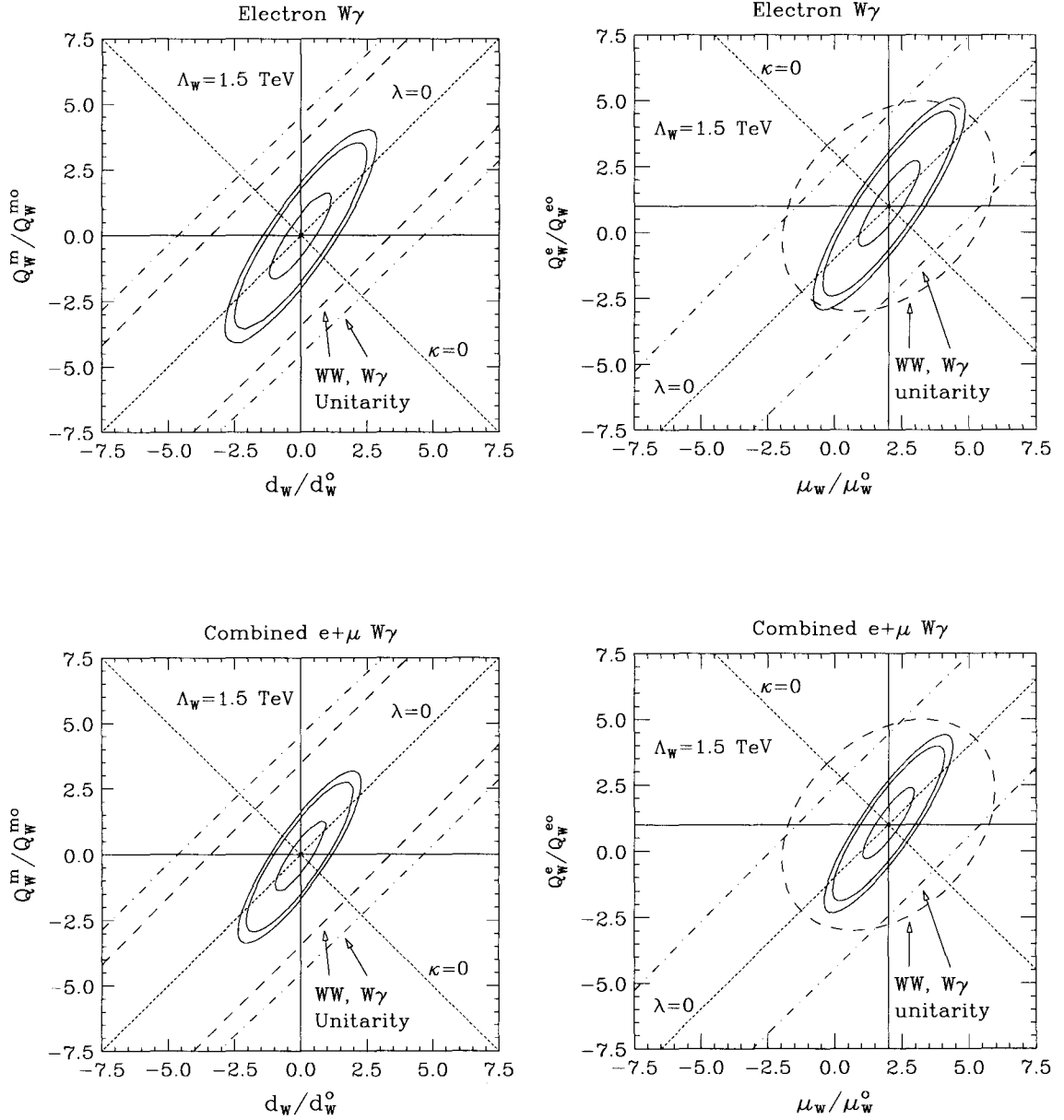


Figure 7.11: Limits on electromagnetic W moments at 68%, 90% and 95% CL (inner, middle and outer ellipse) in the electron and combined electron + muon channel. Displayed are also the theoretical WW and W γ unitarity bounds, and the axes on which either the coupling λ or κ would vanish.

where for each of the quoted limits the three other parameters were set to their Standard Model values. One dimensional bounds on the electromagnetic W moments at various confidence levels are summarized in Appendix A.

Since the relation $r_W^2 - 1 = \langle R_W^2 \rangle / \langle (R_W^0)^2 \rangle - 1 = \Delta\kappa + \lambda$ is equivalent to that for the parameter $g_W - 2$, the limits on $r_W^2 - 1$, corresponding to the mean-squared charged radius of the W boson (Equation 2.10), are identical to those on $g_W - 2$. The normalization factor $\langle (R_W^0)^2 \rangle$ is the square of the reduced Compton wavelength of the W boson, $\lambda_W^2 \equiv \langle (R_W^0)^2 \rangle = 1/M_W^2$.

Equivalently, we define for the transition moments of the Z boson:

$$\begin{aligned} \delta_{Z_T}^* &\equiv \delta_{Z_T} \left[\frac{M_Z^2}{k^2} \right] = \sqrt{2} (h_{30}^Z - h_{40}^Z) \\ q_{Z_T}^m &= \sqrt{10} (2h_{30}^Z) \\ g_{Z_T}^* &\equiv g_{Z_T} \left[\frac{M_Z^2}{k^2} \right] = \sqrt{2} (h_{10}^Z - h_{20}^Z) \\ q_{Z_T}^e &= \sqrt{10} (2h_{10}^Z) \end{aligned}$$

with the classical transition moments of the Z boson, $\mu_{Z_T}^0 = d_{Z_T}^0 = -\frac{e}{2M_Z}$ and $Q_{Z_T}^{e0} = Q_{Z_T}^{m0} = \frac{e}{M_W^2}$.

The \mathcal{CP} -conserving factors δ_{Z_T} and g_{Z_T} are a function of the photon momentum k , and are therefore rather ill-defined in terms of representing moments associated with transitions between initial and final states. In order to be able to set energy independent experimental limits, we redefined δ_{Z_T} and g_{Z_T} by multiplying with a factor $\frac{M_Z^2}{k^2}$.

The corresponding limit contours are shown in Figure 7.12 for the combined electron + muon data sample. By constraining three moments to their Standard Model values we extract one-dimensional limits on the remaining parameter at 95%

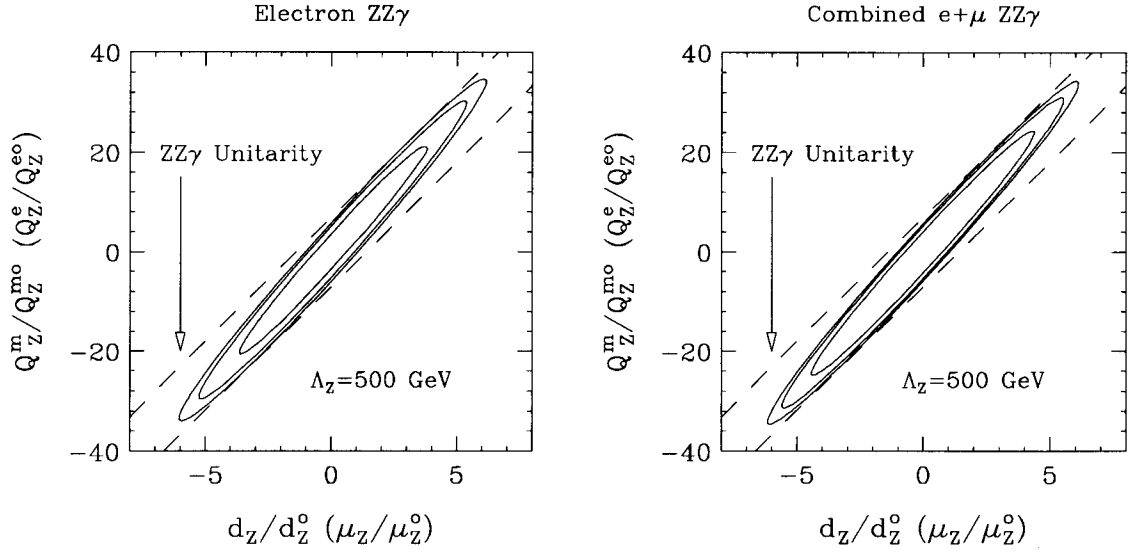


Figure 7.12: Limits on electromagnetic transition moments for $Z\gamma$ processes at 68%, 90% and 95% CL (inner, middle and outer ellipse) in the individual electron and combined electron + muon channel. Displayed are also the theoretical $ZZ\gamma$ unitarity bounds.

CL for a form factor scale $\Lambda_W = 500$ GeV :

$$\begin{aligned}
 -1.1 < \delta_{Z_T}^* (g_{Z_T}^*) < 1.1 & \quad \text{for } q_{Z_T}^m (q_{Z_T}^e) = 0 \\
 -6.0 < q_{Z_T}^m (q_{Z_T}^e) < 6.0 & \quad \text{for } \delta_{Z_T}^* (g_{Z_T}^*) = 0
 \end{aligned}$$

One dimensional bounds on the electromagnetic Z transition moments at various confidence levels are summarized in Appendix A.

Chapter 8

Results from the Ongoing Tevatron Run

In the previous chapters, we have discussed the analysis of $\approx 20pb^{-1}$ data from the Tevatron Run 1a. When we add recent data from the ongoing Run 1b, there is to date (Spring 1995) an almost four times larger data set available. It is of most interest to compare the Run 1a measurements with results obtained from these high statistics samples.

Efficiencies, acceptances and also some of the analysis cuts will change slightly for a final Run 1b analysis due to the increased luminosity during the present run. A complete analysis will be done after the completion of Run 1b, presumably in Spring 1996. Therefore, since we here use existing cuts and efficiencies from Run 1a, the following results can only be preliminary.

8.1 Preliminary Measurement of

$$\sigma \cdot B(W\gamma \rightarrow e\nu_e\gamma) \text{ and } \sigma \cdot B(Z\gamma \rightarrow e^+e^-\gamma)$$

The W and Z boson identification, as well as the photon selection are identical to those used in the Run 1a analysis (Chapter 5). Most recent studies have shown that the electron identification efficiencies for Run 1b differ only negligibly from the corresponding Run 1a efficiencies. Some of the photon efficiencies are somewhat lower in Run 1b due to the higher luminosity. Particularly the isolation efficiencies are affected by an increased underlying event activity. However, the differences are rather small; in Run 1b the combined efficiency for the *ISO4*, *N3D* and *$\Sigma PT4$* isolation requirements for a 10 GeV photon is about 2.5% lower than in Run 1a, and decreases to differences less than 1% for photon transverse energies above 30 GeV.

In an analysis of the inclusive W and Z samples, corresponding to a combined Run 1a+b data set of 67 pb^{-1} , we extracted 75 (34) $W\gamma$ and 18 (13) $Z\gamma$ events in the electron (muon) channel. Using the probabilities $\mathcal{P}_i(\text{jet} \rightarrow \gamma)$ from Chapter 6, we determined the QCD jet fragmentation background for $W\gamma$ ($Z\gamma$) to 20.6 ± 3.6 (1.4 ± 0.4) events in the combined electron + muon channel. The other background contributions (one-legged $Z + \gamma$ and $(W \rightarrow \tau\nu) + \gamma$) are estimated to 5.8 ± 0.4 events from a Baur plus Fast Monte Carlo simulation. Tables 8.1 and 8.2 summarize the preliminary numbers of background and signal events in the Run 1a+b electron and combined electron + muon $W\gamma$ ($Z\gamma$) data samples.

Using this background estimate and the efficiencies and acceptances from Section 5.4 and 5.5, we measured the cross section \times branching ratio for $W\gamma$ and $Z\gamma$ production ($E_T^\gamma > 7 \text{ GeV}$, $\Delta R_{\ell\gamma} > 0.7$) in the combined electron + muon channel

Sample	QCD	τ Channel	$Z\gamma$	N_{tot}
$W\gamma$ (electron)	13.8 ± 2.4	1.1 ± 0.1	1.2 ± 0.1	16.1 ± 2.4
$W\gamma$ (electron + muon)	20.6 ± 2.7	4.2 ± 0.2	1.6 ± 0.1	26.4 ± 2.7
$Z\gamma$ (electron)	0.9 ± 0.3	< 0.1	–	0.9 ± 0.3
$Z\gamma$ (electron + muon)	1.4 ± 0.3	< 0.1	–	1.4 ± 0.3

Table 8.1: Summary of the backgrounds in the preliminary Run 1a+b $W\gamma$ and $Z\gamma$ data samples for the electron and combined electron + muon channels (\pm stat.). N_{tot} is the total number of background.

to

$$\sigma \cdot B(W\gamma \rightarrow \ell\nu\ell\gamma) = 20.7 \pm 3.7 \text{ pb},$$

$$\sigma \cdot B(Z\gamma \rightarrow \ell^+\ell^-\gamma) = 5.7 \pm 1.4 \text{ pb},$$

where $\ell = e + \mu$. The errors are statistical. In case of $W\gamma$ ($Z\gamma$) production, the relative uncertainty is 18% (25%), a factor of 1.78 (1.52) lower than in Run 1a, which scales with the square-root of the luminosity ratios $\sqrt{67\text{pb}^{-1}/19.6\text{pb}^{-1}} = 1.85$. These updated results compares well with the Standard Model predictions of 18.6 ± 2.9 pb ($W\gamma$) and 4.8 ± 0.6 pb ($Z\gamma$).

Of particular note, the $W\gamma/Z\gamma$ cross section ratio is with $3.6_{-1.2}^{+2.0}$ dramatically different from the ratio of the inclusive W to Z cross sections (≈ 11), proving the presence of gauge cancellations in the $W\gamma$ sector. The Standard Model prediction is $\sigma \cdot B(W\gamma \rightarrow \ell\nu\ell\gamma)/\sigma \cdot B(Z\gamma \rightarrow \ell^+\ell^-\gamma) = 4.0 \pm 0.1$.

8.2 Kinematic Distributions

In this paragraph, we present the various updated physics distributions. Figure 8.5 and Figure 8.4a show the updated distribution for the spectrum of the transverse

Sample	N_{obs}	Signal	Prediction
$W\gamma$ (electron)	75	58.9 ± 9.0	53.5 ± 6.8
$W\gamma$ (electron + muon)	109	82.6 ± 10.8	75.3 ± 8.0
$Z\gamma$ (electron)	18	17.1 ± 5.7	16.2 ± 1.8
$Z\gamma$ (electron + muon)	31	29.6 ± 6.7	24.9 ± 1.9

Table 8.2: Comparison of the preliminary Run 1a+b $W\gamma$ and $Z\gamma$ signal in the electron and combined electron + muon channels to the Standard Model prediction obtained from Baur plus Fast Monte Carlo calculations (\pm stat.). N_{obs} is the number of observed events.

photon energy for $W\gamma$ and $Z\gamma$ processes, respectively. The data are compared to the Baur plus Fast Monte Carlo prediction including background. Again, we do not observe any excess of high E_T photon events which would indicate the presence of anomalous couplings. However, we note the occurrence of a rather clean $Z\gamma$ event with a remarkable photon E_T of 192 GeV, resulting in an extremely high three body mass of $M_{ee\gamma} \sim 420$ GeV/ c^2 [79]. Both electrons are nicely isolated and form a dielectron mass of $M_{ee} \sim 90$ GeV/ c^2 .

The electron clusters, together with the photon cluster, are shown in Figure 8.1, which depicts a so-called Lego¹ plot. The location of the photon (to the left) and electron is symbolized by a tower whose height is proportional to the particle's energy deposition in the calorimeter. The towers are positioned on a projective plane in the (η, ϕ) space. To easily visualize the detector geometry, form in mind a cylinder with a symmetry axis in η -direction by rolling up the plane along the azimuth angle ϕ . The symmetry axis corresponds to the location of the beam axis, and the cylinder surface to the calorimetry area.

In the CTC display, one can see two opposite-charged high P_T tracks pointing

¹LEGO[®] is a registered trademark of the LEGO Group.

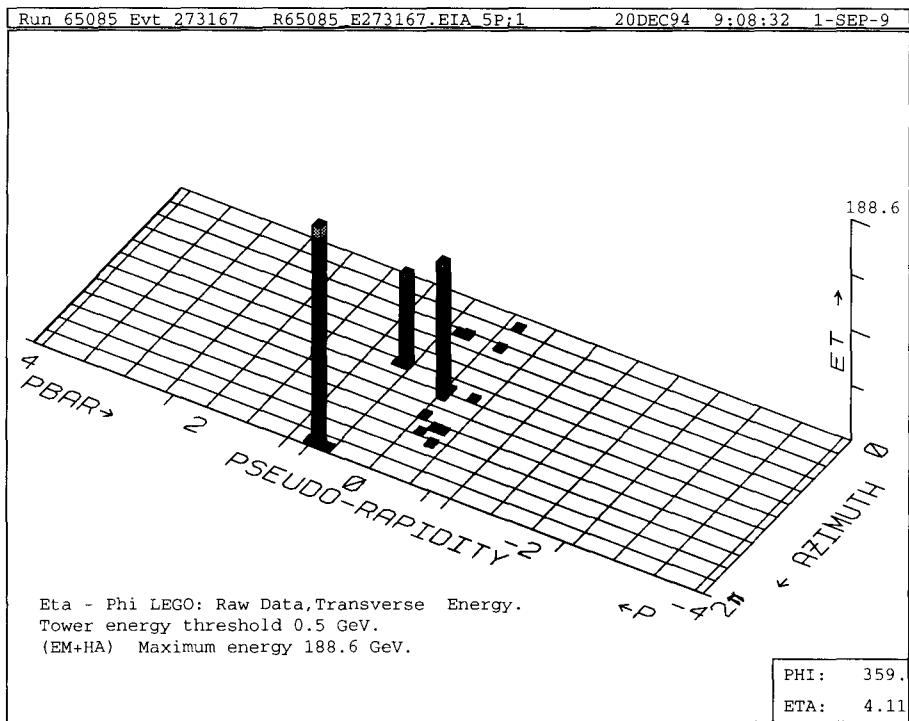


Figure 8.1: Lego plot of a $Z\gamma$ event with a $E_T \sim 200$ GeV photon. Shown is a (η, ϕ) projection of the CDF calorimeters. The two electron clusters are located to the right of the photon cluster.

to the calorimeter cluster (shaded boxes in Figure 8.3). The third cluster has no track associated with, and must therefore stem from a photon or jet. However, jet fragmentation into neutral mesons at 200 GeV is highly unlikely. A Monte Carlo study has shown that the probability for $Z\gamma$ events to occur with a high E_T photon forming an invariant three body mass of $M_{e\bar{e}\gamma} > 400$ GeV/ c^2 , is less than 0.05%. This is a conservative estimate, as Drell-Yan + γ contributions, i.e. $Z\gamma$ events with a Z mass larger than the upper mass limit in the Z selection, are included in the simulation.

The event appears to be relatively ‘quiet’; there is no sign of significant jet activities in the Lego plot and only tracks with very low P_T , in the order of less

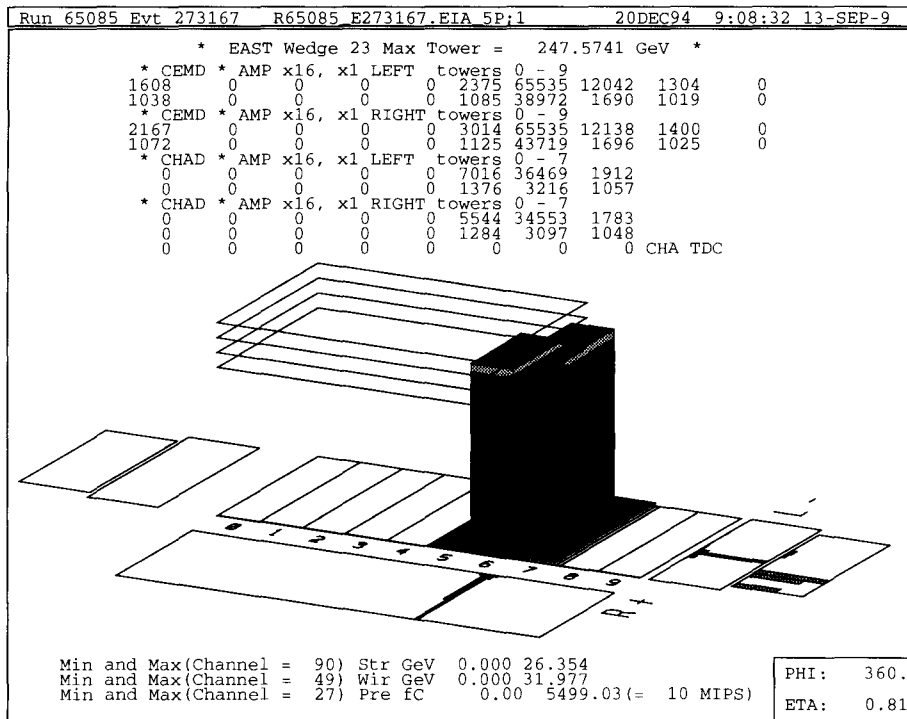


Figure 8.2: Display of the photon energy deposition in ‘tower 6’ of the Central Electromagnetic Calorimeter. The corresponding projections of the shower profile is shown in the CES strip chamber histograms. (The box to the very right represents the CPR response, which can be ignored here.)

than 1 GeV/c, are reconstructed by the CTC (Figure 8.3). Yet, it is not included in our $Z\gamma$ data sample. The reason is, the photon shower profile in the CES is so narrow that the CDF offline code assigned a high CES χ^2_{ces} above 20, expressing a bad match to the ‘standard’ testbeam profile (see Section 4.2.3). Figure 8.2 shows the two ‘spiky’ shower profiles in the CES display and the energy deposition in calorimeter tower 6.

The occurrence of all other $Z\gamma$ (or $W\gamma$) events with a high E_T photon in Figure 8.4a (Figure 8.5) are well predicted by the Standard Model. As an example, we calculated the Standard Model probability for detecting a $W\gamma$ event in the combined electron + muon channel with a transverse cluster masses, M_{TC} , higher than

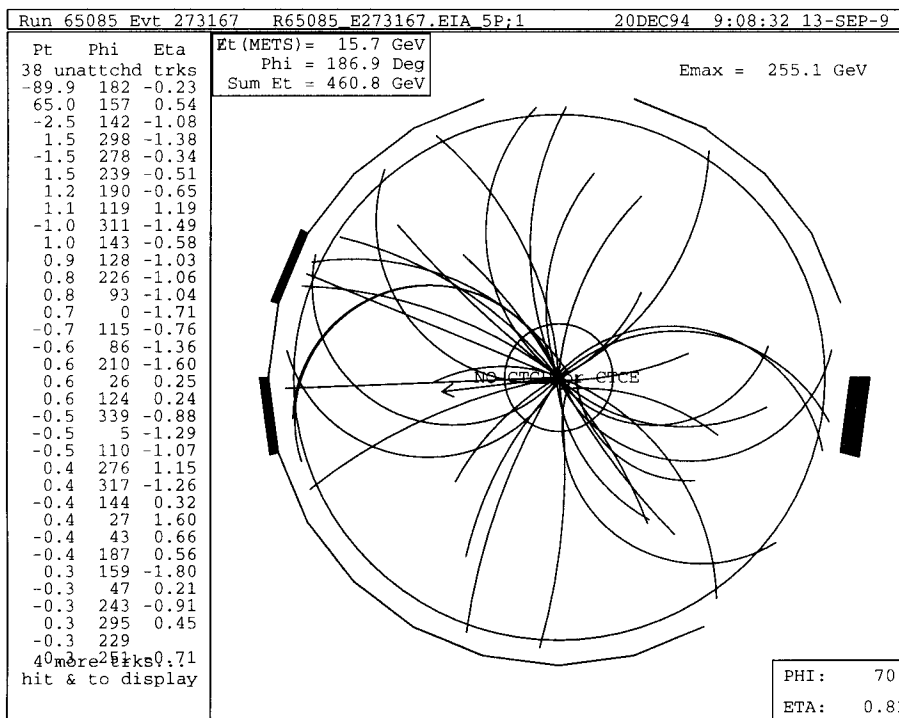


Figure 8.3: Cross section of the Central Tracking Chamber (not to scale). Two opposite-signed, three-dimensional high P_T tracks are pointing electron clusters (shaded boxes). No high P_T track is associated with the photon cluster. Several low P_T track below ≈ 2 GeV are also shown.

100 GeV/c² (120 GeV/c²). The result is 20% (9%). In our Run 1a+b data sample, we have 15 (4) such events (Figure 8.6b), corresponding to 24% (7%) of the total number of events in the sample.

In summary, we find no evidence of anomalous W-photon or Z-photon couplings in any of the kinematic distributions of the photon transverse energy (Figure 8.5 for $W\gamma$ and Figure 8.4a for $Z\gamma$), of the $W\gamma$ photon-lepton separation (Figure 8.6a), of the $W\gamma$ transverse cluster mass (Figure 8.6b), or of the $Z\gamma$ three-body mass (Figure 8.4b). All distributions are in very good agreement with the Standard Model predictions. Note, that Figure 8.5 verifies that the low number of events in the 7–11 GeV bin of the photon E_T spectrum, as measured in the Run 1a analysis

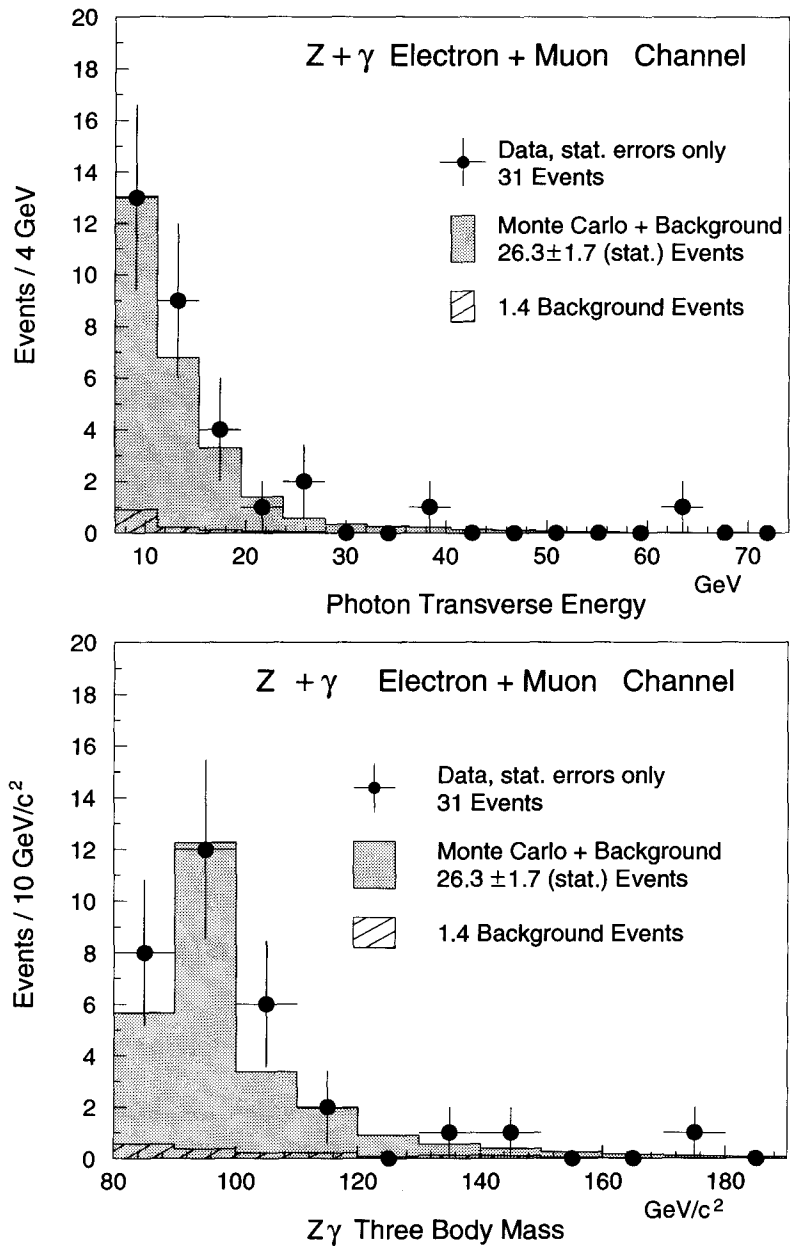


Figure 8.4: Comparison of observed to predicted a) transverse photon energy b) $e\bar{e}\gamma$ three-body mass spectrum for Z + central photon events in preliminary 67 pb^{-1} electron + muon data.

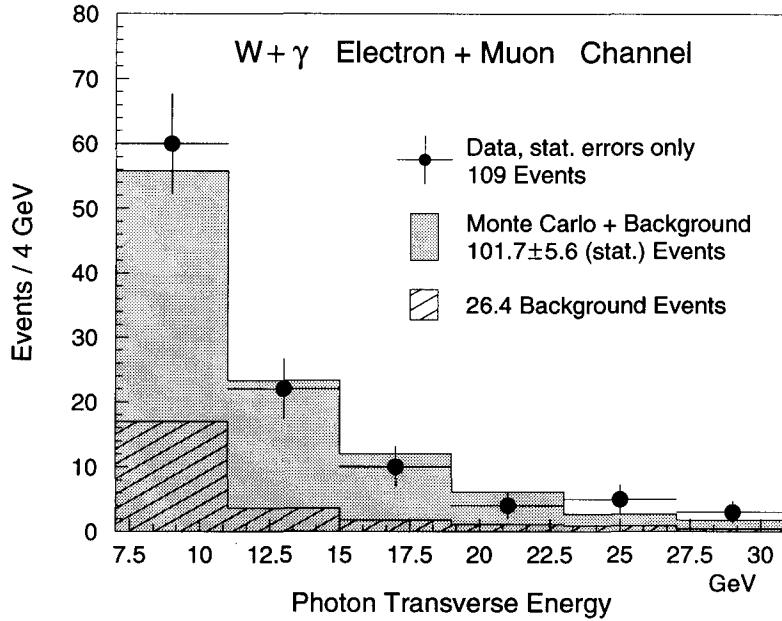


Figure 8.5: Comparison of observed to predicted transverse photon energy spectrum for $W + \text{central photon}$ events in preliminary 67 pb^{-1} electron + muon data. Four events with the following photon transverse energies are outside the plotted range: 37 GeV, 46 GeV, 48 GeV and 49 GeV.

(Figure 7.2), is indeed a statistical downward fluctuation.

8.3 Preliminary Limits on Anomalous Couplings

In direct analogy to the procedure described in Section 7.3, we update the limits on anomalous couplings using the the combined electron + muon Run 1a+b data set. A log-likelihood fit of the photon E_T spectrum (Figure 8.5 and Figure 8.4a) yields the following preliminary one-dimensional bounds on $W\gamma$ and $Z\gamma$ couplings at 95% CL:

W-Photon coupling limits ($\Lambda_W = 1.5 \text{ TeV}$)

$$\begin{aligned}
 -1.8 < \Delta\kappa(\tilde{\kappa}) < 2.0 & \quad \text{for} \quad \lambda(\tilde{\lambda}) = 0 \\
 -0.7 < \lambda(\tilde{\lambda}) < 0.6 & \quad \text{for} \quad \Delta\kappa(\tilde{\kappa}) = 0
 \end{aligned}$$

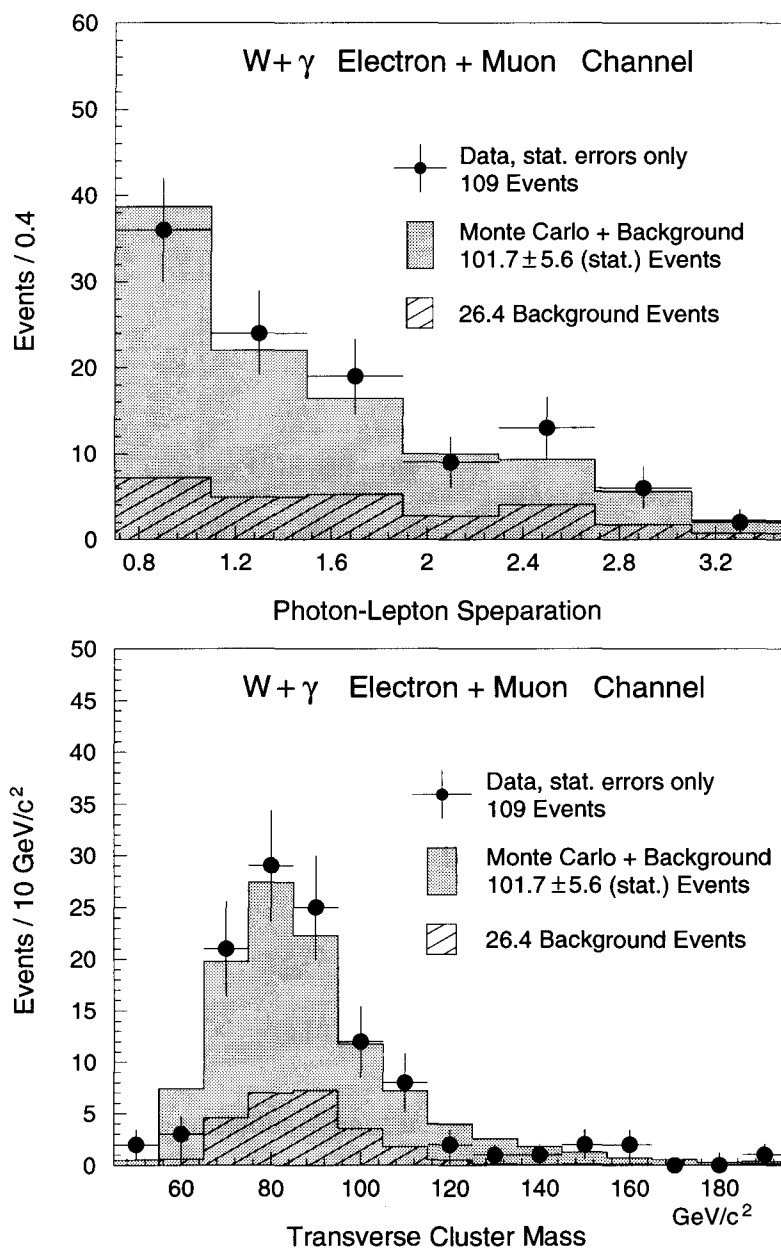


Figure 8.6: Comparison of observed to predicted a) photon-lepton separation, b) transverse cluster mass spectrum for $W + \text{central photon}$ events in preliminary 67 pb^{-1} electron + muon data.

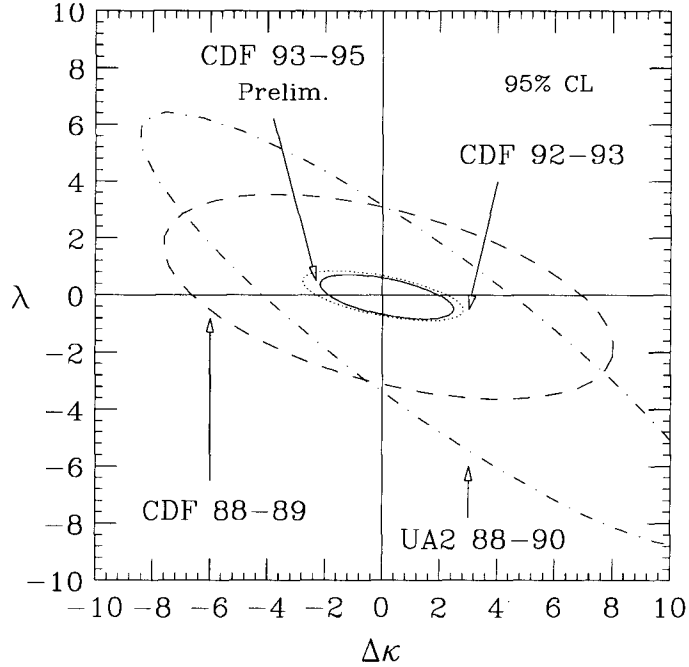


Figure 8.7: Comparison of limit contours at 95% CL for the \mathcal{CP} -conserving coupling pair $(\Delta\kappa, \lambda)$, measured at hadron colliders between the years 1988 and 1995.

Z-Photon coupling limits ($\Lambda_Z = 0.5$ TeV)

$$\begin{aligned}
 -1.6 < h_{10}^Z(h_{30}^Z) < 1.6 & \quad \text{for } h_{20}^Z(h_{40}^Z) = 0 \\
 -0.4 < h_{20}^Z(h_{40}^Z) < 0.4 & \quad \text{for } h_{10}^Z(h_{30}^Z) = 0
 \end{aligned}$$

As discussed in the previous Chapter, Section 7.3, systematic uncertainties are included in the determination of these limits.

Figure 8.7 compares limits contours measured at the hadron collider experiments CDF and UA2 to illustrate the improvement in the sensitivity during a decade. The integrated luminosity has increased since 1988 by more than an order of magnitude. At the same time, the CDF bounds on anomalous couplings have decreased by a factor of 4–6. With data sets larger than 100 pb^{-1} by the end of Run 1b, further improvement, though less substantial, can be expected. A comparison

of our results with measurements by the DØ Collaboration will be discussed in the last Chapter.

Chapter 9

$W\gamma$ Production at High Photon Rapidities

The Standard Model predicts that $W + \text{photon}$ events with large angular separation between the photon and the charged lepton arise predominantly from $W\gamma$ production (Figure 2.1 d–e) rather than from radiative events (Figure 2.1 c). The central calorimeter at CDF covers approximately 2 units of pseudorapidity, making it difficult to find events with large photon-lepton separation using only this detector. Since the majority of charged W decay leptons in $p\bar{p}$ collisions are produced into the central region, the best way to collect additional $W\gamma$ production events is to extend the search for high energy photons to larger rapidities. The detector that covers the next higher rapidity range after the central calorimeter is the plug calorimeter (Section 4.2). Searching for photons in this detector expands the possible photon-lepton pseudorapidity difference by another 2.6 units.

In this chapter, the extension of the analysis to search for photons in the plug calorimeters is described. It is the first photon analysis at CDF performed over the rapidity coverage of the plug calorimeters.

The ‘plug photon analysis’, which differs in many ways from the ‘central photon analysis’, was performed when a preliminary data set of about $\approx 55 \text{ pb}^{-1}$ from Run 1b was readily available. In order to measure various Standard Model predictions with maximal statistical significance, we combined the Run 1a and 1b data sets ($\approx 75 \text{ pb}^{-1}$).

At the end of Run 1b the final integrated luminosity for Run 1 is expected to be $120 - 140 \text{ pb}^{-1}$. The central and plug photon analyses presented in this thesis can then be used as basis for an extended analysis of $W\gamma$ and $Z\gamma$ production covering a photon rapidity region of $|\eta_{det}| < 2.4$, which corresponds to a maximum photon-lepton rapidity difference of 3.5. In addition, with increased luminosity it will be interesting to look for exotic events such as $W\gamma\gamma$ or $Z\gamma\gamma$, where one of the photons may be found in either the central or plug region. And lastly, there is a possibility to include the FEM Calorimeter ($2.4 < |\eta| < 4.2$) in the photons search, because the definition of a photon in the plug and forward region are rather similar. However, serious problems like a reliable determination of efficiencies and jet fragmentation backgrounds will have to be overcome.

9.1 Event selection

The plug calorimeter covers the forward/backward pseudorapidity region up to $|\eta| = 2.4$. We define plug photons as follows (see also Table 9.1) :

- The cluster has to be found in a fiducial plug region.
- The transverse photon energy E_T must be greater than 7 GeV.
- The electron must be isolated in a cone of $\Delta R_{e\gamma} < 0.4$,

	Cut
Pseudorapidity Range	$1.1 < \eta < 2.4$
Transverse Energy	$E_T > 7.0 \text{ GeV}$
Isolation	$ISO4 \equiv \frac{E_{T,\Delta R < 0.4} - E_{T,cluster}}{E_{T,cluster}} < 0.15$
Energy Ratio HAD/EM	$HAD/EM < 0.028 + 0.00019 \cdot E \text{ (GeV)}$
VTX Occupancy	$f_{vtx} < 0.4$
3×3 Tower Profile	$\chi_{3 \times 3} < 5$
Strip Profile in η -view	$\chi_\eta^2 < 20$
Strip Profile in ϕ -view	$\chi_\phi^2 < 20$

Table 9.1: Summary of plug photon requirements.

$$ISO4 \equiv \frac{E_{T,\Delta R < 0.4} - E_{T,cluster}}{E_{T,cluster}} < 0.15.$$

- The ratio of hadronic energy to electromagnetic energy must be less than

$$HAD/EM < 0.028 + 0.00019 \cdot E,$$

where E is the total energy of the PEM cluster.

- The VTX hit occupancy must be less than 0.4.
- The 3×3 tower profile must have a $\chi_{3 \times 3}$ less than 5.
- In the PES region $1.28 < |\eta| < 1.78$, where a fit of the strip shower profile is available, the strip chamber χ^2 in the η - and ϕ -view must be less than 20.

18 (42) $W\gamma$ candidates passed these selection criteria in the inclusive electron W sample from Run 1a (Run 1b). Combining the preliminary data set from Run 1b ($\approx 55 \text{ pb}^{-1}$) with the Run 1a data ($\approx 20 \text{ pb}^{-1}$), the total electron + muon W sample consists of $\approx 75 \text{ K}$ events.

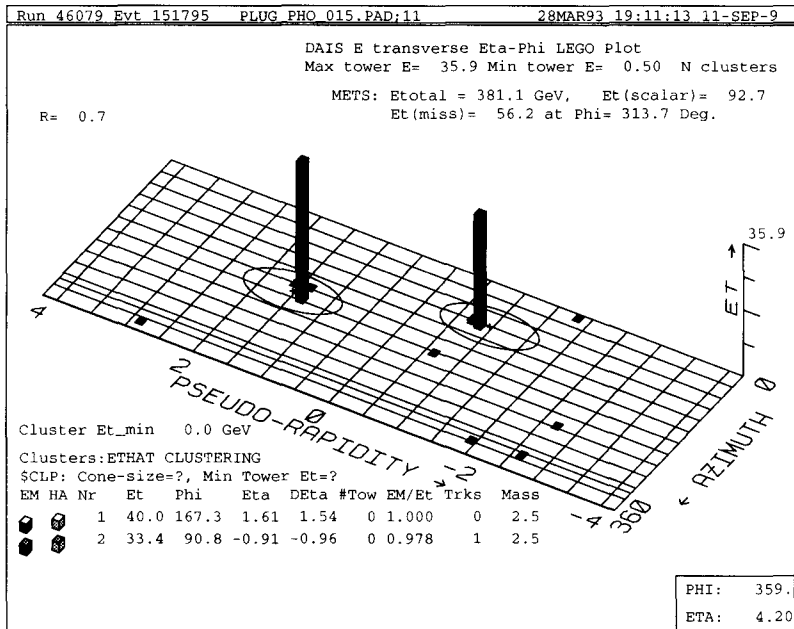


Figure 9.1: Two-dimensional projection of the CDF calorimeters into the (η, ϕ) space. The height of the towers represents the electromagnetic energy deposition of a 30 GeV central W decay electron (right tower) and a 41 GeV plug photon. The ellipses around the tower mark the boundaries of a cone with radius $\Delta R_{e\gamma} = 0.7$.

As an example, Figures 9.1 – 9.3 show the display of a $W\gamma$ event with an $E_T = 30$ GeV electron and an $E_T = 41$ GeV plug photon. The missing transverse energy is 56 GeV.

In Figure 9.1, a Lego plot of the event, the electron cluster (to the right) and the photon cluster are nicely isolated and separated from each other. There is no jet activity in the event. The shower profile of the plug photon in the η - and ϕ -view of the finely grained strip chamber PES is depicted in Figure 9.2 (STRIP). Such a profile is typical for photon candidates that are most likely not from background events. Also shown is the one-dimensional projection of the energy deposition in the PEM calorimeter (CAL).

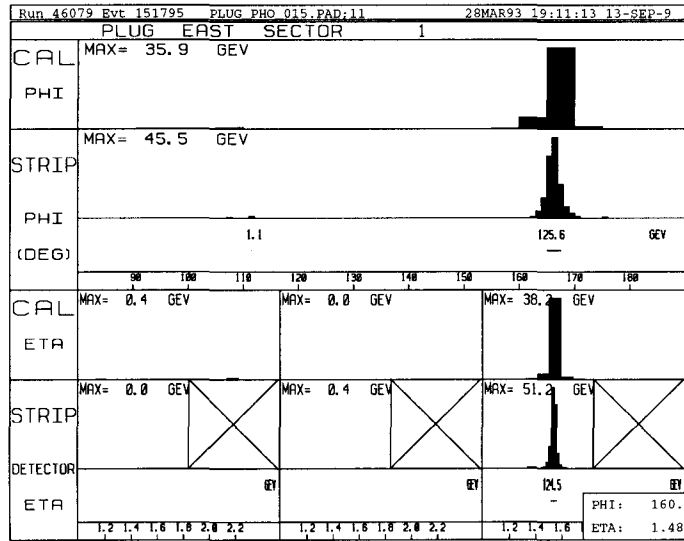


Figure 9.2: Projection of the photon shower profile in the η - and ϕ -views, as measured by the plug calorimeter (CAL) and strip chamber (STRIP).

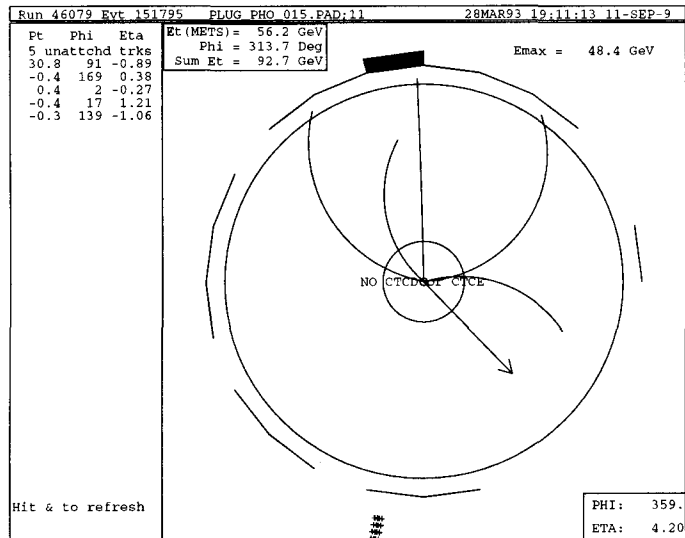


Figure 9.3: Track display of the W decay electron of a W + plug photon event in the Central Tracking Chamber (straight line). The shaded box represents the corresponding energy deposition. The arrow points in the direction of the neutrino momentum vector ('missing energy').

In Figure 9.3, the high P_T track of the W decay electron in the CTC appears as a straight line pointing to a shaded rectangle which represents the electron’s energy deposition in the calorimeter. The arrow points in the direction of the neutrino momentum (‘missing energy’). The event is very clean; only four low momentum tracks ($\lesssim 0.4$ GeV/c) from underlying processes are reconstructed.

9.2 Efficiencies

The following section discusses the determination of the efficiencies of the plug photon selection cuts.

The isolation efficiency $\epsilon_{iso4}^{pem\gamma}$ was calculated at random points in the inclusive W/Z data samples in analogy to the algorithm used for the determination of the isolation efficiency of central photons, $\epsilon_{iso4}^{\gamma} \equiv \epsilon_{iso4}^{cem\gamma}$, described in Chapter 5.4. In the plug region, the variable $ET4$ is measured by summing up the energy deposition in cone of $\Delta R_{\ell\gamma} = 0.4$ at an arbitrary point of the plug calorimeter and subtracting the energy of a cluster, representing a photon, with a typical shape of maximal 5×5 towers. A list of clusters of plug electrons from a ‘loose’ Z sample served as a map to define the shape and size of typical plug photon cluster matrices.

The results are shown in Table 9.2 for Run 1a and 1b. Due to the higher luminosity in Run 1b, the plug isolation efficiencies are lower in Run 1a. In both cases, the *ISO4* cut is fully efficient for energies above 100 GeV.

For the same reason, the efficiency for the VTX occupancy cut, $\epsilon_{vtx}^{pem\gamma}$, is lower in Run 1b than in Run 1a. To measure $\epsilon_{vtx}^{pem\gamma}$, the number of random rays pointing to the plug calorimeter in the W sample were counted. The ratio of random rays having an occupancy less than 0.4 at the VTX intersection point to the total number defines $\epsilon_{vtx}^{pem\gamma}$ (Table 9.3).

E_T Bin (GeV)	Run 1a	Run 1b
7–11	87.3 – 93.8	84.7 – 90.9
11–15	93.8 – 96.6	90.9 – 95.6
15–20	96.6 – 98.0	95.6 – 97.5
20–30	98.0 – 99.1	97.5 – 98.7
30–45	99.1 – 99.6	98.7 – 99.2
45–65	99.6 – 99.7	99.2 – 99.5
65–100	99.7 – 99.9	99.5 – 99.7

Table 9.2: E_T -dependent plug photon isolation efficiencies, $\epsilon_{iso4}^{pem\gamma}$, in %, determined at random points in the W sample (electron channel).

Unfortunately, there are no reliable plug testbeam data available to study—similarly to the central photon analysis—the efficiencies for the sliding HAD/EM cut and the shower profile quality cuts $\chi_\eta^2 < 20.0$, $\chi_\phi^2 < 20.0$ and $\chi_{3\times3}^2 < 5.0$. The purpose of choosing a sliding HAD/EM cut with a term linear in the cluster energy is twofold. First, due to energy leakage the efficiency of a constant cut value would be energy dependent, which is not desirable. And secondly, a sliding cut suppresses background at low photon energies while keeping a high efficiency at all energies.

Since a reasonably high statistics sample is needed in order to study the energy dependence of the HAD/EM cut, we use the 15 GeV plug photon/electron triggers in lieu of testbeam data. Besides having a transverse energy above 15 GeV, a 3×3

Data Sample	Run 1a	Run 1b
$\epsilon_{vtx}^{pem\gamma}$	87.0 ± 0.3 %	81.5 ± 0.1 %

Table 9.3: VTX occupancy efficiency for plug photons with an VTX occupancy less than 0.4, determined by studying random rays in the W sample (electron channel). The errors are statistical.

	a	b (1/GeV)
Set 1	0.0281 ± 0.0040	0.00020 ± 0.000050
Set 2	0.0280 ± 0.0038	0.00019 ± 0.000042
Set 3	0.0300 ± 0.0046	0.00018 ± 0.000055

Table 9.4: Coefficients a and b for the sliding cut $HAD/EM(E) < a + b \cdot E$ at 95% efficiency. The errors represent the uncertainties of the fit.

tower $\chi_{3 \times 3}^2 < 6$ and a ratio $HAD/EM < 0.125$, there is no further requirement on the trigger clusters. To measure the HAD/EM efficiency, we select electron triggers that have a VTX occupancy greater than 0.5 and apply a very tight isolation cut $ISO4 < 0.019$. Relaxing this isolation requirement was found to increase the hadronic contamination in the sample. Cutting tighter leaves the efficiency result unchanged, but increases the statistical uncertainty.

In the energy region $20 < E < 130$ GeV, a linear function was found to be a good approximation for a fit of the HAD/EM cut values at constant efficiency, which we arbitrarily set to 95%. We determined the coefficients a and b in the function $HAD/EM(E) < a + b \cdot E$ by fitting the cut values at 95% efficiency as a function of energy. Because we had to choose rather large bin sizes due to the limited statistics, we calculated the coefficients for three different energy binnings. The results are expected to be independent of the chosen bin sizes. Figure 9.4 shows the curves for the three sets fitted to the function $HAD/EM(E) = a + b \cdot E$, and Table 9.4 summarizes the coefficients resulting from that fit. The numbers are indeed independent of the binning. The final result for an energy independent HAD/EM cut is the weighted average of the three fits: $HAD/EM = 0.028 + 0.00019 \cdot E$ with an efficiency of $\approx 95\%$.

If we, in return, apply the sliding HAD/EM cut to each energy bin of the three

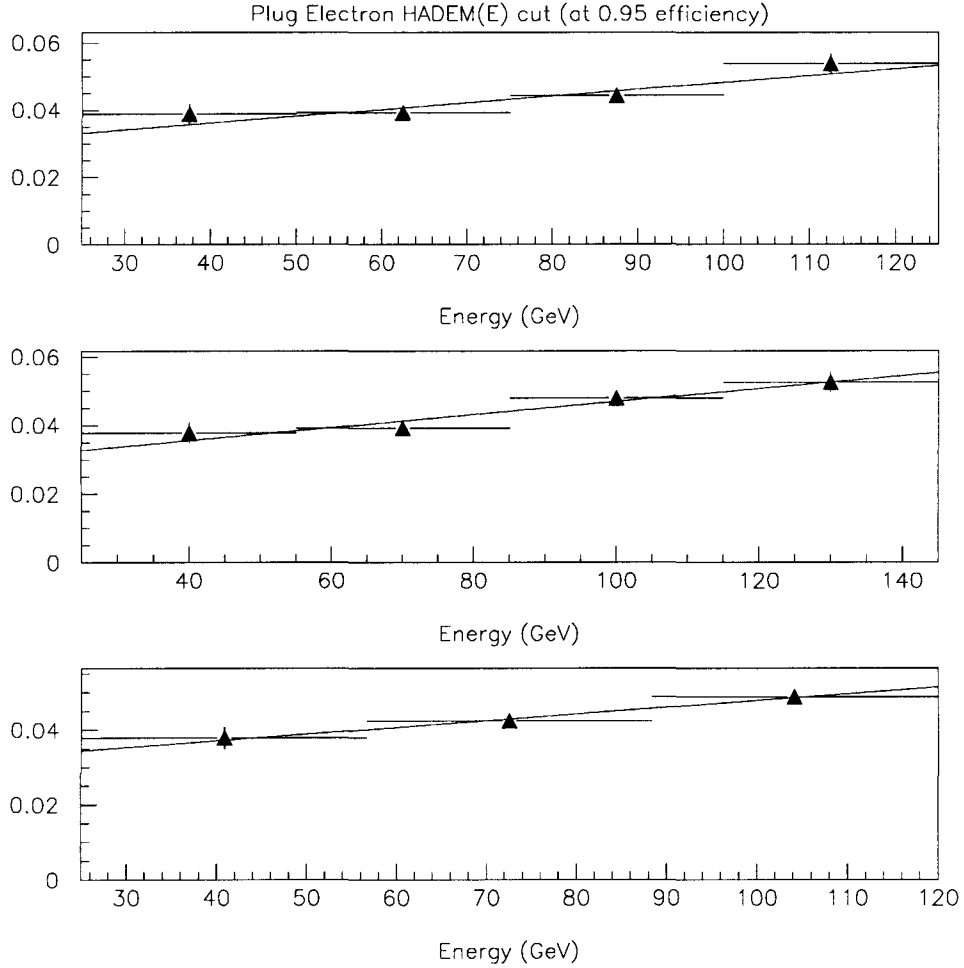


Figure 9.4: HAD/EM cut values at an energy dependent efficiency of 95% for three sets of bin sizes, determined using P15 plug triggers.

P15 sets, we should obtain a constant efficiency of about 95% for each individual bin. Table 9.5 shows that this is the case for a variety of energy ranges.

To make the measurement of the photon efficiencies for the $W + \text{plug photon}$ analysis, we determined $\epsilon_{had/em}$ from a data set of Z bosons with a ‘loose’ decay electron in the plug. We apply standard analysis cuts to the central leg of the Z (Chapter 5) and require the fiducial plug leg to pass the following cuts: $80 < M_{ee} < 100 \text{ GeV}/c^2$, $VTX \text{ occupancy} > 0.5$ and $ISO4 < 0.15$. The efficiency is

Set 1	25 – 50 GeV	50 – 75 GeV	75 – 100 GeV	100 – 125 GeV
N_{tot}	188	165	78	32
$\epsilon_{had/em}$	$94.7 \pm 1.7\%$	$94.5 \pm 1.8\%$	$94.9 \pm 2.6\%$	93.8 ± 4.4
Set 2	25 – 55 GeV	55 – 85 GeV	85 – 115 GeV	115 – 145 GeV
N_{tot}	233	158	61	20
$\epsilon_{had/em}$	$94.8 \pm 1.5\%$	$94.9 \pm 1.8\%$	$95.1 \pm 2.8\%$	95.0 ± 5.0
Set 3	25 – 60 GeV	60 – 95 GeV	95 – 120 GeV	—
N_{tot}	273	146	39	—
$\epsilon_{had/em}$	$94.9 \pm 1.4\%$	$95.2 \pm 1.8\%$	$94.9 \pm 3.6\%$	—
	total energy range			
N_{tot}	481			
$\epsilon_{had/em}$	$94.2 \pm 1.1\%$			

Table 9.5: Efficiencies (\pm stat.) for the cut $HAD/EM(E) < 0.028 + 0.00019 \cdot E$ in various energy regions, determined from plug electron samples.

then defined as the ratio of plug electrons that pass the HAD/EM cut over the total number of events. We find $\epsilon_{had/em} = 94.4 \pm 1.0\%$ using the ‘loose’ Z sample of Run 1a, and $\epsilon_{had/em} = 94.7 \pm 0.6\%$ using a preliminary set of ‘loose’ Z events from Run 1b. The errors are statistical. The agreement with the expected 95% efficiency is excellent for both runs.

In complete analogy, we measured the efficiencies for the χ^2 cuts using a ‘loose’ Z sample from Run 1a and Run 1b. In this case, the ‘loose’ plug leg is defined as follows: $80 < M_{ee} < 100 \text{ GeV}/c^2$, $VTX \text{ occupancy} > 0.5$ and $HAD/EM < 0.028 + 0.00019 \cdot E$, where E is the total energy of the plug electron. We find an efficiency of $\approx 97\%$ for the χ^2 variables.

The final efficiencies of all shower variables are summarized in Table 9.6. We expect and find no statistically significant differences between the results in Run 1a and Run 1b.

Cut	Run 1a	Run 1b
N_{tot}	540	1654
$\epsilon_{had/em}^{pem\gamma}$	$94.4 \pm 1.0\%$	$94.7 \pm 0.6\%$
N_{tot}	514	1596
$\epsilon_{\chi^2_{3 \times 3}}^{pem\gamma}$	$97.1 \pm 0.8\%$	$96.7 \pm 0.5\%$
N_{tot}	296	879
$\epsilon_{\chi^2_{\eta} + \chi^2_{\phi}}^{pem\gamma}$	$97.6 \pm 0.9\%$	$96.5 \pm 0.6\%$

Table 9.6: Efficiencies (\pm stat.) of shower variables determined from ‘loose’ plug Z electron samples. N_{tot} is the sample size.

9.3 Background

As for central photons, QCD jets misidentified as single isolated photons are the main background source in the plug photon samples.

In Chapter 6, we discussed the measurement of QCD background in the central region of the CDF detector. The probability that a jet fakes a photon in the $W\gamma$ or $Z\gamma$ sample was determined from a large QCD sample, the 16 GeV photon trigger P16. We found in the P16 sample a non-negligible number of direct photons from Compton-like processes, which had to be subtracted off in the calculation of the jet fragmentation probability $\mathcal{P}_i(jet \rightarrow '\gamma')$. To estimate this fraction, a method based on the study of the shape of the CES shower profile was used.

Unfortunately, such a tool is not available in the plug region. Even worse, only a fraction of the plug rapidity range is covered by the high resolution strip chamber PES. We therefore had to develop an alternative method to estimate the number of direct photons in the plug region. In the following, we are going to discuss an approach which makes use of the fact that isolated photons and jets differ by the fraction of the electromagnetic energy around the photon or jet cluster.

As a QCD sample, we use the 16 GeV isolated photon trigger (P16) from Run 1a and—independently—a preliminary subsample of the 23 GeV photon trigger (P23) from Run 1b ($\approx 50 \text{ pb}^{-1}$). Apart from the different energy threshold, the two photon samples are rather similar. Differences are the slightly larger fiducial CES region, within which the P23 trigger accepts events at Level 3 ($|x_{wire}| < 21 \text{ cm}$, $9 \text{ cm} < |z_{strip}| < 217 \text{ cm}$), and a looser P23 isolation requirement [46]. For the following background study, we selected P23 trigger events with $ISO4 < 0.1$, which is identical to the isolation cut applied to the trigger electron in the inclusive central W (Z) sample. The P16 trigger identification was described in Section 6.1.

The results, which we will obtain from the P23 sample further below, can assumed to be independent of a particular trigger selection up to photon transverse energies of about 55 GeV, as we raised the P23 trigger threshold from 23 GeV to 55 GeV when selecting non-trigger events above 19 GeV. This reduces the possibility of having triggered on one member of, for instance, a diphoton or dijet event, and selecting the other member for our studies. Such a trigger selection would affect the ratio of electromagnetic objects that pass the plug photon analysis requirements to jets in the calculation of the jet fragmentation probability according to Equation 6.1.

In analogy to the central QCD background analysis (Section 6.1), we determine the probability for a jet in the plug region of the P23 (P16) sample to fragment into neutral mesons which are subsequently misidentified as photons. The number of electromagnetic objects passing the plug photon selection criteria (fake photons) and the number of jets in the plug region are summarized in Table 9.7. The list is split up into two sets, one for the detector region where PES strip chamber information is available ($1.28 < |\eta| < 1.78$), the other for the part where the PES

Sample	E_T Bin	EM, no PES	EM, PES	Jets, no PES	Jets, PES
P23	7-11	168	141	143294	147728
P16		47	41	35199	37158
P23	11-15	110	93	71876	69022
P16		30	36	19479	18502
P23	15-19	80	55	41002	37217
P16		26	22	13132	11586
P23 [†]	19+	9	19	17135	16717
P16		44	52	53170	53404

Table 9.7: Number of electromagnetic objects (EM) passing the plug photon analysis cuts and number of jets in the QCD trigger samples P23 and P16 per E_T bin (in GeV) for the two rapidity regions $1.28 < \eta < 1.78$ (PES) and $1.10 < \eta < 1.28$ or $1.78 < \eta < 2.40$ (no PES). [†] Minimum trigger transverse energy raised to 55 GeV.

is not installed ($1.10 < |\eta| < 1.28$ or $1.78 < |\eta| < 2.40$).

Direct photons are present in the P23 (P16) samples not only in the central region, but at higher rapidities as well, and have to be (statistically) removed from the set of fake plug photons. But instead of using a shower profile method to estimate their number, we analyze the electromagnetic energy fraction in a cone of $\Delta R_{\ell\gamma} = 0.7$. This quantity is defined as

$$EMF7 = \frac{E_T}{E_T \cdot (1 + HAD/EM) + ET7}, \quad (9.1)$$

where $ET7$ is the sum of the transverse energy on a cone of $\Delta R_{\ell\gamma} = 0.7$ around the cluster centroid. The cluster itself is excluded from the summation.

Since jet showers consist of mostly hadrons, we expect a relatively small electromagnetic fraction $EMF7$ for jets ¹. In contrast, isolated photon clusters character-

¹As in the discussion of the shower profile method, the word ‘jet’ stands for ‘fake photons from

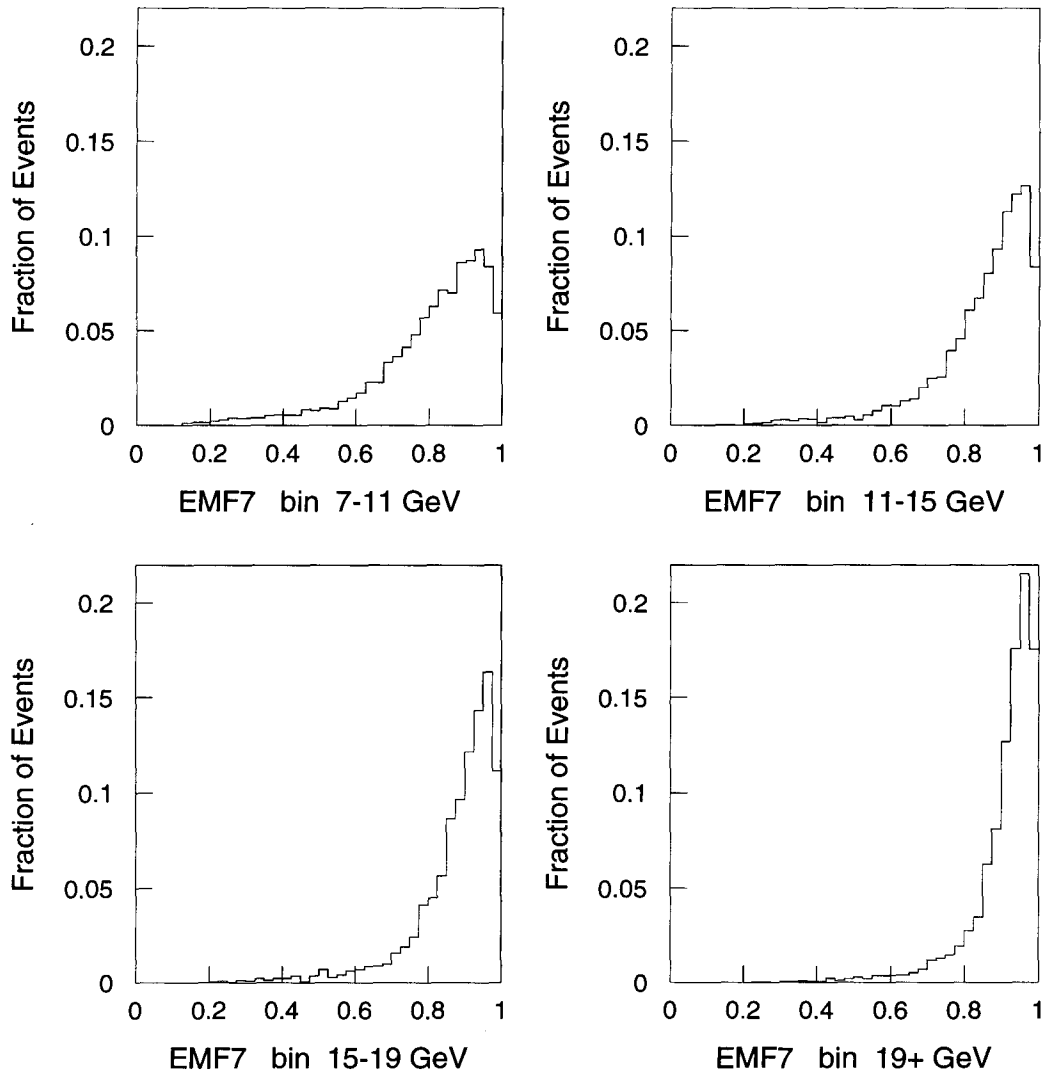


Figure 9.5: $EMF7$ spectra for photons from ‘hybrid’ Monte Carlo studies in the photon trigger sample P23 for each analysis bin.

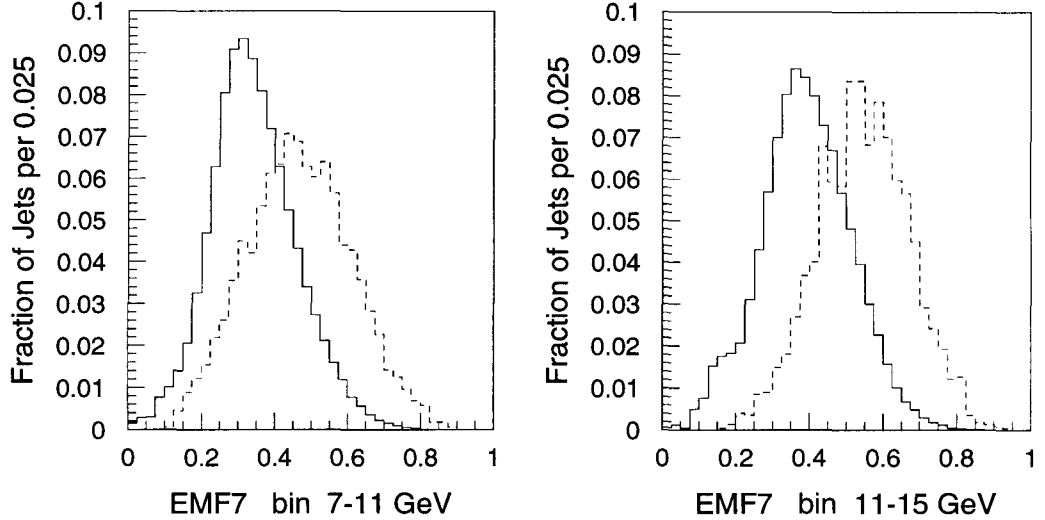


Figure 9.6: Comparison of the ‘W+jet’ jet $EMF7$ spectrum (solid line) with the P23 ‘ $\chi^2_{3 \times 3} > 6$ ’ jet $EMF7$ spectrum (dashed line), as defined in the text, for the first two analysis bins.

istically have only minor hadronic contaminations. Their electromagnetic fractions tend to be closer to 100%.

The hope is, that the $EMF7$ distributions for photons and jets differ to an extent, that they can be distinguished from each other. To study this question, the $EMF7$ spectrum of a *photon* was simulated by measuring $ET7$ at random positions in the plug region of the P23 (P16) sample. $EMF7$ was calculated according to Equation 9.1 by assigning a random value for the quantities E_T and HAD/EM at each random point. These values were weighted according to a typical E_T and HAD/EM distribution of the electromagnetic clusters. Figure 9.5 shows the resulting ‘hybrid Monte Carlo’ $EMF7$ spectra of plug photons for each analysis bin ² in the P23 sample. The corresponding spectra from random point studies in

jet fragmentation into neutral mesons that pass all plug photon analysis requirements’.

²The binning in E_T is identical to the one in the plug (and central) photon analysis. We continue to call these bins ‘analysis bins’.

the P16 sample are very similar. As expected, most high energy photons above 15 GeV have $EMF7 \gtrsim 0.8$. As the energy decreases, an increasing fraction of photons tends to populate the $EMF7$ region below ≈ 0.8 .

Our goal is to show that only a negligible fraction of jets has a high $EMF7$ value, which would give us the means to identify direct photons in this region. Studying $EMF7$ distributions of *jets*, however, is difficult because ideally a jet-only data sample in which each jet is associated with an electromagnetic cluster by the CDF offline code is needed to estimate the number of events surviving the plug photon selection requirements in the high $EMF7$ region. Any such jet data set implicitly contains direct photons. However, it is possible to define samples that are adequate for our purpose.

From previous CDF measurements, which dealt with studies of 3×3 tower shower profiles, it is known that high $\chi_{3 \times 3}^2$ values, typically above 3, strongly antiselect direct photons [80]. Hence, in order to define a sample with an enhanced number of jets in the P23 (P16) sample, we ‘invert’ the $\chi_{3 \times 3}^2$ cut by requiring electromagnetic objects to have $\chi_{3 \times 3}^2 > 6$. This way, only few direct photons are presumed to be left in the sample. Such a sample will give conservative answers, in a sense that—due to the direct photon contamination—more events with high $EMF7$ values will survive the photon selection requirements than would in a jet-only sample. The jets in a $W + \text{jet}$ data set can be assumed to represent such a jet-only sample. However, only a fraction of these jets are associated with an electromagnetic object by the clustering algorithm. Because of that, the jet $EMF7$ spectrum will be shifted towards lower values. Using the $W + \text{jet}$ data, we expect to obtain somewhat too optimistic answers as we underestimate the number of jet events in the highest $EMF7$ bin.

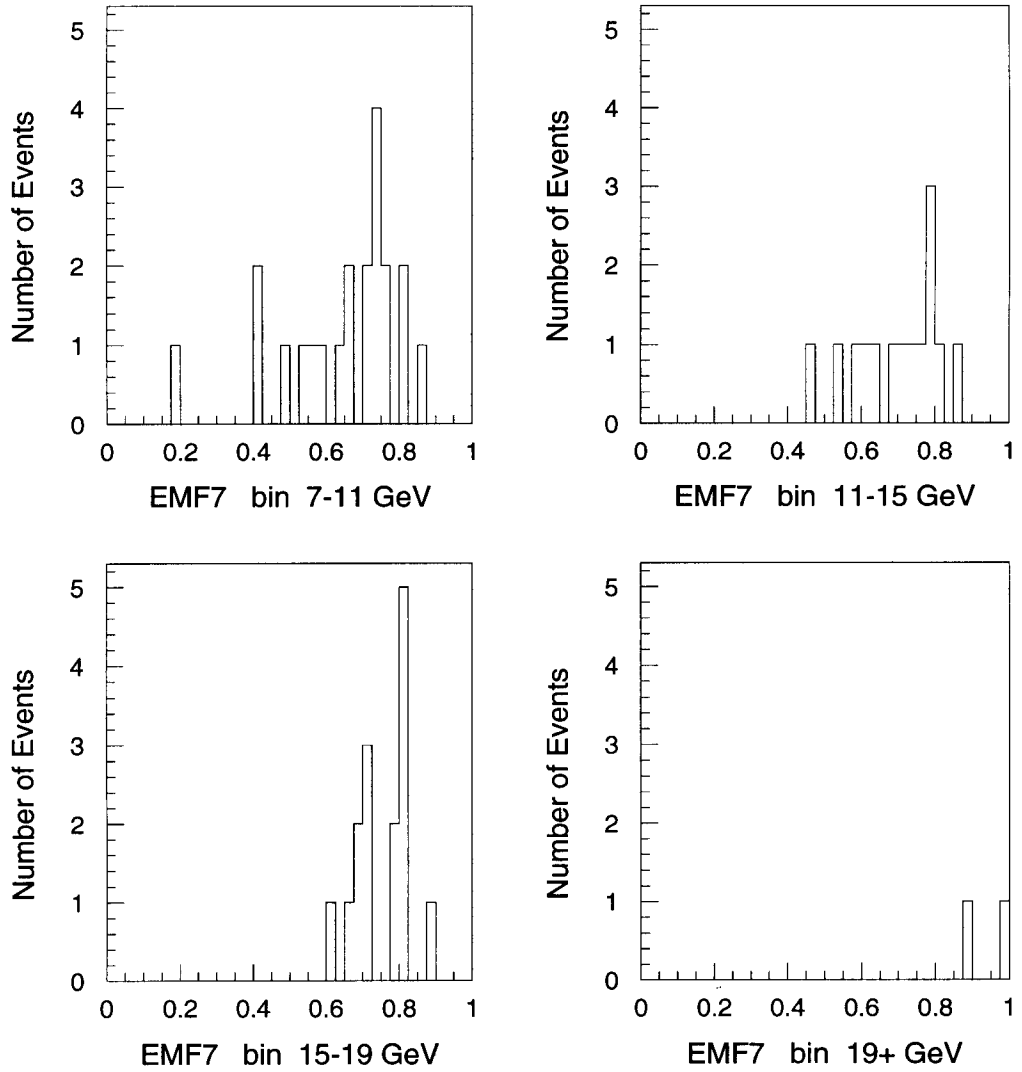


Figure 9.7: The P23 ' $\chi^2_{3 \times 3} > 6$ ' jet $EMF7$ spectrum in the rapidity region not covered by the PES, after applying all plug photon analysis requirements (except $\chi^2_{3 \times 3} < 5$) for each analysis bin.

In Figure 9.6, we compare the ‘W + jet’ jet spectrum with the ‘ $\chi_{3 \times 3}^2 > 6$ ’ jet spectrum as a function of $EMF7$ for the first two analysis bins. The two distributions are slightly displaced from each other in the expected way. The $EMF7$ spectrum of a jet-only sample, in which the clustering algorithm associates the jet with an electromagnetic object, presumably lies somewhere in between.

In either case, one finds relatively little overlap with the photon $EMF7$ distributions (Figure 9.5) at high $EMF7$ values. If we additionally impose the plug photon requirements, except $\chi_{3 \times 3}^2 < 5$, onto the ‘ $\chi_{3 \times 3}^2 > 6$ ’ jet spectrum, we find only very few events left in the region at high $EMF7$ in each analysis bin. This is illustrated in Figure 9.7 for the plug region not covered by the PES; the equivalent plot for the other region covered by the PES is very similar. It is likely that a large fraction of these remaining events are indeed direct photons. We conclude from this rather heuristic argumentation, that above a certain $EMF7$ value the majority of events in the P23 (P16) jet sample, which pass the plug photon selection criteria, are direct photons with a small contribution of real jets. A numerical estimate for these contributions will be given below.

To estimate the number of direct photons in the P23 (P16) sample, we divide the $EMF7$ distribution of the P23 (P16) electromagnetic clusters that pass all photon analysis cuts (fake photons) into bins of equal size so that the highest bin can be assumed to contain predominantly direct photon events and only a negligible number of jets. We then bin the direct photon $EMF7$ distribution in an equal manner and match its highest bin to the corresponding bin of the P23 (P16) $EMF7$ fake photon spectrum. Such a fit directly defines the direct photon $EMF7$ distribution in shape and size. Integration over the fitted curve yields the number of the direct photon contamination, that to measure we had in mind.

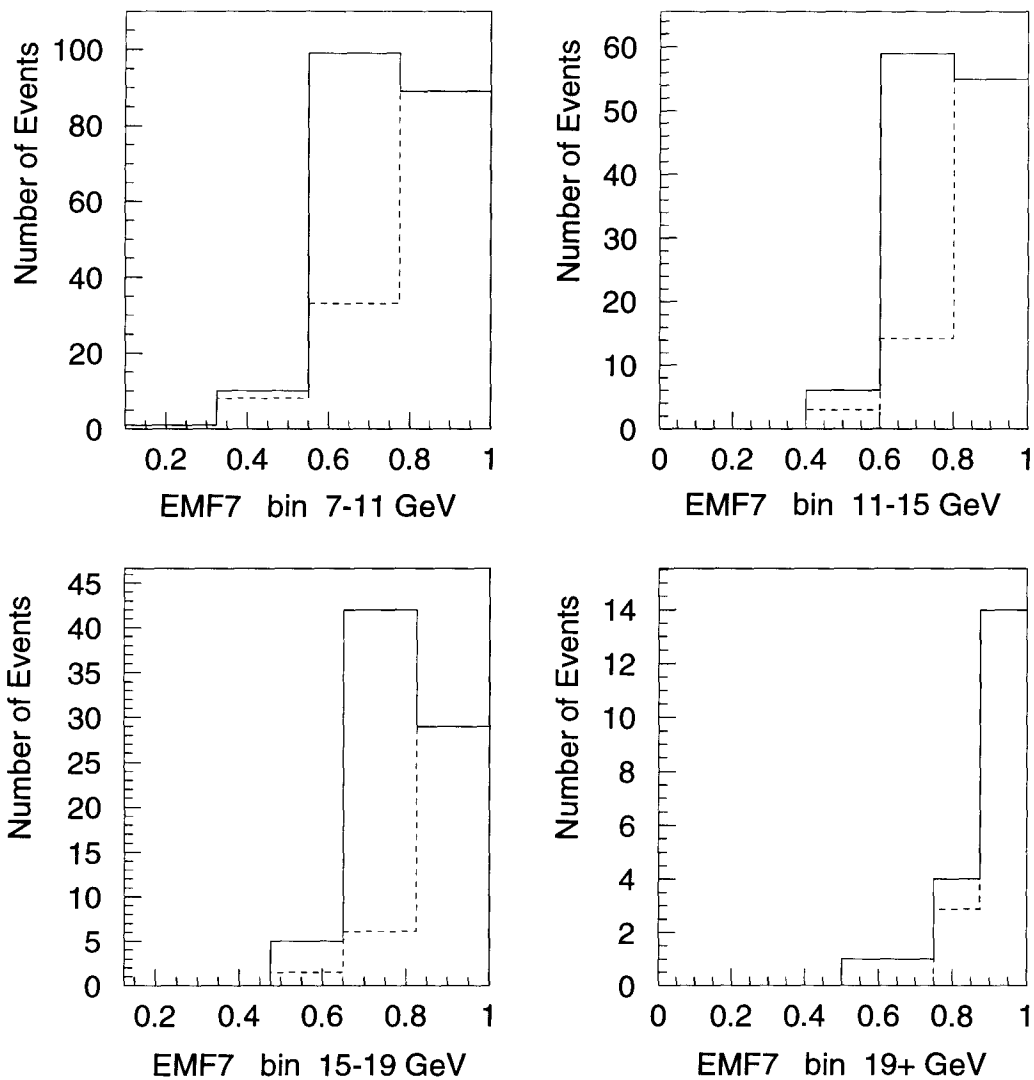


Figure 9.8: P23 $EMF7$ distributions in the plug region covered by the PES for each analysis bin. The dashed line shows the spectrum of the direct photon contamination.

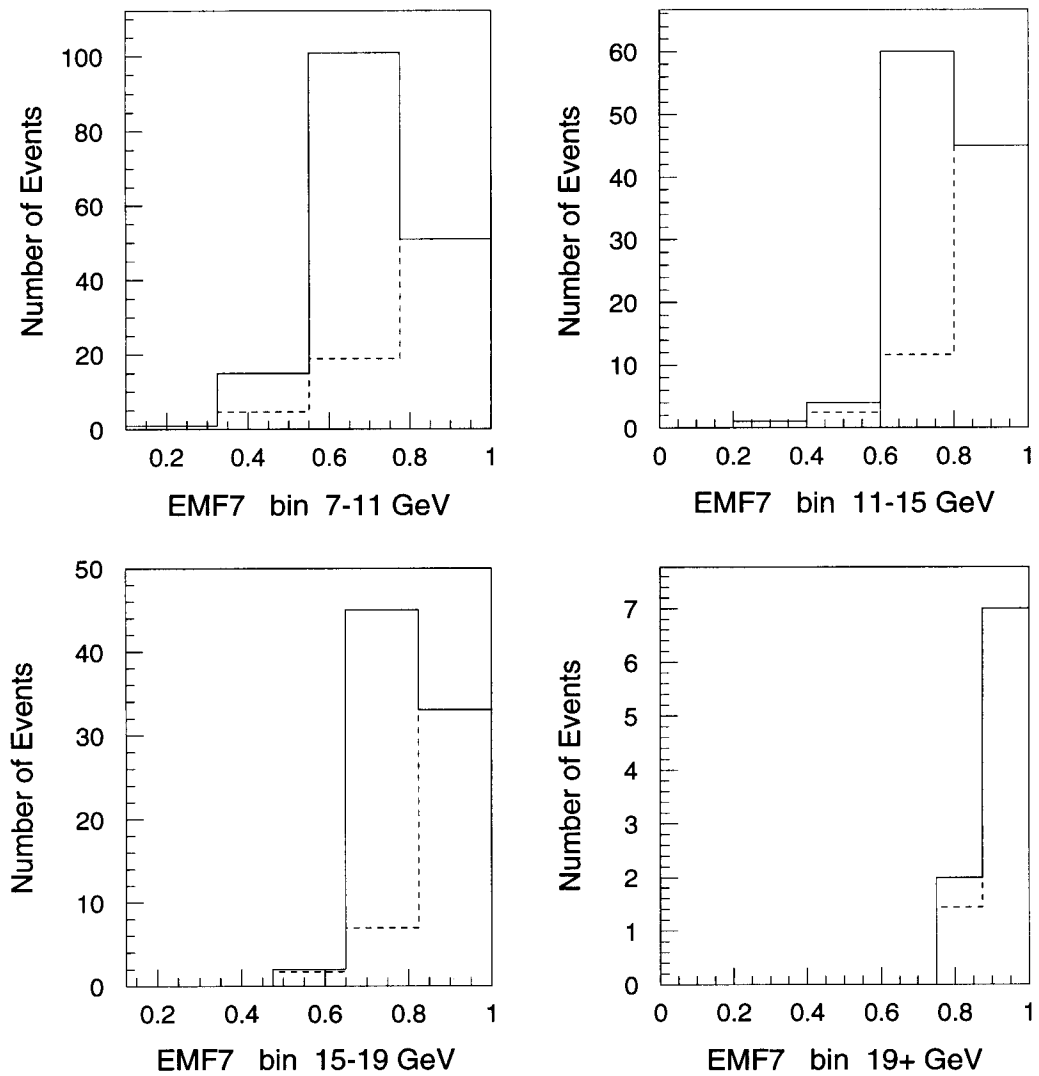


Figure 9.9: P23 $EMF7$ distributions in the plug region not covered by the PES for each analysis bin. The dashed line shows the spectrum of the direct photon contamination.

	E_T Bin	PES		no PES	
		$N_{dir\gamma}$	N_{bkgr}	$N_{dir\gamma}$	N_{bkgr}
P23	7–11	100.1	$40.9 \pm 12.3 \pm 8.2$	79.1	$88.9 \pm 11.1 \pm 23.3$
P16		23.1	$17.9 \pm 8.8 \pm 8.2$	20.9	$26.1 \pm 5.4 \pm 6.4$
P23	11–15	59.2	$33.8 \pm 8.8 \pm 7.1$	57.4	$52.6 \pm 8.8 \pm 13.4$
P16		21.5	$14.5 \pm 5.3 \pm 4.1$	13.8	$16.2 \pm 4.3 \pm 3.8$
P23	15–19	33.4	$21.6 \pm 6.6 \pm 6.7$	38.7	$37.4 \pm 7.3 \pm 8.1$
P16		15.4	$6.6 \pm 4.4 \pm 2.7$	12.7	$13.3 \pm 4.1 \pm 3.4$
P23	19+	17.3	$1.7 \pm 4.6 \pm 0.4$	8.7	$0.3 \pm 3.3 \pm 0.6$
P16		41.0	$11.0 \pm 17.3 \pm 3.2$	27.6	$16.4 \pm 6.0 \pm 4.4$

Table 9.8: Number of the direct photons $N_{dir\gamma}$ and number of background events (fake photons from jet fragmentation), N_{bkgr} , in the rapidity regions $1.28 < \eta < 1.78$ (PES) and $1.10 < \eta < 1.28$ or $1.78 < \eta < 2.40$ (no PES) of the P16 and P23 photon trigger samples (\pm stat. \pm syst.). All events pass the plug photon analysis requirements. The results are obtained via a study of the electromagnetic fraction in a cone of $\Delta R_{\ell\gamma} = 0.7$ of a cluster (*EMF7*).

This measurement needs to be done separately for each analysis bin and for the two plug regions, covered and not covered by the PES. As an example, Figure 9.8 (Figure 9.9) shows for the rapidity region covered (not covered) by the PES, the *EMF7* distributions of all clusters in the P23 sample that pass the plug photon requirements for each analysis bin. The spectrum of the direct photon contamination is overlaid (dashed curve).

Since we are statistically very limited and the magnitude of the statistical as well as the systematic error is governed by the number of events in the highest *EMF7* bin, we chose the highest *EMF7* bin as large as possible. Its maximum size is constrained by the requirement that the number of jet events in the highest *EMF7* bin be small. This situation is different for each analysis bin because the jet and direct photon *EMF7* spectra are shifted towards larger values for increasing

Sample	E_T Bin (GeV)	$\mathcal{P}_i^{pem}(jet \rightarrow '\gamma')$	
		no PES	PES
P23 P16	7 – 11	62.0 \pm 7.5 \pm 16.3 74.1 \pm 15.3 \pm 18.2	27.2 \pm 8.3 \pm 12.1 48.2 \pm 15.6 \pm 22.1
P23 P16	11 – 15	73.2 \pm 12.2 \pm 18.6 83.2 \pm 22.1 \pm 19.5	49.0 \pm 12.7 \pm 18.7 78.4 \pm 28.6 \pm 22.2
P23 P16	15 – 19	91.2 \pm 17.8 \pm 19.8 101.3 \pm 31.2 \pm 25.9	58.0 \pm 17.7 \pm 26.9 57.0 \pm 38.0 \pm 23.3
P23 P16	19+	1.8 \pm 19.3 \pm 14.0 30.8 \pm 11.3 \pm 8.3	10.2 \pm 27.5 \pm 7.6 20.6 \pm 13.7 \pm 6.0

Table 9.9: Fragmentation probability $\mathcal{P}_i^{pem}(jet \rightarrow '\gamma')$ in the plug rapidity regions $1.28 < \eta < 1.78$ (PES) and $1.10 < \eta < 1.28$ or $1.78 < \eta < 2.40$ (no PES) determined with the P16 and P23 trigger samples. The numbers are in units of 10^{-5} (\pm stat. \pm syst.) .

energies. However, as the results should not depend on the chosen binning, we determined the direct photon estimate for three different $EMF7$ bin sizes (± 0.025) and interpreted the difference as one part of the systematic error. Another part comes from a estimate of the overall uncertainty due to the small fraction of jets in the highest $EMF7$ bin, which we will discuss more quantitatively further below.

The final result for number of direct photons, which is summarized in Table 9.8, is the weighted average of the results for the three $EMF7$ bin sizes. The weight factors are given by the number of events in the highest $EMF7$ bin. Table 9.8 also lists the number of fake photon events per analysis bin that pass the plug photon cuts after subtracting the fraction of direct photons.

The calculation of the jet fragmentation probability in the plug $\mathcal{P}_i^{pem}(jet \rightarrow '\gamma')$ is equivalent to the one of the central background analysis. According to Equation 6.1, the number of fake photon events is divided, bin by bin, by the number of extra jets in the plug that are $\Delta R > 0.7$ away from the trig-

Sample	E_T Bin (GeV)	no PES	PES	Total
Run 1a Run 1b	7 – 11	2066 7047	2191 6470	4257 13517
Run 1a Run 1b	11 – 15	840 2606	810 2816	1650 5422
Run 1a Run 1b	15 – 19	363 1091	326 1167	689 2258
Run 1a Run 1b	19+	670 2044	581 1836	1251 3880

Table 9.10: Number of jets per analysis bin with $\Delta R_{jet \ell} > 0.7$ in the electron $W\gamma$ sample for the photon rapidity regions $1.28 < \eta < 1.78$ (PES) and $1.10 < \eta < 1.28$ or $1.78 < \eta < 2.40$ (no PES)

ger cluster. The fragmentation probabilities are in the order of $\lesssim 10^{-3}$ in the lower transverse energy range between 7 and 19 GeV (Table 9.9). At higher energies, the probability decreases.

The jet fragmentation probabilities in the central photon analysis are of similar order of magnitude. Differences are expected due to the different definition of a photon in the two detector regions.

The numbers determined from the P16 and P23 samples agree with each other within the relatively large uncertainties; the final QCD background estimate obtained via either sample is comparable within errors. Because of the smaller uncertainty in the P23 results—due to the larger sample size, we will use the P23 numbers exclusively in the following discussion.

Multiplication of the fragmentation probabilities with the number of jets in the $W\gamma$ samples, which are $\Delta R_{\ell\gamma} > 0.7$ away from the W decay lepton (Figure 9.10), yields the number of background events in each bin for the two regions covered and not covered by the PES. Tables 9.12 summarize the total number of

Sample	Tauonic Decays	One-Legged $Z\gamma$
W (electron)	1.05 ± 0.08	2.29 ± 0.17
W (electron + muon)	1.48 ± 0.10	3.92 ± 0.30

Table 9.11: Summary of non-QCD backgrounds in the Run 1a+b central W + plug photon data sample in the individual electron and combined electron + muon channels, obtained from Baur plus Fast Monte Carlo studies.

background events in each analysis bin for the electron channel for the Run 1a and the preliminary Run 1b plug data sets. We find an overall QCD jet fragmentation background of 15.1 ± 5.3 events.

Other non-QCD background contributions from misidentified $Z\gamma$ and τ channel $W\gamma$ events are small. A Baur plus Fast Monte Carlo study provides an estimate of 3.3 ± 0.3 events in the electron channel. Table 9.11 lists the individual contributions.

In Section 9.4, we will include $W\gamma$ data from the muon decay channel to maximize the statistics. In analogy to the discussion above, we found for this channel in a preliminary background study 4.2 ± 2.1 and 2.1 ± 0.2 events due to QCD jet fragmentation and non-QCD background, respectively [81].

Finally, the total background for the 75 pb^{-1} central W + plug photon sample in combined electron + muon channel becomes 24.7 ± 5.3 events.

The crucial point in the described method is the assumption that the number of jets in the highest bin of the P23 (P16) $EMF7$ spectrum is negligible. There are several indications that such an assumption is reasonable: As shown in Figure 9.6, jet events do not tend to be populated in high $EMF7$ regions—even when the sample is contaminated with electromagnetic objects. Moreover, if we apply the photon selection cuts (except for the $\chi_{3 \times 3}^2$ cut, which is ‘inversed’) to the jet selection, we find only a negligible number of events in the region of the highest $EMF7$ bin for

E_T Bin (GeV)	QCD Background in Plug, e	
	Run 1a	Run 1b
7–11	$1.9 \pm 0.3 \pm 0.6$	$6.2 \pm 1.1 \pm 1.9$
11–15	$1.0 \pm 0.2 \pm 0.3$	$3.3 \pm 0.7 \pm 1.0$
15–19	$0.6 \pm 0.2 \pm 0.2$	$1.8 \pm 0.6 \pm 0.6$
19+	$0.1 \pm 0.3 \pm 0.1$	$0.2 \pm 0.9 \pm 0.3$
7+	$3.6 \pm 1.0 \pm 1.2$	$11.5 \pm 3.3 \pm 3.8$

Table 9.12: Total number of QCD background events per analysis bin (\pm stat. \pm syst.) for the Run 1a+b central W + plug photon sample in the electron channel, determined from the P23 photon trigger sample.

each analysis bin. Independent Monte Carlo studies have shown similar results [82] [83].

Quantitatively, we are interested in an estimate of the number of jets in the highest $EMF7$ bin, \hat{n}_{jet} . We obtain such an estimate by using the ‘W + jet’ and ‘ $\chi_{3 \times 3}^2 > 6$ ’ jet $EMF7$ spectra, introduced above. Two different methods are considered:

Method 1.

We determine in the W + jet sample the fraction of jets in the highest $EMF7$ bin, $\hat{N}^{Wjet}/N_{tot}^{Wjet}$, and multiply this ratio by the total number of electromagnetic clusters in the P23 sample n_{em} .

$$\hat{n}_{jet} = n_{em} \cdot \frac{\hat{N}^{Wjet}}{N_{tot}^{Wjet}} \quad (9.2)$$

Method 2.

Making the assumption that half of the events in the highest bin of the P23 fake photon $EMF7$ distribution are jets, we divide this number by the total number of

events in the same distribution to obtain an upper limit for the fraction of jets in the highest *EMF7* bin of any jet-only data sample, \hat{f}_{jet} . We convert this fraction into an absolute number by multiplying with the total number of events, $N_\gamma^{\chi^2}$, in the ‘ $\chi_{3 \times 3}^2 > 6$ ’ jet spectrum, which pass the plug photon requirements. If we want to translate this number into an estimate of the corresponding number of jets in the P23 sample, we need to account for the different sample sizes by multiplying with the ratio of the total number of events (jets) in both samples, $n_{em}/N_{tot}^{\chi^2}$. We hereby make the assumption that all electromagnetic clusters in the P23 samples are jets.

$$\hat{n}_{jet} = \hat{f}_{jet} \cdot N_\gamma^{\chi^2} \cdot \frac{n_{em}}{N_{tot}^{\chi^2}} \quad (9.3)$$

Note, that *all* assumptions made in this method are of conservative nature.

Table 9.13 summarizes the number of events predicted in the highest *EMF7* bin by these methods for each analysis bin. As expected, the estimate in *Method 2* is more conservative than the one in *Method 1*, except for the 19+ GeV bin, where the statistical uncertainty is largest (70% in *Method 2*).

Based on these results, we estimate an additional systematic error in the determination of the direct photon contamination by assuming that 10% of the events in the highest fake photon *EMF7* bin are jets.

9.3.1 Comparison of the Shower Profile Method with the *EMF7* Method

The *EMF7* method was developed for the plug region because no other algorithm for estimating the direct photon contamination in the photon samples existed. The method, however, is not constrained to a particular detector region. It can also be

E_T Bin (GeV)	Method 1.		Method 2.	
	absolute	relative	absolute	relative
7–11	3.7	7.3%	4.9	9.6%
11–15	1.9	4.2%	4.2	9.3%
15–19	1.5	4.5%	4.6	13.9%
19+	0.76	10.9%	0.22	3.1%

Table 9.13: Absolute and fractional number of jets in the highest P23 $EMF7$ bin, estimated by the two methods discussed in the text, per analysis bin.

considered an alternative to the shower profile method used in the central QCD background analysis. Redetermination of the number of *central* direct photons provides two independent results and serves as a cross check for both methods.

The $EMF7$ method is applied in the central region in complete analogy to the direct photon analysis in the plug, described above. We create Hybrid Monte Carlo $EMF7$ spectra of photons by throwing random cones in the central region of the P23 (P16) sample. For each of the four analysis bins, we match the highest bin of the Monte Carlo photon $EMF7$ distribution to the highest bin of the P23 (P16) $EMF7$ distribution with the same binning. The bin sizes are maximized so that the jet contamination in the highest $EMF7$ bin is negligible ($\lesssim 10\%$). Integration over the fitted photon $EMF7$ distribution for each analysis bin yields the direct photon estimate. Table 9.14 compares the results obtained with the $EMF7$ method to those obtained with the shower profile method in the central photon analyses. We find a good overall agreement for all analysis bins in both photon samples P16 and P23.

	E_T Bin	$N_{tot\gamma}$	$N_{dir\gamma}$	Shower Profile	$N_{dir\gamma}$	$EMF7$		
P23	7 – 11	446	206.8	± 33.8	± 68.5	253.2	± 23.4	± 42.3
P16		90	33.8	± 14.9	± 13.5	34.3	± 6.1	± 8.1
P23	11 – 15	69	28.2	± 10.9	± 8.6	41.0	± 9.3	± 4.9
P16		45	30.2	± 9.1	± 5.7	29.4	± 8.5	± 5.0
P23	15 – 19	27	27.0	± 7.2	± 3.6	20.7	± 6.6	± 2.3
P16		27	18.2	± 6.8	± 3.4	9.3	± 4.4	± 1.8
P23	19+	17	8.0	± 31.3	± 36.4	(21.8)	± 6.8	± 1.2
P16		54	44.8	± 12.8	± 15.9	42.9	± 8.3	± 6.0

Table 9.14: Comparison of the number of the direct photons $N_{dir\gamma}$ (\pm stat. \pm syst.) obtained via the shower profile or $EMF7$ method in the central region of the QCD samples P16 and P23, per analysis bin (in GeV). $N_{tot\gamma}$ is the total number of electromagnetic clusters that pass all central photon analysis cuts.

9.4 Kinematic Distributions

In the following section, we include the results from the muon $W +$ plug photon analysis in order to maximize statistics. Applying the plug photon analysis cuts, discussed in Section 9.1, to the preliminary inclusive Run 1a+b muon W data sample we find $6 + 15 = 21$ events. The QCD jet fragmentation background is obtained in analogy to the discussion above by adding up the products of plug jet fragmentation probability per analysis bin i , $\mathcal{P}_i^{pem}(jet \rightarrow \gamma')$ (Table 9.9) times the number of jets in the muon $W +$ jet sample.

The total $W +$ plug photon sample in the combined electron + muon W decay channel consists of 81 ± 9 (stat.) events. In the following, we are going to show kinematic distributions of these 81 measured events, together with the Standard Model distributions.

Figure 9.10 (Figure 9.11) compares the photon transverse energy (transverse cluster mass M_{TC}) to the QCD background corrected Standard Model prediction.

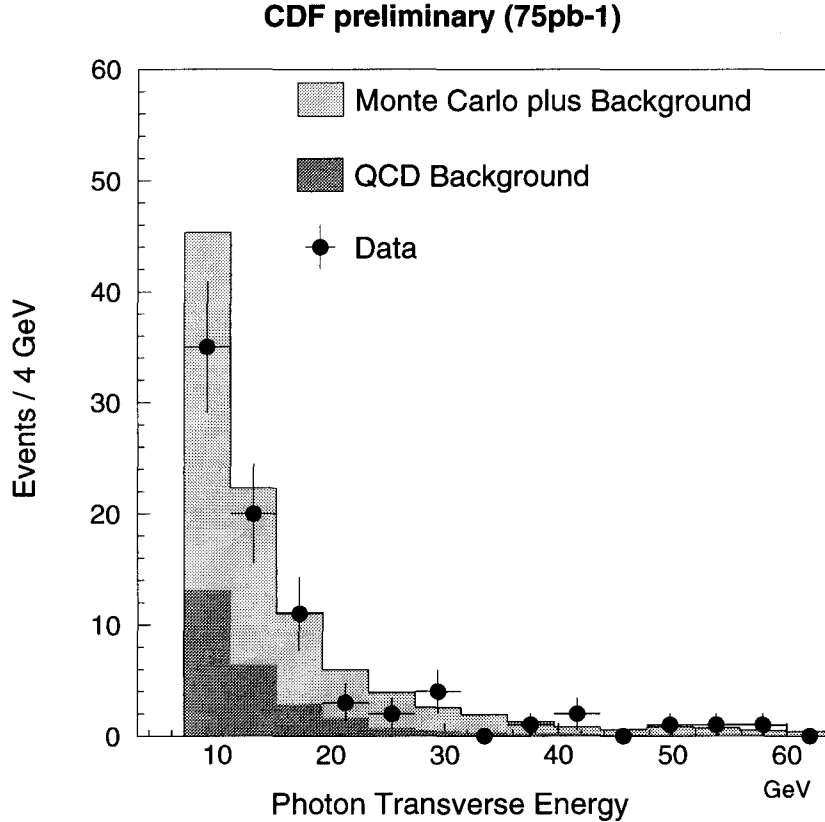


Figure 9.10: Transverse photon energy spectrum for central $W + \text{photon}$ events.

The shape of the QCD background distribution for these and the following plots is defined by the shape of the corresponding jet spectrum in $W + \text{jet}$ events, where each of the jets is weighted by the fragmentation probability, depending on its energy.

The measurements agree well with the Standard Model predictions. As for the central photon $W\gamma$ analysis, no significant number of high events with high transverse momentum or transverse cluster mass, which would give evidence for non-Standard Model couplings, are found.

Two other remarkable Standard Model predictions, which have not been experimentally observed, are a large asymmetry in photon rapidity distributions and a

CDF preliminary (75pb-1)

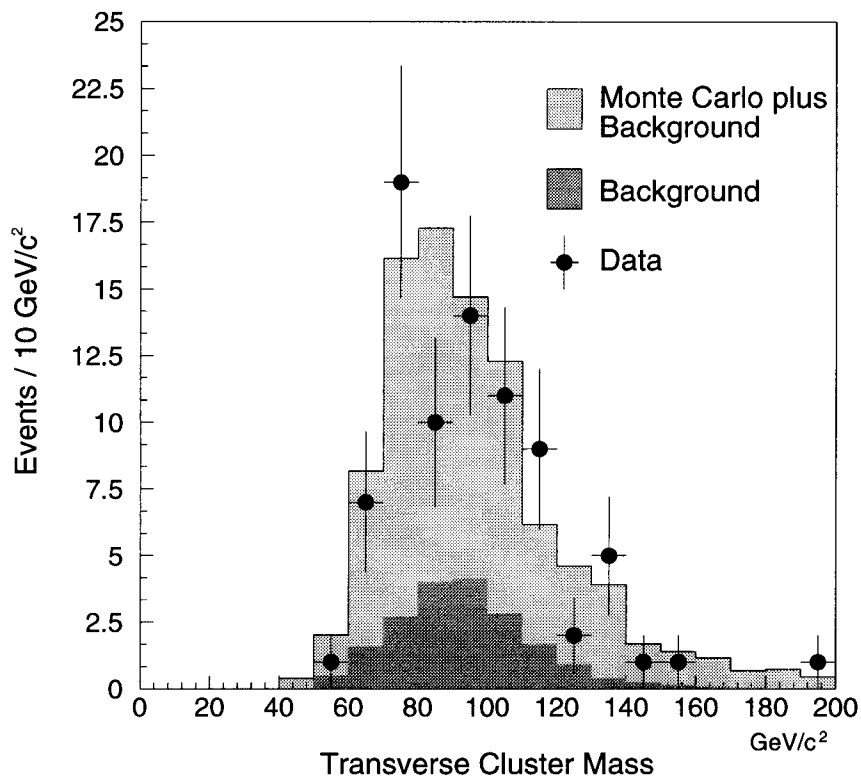


Figure 9.11: Transverse cluster mass distribution for central W + plug photon events.

dip in various angular distributions due to gauge cancellations (Section 2.1). Since background events largely fill up the dip, a significant analysis of this phenomenon will only be possible when a sufficient amount of data will be available, which is expected by the end of Run 1b. However, the photon rapidity asymmetries are already accessible for observation, as will be discussed in the next section.

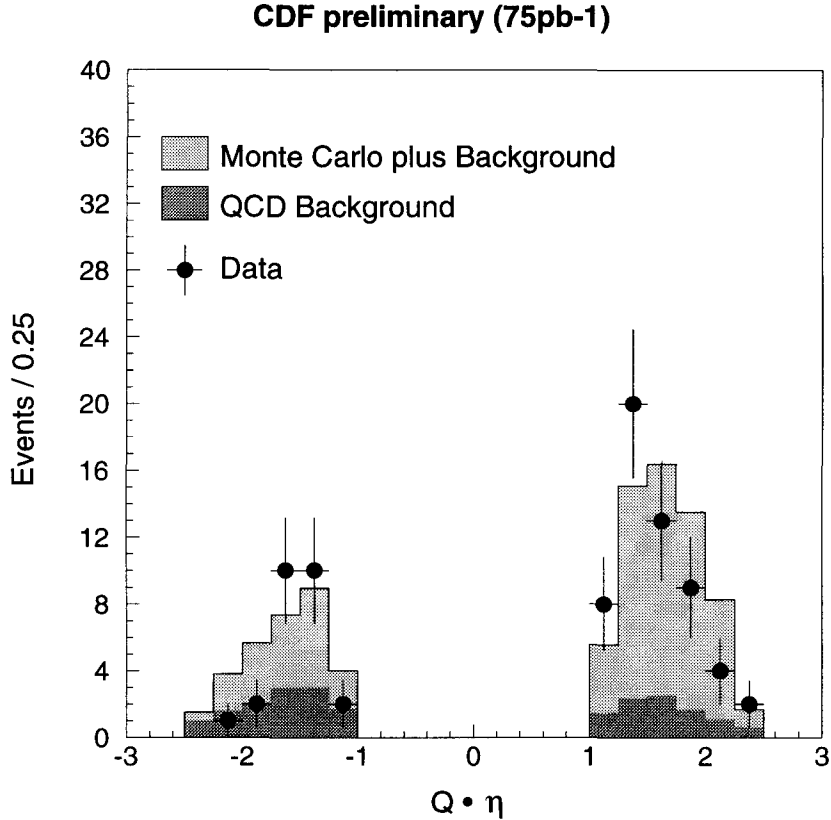


Figure 9.12: Charge-signed photon pseudorapidity distribution for central W + plug photon events.

9.5 Asymmetries in Photon Rapidity Distributions

Events with a central W electron and plug photon give us the opportunity to study rapidity correlations predicted for $W\gamma$ processes by the Standard Model. The observed effects are far less pronounced for the predominantly small photon lepton separations in central W + central photon events. In the following, we are going to report on the measurement of a large asymmetry in both the W charge-signed pseudorapidity difference between the photon and the W decay lepton, $Q_W \cdot \Delta\eta_{\gamma\ell}$, and the photon pseudorapidity distribution, $Q_W \cdot \eta_\gamma$. We analyzed the data sample

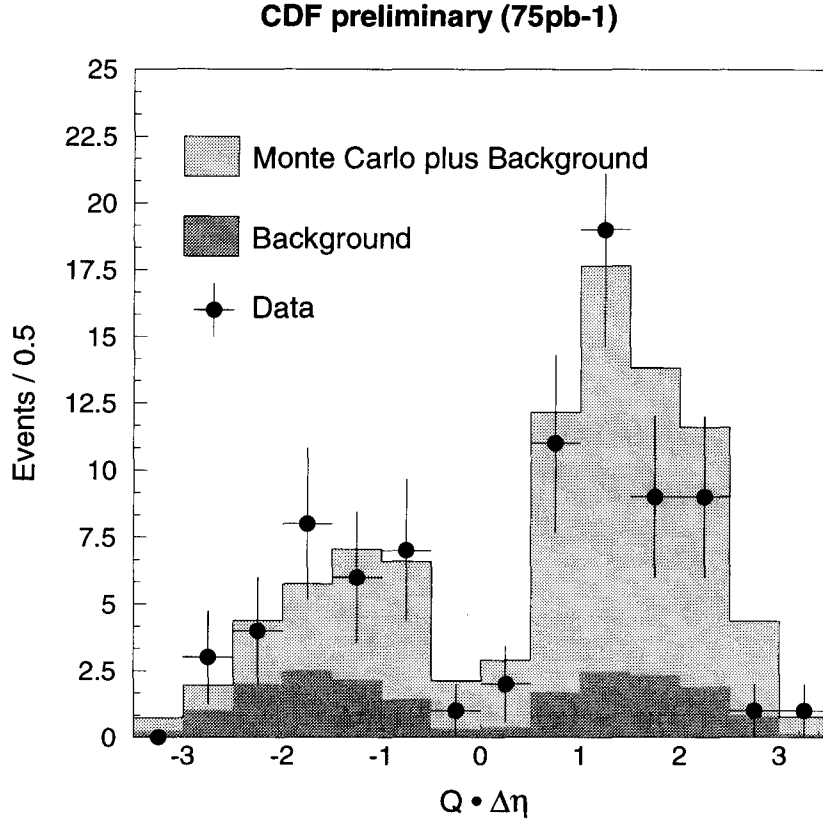


Figure 9.13: Charge-signed pseudorapidity difference between the photon and the W decay lepton in central W + plug photon events.

of about 75 pb^{-1} central W + plug photon events, as defined above.

In Figure 9.12 and Figure 9.13 we compare the measured distributions for $Q_W \cdot \eta_\gamma$, and $Q_W \cdot \Delta\eta_{\gamma\ell}$, to their Standard Model plus background predictions. Again, the Standard Model calculation was performed with the Baur event generator and the Fast Monte Carlo detector simulation. In both cases, we observe a strong rapidity asymmetry. The measured and theoretical distributions compare well.

Quantitatively, the predicted Monte Carlo ratio of the number of events with positive-signed values over the total number of events for both distributions is 76% for the chosen cuts. In the experiment, we find $77 \pm 7\%$ and $70 \pm 8\%$ for $Q_W \cdot \eta_\gamma$ and $Q_W \cdot \Delta\eta_{\gamma\ell}$, respectively. Background, which is assumed to be symmetrically

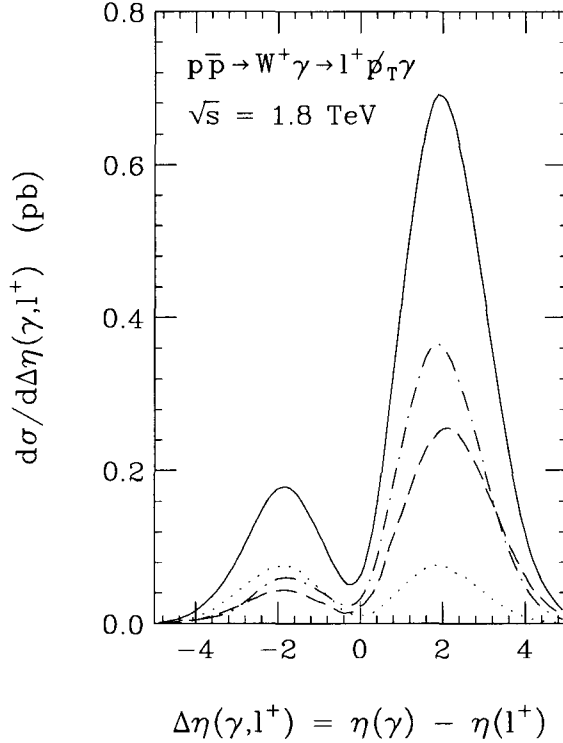


Figure 9.14: Photon-lepton pseudorapidity difference, $d\hat{\sigma}/d\Delta\eta(\gamma, \ell^+)$ for $W^+\gamma$ processes, calculated with the Baur Monte Carlo in the Born approximation. The following interactions were simulated: sea - sea quark (dotted line), sea - valence quark (dash-dotted line) and valence - valence quark (dashed line). The solid line shows the sum of these contributions. The plot is taken from Ref. [19], where also the corresponding selection cuts are discussed.

distributed in both cases, has been subtracted from the data. The errors come from statistical uncertainties in the data and backgrounds.

The asymmetries originate from differences in the electric charge of the u and d quarks. As the photon-quark cross section increases with the quark charge, the photon in $W^+(W^-)\gamma$ production couples predominantly to the u- (\bar{u} -) quark inside the (anti)proton and is therefore emitted in (opposite to) the beam direction. Thus, the number of photon in the region of positive (negative) pseudorapidity and of positive (negative) pseudorapidity differences between the photon and the decay lepton is enhanced.

		Data	Prediction
a)	$Q_W \cdot \Delta\eta_{\gamma\ell}$	0.70 ± 0.08	0.76 ± 0.04
b)	$Q_W \cdot \eta_\gamma$	0.77 ± 0.07	0.76 ± 0.04

Table 9.15: Ratio of the number of positive-signed values to the total number of events for a) the W charge-signed pseudorapidity difference between the photon and the W decay lepton and b) the W charge-signed pseudorapidity of the photon. The numbers are corrected for background. The uncertainties are statistical.

Only valence quarks interactions contribute to the asymmetry effect. Sea - sea quark collisions lead to a symmetric curve, because the distribution of sea - quarks and sea - antiquarks in the proton (or antiproton) is identical [19]. This is shown for $W^+\gamma$ production in Figure 9.14, which also illustrates the strong asymmetry due to valence-sea and valence-valence quark interactions. The asymmetric curves exhibit a pronounced dip at $Q_W \cdot \Delta\eta_{\gamma\ell} = -1/3$, while the dip of the symmetric sea - sea quark distribution is located at $Q_W \cdot \Delta\eta_{\gamma\ell} = 0$. The overall cross-section, however, is not affected by the latter, as sea - sea quark contributions are small; a pronounced asymmetry in the $Q_W \cdot \Delta\eta_{\gamma\ell}$ distribution with a dip at $Q_W \cdot \Delta\eta_{\gamma\ell} = -1/3$ prevails.

Note that the dip in the $Q_W \cdot \Delta\eta_{\gamma\ell}$ distribution is not caused by gauge cancellations only. It is largely due to detector acceptance effects. Since we study plug photons in combination with central W's, the acceptance at small photon-lepton separations in η is reduced for geometrical reasons. To undertake a significant study of the dip, we have to exploit a larger data set comprising the complete photon rapidity range from -2.4 to 2.4 . This goal might be achievable by the end of the ongoing run.

Chapter 10

Conclusions

10.1 Summary of Results

We have discussed the study of weak boson - photon couplings based on data sets taken by CDF during the Tevatron Run 1a (1992–93). The results presented in Chapter 5 – 7 were published in two papers in Physics Letter Review, 1995 [84] [85].

In close analogy to the Run 1a measurements, an analysis of most recently collected data from the ongoing Run 1b (94 – Spring 95) has been performed. The combined Run 1a+b data sample has a size approximately three times larger than the Run 1a data set.

We began the analysis with extracting a well-defined $W\gamma$ and $Z\gamma$ sample in the electron and muon [78] decay channels. Special techniques had to be developed to estimate the background contributions—mainly fake photons from QCD jet fragmentation. Other non-QCD backgrounds were determined with the Baur Monte Carlo as event generator and the Fast Monte Carlo as the CDF detector simulation. These programs were also used for the Standard Model simulation of $W\gamma$ and $Z\gamma$

processes.

We found that the measured cross sections $\sigma \cdot B(W\gamma \rightarrow e\nu_e\gamma)$ and $\sigma \cdot B(Z\gamma \rightarrow e^+e^-\gamma)$ as well as various kinematic distributions compare well with the Standard Model predictions. No deviations were found in the either data set from Run 1a or Run 1a+b combined. The preliminary measurements using the larger data sample from Run 1a+b are consistent with the published results from Run 1a, which we are going to summarize in the following:

We measure the cross sections in the combined electron + muon channel ($\ell = e + \mu$):

$$\sigma \cdot B(W\gamma \rightarrow \ell\nu_\ell\gamma) = 13.2 \pm 4.5 \text{ pb} \quad \text{and} \quad \sigma \cdot B(Z\gamma \rightarrow \ell^+\ell^-\gamma) = 5.1 \pm 1.9 \text{ pb}.$$

The ratio of $W\gamma$ to $Z\gamma$ cross sections is a factor of about 3 times lower than the inclusive W to Z cross section, thus confirming the presence of destructive interference effects between $W\gamma$ Feynman diagrams, as predicted by the Standard Model. These so-called gauge cancellations lead to a reduced number of photon events at high energies, and therefore to a smaller total cross section.

W-photon and Z-photon production are sensitive to possible anomalous couplings, whose presence would indicate novel interactions beyond the Standard Model at higher energies. The low energy effects can be parameterized in form of coupling constants, which must vanish within the realm of the Standard Model. A fit of the transverse energy spectrum of the photon in $W\gamma$ or $Z\gamma$ events yields bounds on anomalous couplings. We measure at 95% CL:

W-Photon \mathcal{CP} -conserving coupling limits ($\Lambda_W = 1.5$ TeV)

$$\begin{aligned} -2.3 < \Delta\kappa < 2.2 & \quad \text{for} \quad \lambda = 0 \\ -0.7 < \lambda < 0.7 & \quad \text{for} \quad \Delta\kappa = 0 \end{aligned}$$

Z-Photon \mathcal{CP} -conserving coupling limits ($\Lambda_Z = 0.5$ TeV)

$$\begin{aligned} -3.0 < h_{30}^Z < 2.9 & \quad \text{for} \quad h_{20}^Z = 0 \\ -0.7 < h_{40}^Z < 0.7 & \quad \text{for} \quad h_{10}^Z = 0 \\ -3.1 < h_{30}^\gamma < 3.1 & \quad \text{for} \quad h_{20}^\gamma = 0 \\ -0.8 < h_{40}^\gamma < 0.8 & \quad \text{for} \quad h_{20}^\gamma = 0 \end{aligned}$$

The limits on the \mathcal{CP} -violating couplings differ by less than 3%. Bounds on more meaningful physical quantities, the electromagnetic (transition) moments of the W (Z) boson, can be extracted from these limits:

$$\begin{aligned} -1.2 < g_W - 2 (\delta_W) < 1.1 & \quad \text{for} \quad q_W^e - 1 (q_W^m) = 0 \\ -1.6 < q_W^e - 1 (q_W^m) < 1.7 & \quad \text{for} \quad g_W - 2 (\delta_W) = 0 \\ -1.1 < \delta_{Z_T}^* (g_{Z_T}^*) < 1.0 & \quad \text{for} \quad q_{Z_T}^m (q_{Z_T}^e) = 0 \\ -6.0 < q_{Z_T}^m (q_{Z_T}^e) < 6.0 & \quad \text{for} \quad \delta_{Z_T}^* (g_{Z_T}^*) = 0 \end{aligned}$$

The electric dipole and quadrupole (transition) moments, corresponding to the parameters δ and q^e , as well as the magnetic dipole and quadrupole (transition) moments, corresponding to the parameters g and q^m , are normalized by their classical (transition) moments.

The quoted form factor scales Λ_V ($V = W$ or Z) represent the maximum energy probed in the individual measurement. They translate into distance scale sensitivities of

$$L_W = \frac{1}{\Lambda_W} = 1.3 \cdot 10^{-4} \text{ fm} \quad \text{and} \quad L_Z = \frac{1}{\Lambda_Z} = 4.0 \cdot 10^{-4} \text{ fm}.$$

In the preliminary analysis of 67 pb^{-1} using a combined Run 1a+b data set (Chapter 8), the statistical uncertainty in the cross section measurements has decreased by about 60%. The limits on anomalous $W\gamma$ ($Z\gamma$) couplings improved by about 10–20% (45%). Since Run 1b is still ongoing, the $W\gamma$ and $Z\gamma$ analyses, as discussed in this thesis, will have to be repeated by the end of the run to update and improve the present results.

Additionally, we have observed a pronounced asymmetry in photon rapidity distributions in a further analysis of Run 1a+b data. We found 77% and 70% of all photons at high pseudorapidities ($1.1 < |\eta_{det}| < 2.4$) have a positive charge-signed pseudorapidity and a positive charge-signed pseudorapidity difference between the photon and the W decay lepton, respectively. The Standard Model predicts 76% for both cases.

10.2 Other Measurements of Vector Boson Self-Interactions at CDF and DØ

Parallel to the measurement that has been described in this thesis, the DØ Collaboration has analyzed $W\gamma$ and $Z\gamma$ data sets from the same Tevatron Run 1a¹. DØ selected photons in the pseudorapidity range $|\eta| < 1.1$ and $1.5 < |\eta| < 2.5$, $\Delta R_{\ell\gamma} > 0.7$ away from the W (Z) decay lepton(s).

CDF and DØ have also searched for WW and WZ processes. CDF has analyzed the $WW, WZ \rightarrow \ell\nu jj$ and $WZ \rightarrow \ell\ell jj$ channels [86], whereas DØ has

¹Preliminary DØ results from the ongoing Run 1b are presently not available.

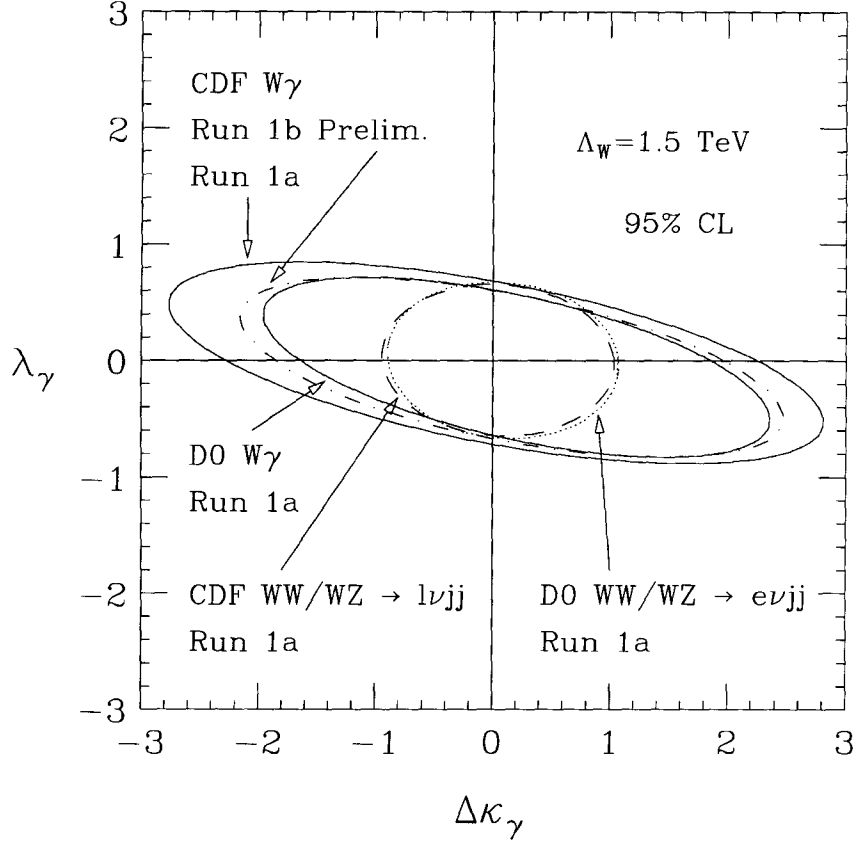


Figure 10.1: Comparison of two-dimensional limit contours at 95% CL for the \mathcal{CP} -conserving couplings λ and $\Delta\kappa$ measured by CDF and $D\bar{O}$ from analyzing $W\gamma$ and WW, WZ processes. The scale sensitivity is 1.5 TeV. $\Delta\kappa_\gamma = \Delta\kappa_Z$ and $\lambda_\gamma = \lambda_Z$ is assumed in the WW/WZ analyses. In other scenarios weaker limits result. The $W\gamma$ analysis does not depend on such assumptions.

studied $WW, WZ \rightarrow e\nu jj$ [39] and $WW \rightarrow \ell\nu\nu$ [87] decays ($\ell = e$ or μ for both experiments).

The general philosophy behind all these analyses is to compare—in a specific way—the number of observed events to the number of predicted events within cuts, in order extract direct limits on $WW\gamma$ and WWZ anomalous couplings.

CDF analyzes the P_T distribution of the dijet system, P_T^{jj} , interpreted as hadronic W/Z decay, and finds one candidate in the $\ell\nu jj$ and none in the $\ell\ell jj$ channel after cutting at $P_T^{jj} > 130$ GeV/c (100 GeV/c) for leptonic W (Z) events.

Cutting at high P_T^{jj} or $P_T^{e\nu}$ eliminates not only background, but also the SM signal. However, sensitivity to anomalous couplings is retained. Limits on these couplings are measured by calculating the probability for the number of observed WW and WZ candidates to fluctuate to the number of events predicted by the Standard Model, including systematic uncertainties. The results, quoted below, are conservative since no background subtraction is performed.

DØ measures one $WW, WZ \rightarrow e\nu jj$ candidate with $P_T^{e\nu} > 130$ GeV/c, but obtains improved limits on anomalous couplings by performing a series of background subtracted fits to the P_T^W spectrum, with a P_T^W cut changed from 25 GeV/c to 130 GeV/c. In this analysis, a detailed background study was necessary.

Figure 10.1 and Figure 10.2 summarize and compare the results in form of two-dimensional contours with those obtained in this work.

Although the DØ limits from the $W\gamma$ ($Z\gamma$) analysis are based on a lower luminosity², they are about 20% (30%) smaller than the corresponding CDF bounds. The non-occurrence of events with high energy photons in the DØ analyses account for this difference.

The limits on $\Delta\kappa$ from the WW, WZ analyses are significantly better than those from $W\gamma$ analyses, whereas the bounds on λ are similar in both cases. However, in the WW, WZ analyses, it is assumed that $\Delta\kappa_\gamma = \Delta\kappa_Z$ and $\lambda_\gamma = \lambda_Z$. If anomalous couplings exist, this equality is most likely not true. Any other correlation between the couplings would result in weaker limits, depending on the assumption made [27]. On the other hand, the $W\gamma$ analysis does not depend on any such assumption.

This difference in the results displayed in Figure 10.1 is due to the fact that

²Data taking at DØ has to be interrupted every time a bunch in the Main Ring passes through the DØ detector.

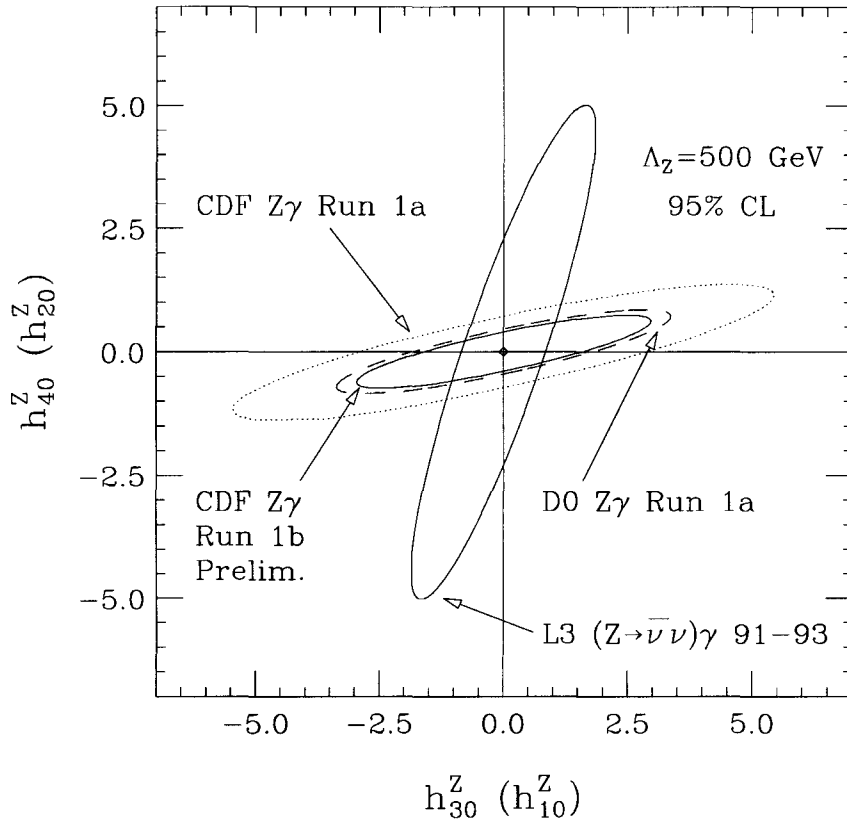


Figure 10.2: Comparison of two-dimensional limit contours at 95% CL for the \mathcal{CP} -conserving couplings h_3^Z and h_4^Z measured from analyzing $Z\gamma$ production in the electron + muon (CDF and $D\bar{O}$) and neutrino (L3) decay channel. The scale sensitivity is 500 GeV. The displayed bounds are the most stringent to date.

contributions to the WW helicity amplitudes for $\Delta\kappa$ grow as $(\sqrt{\hat{s}}/M_W)^2$, while those for $W\gamma$ processes are proportional to $\sqrt{\hat{s}}/M_W$ only. In case of λ , however, this factor is identical in *both* cases ($(\sqrt{\hat{s}}/M_W)^2$).

$D\bar{O}$ limits from analyzing $WW \rightarrow \ell\ell\nu\nu$ are not shown as they are significantly weaker than the displayed bounds.

10.3 The Future

By the end of the first decade of the next millenium high energy physics experiments at the Large Hadron Collider, LHC, and the upgraded Tevatron, TEV^* , are

expected to yield drastic improvements in probing vector boson self-interactions. Only a new powerful e^+e^- collider, such as the presently discussed Next Linear Collider, NLC, will be able to compete. In the intermediate future, LEP II will be able to add significant contributions to the existing knowledge. Although vector boson self-interactions can also be studied at HERA in single W and Z production, integrated luminosities in the order of 1 fb^{-1} are needed in order to achieve a sensitivity comparable to the present day situation [89]. To obtain such large data sets, several years of data taking will be necessary.

In the following we will briefly discuss the expected sensitivities of LHC, TEV*, NLC and LEP II for anomalous couplings. The quoted results are based on theoretical calculations using specific event selection cuts, and depend on several theoretical assumptions as well as an accurate estimate of the background contamination, efficiency determination etc. [90]. They serve only to outline future prospects; the actual sensitivities in the various experiments may differ.

10.3.1 Anomalous Couplings at the Hadron Colliders TEV * and LHC

At the Tevatron, with the the Main Injector upgrade [91] completed, an integrated luminosity of 1 fb^{-1} can be achieved around the turn of this century. Through further upgrades the luminosity could be increased by a factor of 10 in a more distant future (TEV*).

With an integrated luminosity of 10 fb^{-1} , sensitivities on the WWV³ (ZZ γ , Z $\gamma\gamma$) couplings are expected in the order of 10^{-1} – 10^{-2} (10^{-2} – 10^{-3}). Figure 10.3

³The symbol V used for the definition of couplings stands for γ or Z , everywhere in this paragraph.

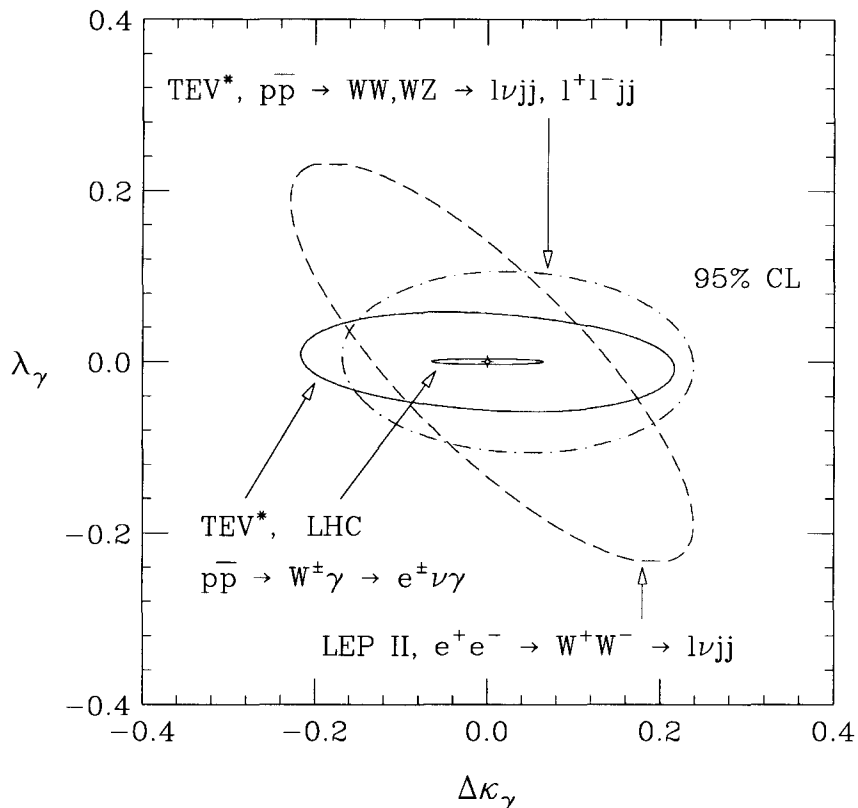


Figure 10.3: Expected sensitivities on the \mathcal{CP} -conserving couplings κ_γ and λ_γ at LHC, TEV* and LEP II. The 95% CL contours are calculated in the HISZ scenario [27].

compares the sensitivities on the anomalous couplings λ_γ and $\Delta\kappa_\gamma$ at 95% CL with those expected from LEP II at $\sqrt{s} = 190$ GeV based on data sets of 500 pb^{-1} . A similar comparison for the prospective bounds on the $Z\gamma$ couplings h_3^Z and h_4^Z is shown in Figure 10.4. If an order of magnitude smaller integrated luminosity is assumed, i.e. 1 fb^{-1} , the measurements will be a factor of 2–3 less sensitive.

Generally speaking, the sensitivities on $W\gamma$ couplings in future experiments at LEP II and TEV* are rather similar; however, when correlations between two couplings are taken into account, the Tevatron will be more sensitive to the coupling parameter λ than LEP II. There is only a negligible form factor sensitivity of these

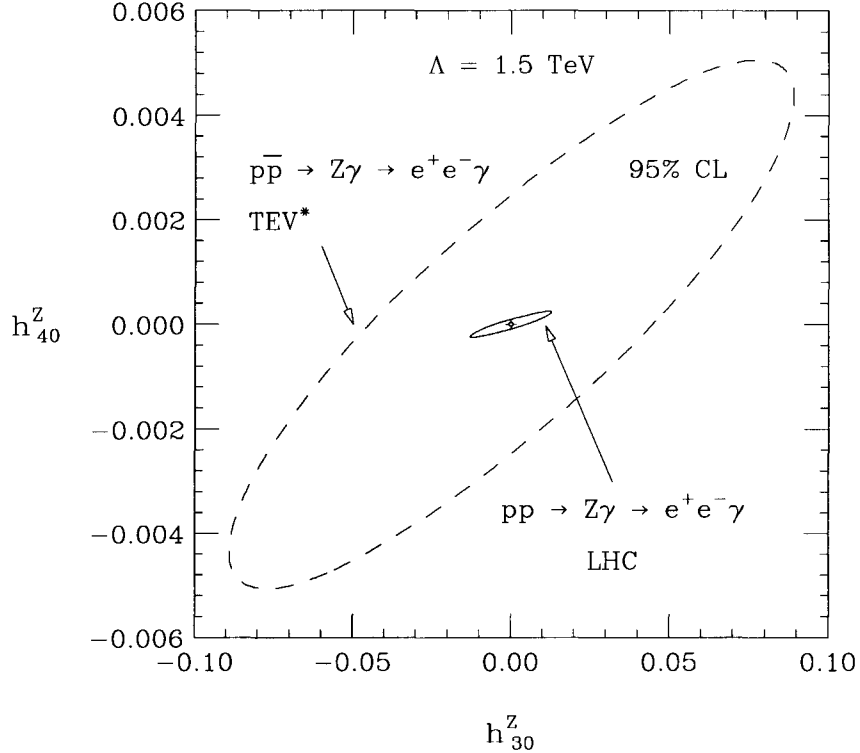


Figure 10.4: Expected sensitivities at 95% CL on the \mathcal{CP} conserving couplings h_3^Z and h_4^Z at LHC and TEV*.

results in both experiments.

Due to the higher center-of-mass energy, and the strong increase of anomalous contributions to the cross section with energy, Tevatron experiments will also measure significantly better bounds on $ZZ\gamma$ ($Z\gamma\gamma$) couplings than those at LEP II. At the Tevatron, these limits depend on the form factor scale assumed. For a further discussion of LEP II, see Section 10.3.1

With the demise of the Superconducting Supercollider, SSC, the Large Hadron Collider will be the only accelerator in the foreseeable future operating in the multi-TeV range. Highest energies are crucial for the search for anomalous couplings as their sensitivity is proportional to $\sqrt{\hat{s}}/M_W$.

Presence of anomalous couplings causes an excess of events with high photon

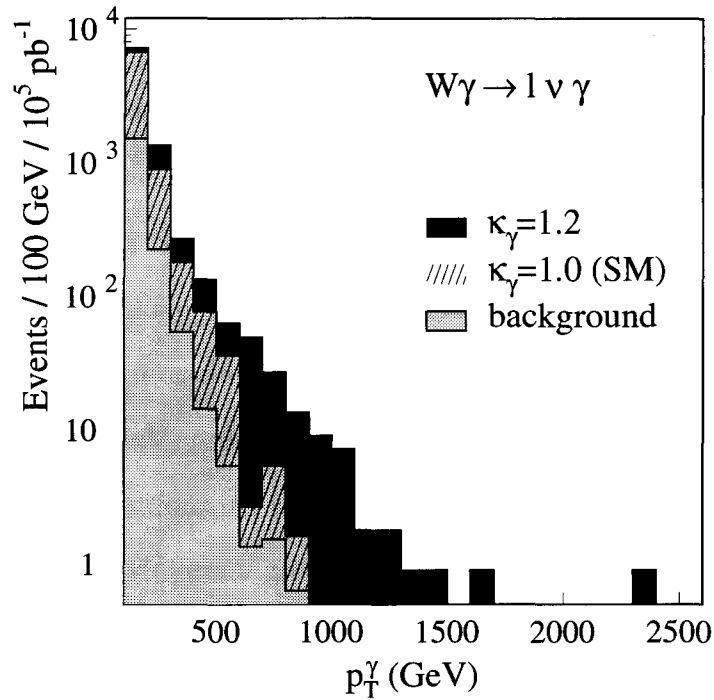


Figure 10.5: Expected photon E_T spectrum at ATLAS for Standard Model (SM) and anomalous ($\kappa_\gamma = 1.2$) W-photon couplings.

energy. At the LHC, photons in the TeV range are expected for an integrated luminosity of 100 fb^{-1} . Figure 10.5 shows the simulation of a typical photon E_T distribution from $W\gamma$ processes at ATLAS, one of the two planned multipurpose detectors at LHC. From a fit of this curve, we expect approximately an order of magnitude better limits than at TEV* with 10 fb^{-1} . As LHC energies are high, the assumed form factor scale affects non-negligibly the bounds on WWV couplings and, to an even stronger degree, on $Z\gamma$ couplings. A maximum scale up to 10 TeV (6 TeV) can be probed in WV ($Z\gamma$) production.

At LHC, since the $t\bar{t}$ production cross section is about a factor of ≈ 20 larger than the W^+W^- production cross section, $t\bar{t}$ processes will be a serious background to the semileptonic W^+W^- analysis. For double leptonic W^+W^- decays, this

background can be suppressed by vetoing events with jet activity. Studying $W\gamma$ or double leptonic W^+W^- , WZ production rather than semihadronic W^+W^- , WZ production will therefore be more sensitive to anomalous couplings.

In general, we expect sensitivities on the anomalous WWV couplings λ_γ ($\Delta\kappa_\gamma$) of better than $\mathcal{O}(10^{-2})$ ($\mathcal{O}(10^{-1})$). Specifically for $\Delta\lambda_\gamma$, even stronger limits in the order of less than 10^{-3} can be envisioned. For the anomalous $Z\gamma V$ couplings h_3^V (h_4^V), the expected bounds are $\mathcal{O}(10^{-3})$ ($\mathcal{O}(10^{-5})$). To achieve such sensitivities, a jet veto ($E_{T,jet} > 50$ GeV) must be imposed, thereby reducing—at LHC energies—large NLO QCD corrections, as well as $t\bar{t}\gamma$ and $b\bar{b}\gamma$ backgrounds.

The LHC obviously offers a great opportunity to discover new physics beyond the Standard Model, associated with vector boson self-interactions. On the other hand, a precise measurement of gauge cancellations in form of the radiation zero ‘dip’, can be easier observed at the Tevatron, provided a sufficiently large luminosity will be available. For such kind of physics, the lower energy at which the Tevatron operates turns out to be of advantage, since at the LHC, due to its higher center-of-mass energy, sizeable QCD corrections are expected to obscure the dip.

10.3.2 Anomalous Couplings at the e^+e^- Colliders LEP II and NLC

The analysis of W^+W^- processes at e^+e^- colliders, compared to hadron colliders, has several advantages. Due to small background contributions the event characteristics is very clean, and the reconstruction of the leptonically decaying W bosons is easier than in $p\bar{p}$ collisions, where a twofold ambiguity of the longitudinal neutrino momentum exists. Moreover, *large* statistics data samples are expected.

A drawback is the energy at which LEP II operates. Although the sensitivity

to anomalous gauge boson couplings is drastically improved at LEP II compared to LEP I, the gauge cancellations are still not fully operative at a center-of-mass energy only slightly above the W pair threshold (176 – 190 GeV). Limits on the couplings $\Delta\kappa_\gamma$ and λ_γ are expected in the range between 15 and 20% (Figure 10.3). They are strongly correlated, in contrast to those obtained through hadronic collisions. On the other hand, these limits are very insensitive to the form factor scale and power assumed.

LEP II bounds on $ZZ\gamma$ and $Z\gamma\gamma$ couplings, derived from $e^+e^- \rightarrow Z\gamma \rightarrow \bar{\nu}\nu\gamma$ and $e^+e^- \rightarrow Z\gamma \rightarrow \mu^+\mu^-\gamma$, respectively, are expected to improve to values in the order of approximately 0.5. The limit contours shown in Figure 10.4 for $ZZ\gamma$ couplings are for a form factor scale of 1 TeV and an integrated luminosity of 500 pb^{-1} . The results, however, do not depend on this scale due to the small center-of-mass energy at LEP I.

The expected bounds on h_3^Z are significantly better than the present day limits from the Tevatron. Hadronic colliders, on the other hand, give stronger bounds on the coupling parameter h_4^Z because its contribution to the $Z\gamma$ cross section increases strongly with the center-of-mass energy. The different energy dependence of h_3^Z and h_4^Z lead to an ellipse whose axes are rotated with respect to the Tevatron curves; the two experiments are nicely complementary.

Much better limits on the anomalous couplings are expected from experiments at the Next Linear Collider, NLC. If built as proposed, the NLC will collide electrons with positrons at a center-of-mass energy $\sqrt{s} = 500 \text{ GeV}$ and a luminosity of $8 \cdot 10^{33} \text{ cm}^{-2}\text{s}^{-1}$, and might later be upgraded to $1.9 \cdot 10^{34} \text{ cm}^{-2}\text{s}^{-1}$ at $\sqrt{s} = 1.5 \text{ TeV}$ [92]. At energies much above the WW production threshold, gauge cancellations are fully operative [93], and the LEP II limits could be improved by two to three

orders of magnitude in very similar analyses [94]. Sensitivities in the order of 10^{-3} or better for both WWV and $Z\gamma V$ couplings are expected. The NLC will not only be competitive with LHC, but might even do better in some cases.

The NLC could also be operated as photon collider using laser backscattering [95]. New exciting modes such as $e\gamma \rightarrow W\nu$ [98] [97], $\gamma\gamma \rightarrow W^+W^-$ [97] or $\gamma e \rightarrow Ze$ [99] would open up for an even closer investigation of vector boson self-couplings.

Appendix A

Summary of Limits

The following Tables summarize the limits on the anomalous $W\gamma$ and $Z\gamma$ couplings and the electromagnetic (transition) moments of the W (Z) boson as measured from the Tevatron Run 1a data set of about 20 pb^{-1} in the individual electron and combined electron + muon channel.

Confidence Level	$\Delta\kappa$ ($\lambda = 0.0$)	λ ($\Delta\kappa = 0.0$)
Electron		
68%	$-1.7 < \Delta\kappa < 1.7$	$-0.5 < \lambda < 0.5$
90%	$-2.4 < \Delta\kappa < 2.4$	$-0.8 < \lambda < 0.8$
95%	$-2.8 < \Delta\kappa < 2.7$	$-0.9 < \lambda < 0.9$
Combined Electron + Muon		
68%	$-1.4 < \Delta\kappa < 1.4$	$-0.4 < \lambda < 0.4$
90%	$-2.0 < \Delta\kappa < 2.0$	$-0.6 < \lambda < 0.6$
95%	$-2.3 < \Delta\kappa < 2.2$	$-0.7 < \lambda < 0.7$

Table A.1: Summary of the one-dimensional limits on the coupling parameters $\Delta\kappa$ and λ for a form factor scale of 1.5 TeV.

Confidence Level	$\tilde{\kappa}$ ($\tilde{\lambda} = 0.0$)	$\tilde{\lambda}$ ($\tilde{\kappa} = 0.0$)
Electron		
68%	$-1.7 < \tilde{\kappa} < 1.7$	$-0.5 < \tilde{\lambda} < 0.5$
90%	$-2.4 < \tilde{\kappa} < 2.4$	$-0.8 < \tilde{\lambda} < 0.8$
95%	$-2.7 < \tilde{\kappa} < 2.7$	$-0.9 < \tilde{\lambda} < 0.9$
Combined Electron + Muon		
68%	$-1.3 < \tilde{\kappa} < 1.3$	$-0.4 < \tilde{\lambda} < 0.4$
90%	$-1.9 < \tilde{\kappa} < 1.9$	$-0.6 < \tilde{\lambda} < 0.6$
95%	$-2.2 < \tilde{\kappa} < 2.2$	$-0.7 < \tilde{\lambda} < 0.7$

Table A.2: Summary of the one-dimensional limits on the coupling parameters $\tilde{\kappa}$ and $\tilde{\lambda}$ for a form factor scale of 1.5 TeV.

Confidence Level	h_{30}^Z ($h_{40}^Z = 0.0$)	h_{40}^Z ($h_{30}^Z = 0.0$)
	Electron	
68%	$-1.7 < h_{30}^Z < 1.7$	$-0.4 < h_{40}^Z < 0.5$
90%	$-2.6 < h_{30}^Z < 2.6$	$-0.6 < h_{40}^Z < 0.7$
95%	$-3.0 < h_{30}^Z < 2.9$	$-0.7 < h_{40}^Z < 0.8$
	Combined Electron + Muon	
68%	$-2.1 < h_{30}^Z < 2.1$	$-0.5 < h_{40}^Z < 0.5$
90%	$-2.7 < h_{30}^Z < 2.7$	$-0.7 < h_{40}^Z < 0.6$
95%	$-3.0 < h_{30}^Z < 2.9$	$-0.7 < h_{40}^Z < 0.7$

Table A.3: Summary of the one-dimensional limits on the $ZZ\gamma$ coupling parameters h_{30}^Z and h_{40}^Z for a form factor scale of 500 GeV.

Confidence Level	h_{10}^Z ($h_{20}^Z = 0.0$)	h_{20}^Z ($h_{10}^Z = 0.0$)
	Electron	
68%	$-1.8 < h_{10}^Z < 1.8$	$-0.5 < h_{20}^Z < 0.5$
90%	$-2.5 < h_{10}^Z < 2.5$	$-0.7 < h_{20}^Z < 0.7$
95%	$-2.9 < h_{10}^Z < 2.9$	$-0.8 < h_{20}^Z < 0.8$
	Combined Electron + Muon	
68%	$-2.0 < h_{10}^Z < 2.0$	$-0.5 < h_{20}^Z < 0.5$
90%	$-2.6 < h_{10}^Z < 2.6$	$-0.7 < h_{20}^Z < 0.7$
95%	$-2.9 < h_{10}^Z < 2.9$	$-0.7 < h_{20}^Z < 0.7$

Table A.4: Summary of the one-dimensional limits on the $ZZ\gamma$ coupling parameters h_{10}^Z and h_{20}^Z for a form factor scale of 500 GeV.

Confidence Level	$h_{30}^\gamma (h_{10}^\gamma) (h_{40}^\gamma (h_{20}^\gamma) = 0.0)$	$h_{40}^\gamma (h_{20}^\gamma) (h_{30}^\gamma (h_{10}^\gamma) = 0.0)$
Electron		
68%	$-1.9 < h_{30}^\gamma (h_{10}^\gamma) < 1.9$	$-0.5 < h_{40}^\gamma (h_{20}^\gamma) < 0.5$
90%	$-2.7 < h_{30}^\gamma (h_{10}^\gamma) < 2.7$	$-0.7 < h_{40}^\gamma (h_{20}^\gamma) < 0.7$
95%	$-3.1 < h_{30}^\gamma (h_{10}^\gamma) < 3.1$	$-0.8 < h_{40}^\gamma (h_{20}^\gamma) < 0.8$
Combined Electron + Muon		
68%	$-2.2 < h_{30}^\gamma (h_{10}^\gamma) < 2.2$	$-0.5 < h_{40}^\gamma (h_{20}^\gamma) < 0.5$
90%	$-2.8 < h_{30}^\gamma (h_{10}^\gamma) < 2.8$	$-0.7 < h_{40}^\gamma (h_{20}^\gamma) < 0.7$
95%	$-3.1 < h_{30}^\gamma (h_{10}^\gamma) < 3.1$	$-0.8 < h_{40}^\gamma (h_{20}^\gamma) < 0.8$

Table A.5: Summary of the one-dimensional limits on the $Z\gamma\gamma$ coupling parameters h_{10}^γ and h_{20}^γ for a form factor scale of 500 GeV.

Confidence Level	$g_W (q_W^e = 1.0)$	$q_W^e (g_W = 2.0)$
Electron		
68%	$-0.9 < g_W - 2 < 0.9$	$-1.3 < q_W^e - 1 < 1.3$
90%	$-1.3 < g_W - 2 < 1.3$	$-1.7 < q_W^e - 1 < 1.7$
95%	$-1.4 < g_W - 2 < 1.4$	$-1.9 < q_W^e - 1 < 1.9$
Combined Electron + Muon		
68%	$-0.7 < g_W - 2 < 0.7$	$-1.0 < q_W^e - 1 < 1.0$
90%	$-1.0 < g_W - 2 < 1.0$	$-1.4 < q_W^e - 1 < 1.4$
95%	$-1.1 < g_W - 2 < 1.1$	$-1.6 < q_W^e - 1 < 1.6$

Table A.6: Summary of the one-dimensional limits on the \mathcal{CP} -conserving electromagnetic moments g_W and q_W^e for a form factor scale of 1.5 TeV.

Confidence Level	d_W ($q_W^m = 0.0$)	q_W^m ($d_W = 0.0$)
Electron		
68%	$-0.9 < d_W < 0.9$	$-1.3 < q_W^m < 1.3$
90%	$-1.3 < d_W < 1.3$	$-1.7 < q_W^m < 1.7$
95%	$-1.4 < d_W < 1.4$	$-2.0 < q_W^m < 2.0$
Combined Electron + Muon		
68%	$-0.7 < d_W < 0.7$	$-1.0 < q_W^m < 1.0$
90%	$-1.0 < d_W < 1.0$	$-1.4 < q_W^m < 1.4$
95%	$-1.1 < d_W < 1.1$	$-1.6 < q_W^m < 1.6$

Table A.7: Summary of the one-dimensional limits on the \mathcal{CP} -violating electromagnetic moments d_W and q_W^m for a form factor scale of 1.5 TeV.

Confidence Level	δ_{Z_T} (g_{Z_T})	$q_{Z_T}^m$ ($q_{Z_T}^e$)
Electron		
68%	$-0.7 < \delta_{Z_T}^*(g_{Z_T}^*) < 0.7$	$-3.4 < q_{Z_T}^m(q_{Z_T}^e) < 3.4$
90%	$-0.8 < \delta_{Z_T}^*(g_{Z_T}^*) < 0.8$	$-5.2 < q_{Z_T}^m(q_{Z_T}^e) < 5.2$
95%	$-1.0 < \delta_{Z_T}^*(g_{Z_T}^*) < 1.0$	$-6.0 < q_{Z_T}^m(q_{Z_T}^e) < 6.0$
Combined Electron + Muon		
68%	$-0.7 < \delta_{Z_T}^*(g_{Z_T}^*) < 0.7$	$-4.0 < q_{Z_T}^m(q_{Z_T}^e) < 4.0$
90%	$-0.9 < \delta_{Z_T}^*(g_{Z_T}^*) < 0.9$	$-5.5 < q_{Z_T}^m(q_{Z_T}^e) < 5.5$
95%	$-1.1 < \delta_{Z_T}^*(g_{Z_T}^*) < 1.1$	$-6.0 < q_{Z_T}^m(q_{Z_T}^e) < 6.0$

Table A.8: Summary of the one-dimensional limits on the electromagnetic transition moments for Z-photon processes for a form factor scale of 500 GeV.

Appendix B

Jet Identification

Partons materialize into jets of hadrons. The jets carry energy and momentum of the parton from which they originated. As the hadrons associated with a jet deposit their energy in the calorimeter, a special clustering algorithm is used to discern the calorific signature of the jet. It is designed to combine the total energy deposited to a matrix of cluster towers. The jet clustering algorithm is therefore different from the one described in Section 4.2.3 for clustering electrons (photons).

The matrix is formed by selecting all towers above a transverse energy of 0.2 GeV within $\Delta R < 0.7$ around a seed tower. The cluster's center-of-gravity in E_T is calculated. As a result, additional towers now lying inside the cone of radius $\Delta R < 0.7$ are added to the matrix; vice-versa, towers outside the cone are removed from the list. Again, the center-of-gravity is determined and towers included in or subtracted from the matrix covering an area $\Delta R < 0.7$ around the new centroid. The process continues until a cluster centroid is found so that no towers have to be added or removed.

Most of the jet energy at CDF is contained in a cone of radius $\Delta R = 0.7$. Larger cones would lead to an increased overlap between jets clusters in an event.

Monte Carlo studies have shown that the described algorithm can reconstruct jets above an uncorrected $E_T > 5$ GeV.

Several corrections have to be applied to the jet found. The energy of a jets may be mismeasured because of uninstrumented detector regions or underlying events, and as a result of non-linearities in hadron calorimeters, since not all jet components will interact with the iron nuclei and deposit their energy in the detector material. Clustering effects additionally contribute to differences in the measured jet and original parton energy. To take account of these effects, a correction was applied to the jet four-vector.

A relative jet correction as a function of the pseudorapidity was measured by 'balancing' the jet, knowing that a dijet in an ideal detector must have a balanced transverse momentum. This method corrects jets back to an equivalent jet in the central region ($0.2 < |\eta| < 0.7$) where the jet response was found to be flat in various analyses and non-linearities are well understood.

An absolute jet energy correction is determined from Monte Carlo studies in order to measure as correctly as possible the energy of the parton that originated the jet. To create the Monte Carlo jet sample, gluons were fragmented with ISAJET routines, which were tuned to agree with the charged particle fragmentation observed by CDF, and run through a full QFL detector simulation.

To subtract contributions from underlying events due to spectator partons, the average transverse energy density in a data sample with very loose trigger selection criteria ('minimum bias trigger') is measured and corrected back to the parton level based on the knowledge of detector non-linearities at low transverse momenta and QFL Monte Carlo studies.

Appendix C

Electron Efficiencies

Electron identification efficiencies are determined from a 'loose' Z sample, as described in Ref. [65] in more detail. The Z events are selected by applying tight cuts on the central electron and requiring the presence of another electron anywhere in the detector. Both electron must form an invariant mass very close to the Z mass. The efficiencies are measured by observing the fraction of second legs that pass the electron identification cuts.

The efficiencies for the cuts that define the W and central Z electron are summarized in Table C.1. Looser requirements are used to identify the second leg of the Z boson. Tables C.2 – C.4 list the corresponding efficiencies for the three detector regions. The total efficiency in the central region has small corrections due to E/P and track reconstruction inefficiencies applied. For completeness, the Level 1–3 trigger efficiencies are given in Table C.5.

Combining these results, the W selection efficiency becomes $\epsilon_W = T^e \cdot c_1 = 75.4 \pm 1.0\%$. The Z selection efficiency is $\epsilon_Z = T^e \cdot c_1 [F_{cc}(2c_2 - T^e \cdot c_1) + F_{cp} \cdot p + F_{cf} \cdot f] = 72.9 \pm 1.6\%$, where F_{cx} are the fractions of Z's with a central (x=c), plug (x=p) or forward (x=f), c_1 , c_2 , p and f are the total electron efficiencies from Table C.1

– Table C.4 and T^e is the total trigger efficiency.

<i>HAD/EM</i>	100.0 $^{+0.0\%}_{-0.5\%}$
<i>ISO4</i>	97.3 $\pm 0.5\%$
Lateral Shower Profile	98.0 $\pm 0.4\%$
E/P	95.0 $\pm 0.7\%$
Track - Profile Match Δx	94.1 $\pm 0.8\%$
Track - Profile Match Δz	98.2 $\pm 0.4\%$
CES Strip / Wire χ^2	95.0 $\pm 0.7\%$
All Cuts	85.1 $\pm 1.1\%$
Tracking, E/P Corrections	99.2 $\pm 0.4\%$
Total Efficiency c_1	84.5 $\pm 1.2\%$

Table C.1: Central W and Z electron selection efficiencies.

<i>HAD/EM</i>	100.0 $^{+0.0\%}_{-0.5\%}$
<i>ISO4</i>	97.3 $\pm 0.5\%$
E/P	95.0 $\pm 0.7\%$
All Cuts	92.4 $\pm 0.7\%$
Tracking, E/P Corrections	99.2 $\pm 0.4\%$
Total Efficiency c_2	91.7 $\pm 0.8\%$

Table C.2: Second central Z electron selection efficiencies.

HAD/EM	$100.0^{+0.0\%}_{-0.3\%}$
$ISO4$	$96.4 \pm 0.9\%$
$\chi^2_{3 \times 3}$	$95.2 \pm 1.1\%$
Total Efficiency p	$90.9 \pm 1.4\%$

Table C.3: Plug Z electron selection efficiencies.

HAD/EM	$100.0^{+0.0\%}_{-1.8\%}$
$ISO4$	$85.9 \pm 4.4\%$
Total Efficiency f	$85.9 \pm 4.4\%$

Table C.4: Forward Z electron selection efficiencies.

Level 1	$99.2 \pm 0.1\%$
Level 2	$91.5 \pm 0.3\%$
Level 3	$98.2 \pm 0.1\%$
Total Trigger Efficiency, T^e	$89.2 \pm 0.3\%$

Table C.5: Electron Trigger Efficiencies.

Bibliography

- [1] S.L. Glashow, *Nucl. Phys.* **22**, 579 (1961); A. Salam in *Elementary Particle Theory*, ed. by N. Svartholm (Almqvist and Wiksells, Stockholm, 1968); S. Weinberg, *Phys. Rev. Lett.* **19**, 1264 (1967).
- [2] R.P. Feynman *Phys. Rev.* **74**, 939 (1949); J. Schwinger, *Phys. Rev.* **73**, 416 (1948); S. Tomonaga *Phys. Rev.* **74**, 224 (1948).
- [3] G. Arnison et al., *Phys. Lett.* **B122**, 103 (1983); M. Banner et al., *Phys. Lett.* **B122**, 476 (1983).
- [4] F. Abe et al., *Phys. Rev. Lett.* **74**, 2626 (1995); F. Abe et al., *Phys. Rev. Lett.* **73**, 225 (1994); F. Abe et al., *Phys. Rev.* **D50**, 2966 (1994).
- [5] S. Abachi et al., *Phys. Rev. Lett.* **72**, 2138 (1994); S. Abachi et al., *Phys. Rev. Lett.* **74**, 2422 (1995); S. Abachi et al., *Phys. Rev.* **D52**, 4877 (1995).
- [6] D.H. Perkins, (1987;) *Introduction to High Energy Physics*, Addison Wesley Co. Inc., Menlo Park (1987); F. Halzen and A.D. Martin, *Quarks and Leptons*, Wiley, New York (1984).
- [7] D. Schaile, CERN-PPE/94-162, to appear in the *Proceedings of the "27th International Conference on High Energy Physics"*, Glasgow, Scotland, 1994; The LEP Collaborations, CERN-PPE/94-187.
- [8] F.M. Renard, *Nucl. Phys.* **B196**, 93 (1982); R. Barbieri, H. Harari and M. Leurer, *Phys. Lett.* **B141**, 455 (1985); J.P. Eboli, A.V. Olinto, *Phys. Rev.* **D38**, 3461 (1988).
- [9] C.N. Yang and R.L. Mills, *Phys. Rev.* **96**, 191 (1954)
- [10] P. Renton, *Electroweak Interactions: An Introduction to the Physics of Quarks and Leptons* (1990), Cambridge.
- [11] Y. Nambu, *Phys. Rev.* **4**, 280 (1960); J. Goldstone *Nuovo Cim.* **19**, 154 (1961), P.W. Higgs *Phys. Rev. Lett.* **13**, 508 (1964); P.W. Higgs *Phys. Rev.* **145**, 1156 (1966).

- [12] Fayyazuddin and Riazuddin, *Quantum Mechanics* (1990), World Scientific, Singapore .
- [13] U. Baur and D. Zeppenfeld, *Nucl. Phys.* **B308**, 127 (1988).
- [14] U. Baur and E.L. Berger, *Phys. Rev.* **D41**, 1476 (1990).
- [15] M. Bilenky et al., *Nucl. Phys.* **B409**, 22 (1993).
- [16] T.D. Lee and C.N. Yang, *Phys. Rev.* **128**, 885 (1962); L.D. Landau and E.M. Lifshitz, *Quantum Mechanics* (Addison-Wesley Publishing Co, Inc., Reading, MA, 1965); H. Aronson, *Phys. Rev.* **186**, 1434 (1969); K.J. Kim and Y.-S. Tsai, *Phys. Rev.* **D7**, 3710 (1973).
- [17] R.W. Brown et al., *Phys. Rev.* **D20**, 1164 (1979), K.O. Mikaelian et al., *Phys. Rev. Lett.* **43**, 746 (1979).
- [18] K.O. Mikaelian, *Phys. Rev.* **D17**, 750 (1978); K.O. Mikaelian, M.A. Samuel and D. Sahdev, *Phys. Rev. Lett.* **43**, 746 (1979); R.W. Brown, K.O. Mikaelian, D. Sahdev, *Phys. Rev.* **D20**, 1164 (1979); T.R. Grose and K.O. Mikaelian, *Phys. Rev.* **D23**, 123 (1981); C.J. Goebel, F. Halzen and J.P. Leveille, *Phys. Rev.* **D23**, 2682 (1981); S.J. Brodsky and R.W. Brown, *Phys. Rev. Lett.* **49**, 966 (1982); M.A. Samuel, *Phys. Rev.* **D27**, 2724 (1983); R.W. Brown, K.L. Kowalski and S.J. Brodsky, *Phys. Rev.* **D28**, 624 (1983); R.W. Brown and K.L. Kowalski, *Phys. Rev.* **D29**, 2100 (1984).
- [19] U. Baur, S. Errede, G. Landsberg, *Phys. Rev.* **D50**, 1917 (1994).
- [20] F. Abe et al., *FERMILAB-PUB-94/244-E* (1994), to be published in *Phys. Rev. D* .
- [21] K. Hagiwara, R.D. Peccei and D. Zeppenfeld, *Nucl. Phys.* **B282**, 253 (1987).
- [22] F. Boudjema, private communication.
- [23] U. Baur and D. Zeppenfeld, *Phys. Lett.* **B201**, 383 (1988).
- [24] U. Baur and E.L. Berger, *Phys. Rev.* **D47**, 4889 (1993).
- [25] J. Alitti, et al., *Phys. Lett.* **B277**, 194 (1992).
- [26] A. De Rujula et al., *Nucl. Phys.* **B384**, 31 (1992); P. Hernández and F.J. Vegas, *Phys. Lett.* **B307**, 116 (1993); C. Burgess and D. London, *Phys. Rev. Lett.* **69**, 3428 (1992); C. Burgess and D. London, *Phys. Rev.* **D48**, 4337 (1993).

- [27] K. Hagiwara, S. Ishihara, R. Szalapski and D. Zeppenfeld, *Phys. Lett.* **B283**, 353 (1992) and *Phys. Rev.* **D48**, 2182 (1993).
- [28] M.S. Alam et al., *Phys. Rev. Lett.* **74**, 2885 (1995).
- [29] F. Boudjema, K. Hagiwara, C. Hamzaoui, and K. Numata, *Phys. Rev.* **D4**, 2223 (1991).
- [30] M. Suzuki, *Phys. Lett.* **B153**, 289 (1985).
- [31] J.A. Grifols, S.Peris and J. Sola, *Int. J. Mod. Phys.* **A3**, 225 (1988).
- [32] J.J. van der Bij, *Phys. Rev.* **D35**, 1088 (1987).
- [33] W.J. Marciano and A. Queijeiro, *Phys. Rev.* **D33**, 3449 (1986).
- [34] J. Bailey et al., *Nucl. Phys.* **B150**, 1 (1979); E.R. Cohen, B.N. Taylor *Rev. Mod. Phys.* **59**, 1121 (1987).
- [35] M. Acciarri et al., *Phys. Lett.* **B346**, 190 (1995).
- [36] K. Hagiwara , J. Woodside and D. Zeppenfeld, *Phys. Rev.* **D41**, 2113 (1990).
- [37] D. Carlsmith and L. Zhang, *CDF-Note* 2951, 1995.
- [38] S. Abachi et al., *Phys. Rev. Lett.* **75**, 1023 (1995).
- [39] L.-P. Chen, *DØ-Note* 2424A, 1995.
- [40] F. Abe et al., *Phys. Rev. Lett.* **75**, 1017 (1995).
- [41] S. Abachi et al., *Nucl. Instr. Meth.* **A338**, 185 (1994).
- [42] F. Abe et al., *Nucl. Instr. Meth.* **A271**, 387 (1988).
- [43] 'The Collider Detector at Fermilab', North Holland Physics Publishing, 1988.
- [44] D. Amidei et al., *Nucl. Instr. Meth.* **A350**, 73 (1994).
- [45] F. Abe et al., to be published in *Phys. Rev. D* .
- [46] D. Amidei et al., *Nucl. Instr. Meth.* **A269**, 51 (1988)and *FERMILAB-PUB-94/232-E* (1994).
- [47] G. Drake et al., *Nucl. Instr. Meth.* **A269**, 68 (1988).
- [48] E. Barsotti et al., *Nucl. Instr. Meth.* **A269**, 82 (1988).

- [49] U. Baur and E.L. Berger, *Phys. Rev.* **D41**, 1476 (1990); U. Baur and E.L. Berger, *Phys. Rev.* **D47**, 4889 (1993).
- [50] G. Peter Lepage, *J. Comp. Phys.* **27**, 192, Academic Press (1978); G. Peter Lepage, CLNS-80/447 (1980).
- [51] H. Plathow-Besch, *Computer Phys. Comm.* **75**, 396 (1993).
- [52] A.D. Martin, R.G. Roberts and W.J. Stirling, *Phys. Lett.* **B306**, 145 (1993).
- [53] F. Abe et al., *Phys. Rev. Lett.* **74**, 850 (1995).
- [54] M. Kobayashi and M. Maskawa, *Prog. Theor. Phys.* **49**, 652 (1973).
- [55] U. Baur, E.W.N. Glover and J.J. van der Bij, *Nucl. Phys.* **B318**, 106 (1989).
- [56] U. Baur, T. Han and J. Ohnemus *Phys. Rev.* **D48**, 5140 (1993); U. Baur, J. Ohnemus and T. Han *Phys. Rev.* **D51**, 3381 (1995).
- [57] J. Ohnemus, *Phys. Rev.* **D50**, 1931 (1994); J. Ohnemus, *Phys. Rev.* **D51**, 1068 (1995).
- [58] QFL Monte Carlo, The CDF Collaboration.
- [59] S. Errede, private communication.
- [60] F. Abe et al., *Phys. Rev. Lett.* **66**, 2951 (1991); F. Abe et al., *Phys. Rev. Lett.* **67**, 2937 (1991).
- [61] F.E. Paige and S.D. Protopopescu, BNL Report No. BNL38034 (1986).
- [62] F.A. Berends , W.T. Giele, H. Kuijf and B. Tausk, *Nucl. Phys.* **B357**, 32 (1991).
- [63] G. Marchesini and B.R. Webber, *Nucl. Phys.* **B310**, 461 (1992); G. Marchesini et al., *Computer Phys. Comm.* **67**, 465 (1992).
- [64] F. Abe et al., *Phys. Rev. Lett.* **75**, 11 (1995); F. Abe et al., *Phys. Rev.* **D52**, 4784 (1995).
- [65] F. Abe et al., *Phys. Rev. Lett.* **73**, 1994 (220); F. Abe et al., *Phys. Rev.* **D52**, 2624 (1995).
- [66] P.N. Harriman, A.D. Martin, R.G. Roberts and W.J. Stirling, *Phys. Rev.* **D42**, 798 (1990).
- [67] A.D. Martin, R.G. Roberts and W.J. Stirling, *Phys. Rev.* **D47**, 867 (1993).

- [68] J. Botts et al., *Phys. Lett.* **B304**, 159 (1993).
- [69] H.-U. Bengtsson and T. Sjöstrand, *Computer Phys. Comm.* **67**, 43 (1987); T. Sjöstrand, *Computer Phys. Comm.* **39**, 347 (1986).
- [70] F. Abe et al., *FERMILAB-PUB-94/171-E* (1994), submitted to *Phys. Rev. D*.
- [71] F. Abe et al., *Phys. Rev. Lett.* **71**, 679 (1993).
- [72] G. Alexander et al., *Phys. Lett.* **B265**, 462 (1991).
- [73] P.D. Acton et al., *Zeit. Phys.* **C58**, 387 (1993).
- [74] R.M. Harris, *Proceedings of the "Workshop on Hadron Structure Functions and Parton Distributions"*, Fermilab, Illinois, 1991, and *FERMILAB-CONF-90/118-E* (1991).
- [75] 'Review of Particle Properties', *Phys. Rev.* **D45**, VI.21 (1992).
- [76] R.M. Harris, R. Blair and S. Kuhlmann *CDF-Note* 1509, 1991.
- [77] T. Müller, private communication.
- [78] M.F. Vondracek, Ph.D thesis, University of Illinois at Urbana-Champaign (1994).
- [79] R.G. Wagner, *Proceedings of the "W γ Z International Symposium on Vector Boson Self-Interactions"*, Los Angeles, California, 1995.
- [80] A. Gordon, D. Kestenbaum, M. Franklin and P. Hurst *CDF-Note* 1811, 1992
- [81] D. Benjamin et al., *CDF-Note* 3206, 1994.
- [82] D. Benjamin et al., *CDF-Note* 2132, 1993.
- [83] D. Benjamin et al., *CDF-Note* 2229, 1993.
- [84] F. Abe et al., *Phys. Rev. Lett.* **74**, 1936 (1995).
- [85] F. Abe et al., *Phys. Rev. Lett.* **74**, 1941 (1995).
- [86] F. Abe et al., *Phys. Rev. Lett.* **75**, 1017 (1995).
- [87] S. Abachi et al., *Phys. Rev. Lett.* **75**, 1023 (1995).

- [88] L.-P. Cheng, H.T., Diehl, private communication; H.T. Diehl, *Proceedings of the "Tenth Topical Workshop on $p\bar{p}$ Collider Physics"*, Fermilab, Illinois, 1995, and *FERMILAB-CONF-95/165-E* (1995), *FERMILAB-CONF-95/250-E* (1995).
- [89] U. Baur and D. Zeppenfeld, *Nucl. Phys.* **B325**, 253 (1989); C.S. Kim, J. Lee and H.S. Song, *Zeit. Phys.* **C63**, 673 (1994); R. Walczak, *Proceedings of the "W γ Z International Symposium on Vector Boson Self-Interactions"*, Los Angeles, California, 1995.
- [90] H. Aihara et al., *FERMILAB-PUB-95/031* (1995).
- [91] D. Amidei et al., *Proceedings of the "DPF'94 Conference"*, Albuquerque, New Mexico, 1994 and *FERMILAB-CONF-94/249-E* (1994); S. Holmes and Y.A. Yarba, *XIV Conference on Charged Particle Accelerators*, Protvino, Russia, 1994, and *FERMILAB-CONF-94/360* (1994).
- [92] R.D. Ruth, *SLAC-PUB-6751* (1995).
- [93] U. Baur, private communication.
- [94] D. Choudhury and F. Cuypers, *Phys. Lett.* **B325**, 500 (1994) and *Nucl. Phys.* **B429**, 33 (1994); A. Miyamoto, *Proceedings of the "Workshop on Physics and Experiments with Linear e^+e^- Colliders"*, Waikoloa, Hawaii, 1993.
- [95] I.F. Ginzburg et al., *Nucl. Instr. Meth.* **205**, 47 (1983) and *Nucl. Instr. Meth.* **219**, 5 (1983); V.I. Telnov, *Nucl. Instr. Meth.* **294**, 72 (1990).
- [96] E. Yehudai, *Phys. Rev.* **D41**, 33 (1990).
- [97] S.Y. Choi and F. Schrempp, *Phys. Lett.* **B272**, 149 (1991).
- [98] E. Yehudai, *Phys. Rev.* **D44**, 3434 (1991).
- [99] S.Y. Choi, *Zeit. Phys.* **C68**, 163 (1995).